

**Evolution of Nanocrystallites in Soft and Hard Nanocomposite Magnetic Materials  
and Characterization of Magnetic Properties of Fe and Co-Based Metglass**



by

**Sheikh Manjura Hoque  
DOCTOR OF PHILOSOPHY  
Department of Physics**



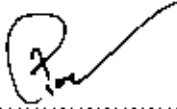
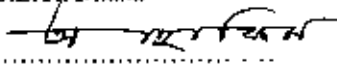
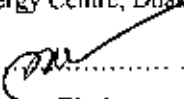
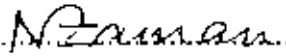

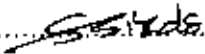
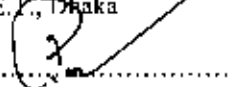
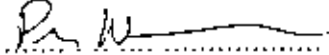
**BANGLADESH UNIVERSITY OF ENGINEERING & TECHNOLOGY**

2007



The thesis titled, "Evolution of Nanocrystallites in Soft and Hard Nanocomposite Magnetic Materials and Characterization of Magnetic Properties of Fe and Co-Based Metglass" submitted by Sheikh Manjura Hoque Roll No : P04041401P Session April 2004 has been accepted as satisfactory in partial fulfillment of the degree of Doctor of Philosophy on 5<sup>th</sup> December, 2007

**BOARD OF EXAMINERS**

- |    |   |                        |
|----|---|------------------------|
| 1. |                                        |                        |
|    | Dr. Md. Feroz Alam Khan<br>(Supervisor)<br>Professor, Dept. of Physics<br>B.U.E.T., Dhaka                               | Chairman               |
| 2. |                                        |                        |
|    | Dr. A. K. M. Abdul Hakim<br>(Co-supervisor)<br>Head, Materials Science Division,<br>Atomic Energy Centre, Dhaka         | Member                 |
| 3. |                                        |                        |
|    | Dr. Abu Ilashan Bhuiyan<br>Professor, Dept. of Physics<br>B.U.E.T., Dhaka   | Member                 |
| 4. |                                      |                        |
|    | Dr. Nazma Zaman<br>Professor, Dept. of Physics<br>B.U.E.T., Dhaka   | Member                 |
| 5. |                                      |                        |
|    | Dr. Nasrul Haque<br>Professor, Dept. of Materials and Metallurgical Engineering<br>B.U.E.T., Dhaka                      | Member                 |
| 6. |                                      |                        |
|    | Dr. Shubendra Shekhar Sikder<br>Professor, Dept. of Physics<br>K.U.E.T., Dhaka  | Member                 |
| 7. |                                      |                        |
|    | Dr. Md. Feroz Alam Khan<br>Head, Dept. of Physics<br>B.U.E.T., Dhaka  | Member<br>(Ex-officio) |
| 8. |                                      |                        |
|    | Dr. Per Nordblad<br>Professor, Solid State Physics, Dept. of Engineering Science<br>Uppsala University, Uppsala, Sweden | Member<br>(External)   |

## CANDIDATE'S DECLARATION

It is hereby declared that this thesis or any part of it has not been submitted elsewhere for the award of any degree or diploma.

*Sheikh Manjura Hoque*

Signature of the Candidate

SHEIKH MANJURA HOQUE

Name of the Candidate

-

**Table of Contents**

<b>Title</b>	<b>Page No.</b>
List of figures	vi
List of tables	xii
List of symbols	xiii
Acknowledgement	xv
Abstract	xvi
<b>Chapter 1 Introduction</b>	<b>1</b>
<b>Chapter 2 Soft and hard Exchange-biased system</b>	
2.1 Fe-based soft nanocomposite magnetic materials	4
2.1.1 Formation of the nanocrystalline state	4
2.1.2 Microstructure-Property Relationship	9
2.2 Co-based soft nanocomposite magnetic materials	11
2.2.1 Theory of Magnetoinductance and Giant Magnetoimpedance	11
2.2.2 GMI phenomenon of Co-rich amorphous alloy	13
2.2.3 Applications of GMI	15
2.3 Fe-based hard nanocomposite magnetic materials	15
2.3.1 Microstructure	16
2.3.2 Magnetic Behavior	20
2.3.3 Technological Realization	21
<b>Chapter 3 Experimentals</b>	
3.1 Melt spin system	25
3.1.1 Preparation of Fe and Co-based soft magnetic ribbon by melt spin system	25
3.1.2 Preparation of Fe-based hard magnetic ribbon by melt spin system	26
3.2 Thermal Analysis Techniques	26
3.2.1 Differential Thermal Analysis (DTA)	26
3.2.2 Differential scanning calorimetry (DSC)	29
3.3 Powder Diffraction	34
3.3.1 Theoretical Considerations	34
3.3.2 Applications	37
3.3.3 Philips X'Pert Pro Multipurpose X-ray Diffractometer	40
3.4 Hysteresisgraph	41
3.4.1 Measurement of an Initial BH-Curve	41
3.4.2 AC BH-Curve Measurements	42
3.4.3 Materials Geometries	42

3.4.4 AMH-20 Low Frequency Automatic Hysteresisgraph System	45
3.5 Vibrating sample magnetometer (VSM)	46
3.5.1 Principle	47
3.5.2 Applications	48
3.5.3 DMS 880 VSM	48
3.6 SQUID magnetometers	49
3.6.1 Basic Components	50
3.6.2 The Features of MPMS XL	51
3.6.3 Specifications	53
3.7 Initial Permeability measurements	54
3.7.1 Inductance Analyzer	55
3.7.2 Impedance Analyzer	55
<b>Chapter 4 Results and Discussions on Fe-based soft nanocomposites</b>	
4.1 Structural and Magnetic Properties of $\text{Fe}_{73}\text{Cu}_1\text{Nb}_{3.5}\text{Si}_{14}\text{B}_{8.5}$	57
4.2 Structural and Magnetic Properties of $\text{Fe}_{73.5}\text{Cu}_1\text{Ta}_3\text{Si}_{13.5}\text{B}_9$	67
4.3 Structural and Magnetic Properties of $\text{Fe}_{75.5}\text{Cu}_{0.6}\text{Nb}_{2.4}\text{Si}_{13}\text{B}_{8.5}$	78
<b>Chapter 5 Results and Discussions on Co-based soft nanocomposites</b>	
5.1 Structural and Magnetic Properties of $\text{Co}_{68}\text{Fe}_4\text{Ni}_1\text{Si}_{15}\text{B}_{12}$	88
5.2 Structural and Magnetic Properties of $\text{Co}_{68}\text{Fe}_4\text{Ni}_2\text{Si}_{15}\text{B}_{12}$	92
5.3 Structural and Magnetic Properties of $\text{Co}_{67}\text{Fe}_4\text{Mo}_2\text{Si}_{15}\text{B}_{12}$	99
<b>Chapter 6 Results and Discussions on Fe-based hard nanocomposites</b>	
6.1 Structural and Magnetic Properties of $(\text{NdPr})_4\text{Fe}_{71}\text{Co}_3\text{Cu}_{0.5}\text{Nb}_1\text{B}_{18.5}$	103
6.2 Structural and Magnetic Properties of $\text{Nd}_4\text{Fe}_{73.5}\text{Co}_3\text{Hf}_{0.5}\text{Ga}_{0.5}\text{B}_{18.5}$	109
6.3 Structural and Magnetic Properties of $\text{Nd}_3\text{Tb}_1\text{Fe}_{76}\text{Cu}_{0.5}\text{Nb}_1\text{B}_{18.5}$	117
<b>Chapter 7 Conclusions</b>	124
<b>References</b>	127
<b>List of Publications Related to This Thesis Work</b>	134

<b>List of Figures</b>	<b>Page No</b>
<b>Chapter 2</b>	<b>5</b>
Fig. 2.1 Dependence of coercivity, $H_c$ , in the whole range of grain size in the nanometer regime up to macroscopic grain sizes.	8
Fig. 2.2. Evolution of $\alpha$ -Fe(Si) nanocrystallites from amorphous matrix.	19
Fig. 2.3. Schematic one-dimensional model of the microstructure and micromagnetic structure of the exchange-coupled composite material as a basis for the calculation of the critical dimensions of the phase regions	22
Fig. 2.4. Typical demagnetization curves $M(H)$ (schematic). (a) Exchange-spring magnet with optimum microstructure (b) with overaged microstructure (c) Conventional single ferromagnetic phase magnet (d) Mixture of two independent ferromagnetic phases with largely different hardness (constricted loop)	
<b>Chapter 3</b>	<b>26</b>
Fig. 3.1. Schematic diagram of melt spin system.	28
Fig. 3.2. Schematic illustration of a DTA cell.	32
Fig. 3.3. Diagram of a heat flux differential scanning calorimeter.	32
Fig. 3.4. Diagram of a power compensated differential scanning calorimeter.	33
Fig. 3.5. A schematic DSC curve demonstrating appearance of several common features.	36
Fig. 3.6. Miller indices of different planes.	37
Fig. 3.7. Bragg reflection of two parallel incident rays 1 and 2.	39
Fig. 3.8. THETA:2-THETA goniometer.	40
Fig. 3.9. THETA:THETA goniometer.	41
Fig. 3.10. Diffractometer Slit System.	43
Fig. 3.11. Schematic diagram of commercial hysteresisgraph.	45
Fig. 3.12. Standard Epstein frame.	45
Fig. 3.13. Testing individual strip sample.	46
Fig. 3.14. (a) Walker Scientific AMH-20 Low Frequency Automatic Hysteresisgraph System for Soft Magnetic Materials. (b) AMH-20 Output.	48
Fig. 3.15. Block diagram of vibrating sample magnetometer.	51
Fig. 3.16. SQUID magnetometer principle.	52
Fig. 3.17. Cut view of a typical superconducting pick-up coils.	52
Fig. 3.18. Second-order gradiometer magnet.	53
Fig. 3.19. Illustration of an RSO measurement with a small amplitude. (a) shows the ideal SQUID response for a dipole and (b) shows the movement of the sample within the SQUID pickup coils.	

## Chapter 4

- Fig. 4.1.1. Differential thermal analysis curves of as-cast amorphous ribbons of at different heating rate. 59
- Fig. 4.1.2. Differential thermal analysis curves of as-cast and annealed samples at the heating rate of 50K/min. 59
- Fig. 4.1.3. Kissinger's plot to determine the activation energy of Fe(Si) phase. 59
- Fig. 4.1.4. Kissinger's plot to determine the activation energy of iron boride phase. 59
- Fig. 4.1.5. X-ray diffraction patterns of the amorphous and annealed samples at different annealing temperature for 1 hour. 61
- Fig. 4.1.6. Variation of lattice parameter,  $a$  and silicon content, %Si of Fe(Si) nanograins. 61
- Fig. 4.1.7. Variation of grain size of  $\alpha$ -Fe(Si) phase with annealing temperature. 61
- Fig. 4.1.8. Variation of real part initial permeability,  $\mu'$  with measuring temperature for as-cast and annealed samples. 62
- Fig. 4.1.9. Variation of saturation magnetization with temperature with an applied field of 1 Tesla 62
- Fig. 4.1.10. Variation of  $M_s^{1/b}$  with temperature. 62
- Fig. 4.1.11. X-ray diffraction pattern of  $Fe_{73}Cu_1Nb_3Si_{14}B_8$  annealed at 818 K for different annealing time. 64
- Fig. 4.1.12. Annealing time,  $t_a$  dependence of lattice parameter,  $a$ . 64
- Fig. 4.1.13 Annealing time,  $t_a$  dependence of silicon content. 64
- Fig. 4.1.14 Annealing time,  $t_a$  dependence of grain size,  $D$ . 64
- Fig. 4.1.15. (a) annealing temperature dependence of initial permeability annealed for 1 hr. at 1 kHz; (b) Annealing time dependence of initial permeability at the annealing temperature of 818 K at 1 kHz. 66
- Fig. 4.1.16. Frequency dependence of real,  $\mu'$  and imaginary part,  $\mu''$ , of complex initial permeability for as-cast and annealed samples at 823 K for 10 minutes. 66
- Fig. 4.2.1 DTA curves of amorphous ribbons at different heating rate of 10,20,30,40 and 50 K/min from below to above. 70
- Fig. 4.2.2 DTA curves of as-cast and samples annealed at 773, 798, 818 K. 70
- Fig. 4.2.3. Kissinger plot for the determination of the activation energy for the formation of Fe(Si) phase in  $Fe_{73.5}Cu_1Ta_3Si_{13.5}B_9$ . 70
- Fig. 4.2.4. Kissinger plot for the determination of activation energy for the formation of  $Fe_2B$  phase in  $Fe_{73.5}Cu_1Ta_3Si_{13.5}B_9$ . 70
- Fig. 4.2.5. Variation of lattice parameter,  $a$  with the annealing temperature  $T_a$ . 71
- Fig. 4.2.6. Variation of silicon content with annealing temperature,  $T_a$ . 71

Fig. 4.2.7. Variation of grain size, D with annealing temperature, $T_a$ .	71
Fig. 4.2.8. Frequency dependence of $\mu'$ at different annealing temperatures.	73
Fig. 4.2.9. Variation of $\mu'$ with annealing temperature, $T_a$ .	73
Fig. 4.2.10. Temperature dependence of $\mu'$ of as cast and annealed sample in the amorphous relaxed state.	75
Fig. 4.2.11. Temperature dependence of $\mu'$ in the nanocrystalline state.	75
Fig. 4.2.12. Temperature dependence of $\mu'$ after the evolution of $Fe_2B$ .	75
Fig. 4.2.13. Variation of saturation magnetization of $Fe_{73.5}Cu_1Ta_3Si_{13.5}B_9$ alloy with temperature.	78
Fig. 4.2.14. Variation of $\mu'$ with annealing time at different annealing temperature.	78
Fig. 4.3.1. DSC curves of as-cast and annealed samples at different heating rates of 20 K/min.	80
Fig. 4.3.2. Kissinger plot for the determination of activation energy of crystallization of $\alpha$ -Fe(Si) phase.	81
Fig. 4.3.3. Kissinger plot for the determination of activation energy of crystallization of iron boride phase.	81
Fig. 4.3.4. Variation of initial permeability, $\mu'$ with temperature for samples with different annealing temperatures in the amorphous state of the material.	83
Fig. 4.3.5. Variation of initial permeability, $\mu'$ with temperature for samples with different annealing temperatures in the nanocrystalline state of the material.	83
Fig. 4.3.6. Variation of initial permeability, $\mu'$ with temperature for samples with different annealing temperatures after the evolution of iron boride phase.	83
Fig. 4.3.7. Variation of initial permeability, $\mu'$ and loss factor, $\tan \delta / \mu'$ with annealing temperature at $f = 1$ kHz.	86
Fig. 4.3.8. Variation of initial permeability, $\mu'$ and loss factor, $\tan \delta / \mu'$ with annealing time for the annealing temperature of 828 K.	86
Fig. 4.3.9. Temperature dependence of magnetization, M of as-cast sample with an applied field of 20 Oe.	86
<b>Chapter 5</b>	
Fig. 5.1.1. DSC traces of as-cast sample of $Co_{61}Fe_4Ni_7Si_{15}B_{12}$ for different heating rate.	90
Fig. 5.1.2. Kissinger's plot for the determination of activation energy of crystallization.	90
Fig. 5.1.3. X-ray diffraction patterns of as-cast and sample annealed at 693 K for 1 hr.	90
Fig. 5.1.4. Temperature dependence of magnetization with the applied field of 20 Oe and heating rate of 10 K/min.	90
Fig. 5.1.5. Variation of real ( $\mu'$ ) and imaginary ( $\mu''$ ) part of initial permeability of as-cast and	



annealed samples.	91
Fig. 5.1.6. Variation of initial permeability, $\mu'$ (solid symbol) and relative loss factor $\tan \delta / \mu'$ (open symbol) with annealing temperature, $T_a$ .	91
Fig. 5.1.7. Hysteresis loop of as-cast and sample annealed at 693 K for 1 hr.	
Fig. 5.1.8. M-H curves of as-cast and sample annealed at 693 K for 1 hr.	91
Fig. 5.1.9 (a). Field dependence of GMIR for as-cast and annealed samples	91
Fig. 5.1.9 (b). Field dependence of GMIR of as-cast and annealed samples at 6 MHz.	92
Fig. 5.2.1. DSC traces of as-cast sample of $\text{Co}_{67}\text{Fe}_4\text{Ni}_2\text{Si}_{15}\text{B}_{12}$ for different heating rates.	92
Fig. 5.2.2. Kissinger's plot for the determination of activation energy of crystallization.	94
Fig. 5.2.3. XRD patterns of as-cast and annealed sample of $\text{Co}_{67}\text{Fe}_4\text{Ni}_2\text{Si}_{15}\text{B}_{12}$ .	94
Fig. 5.2.4. Temperature dependence of magnetization of as-cast sample of $\text{Co}_{67}\text{Fe}_4\text{Ni}_2\text{Si}_{15}\text{B}_{12}$ with a heating rate of 10 K/min.	94
Fig. 5.2.5. Frequency dependence real and imaginary part of initial permeability ( $\mu'$ , $\mu''$ ) of as-cast and annealed sample of $\text{Co}_{67}\text{Fe}_4\text{Ni}_2\text{Si}_{15}\text{B}_{12}$ .	96
Fig. 5.2.6. Variation of real part initial permeability $\mu'$ (solid symbol) and relative loss factor $\tan \delta / \mu'$ (open symbol) with annealing temperature, $T_a$ .	96
Fig. 5.2.7. B-H loop of as-cast and sample annealed at 693 K for 30 minutes.	
Fig. 5.2.8. M-H curve of as-cast and sample annealed at 693 K for 30 minutes.	98
Fig. 5.2.9(a). Field dependence of GMIR(%) of as-cast and annealed sample at different temperatures for 30 minutes at 4.5 MHz.	98
Fig. 5.2.9(b). Field dependence of GMIR(%) of as-cast and annealed sample at different temperatures for 30 minutes at 6 MHz.	99
Fig. 5.3.1. DTA curves of $\text{Co}_{67}\text{Fe}_4\text{Mo}_2\text{Si}_{15}\text{B}_{12}$ in the as-cast condition for the heating rate 10 and 50 K/min.	101
Fig. 5.3.2. X-ray diffraction patterns of $\text{Co}_{67}\text{Fe}_4\text{Mo}_2\text{Si}_{15}\text{B}_{12}$ annealed at the initial stage of crystallization temperature 773 K and advanced stage of crystallization temperature 823 K.	101
Fig. 5.3.3 Frequency spectrum of real and imaginary part of permeability ( $\mu'$ , $\mu''$ ) of $\text{Co}_{67}\text{Fe}_4\text{Mo}_2\text{Si}_{15}\text{B}_{12}$ in the as-cast and annealed condition.	101
Fig. 5.3.4. Annealing temperature dependence of initial permeability ( $\mu'$ ) and relative loss factor ( $\tan \delta / \mu'$ ) of $\text{Co}_{67}\text{Fe}_4\text{Mo}_2\text{Si}_{15}\text{B}_{12}$ .	103
Fig. 5.3.5. Variation of initial permeability, $\mu'$ with temperature in the as-cast condition.	
Fig. 5.3.6. Field dependence of magneto-impedance ratio of as-cast and annealed samples of $\text{Co}_{67}\text{Fe}_4\text{Mo}_2\text{Si}_{15}\text{B}_{12}$ .	103

## Chapter 6

- Fig. 6.1.1. DSC trace of  $(\text{NdPr})_4\text{Fe}_{71}\text{Co}_5\text{Cu}_{0.5}\text{Nb}_1\text{B}_{18.5}$  in the as-cast condition with a heating rate of 20 K/min. 106
- Fig. 6.1.2 X-ray diffraction patterns of  $(\text{NdPr})_4\text{Fe}_{71}\text{Co}_5\text{Cu}_{0.5}\text{Nb}_1\text{B}_{18.5}$  for the samples annealed at 873 and 973 K for 10 minutes. 106
- Fig. 6.1.3. Annealing temperature and annealing time dependence of hysteresis loops.
- Fig. 6.1.4. Hysteresis loops of samples of compositions  $(\text{NdPr})_4\text{Fe}_{71}\text{Co}_5\text{Cu}_{0.5}\text{Nb}_1\text{B}_{18.5}$  and  $\text{Nd}_4\text{Fe}_{76}\text{Cu}_{0.5}\text{Nb}_1\text{B}_{18.5}$ . 107
- Fig. 6.1.5. Temperature dependence of magnetization of  $(\text{NdPr})_4\text{Fe}_{71}\text{Co}_5\text{Cu}_{0.5}\text{Nb}_1\text{B}_{18.5}$  and  $\text{Nd}_4\text{Fe}_{76}\text{Cu}_{0.5}\text{Nb}_1\text{B}_{18.5}$  with an applied field of 100 Oe and heating rate of 20 K/min. 107
- Fig. 6.1.6. Recoil hysteresis loops for samples annealed at 873 and 973 K for 10 minutes.
- Fig. 6.1.7. Recoil loop area as a function of reverse field for annealed samples. 109
- Fig. 6.1.8. Measurements of the irreversible portion  $D(H) = -\Delta M_{\text{irrev}}(H)/2M_r$  versus H for the samples annealed at 873, 903 and 973 K. 109
- Fig. 6.1.9. Temperature dependence of hysteresis loops for samples annealed at 873 and 923 K for 10 minutes. 110
- Fig. 6.1.10. Temperature dependence of hysteresis loop parameters for samples annealed at 873 and 923K for 10 minutes 110
- Fig. 6.2.1 Annealing temperature and time dependence of hysteresis loops of  $\text{Nd}_4\text{Fe}_{73.5}\text{Co}_3\text{Hf}_{0.5}\text{Ga}_{0.5}\text{B}_{18.5}$ . 114
- Fig. 6.2.2 X-ray diffraction patterns of  $\text{Nd}_4\text{Fe}_{73.5}\text{Co}_3\text{Hf}_{0.5}\text{Ga}_{0.5}\text{B}_{18.5}$  annealed at 923 K for 5, 10 and 20 minutes. 114
- Fig. 6.2.3. Recoil hysteresis loops for samples annealed at 923 K for 5, 10 and 20 minutes
- Fig. 6.2.4. Recoil loop area as a function of reverse field for annealed samples. 115
- Fig. 6.2.5. Measurements of the irreversible portion  $D(H) = -\Delta M_{\text{irrev}}(H)/2M_r$  versus H for the samples annealed at 923 K for 5, 10 and 20 minutes. 117
- Fig. 6.2.6 Temperature dependence of hysteresis loops for samples annealed at 923 K for 5 and 20 minutes. 118
- Fig. 6.2.7 Temperature dependence of hysteresis loop parameters for samples annealed at 923 K for 5 and 20 minutes 118
- Fig. 6.3.1. DTA trace of  $\text{Nd}_3\text{Tb}_1\text{Fe}_{76}\text{Cu}_{0.5}\text{Nb}_1\text{B}_{18.5}$  in the as-cast condition with a heating rate of 20 K/min. 121
- Fig. 6.3.2. X-ray diffraction pattern of  $\text{Nd}_3\text{Tb}_1\text{Fe}_{76}\text{Cu}_{0.5}\text{Nb}_1\text{B}_{18.5}$  samples in the annealed condition. 121
- Fig. 6.3.3. Hysteresis loops of  $\text{Nd}_3\text{Tb}_1\text{Fe}_{76}\text{Cu}_{0.5}\text{Nb}_1\text{B}_{18.5}$  samples in the annealed condition at

different temperatures.	121
Fig. 6.3.4. Hysteresis loops of samples of compositions $\text{Nd}_3\text{Tb}_1\text{Fe}_{76}\text{Cu}_{0.5}\text{Nb}_1\text{B}_{18.5}$ and $\text{Nd}_4\text{Fe}_{76}\text{Cu}_{0.5}\text{Nb}_1\text{B}_{18.5}$ .	123
Fig. 6.3.5. Temperature dependence of magnetization of $\text{Nd}_3\text{Tb}_1\text{Fe}_{76}\text{Cu}_{0.5}\text{Nb}_1\text{B}_{18.5}$ and $\text{Nd}_4\text{Fe}_{76}\text{Cu}_{0.5}\text{Nb}_1\text{B}_{18.5}$ with an applied field of 100 Oe and heating rate of 20 K/min.	123
Fig. 6.3.6. Recoil hysteresis loops for $\text{Nd}_3\text{Tb}_1\text{Fe}_{76}\text{Cu}_{0.5}\text{Nb}_1\text{B}_{18.5}$ sample annealed at 923 K for 10 min.	123
Fig. 6.3.7. Variation of irreversible component of magnetization $D(H)$ and normalized recoil area with reverse field.	123
Fig. 6.3.8. Temperature dependence of hysteresis loops for samples annealed at 893 and 923 K.	124
Fig. 6.3.9. Temperature dependence of hysteresis loop parameters for samples annealed at 893 and 923 K for 10 minutes.	124

<u>List of Tables</u>	Page No.
Table 2.1 Room temperature values of magnetic properties of some magnetically hard (k-type) and some magnetically soft (m-type) materials	18
Table 4.1 The values of saturation magnetization at different annealing temperature and time	67
Table 4.2. Annealing temperature, $T_a$ dependence of the Curie temperature of amorphous matrix $T_c^{am}$ .	76
Table 4.3. Effect of annealing on structural and magnetic properties of $Fe_{75.5}Cu_{0.6}Nb_{2.4}Si_{13}B_{8.5}$ .	80
Table 4.4. Effect of annealing on the Curie temperature of amorphous phase of $Fe_{75.5}Cu_{0.6}Nb_{2.4}Si_{13}B_{8.5}$ .	84
Table 5.1 $(GMIR)_{max}$ and sensitivity of field dependence of GMIR for different annealing conditions.	91
Table 5.2. $(MIR)_{max}$ for different annealing conditions at 4.5 and 6 MHz.	99
Table 6.1. Hysteresis loop parameters for $(NdPr)_4Fe_{71}Co_3Cu_{0.5}Nb_1B_{18.5}$	106
Table 6.1. Hysteresis loop parameters for $(NdPr)_4Fe_{71}Co_3Cu_{0.5}Nb_1B_{18.5}$	113
Table 6.2. Hysteresis loop parameters of $Nd_4Fe_{73.5}Co_3Hf_{0.5}Ga_{0.5}B_{18.5}$ with the variation of annealing temperature and time.	120

### List of Symbols

Absolute value of admittance	$ Y $
Absolute value of impedance	$ Z $
AC current	$I$
Angular frequency	$\omega$
Anisotropy field	$H_k$
Anisotropy of the hard phase	$K_h$
Anisotropy of the soft phase	$K_m$
Average anisotropy	$\langle K \rangle$
Capacitance	$C$
Coercivity	$H_c$
Conductance	$G$
Critical exponent	$b$
Critical thickness of the hard phase	$b_{ch}$
Critical thickness of the soft phase	$b_{cm}$
Cross-sectional area of toroids	$S$
Curie temperature	$T_c$
Curie temperature of residual amorphous matrix	$T_c^{am}$
DC field demagnetization remanence	$M_d(H)$
Diffraction angle	$\theta$
Energy per unit area of a $180^\circ$ Bloch wall	$\gamma$
Enthalpy of crystallization	$\Delta H$
Equilibrium energy per unit area of a $180^\circ$ Bloch wall	$\gamma_0$
Equilibrium thickness of the Bloch wall	$\delta_0$
Exchange-bias field	$H_{ex}$
Exchange correlation length	$L_u$
Exchange energy density	$E_A$
Exchange stiffness constant	$A$
Frequency	$f$
Full width at half maxima	FWHM
Giant magneto-impedance ratio	GMIR
Grain size	$D$
Heating rate	$\beta$
Imaginary part of initial permeability	$\mu''$
Impedance	$Z$
Inductance	$L$

Initial permeability	$\mu_i$
Inter planner spacing	$d$
Irreversible magnetic field	$H_{ir}$
Loss factor	$\tan \delta$
Magnetization	$M$
Magnetization of the soft phase	$M_{ms}$
Magnetization of the hard phase	$M_{hk}$
Magnetocrystalline anisotropy constant	$K_1$
Magneto-impedance	MI
Magneto-impedance ratio	MIR
Maximum energy product	$(BH)_{max}$
Nucleation field	$H_n$
Number of turns	$N$
Packing fraction	$p$
Peak temperature	$T_p$
Quality factor	$Q$
Reactance	$X$
Real part of initial permeability	$\mu'$
Recoil permeability	$\mu_r$
Remanent ratio	$M_r$
Resistance	$R$
Resistivity	$\rho$
Reversible magnetic field	$H_{rev}$
Saturation magnetization	$M_s$
Saturation polarizatin	$J_s$
Skin depth	$\delta$
Static magnetic field	$H_{dc}$
Susceptance	$B$
Thickness of the Bloch wall	$\delta$
Thickness of the hard phase	$b_k$
Thickness of the soft phase	$b_m$
Total flux	$\Phi$
Volume fraction of the soft phase	$v_m$
Volume fraction of the hard phase	$v_k$
Wavelength	$\lambda$

## Acknowledgement

It is my pleasure to greatly acknowledge the guidance and kind behavior of my supervisor, Dr. Md. Feroz Alam Khan, Professor, Dept. of Physics, Bangladesh University of Engineering and Technology, who has provided consistent support and kind help during the period when this thesis work has been conducted. His suggestions and fruitful discussions helped me to overcome the hurdles many times during this period, which was inevitable to complete this thesis work.

The benevolent support of my co-supervisor, Dr. A. K. M. Abdul Hakim, Head, Materials Science Division, Atomic Energy Centre, Dhaka, is greatly acknowledged without which this thesis work would not have been completed. His teachings and guidance had not only helped me to accomplish this work but would guide me throughout my career.

My acknowledgement and sincere thanks is expressed for support and help provided by Professor Nguyen Chau, Centre for Materials Science, Hanoi National University, Professor Nguyen Xuan Phuc, Director, Institute of Materials Science, Vietnam Academy for Science and Technology and Professor Nguyen Hoang Nghi, Institute of Engineering Physics, Hanoi University of Technology.

I would like to express my sincere thanks and gratitude to Professor Peter Svedlindh to allow me to work with the SQUID in Solid State Physics, Dept. of Engineering Sciences, Uppsala University, Sweden. I also acknowledge the kind concern of Professor Carl G. Ribbing, Professor Ewa Wäckelgård, Mr. Bengt Gotteson and other members of the department.

I would like to express my immense thanks and gratitude to the concerned authority for granting the scholarship of "Prime Minister's Higher Education and Research Fund" for my Ph.D. Programme

I will remain indebted to Dr. Lennart Hasselgren, Director, International Science Programme, Uppsala University, Sweden for his kind concern and support throughout this work and financial assistance provided during the visit to Vietnam and Sweden under the umbrella of BAN-02 project of International Programme for Physical Sciences (IPPS), Uppsala University, Sweden.

I will remain indebted to Dr. C. S. Karim, the Honorable Advisor, Ministry of Agriculture, Government of People's Republic of Bangladesh and the-then Chairman of Bangladesh Atomic Energy Commission, for his encouragement and kind support to conduct my work.

I will remain indebted to Professor A. S. W. Kurny, Dept of Materials and Metallurgical Engineering, Bangladesh University of Engineering and Technology who gave me the first motivation to take research as my profession.

My sincere-most gratitude goes to the members of the Ph.D. Committee, Professor Jiban Podder, Professor Nazma Zamari, Professor Abu Hashan Bhuiyan, of Dept. of Physics, Professor Nasrul Hoque, Dept of Materials and Metallurgical Engineering, Bangladesh University of Engineering and Technology, Professor Shibendra Shekhar Sikder, Dept. of Physics, Khulna University of Engineering and Technology who helped me to develop my work with plenty of suggestions, critical judgment and kind appraisal of my work.

I would like to take this opportunity to express my regardful acknowledgment to Prof. Muminul Haq, Dr. A. K. M. Akther Hossain, Dr. Nazrul Islam, Mrs. Afia Begum, Mr. M. A. Basith and other faculty members of the Department of Physics, B.U.E.T. for their encouragement for my work. I also remember the encouragement of Prof. Md. Fakhrul Islam, Prof. Rezaul Hoque, Prof. Mohar Ali and other faculty members of the Dept. of Materials and Metallurgical Engineering, Bangladesh University of Engineering and Technology.

My indebtedness and gratitude knows no bound for the encouragement and kind support provided by Dr. Shafiqul Islam Bhuiyan, the Chairman, Bangladesh Atomic Energy Commission for my work.

I am also very much indebted to Dr. Farid Uddin Ahmed, Member, Physical Sciences and Dr. Md. Amanullah Choudhury, Director, Physical Sciences, Bangladesh Atomic Energy Commission.

I would like to express my sincere-most thanks and gratitude to Engr. Rezaul Bari, Director, Atomic Energy Centre, Dhaka to provide kind support and help.

My sincere-most gratitude and thanks goes to Dr. D. K. Saha and Mrs. Shireen Akhter, Principal Scientific Officers, Mr. Md. Nazrul Islam Khan, Scientific Officer, Materials Science Division, Atomic Energy Centre, Dhaka for their support and help.

The help of Dr. M. A. Gafur, Research Engineer, Bangladesh Council for Scientific and Industrial Research is greatly acknowledged.

I am very much grateful to Mr. Md. Sultan Mahmud, Mr. Md. Manjurul Haque, Ms. Sarout Noor and other post graduate students of our group and friends who has given lot of encouragement to accomplish this work.

Needless to mention the help of different staffs of Dept. of Physics, Bangladesh University of Engineering and Technology and Materials Science Division, Atomic Energy Centre, Dhaka.

I remember the struggle my beloved mother, Mrs. Mahfuza Begum and my beloved father, (Late) Mr. Sheikh Mahabubul Hoque, who has given me a concept of life, which should be centered on the academic activity. I will not be able to fulfill my debt for their sacrifice throughout my entire life. I also remember the support and help of my brother, Dr. Sheikh Mahfuzul Hoque, sister-in-law, Dr. Adiba Anjum Geeti, sister, Mrs. Mahbuba Hoque, brother-in-law, Engr. M. A. Mozid and other family members without which I could not persevere in my work.

Lastly, I remember the contributions of millions of laborious people whose immense labor, pains and sufferings flourish the civilization to newer dimension, which has facilitated me to live as a human being.



### Abstract

A detailed study has been carried out, on soft and hard nanocomposite magnetic materials, which constitutes, a) Fe-based soft nanocomposite magnetic materials of the compositions:  $\text{Fe}_{73}\text{Cu}_1\text{Nb}_{3.5}\text{Si}_{14}\text{B}_{8.5}$ ,  $\text{Fe}_{75.5}\text{Cu}_{0.6}\text{Nb}_{2.4}\text{Si}_{13}\text{B}_{8.5}$ ,  $\text{Fe}_{73.5}\text{Cu}_1\text{Ta}_1\text{Si}_{13.5}\text{B}_9$ , b) Co-based soft nanocomposite magnetic materials of the compositions:  $\text{Co}_{68}\text{Fe}_4\text{Ni}_1\text{Si}_{15}\text{B}_{12}$ ,  $\text{Co}_{67}\text{Fe}_4\text{Ni}_2\text{Si}_{15}\text{B}_{12}$ ,  $\text{Co}_{67}\text{Fe}_4\text{Mo}_2\text{Si}_{15}\text{B}_{12}$  and c) Fe-based hard nanocomposite magnetic materials of the compositions:  $(\text{NdPr})_4\text{Fe}_{71}\text{Co}_3\text{Cu}_{0.5}\text{Nb}_1\text{B}_{18.5}$ ,  $\text{Nd}_4\text{Fe}_{73.5}\text{Co}_3\text{Hf}_{0.5}\text{Ga}_{0.5}\text{B}_{18.5}$ ,  $\text{Nd}_1\text{Tb}_1\text{Fe}_{76}\text{Cu}_{0.5}\text{Nb}_1\text{B}_{18.5}$ . All the compositions have exhibited qualitative increment of both soft and hard magnetic properties due to the evolution of nanoscaled grains evolved from amorphous precursor by appropriate annealing.

For Fe-based soft nanocomposite magnetic materials, nanometric grains evolving from amorphous precursor by controlled annealing develops the unique properties with the combination of high permeability of the order of  $10^4$  and low relative loss factor of the order of  $10^{-6}$ . Crystallization temperatures are identified by thermal analysis techniques and crystallization products are determined by X-ray diffraction. Optimum grain size has been determined in the range of 10-15 nm from line broadening of fundamental peaks. Temperature dependence of initial permeability,  $\mu'$  is governed by the various stages of crystallization namely, amorphous relaxed state, nanocrystalline state and evolution of iron boride phase. Crystallization temperatures were also determined from temperature dependence of magnetization. Good correlations of transition temperatures have been observed between thermal analysis, X-ray diffraction, temperature dependence of permeability and magnetization.

For Co-based soft amorphous / nanocomposite magnetic materials ultra soft magnetic properties have been observed at optimum annealing temperature characterized by very high initial permeability of the order of  $10^4$  and low relative loss factor of the order of  $10^{-6}$ . Coercivity has been found to decrease significantly for optimized annealed condition compared to as-cast state. Crystallization behavior has been studied by thermal analysis and X-ray diffraction techniques. Correlating the results of X-ray diffraction, thermal analysis and annealing temperature dependence of initial permeability,  $\mu'$  and relative loss factor,

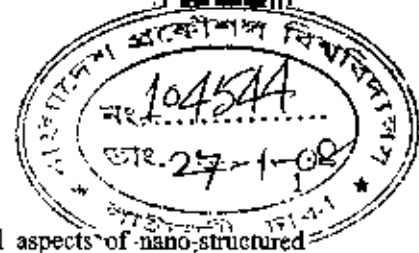
$\frac{\tan \delta}{\mu'}$  it has been found that the magnetic softening of  $\text{Co}_{68}\text{Fe}_4\text{Ni}_1\text{Si}_{15}\text{B}_{12}$  has taken place due to relaxation of the amorphous matrix by relieving internal stresses whereas the magnetic softening of  $\text{Co}_{67}\text{Fe}_4\text{Ni}_2\text{Si}_{15}\text{B}_{12}$  and  $\text{Co}_{67}\text{Fe}_4\text{Mo}_2\text{Si}_{15}\text{B}_{12}$  has taken place in two steps firstly due to relaxation of the amorphous matrix and secondly due to the formation of nanograins during the onset of crystallization. Field dependence of magneto-impedance has been measured for current driving frequency of 4.5 and 6 MHz. At higher frequency, magneto-impedance ratio (MIR) is decreased because the domain wall motion is heavily damped by eddy current and only magnetization rotation is responsible for magnetic permeability.

Fe-based hard nanocomposite magnetic materials, commonly known as exchange-spring magnets, has been found to consist of soft phase such as,  $\text{Fe}_3\text{B}$ ,  $\alpha$ -Fe and hard phase such as  $\text{RFe}_2\text{B}_{14}$  where R is the

rare earth element such as Nd, Pr or Tb. Crystallization temperatures were determined by thermal analysis and crystallization products were determined by X-ray diffraction. Magnetization measurements were performed by SQUID magnetometer. Hysteresis loops were measured at room temperature for different annealing condition in order to observe the variation of magnetic properties with different crystalline phases. Reversible and irreversible component of magnetization has been studied by recoil hysteresis and dc field demagnetization remanence. Temperature dependence of hysteresis loops revealed that below spin reorientation temperatures, variations of magnetization becomes discontinuous at low field leading to constricted hysteresis loops.

## **Chapter 1**

### **Introduction**



This thesis focuses on exploiting some of the scientific and technological aspects of nano-structured magnetic materials. Nanomaterials are generally materials that can have one dimension, two dimensions or three dimensions and can be specified within a size of 100 nanometer ( $1 \text{ nm} = 10^{-9} \text{ meter}$ ). Application area of inorganic nanoparticles are abrasives, catalysts, pigments / coatings, optical devices, electronic devices, magnetic and structural materials. Among the various applications of nanostructured materials the present research work is focused on *nanostructured magnetic materials* prepared from amorphous precursor made by melt-spin system. In the present study, three systems have been undertaken in order to study the magnetization process in the nanostructured exchange-biased system. These are. a) Fe-based soft nanocomposite magnetic materials of the compositions:  $\text{Fe}_{73}\text{Cu}_1\text{Nb}_{3.5}\text{Si}_{14}\text{B}_{8.5}$ ,  $\text{Fe}_{75.5}\text{Cu}_{0.6}\text{Nb}_{2.4}\text{Si}_{13}\text{B}_{8.5}$ ,  $\text{Fe}_{73.5}\text{Cu}_1\text{Ta}_3\text{Si}_{13.5}\text{B}_9$ , b) Co-based soft nano composite magnetic materials of the compositions:  $\text{Co}_{68}\text{Fe}_4\text{Ni}_1\text{Si}_{15}\text{B}_{12}$ ,  $\text{Co}_{67}\text{Fe}_4\text{Ni}_2\text{Si}_{15}\text{B}_{12}$ ,  $\text{Co}_{67}\text{Fe}_4\text{Mo}_2\text{Si}_{15}\text{B}_{12}$  and c) Fe-based hard nano composite magnetic materials of the compositions:  $(\text{NdPr})_4\text{Fe}_{71}\text{Co}_3\text{Cu}_{0.5}\text{Nb}_1\text{B}_{18.5}$ ,  $\text{Nd}_4\text{Fe}_{73.5}\text{Co}_3\text{Hf}_{0.5}\text{Ga}_{0.5}\text{B}_{18.5}$ ,  $\text{Nd}_3\text{Tb}_1\text{Fe}_{76}\text{Cu}_{0.5}\text{Nb}_1\text{B}_{18.5}$ .

The main objectives of the present research work are to synthesize Fe and Co based alloys of the above-mentioned compositions in the amorphous state by using rapid solidification technique and study their magnetic properties with the evolution of different phases by varying annealing condition. Annealing of Fe and Co-based soft nanocomposite magnetic materials have been performed in air and annealing of rare earth content Fe-based hard nanocomposite magnetic materials have been performed in vacuum at different temperatures and holding time under a pressure of  $10^{-3}$  mbar in order to determine optimum condition of annealing. X-ray diffraction technique has been used for the characterization of nanostructured phases. The purpose is to correlate evolution of nanograins, their volume fraction, size and their distribution in the remaining amorphous matrix with the magnetic properties of different compositions.

For Fe-based soft nanocomposite magnetic materials, nanostructured phase of  $\alpha\text{-Fe}(\text{Si})$  evolved from amorphous precursor contains grains having dimension within 10-15 nm. In Fe based soft nanocomposite magnetic materials nanograins are dispersed within the amorphous matrix. Since, nanograins are exchange-coupled through residual amorphous matrix, magnetic anisotropy is averaged out as a result of which permeability value is enhanced by the order of  $10^4$ , which is extraordinarily soft compared to conventional soft magnetic materials [1].

In Fe-based soft nanocomposite magnetic materials, temperature dependence of permeability is governed by the composition of the residual amorphous and nanostructured phases. When the sample is annealed below the crystallization temperature, increase of initial permeability is attributed to the stress relief, increase of packing density of atoms by annealing out micro-voids and changing the degree of chemical disorder. Temperature dependence of permeability curve passes through a maximum just before a sharp fall to near zero with the manifestation of Hopkinson effect characterizing the ferro-paramagnetic transition of the amorphous phase. When the sample is annealed above crystallization temperature, the

sharpness of the fall to lower values of permeability is progressively smeared out with the appearance of a tail in the high temperature region. The crucial role of exchange interaction is clearly evident when the measuring temperature exceeds the Curie temperature of the amorphous matrix ( $T > T_c^{am}$ ) in the temperature dependence of permeability of these biphasic alloys. For  $T > T_c^{am}$ , the intergranular amorphous matrix becomes paramagnetic within which  $\alpha$ -Fe(Si) ferromagnetic nanograins are embedded. The exchange coupling between the nanograins largely ceases to exist. Thus for the measuring temperature  $T > T_c^{am}$ , the initial permeability drops down by almost two orders of magnitude and the coercivity increases correspondingly. When the sample is annealed above the second crystallization temperature obtained from thermal analysis, temperature dependence of permeability is governed by the presence of  $Fe_2B$  phase. Sometimes, presence of boride phase cannot be detected by X-ray diffraction. Since the anisotropy constant  $K_1$  of  $Fe_2B$  ( $430 \text{ kJ / m}^3$ ) is five orders of magnitude higher than the average anisotropy  $\langle K \rangle$  of  $\alpha$ -Fe(Si) nanograins ( $4 \text{ J / m}^3$ ), minor evolution of  $Fe_2B$  phase can cause significant damage to exchange interaction. Temperature dependence of  $\mu'$  reveals the presence of  $Fe_2B$ , which is not possible to detect by X-ray diffraction. Since  $K_1$  of  $Fe_2B$  passes from negative to positive value at 523K, a dramatic rise of  $\mu'$  from a very low value by an order of magnitude at room temperature is expected at 523K for the samples annealed about 873K and above.

Co-based amorphous alloy exhibits superior soft magnetic properties after appropriate annealing treatment below the crystallization temperature. It is widely known that thermal treatment of amorphous materials below their crystallization temperature relaxes the amorphous structure, giving rise to ultra-soft magnetic properties. In the recent studies, it was found that heat treatment below the crystallization temperature in the Co-based amorphous alloy gave rise to the formation of nanocrystalline phase with grain size of about 2 nm, revealed by TEM [2] leading to very high value of initial permeability. According to Herzer [1], the formation of the nanocrystalline phase in the Fe-based alloy containing Cu, annealed above the crystallization temperature, gives rise to reduction of the effective anisotropy because the random oriented anisotropies are averaged out by exchange interaction. Similar effect is believed to exist in the Co-based alloy in the early stage of crystallization [3].

In this work, the aim is to analyze the possible formation of nanocrystalline phases and the relative softening of the magnetic properties in the Co-based amorphous alloy by appropriate thermal treatment. Since enhanced magneto-impedance is a characteristic property of Co-rich amorphous alloy, annealing effect on magneto-impedance in amorphous relaxed state at current driving frequency of 4.5 and 6 MHz have also been investigated. Magneto-impedance (MI) consists of a change of total impedance of a magnetic conductor under the application of a static magnetic field  $H_{dc}$ . The change expressed in giant magneto impedance ratio (GMIR) is determined as follows:

$$\text{GMIR (\%)} = \left( 1 - \frac{Z(H_{dc})}{Z(H_{max})} \right) \times 100$$

where  $Z(H_{dc})$  is the impedance measured in the presence of the dc magnetic field and  $Z(H_{max})$  is the impedance measured at the maximum limit when the impedance does not change any longer with the applied field.

In order to show giant magneto-impedance by any materials several general conditions must be satisfied such as: the materials should be magnetically soft with well-defined anisotropy axis and with small magnetostriction. The coercive field  $H_c$  must be small with narrow hysteresis loop. The materials must have a small resistivity since it carries the ac current. The materials should have a large saturation magnetization  $M_s$  in order to boost the interaction with the external magnetic field. The materials, which meet the above conditions are Co-Fe-Si-B based alloys of the composition around  $\text{Co}_{68}\text{Fe}_{4.5}\text{B}_{12}\text{Si}_{12.5}$  with various dopants.

In Fe-based hard nanocomposite magnetic materials, magnetic properties are characterized by exchange-biased soft and hard nanocomposite phases [4]. Presence of soft nanostructured phase would lead to high value of remanence, which is expected to be greater than 0.5 while presence of hard nanostructured phase would lead to high value of coercivity, which is expected to be greater than 3 kOe in the optimized annealing condition. Remanent ratio greater than 0.5 is highly desirable for development of permanent magnet. Besides high reduced remanence such systems are characterized by high energy product. Extent of exchange coupling affects the shape of hysteresis loop. The demagnetization branch of the hysteresis loop is convex when the soft and hard phases of the sample are exchange coupled in the optimum condition of annealing. When the sample is over-annealed, over-aging of the nanograins would lead to the demagnetization curve being concave. If there were no exchange coupling between phases one would get constructed hysteresis loop. The recoil permeability of an exchange spring magnet is expected to be about 5 times as large as that of a conventional magnet with equal coercive field and saturation magnetization, which signifies reversibility of magnetic moment in the soft phase below certain critical field [5]. Reversibility of magnetization can be studied from dc field demagnetization technique known as DCD technique and recoil hysteresis loops. Temperature dependence of hysteresis loop parameters lead to the variation in the shape of hysteresis loop in low temperature region i.e. in the range of 5-150 K due to spin reorientation of magnetic moment of  $\text{Nd}_2\text{Fe}_{14}\text{B}$  from  $30^\circ$  (from c-axis) to c-axis.

In this thesis, Chapter 2 contains introductory description and brief literature review on three above-mentioned systems. Chapter 3 contains the description of experimental set-ups used in this work. Chapters 4 to 6 contain the experimental results and discussions on three different systems. Finally, Chapter 7 contains the concluding remarks.

## Chapter 2

### *Soft and hard Exchange-biased system*

## 2.1 Fe-based soft nanocomposite magnetic materials

A new class of Fe-based alloys exhibiting superior soft magnetic properties has been discovered for the first time by Yoshizawa et. al. [1]. Nanocrystalline structure of these alloys offers a new opportunity for tailoring soft magnetic materials. The particular characteristic of these types of alloys is its ultrafine microstructure of b.c.c. Fe-Si with grain sizes of 10-15 nm for which their soft properties are derived and after which they were named nanocrystalline.

It is well known that the microstructure, especially, the grain size, essentially determines the hysteresis loop of ferromagnetic materials. Fig. 2.1 summarizes the present understanding of the coercivity,  $H_c$ , in the whole range of structural correlation lengths starting from atomic distances in amorphous alloys over grain sizes,  $D$ , in the nanometer regime up to macroscopic grain sizes [2]. The permeability shows an analogous behavior being essentially inversely proportional to  $H_c$ . The  $1/D$  dependence of coercivity for large grain sizes reflects the conventional rule that good soft magnetic properties require very large grains ( $D > 100 \mu\text{m}$ ). Thus the reduction of particle size to the regime of the domain wall width increases the coercivity  $H_c$  towards a maximum controlled by the anisotropies of materials. Lowest coercivities, however, are again found for smallest structural correlation lengths like in amorphous alloys ("grain size" of the order of atomic distances) and in nanocrystalline alloys for grain sizes  $D < 20 \text{ nm}$ . The new nanocrystalline material fills in the gap between amorphous metals and conventional polycrystalline alloys.

### 2.1.1 Formation of the nanocrystalline state

Principally, nanocrystalline alloys can be synthesized by a variety of techniques such as rapid solidification from the liquid state, mechanical alloying, plasma processing and vapor deposition. Yet, the requirements on the microstructure necessary for the soft magnetic properties rule out quite a number of the available processes. Kuhrt and Schultz [3] have shown, that mechanical alloying seems to be unsuitable for the production of soft magnetic nanocrystalline Fe-Co and Fe-Ni because of the considerable introduction of internal strain into the material, which is inevitably related to the process and cannot be removed without the simultaneous occurrence of undesirable grain growth. Compacted nanometer sized powders prepared by inert gas condensation techniques, although frequently discussed, are also unsuitable for obtaining good soft magnetic properties due to the unfavorable intergranular linkage, which considerably reduce the necessary ferromagnetic coupling between the grains.

Actually, controlled crystallization from the amorphous state seems to be the only method presently available to synthesize nanocrystalline alloys with attractive soft magnetic properties. The amorphous precursor material is prepared either as a thin film by sputtering techniques or as a ribbon by rapid solidification from the melt.



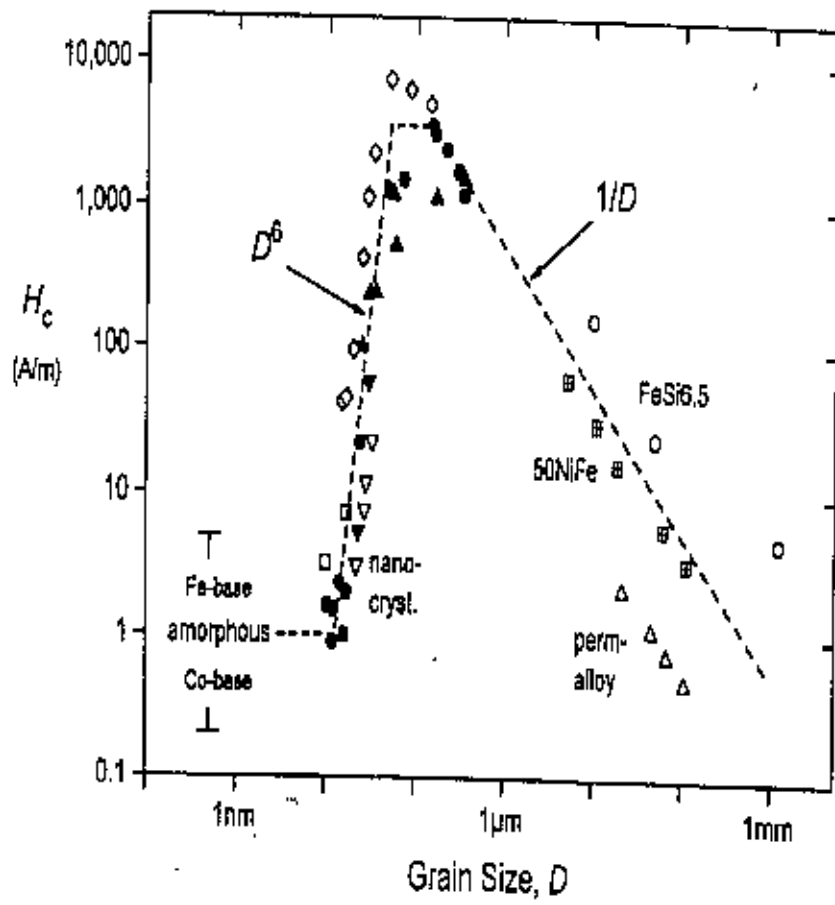


Fig. 2.1 Dependence of coercivity,  $H_c$ , in the whole range of grain size in the nanometer regime up to macroscopic grain sizes [2].

A typical nanocrystalline structure with good soft magnetic properties occurs if the amorphous state is crystallized by the primary crystallization of b.c.c. Fe, before intermetallic phases like Fe-B compounds may be formed. An extremely high nucleation rate and slow growth of the crystalline precipitates both are needed simultaneously in order to obtain a nanoscaled microstructure. It was known before that crystallization of conventional metallic glasses optimized for soft magnetic applications usually yield a relatively coarse grained microstructure of several crystalline phases and, correspondingly, deteriorates soft magnetic properties. Although it appears to be possible to refine the microstructure of such conventional compositions by special annealing techniques like pulse heating [4], such methods are less suitable in view of reproducibility and application. What is needed, is a controlled crystallization behavior upon isothermal annealing. This can be achieved by an appropriate alloy design, in particular, by alloying special elements, which promote the nucleation of b.c.c. Fe, retard the grain growth and simultaneously inhibit the formation of intermetallic phases. The requirement of a good glass forming ability puts further constraints on the accessible alloy compositions.

The optimum alloy composition originally proposed and subsequently not much changed is  $\text{Fe}_{73.5}\text{Cu}_1\text{Nb}_3\text{Si}_{13.5}\text{B}_9$  and can be considered as a typical Fe-Si-B metallic glass composition with small additions of Cu and Nb. The alloy system has a good glass forming ability and is easily accessible by rapid solidification as an originally amorphous ribbon, typically 20  $\mu\text{m}$  thick. The nanocrystalline state is achieved by annealing at temperatures typically between about 773 and 873 K, which leads to primary crystallization of b.c.c. Fe. The resulting microstructure is characterized by randomly oriented, ultra fine grains of b.c.c. Fe-Si (20 at.%) with typical grain sizes of 10-15 nm embedded in a residual amorphous matrix. The remaining amorphous matrix occupies about 20-30% of the volume and separates the crystallites at a distance of about 1-2 nm. These features are the basis for the excellent soft magnetic properties indicated by the high values of the initial permeability of about  $10^4$  and correspondingly low coercivities of less than 1 A/m.

Annealing at more elevated temperatures above 873 K leads to the precipitation of small fractions of boride compounds like  $\text{Fe}_2\text{B}$  or  $\text{Fe}_3\text{B}$  with typical dimensions of 50 nm to 100 nm along with the ultra fine grain structure of b.c.c. Fe-Si. Further increase of the annealing temperature above 973 K, finally yield grain coarsening of Fe(Si). Both the formation of Fe borides and grain coarsening deteriorates the soft magnetic properties significantly.

The formation of the particular nanocrystalline structure is essentially related to the combined addition of Cu and Nb (or other group IV to VI elements) and their low solubility in b.c.c. Fe. Copper enhances the nucleation of the b.c.c. grains while Niobium impedes coarsening and, at the same time, inhibits the formation of boride compounds. The microstructure evolution is schematically illustrated in Fig. 2.2 and can be summarized as follows:

The phase separation tendency between Cu and Fe leads to the formation of Cu-rich clusters, about 5 nm in size and probably still amorphous, in the initial stage of anneating before the onset of the primary

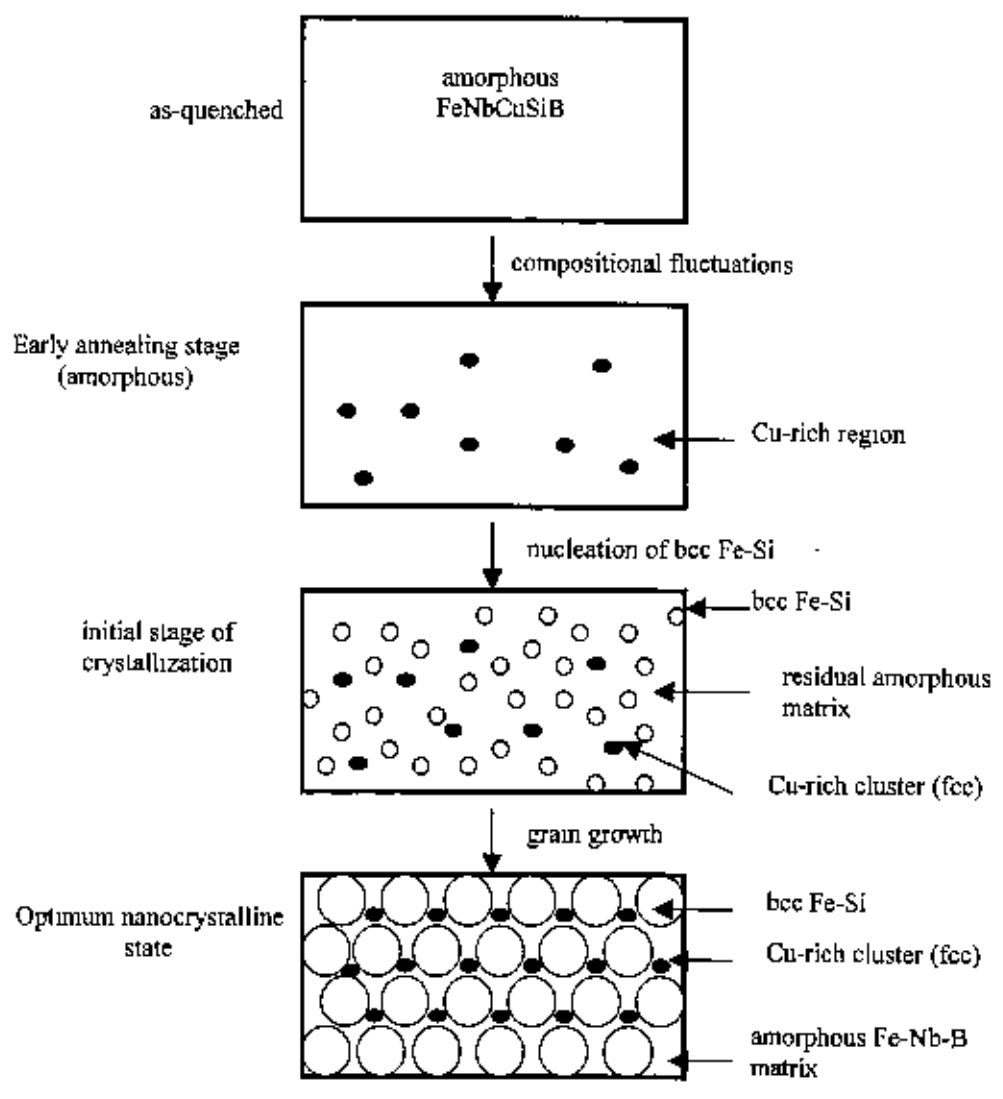


Fig. 2.2. Evolution of  $\alpha$ -Fe(Si) nanocrystallites from amorphous matrix.

crystallization of the b.c.c. Fe-Si phase [5-6]. The presence of Nb, hereby seems to promote the formation of these Cu-rich clusters on a much finer scale than in an Nb-free alloy composition [7]. This cluster formation causes a concentration fluctuation of Fe. Thus, the regions in between the Cu-rich clusters provide a significantly increased density of nucleation sites for the crystallization of b.c.c. Fe. The consequence is an extremely fine nucleation of b.c.c. Fe-Si crystallites at a high rate, which subsequently grow in a diffusion controlled process [8] as the annealing proceeds further. As the b.c.c. Fe phase forms, Nb and B are excluded from the crystallites because of their low solubility in b.c.c. Fe-Si and are enriched in the residual amorphous matrix. At the same time effectively all Si tends to be partitioned into the b.c.c. Fe-Si phase. The enrichment with B and in particular, with Nb increasingly stabilized the residual amorphous matrix and, thus, hinders coarsening of the b.c.c. grains. The presence of Nb at the same time inhibits the formation of Fe boride compounds. The transformation finally ceases in a metastable two-phase microstructure of b.c.c. Fe-Si embedded in an amorphous Fe-Nb-B matrix.

The effect of copper in enhancing the nucleation density, in a way, is unique. Gold is the only element, which has been verified to have a comparable effect on the crystallization behavior [9]. From this, silver, belonging to the same noble metal group, is expected to behave similarly. However, silver is practically immiscible in Fe even in the liquid state, such that alloying of this element into the Fe-Si-B matrix, so far could not be verified successfully. Although essential, Cu-addition alone is not sufficient for the formation of ultra-fine nanograins homogeneously distributed in the amorphous matrix. Its effect is considerably promoted by the simultaneous presence of Nb.

Nb enhances the crystallization temperatures and retards the grain growth by limiting diffusion. In particular, the Nb-addition significantly increases the separation between the two crystallization stages, which promotes the primary crystallization of b.c.c. Fe and stabilizes the residual amorphous matrix against the precipitation of Fe-B compounds. All together leads to an increased number of simultaneously growing and competing crystals resulting in the nanoscaled microstructure upon alloying within the range of 2-3 at.% of Nb

Niobium can be substituted by other group V or VI refractory elements, like Cr, V, Mo, W or Ta which act similarly on the crystallization process and on the magnetic properties [10]. Like Nb, the atomic volumes of these refractory elements are larger than that of Fe, which reduces the diffusion coefficients and, thus, stabilizes the amorphous matrix and slows down the kinetics of grain coarsening [11]. Accordingly the efficiency of these elements for grain size refinement increases in the order of their atomic volumes, i.e.,  $Cr < V < Mo \approx W < Nb \approx Ta$ . Thus finest grain structures and superior magnetic properties in practice require at least a certain amount of the elements Nb or Ta.

It should be stressed again that soft magnetic properties require not only a small grain size but at the same time the absence of boron compounds. The separation between crystallization of b.c.c. Fe and Fe-B compounds not only is determined by Cu and Nb additions but, decreases with increasing boron content.

This puts a further constraint on the alloy composition namely that the boron content should be kept at a low or moderate level to obtain an optimum nanoscaled structure.

From domain observation, it has been found that in the optimum annealed condition, exchange coupling between the nanograins through residual amorphous matrix leads to wide laminar domain of about 400  $\mu\text{m}$ . In the overaged condition, the ultra fine b.c.c. matrix is effectively hardened by the iron boride precipitates although their volume fraction is very small. For samples annealed at 853 K, i.e., in the very initial state of degradation, the domain pattern changes from wide ( $\approx 400 \mu\text{m}$ ) laminar domains to small, only 20  $\mu\text{m}$  wide and irregular domains [12]. The irregular domain pattern scales down by at least two orders of magnitude when the annealing temperature is further increased. The effective hardening caused by the  $\text{Fe}_2\text{B}$  precipitates already at smallest volume fractions is related to their relatively large size of 50-100 nm and, in particular, to their large magnetocrystalline anisotropy constant,  $K_1$ , of about 430  $\text{kJ}/\text{m}^3$ .

It is interesting to observe the temperature dependence of the magnetic properties of such "over annealed" nanocrystalline materials, together with the magneto-crystalline anisotropy constant,  $K_1$ , of  $\text{Fe}_2\text{B}$ . Good soft magnetic properties of the nanocrystalline b.c.c. structure are largely recovered when  $K_1$  ( $\text{Fe}_2\text{B}$ ) passes through zero at 523 K. This particular temperature dependence allows to detect even smallest amounts of borides hardly visible by more direct structural investigations and, thus, provides a most sensitive tool in order to separate whether an eventual degradation of the soft magnetic properties arises from too large b.c.c. grains or from hard precipitates. The deleterious impact of small amounts of boride compounds on the soft magnetic properties is in particular visible in alloy compositions with low silicon and correspondingly high boron content even if heat-treated in an optimum way.

Thus, a basic condition for the formation of a typical nanocrystalline structure is given by a primary crystallization process before stable or meta-stable intermetallic phases are formed. Obviously, this can be attained by (i) alloying additions which lead to clearly separated stages of crystallization  $T_{x1}$  and  $T_{x2}$  and (ii) by annealing at  $T_{x1} < T_a < T_{x2}$  such that only the phase forming at and above  $T_{x1}$  is crystallizing.

### 2.1.2 Microstructure-Property Relationship

Nanocrystalline phase evolving from amorphous precursor by controlled annealing develops the unique properties with combination of the low losses, high permeability and near zero magnetostriction. The major requirements for superior soft magnetic properties are high initial permeability and extremely low coercivity, which is governed by low or vanishing magnetocrystalline anisotropy. The anisotropy constant,  $K_1$  for  $\alpha\text{-Fe}(\text{Si})$ , the constituent phase of FINEMET is about 8  $\text{kJ}/\text{m}^3$ , which is by far too large to explain by itself, the low coercivity ( $H_c < 1 \text{ A}/\text{m}$ ) and high initial permeability ( $\mu_i \approx 10^5$ ). Based on random anisotropy model (RAM) originally developed by Alben et. al. [13], Herzer provided theoretical basis for the superior soft magnetic properties, in which, it was stated that the effective anisotropy contribution of the small randomly oriented bcc  $\text{Fe}(\text{Si})$  grains is essentially reduced by exchange

interaction [14, 15]. The critical scale where the exchange energy starts to balance the anisotropy energy is  $L_0 = \left(\frac{A}{K_1}\right)^{1/2}$  where  $L_0$  is the exchange correlation length,  $A$  is the exchange stiffness constant and  $K_1$  is the magneto-crystalline anisotropy.  $L_0$  takes the value of about 35 nm for the material parameter of bcc Fe - 20 at.% Si that determines the order of the domain wall width. For  $D \approx \frac{L_0}{3}$ , i.e. grain sizes of the order of 10-15 nm, the magnetization will not follow the randomly oriented easy axis of the individual grains, but increasingly is forced to align parallel by exchange interaction. As a consequence, the local anisotropies are averaged out over an increasing number of grains, such that the effective anisotropy constant  $\langle K \rangle$  finally scales down like  $\langle K \rangle \sim \frac{D^6 K_1^4}{A^3}$ . The predicted  $D^6$  dependence of anisotropy,  $\langle K \rangle$  which is clearly related to initial permeability, is a good guiding principal to explain the enhancement of  $\mu_i \approx 10^5$  upon annealing.

The crucial role of exchange interaction is clearly evident when the measuring temperature exceeds the Curie temperature of the amorphous matrix ( $T > T_c^{am}$ ) in the temperature dependence of permeability of these biphase alloys. For  $T > T_c^{am}$ , the intergranular amorphous matrix become paramagnetic within which  $\alpha$ -Fe(Si) ferromagnetic nanograins are embedded. The exchange coupling between the nanograins largely ceases to exist. Thus for the measuring temperature  $T > T_c^{am}$ , the initial permeability drops down by almost two order of magnitude and the coercivity increases correspondingly [16].

For the measuring temperature  $T > T_c^{am}$ , another interesting behavior of superparamagnetism / superferromagnetism can be studied. Gradual increase of annealing temperature increases the volume fractions of crystallites embedded in a still amorphous matrix. Superparamagnetic relaxation in FINEMET type of alloys has been studied for compositions with a high content of refractory metal substituted for Fe such as Cr [17] and Cr / Mo [18]. Franco et. al. [19] have studied superparamagnetic relaxation in FINEMET type of alloy FeCuNbSiB without adding any extra refractory element and they have demonstrated that this behavior is a general characteristic of these nanocrystalline alloys provided the volume fraction of crystallites are very low. If the volume fraction of the nanocrystals and their sizes are small enough and the intergranular matrix is sufficiently thick to minimize the magnetic interactions between them, then superparamagnetic behavior of the nanocrystalline particles is expected. The existence of exchange interactions between crystallites of  $\alpha$ -Fe(Si) through the paramagnetic amorphous matrix in the nanocrystalline alloy of FeCuTaSiB was studied by Kulik and Hernando [20, 21]. Superferromagnetic behavior was observed in nanocrystalline FeCuNbSiB alloys with relatively high volume fractions of crystallites [22].

## 2.2 Co-based soft nanocomposite magnetic materials

Thermal treatment of Co-based amorphous materials below the crystallization temperature relaxes the amorphous structure, giving rise to ultra-soft magnetic properties. Changes in the pre-existing anisotropy direction have been observed in some cases due to rearrangement of atom pairs during heat treatment even in the absence of external magnetic field and applied stresses [23]. In the recent studies, it was found that heat treatment below the crystallization temperature in the Co-based amorphous alloy gave rise to the formation of nanocrystalline phase with grain size of about 2 nm, revealed by TEM [23] leading to very high value of initial permeability. According to Herzer [2, 13], formation of the nanocrystalline phase in Fe-based alloy containing Cu, annealed above the crystallization temperature, gives rise to reduction of the effective anisotropy because the random oriented anisotropies are averaged out by exchange interaction. Similar effect is believed to exist in the Co-based alloy in the early stage of crystallization [24-27].

### 2.2.1 Theory of Magnetoinductance and Giant Magnetoimpedance

#### Magnetoinductance

Magnetoinductive effects in ferromagnetic conductors can be used for various sensors. Hans Christian Oersted of Denmark discovered the principles of magnetoinductance in 1820. He found that whenever electricity flows through a wire, a magnetic field is produced around the wire. This produces magnetization in the conductor called magnetoinductance. If the current varies with time, then the magnetic flux in the conductor also varies and induces an electromotive force between the ends of the conductor that is superimposed on the Ohmic voltage.

In a wire with a circular cross section, the circumferential magnetic field,  $H$ , induced by a constant current with the density  $i$ , is  $H = \frac{ir}{2}$ , where  $r$  is the distance from the wire axis. For a wire with a 1 mm diameter and a current density of  $10^6$  A/m<sup>2</sup>, which is low enough not to increase the temperature by joule heating, the maximum magnitude of a magnetic field on the wire surface is 250 A/m or 3.125 Oe. The circumferential reversal of the conductor magnetization must be of this order or lower to detect the magnetoinductive voltage easily against the Ohmic background signal. Therefore, these applications require soft magnetic metals with high circumferential permeability.

The systematic study of magnetoinductive effects in soft magnetic conductors began with the development of amorphous wires. A large magnetoinductive effects was found in the zero-magnetostrictive, amorphous CoFeSiB wire that has a circumferential, bamboo-like domain structure in the outer shell. When an ac current of 1 kHz conducts through a CoFeSiB wire, sharp peaks are induced on the background Ohmic signal by the circumferential magnetization reversal in the outer shell by applying dc magnetic field. The peak amplitude decreases with an increase of external dc magnetic field.

### Giant Magnetoimpedance

Another magnetoinductive effect observed in soft ferromagnetic metals is GMI. GMI is a classical phenomenon that can be explained thoroughly on the basis of usual electromagnetic concepts in sharp contrast with giant magneto resistance (GMR) effect where resistance is changed by a magnetic field. GMR requires quantum mechanical concepts based on the spin of the carriers and their interactions with the magnetization of the magnetic material. The ac impedance in GMI has a strong dependence on the applied magnetic field. This effect occurs at high frequencies and can be explained by classical electrodynamics. Radio frequency (RF) current is not homogeneous over the cross section of a conductor, it tends to concentrate near the conductor's surface and is called skin effect. The exponential decay of current density from the surface towards the interior of the conductor is described by the skin depth:

$\delta = \sqrt{\frac{2\rho}{\omega\mu}}$ . It depends on the frequency of the RF current  $\omega$ , the resistivity  $\rho$ , and the permeability  $\mu$ . In

nonferromagnetic metals,  $\mu$  is independent of frequency and the applied magnetic field; its value is close to the permeability of vacuum  $\mu_0$ . In ferromagnetic materials, however, the permeability depends on the frequency, the amplitude of the ac magnetic field, the magnitude and orientation of a bias dc magnetic field, mechanical strain and temperature. The high permeability of soft magnetic metals and their strong dependence on the bias magnetic field are the origin of the GMI effect.

Magnetoimpedance (MI) consists of a change of total impedance of a magnetic conductor (usually ferromagnetic) under the application of a static magnetic field  $H_{dc}$ . When an ac current  $I = I_0 e^{j\omega t}$  of magnitude  $I_0$  and angular frequency  $\omega (= 2\pi f$ , with  $f$  the ordinary frequency) flows through the material, it generates, by Ampere's law, a transverse magnetic field inducing some magnetization. At low frequency, the change in the transverse magnetization generates an additional inductive voltage  $V_L$  across the conductor:  $V = RI + V_L$  where  $R$  is the resistance. Hence, MI can be written as  $Z = R + i\omega\phi/I$ , where the imaginary part is given by the ratio of magnetic flux to ac current and field dependence of MI is related to the transverse permeability. When frequency increases the current gets distributed near the surface of the conductor, changing both resistive and inductive components of the total voltage  $V$ . The field dependence of MI is governed by skin depth,  $\delta = \sqrt{\frac{2\rho}{\omega\mu}}$ . The current distribution is governed not only by the shape of

the conductor and frequency but also the transverse magnetization depending on  $H_{dc}$ .

At frequencies above 1 MHz, eddy currents heavily damp the domain wall movements, and only magnetization rotations are responsible for magnetic permeability. The minimum skin depth

$\delta_m = \sqrt{\alpha \left( \frac{\rho}{\gamma\mu_0 M_s} \right)}$  for soft magnetic amorphous alloys is about  $0.1\mu\text{m}$  (where  $\alpha$  is damping

parameter). This gives the maximum values of  $|Z|/R_{dc}$  around 1000. This value of GMI can be achieved only in uniaxial materials with the unit direction of anisotropy perpendicular to the conductor axis. Any



deviation of the unit axis from the perpendicular or any fluctuation of  $H_k$  substantially reduces the GMI effect.

It has been shown experimentally that a large MI often occurs at frequencies of a few MHz. Changing the dc biasing field  $H_{dc}$ , the maximum  $|Z|$  can be as large as a few times the value of  $R_{dc}$ , the dc resistance. At low frequency  $|Z|$  has a peak around  $H_{dc} \sim 0$  and as the frequency increases, the peak moves toward  $H_{dc} \sim \pm H_k$  where  $H_k$  is the anisotropy field. Therefore,  $|Z|$  as a function of  $H_{dc}$  possesses a single or a double peak as the frequency increases. When the direction of anisotropy field is well defined the peaks are sharp.

### 2.2.2 GMI phenomenon of Co-rich amorphous alloy

Giant magneto-impedance (GMI) is a characteristic property of Co-rich amorphous alloys [28-30]. Several general conditions must be satisfied by any material in order to show GMI effect.

- i. The material should be magnetically soft. That is, it should be easily magnetized or in other words must have a relatively narrow hysteresis curve implying, in general, small losses in the course of the magnetization cycle.
- ii. The materials should have a well-defined anisotropy axis. That means there must be a direction along which the magnetization of the material lies on the average in the direction of the easy axis. However, the value of the anisotropy field should be relatively small of the order of a few Oersteds.
- iii. The coercive field  $H_c$  must be small (fraction of an Oersted) with narrow hysteresis loop. Since  $H_c$  and the shape of the hysteresis loops change with the angle the magnetic field makes with the easy axis (or anisotropy axis) of the material, these are taken as the reference point when the field is along the easy axis.
- iv. The ac current  $I = I_0 e^{j\omega t}$ , injected in the material, should be perpendicular to the easy axis (or anisotropy direction) and the magnetic field,  $H_{ac}$  it creates should be small with respect to  $H_k$ .
- v. The material must have a small resistance ( $\leq 100 \mu\Omega \cdot \text{cm}$ ) since it carries the ac current. This is important, since many magnetic materials have large resistivities. Amorphous metals are interesting in that respect since, typically, their resistivities at room temperature are in the range of  $100 \mu\Omega \cdot \text{cm}$ .
- vi. The materials should have a large saturation magnetization  $M_s$  in order to boost the interaction with the external magnetic field.
- vii. The material should have a small magnetostriction (MS). This means, mechanical effects caused by application of a magnetic field should be small. Mechanical stress due to MS alters the soft magnetic properties of the material by acting as an effective anisotropy. This alters the direction of the anisotropy, displacing it from the transverse direction and thereby reducing the value of the MI.

MI effect did not attract much attention until Panina et al [31] and Beach et. al. [32] reported GMI effect in amorphous FeCoSiB wires with small magnetic field and at relatively low frequencies. Machado et. al.

[33] observed such effect in thin films and Beach et. al. [34] in ribbons. Atkinson et. al. [28] and Knobel et. al. [29] have shown that GMI is a classical phenomenon that can be explained thoroughly on the basis of usual electromagnetic concepts. Since early nineties scientists and researchers are pursuing their research to understand the phenomena of GMI and its technological application as sensors for detecting small magnetic field and magnetic heads and specially the GMI effect on Co-based and FINEMET compositions [35-41].

The dramatic variation of the MI with small magnetic field (a few Oersteds) and at relatively low frequencies (tens of MHz) in widely available materials is the origin of the interest in the Giant Magneto Impedance (GMI) effect. The effects of MI occur in widely differing magnitude depending on the geometry, the constituent materials and their layering.

In order to clearly identify GMI, several observations should be made:

- i. A very large change (of the order of at least 100% variation) of the impedance should occur with an external dc magnetic field  $H_{dc}$ . The change expressed in % is defined by the largest value of the ratio:
- ii. 
$$GMIR (\%) = \left( 1 - \frac{Z(H_{dc})}{Z(H_{max})} \right) \times 100 \quad (1)$$
- iii. where  $Z(H_{dc})$  is the impedance measured in the presence of the dc magnetic field and  $Z(H_{max})$  is the impedance measured at the maximum limit when the impedance does not change any longer with the applied field.
- iv. The parameters that characterize the GMI efficiency are the maximum value of GMI and the maximum field sensitivity expressed by the maximum value of derivative of field dependence of GMIR.
- v. The external dc magnetic field  $H_{dc}$  should be of the order of a few Oersteds only.
- vi. The frequency range is of the order of MHz or tens of MHz (excluding any effect based on Ferromagnetic Resonance (FMR) where the frequencies are typically in the GHz range). In many materials this means that the skin depth  $\delta$  (typically microns at these frequencies) is larger than the thickness of the materials (typically a fraction of micron). When the frequency is in the GHz,  $\delta_s$  is generally very small with respect to the thickness. i.e.  $\delta \ll a$ , where  $a$  is the characteristic length scale such as the wire radius or ribbon/film thickness. MI then decreases since permeability becomes insensitive to the field at high enough frequency.
- vii. It should be stressed that in ordinary metals, the skin depth does not depend on permeability, whereas in magnetic materials, the behavior of the permeability depending on geometry, temperature, stress, composition and so on, is reflected in the skin depth. In addition, permeability might be changed by post-processing the material after growth with annealing under the presence or absence of magnetic field or mechanical stress.

### 2.2.3 Applications of GMI

Soft ferromagnetic materials used in GMI applications play a key role in power distribution, make possible the conversion between electrical and mechanical energy, underlie microwave communication and provide both the transducers and the active storage material for data storage in information systems. Since GMI uses soft magnetic materials possessing a large permeability, the first immediate application is devices related to magnetic shielding since it requires the soft properties of the material. There are other applications, which involves GMI. The first of these applications are the detection of very small magnetic fields. Magnetic field sensors are broadly classified in three categories:

- i. Medium to large field detection by Hall and magnetoresistive devices
- ii. Small to medium magnetic field detection by magnetoimpedance and Flux Gate sensors.
- iii. Very small-to-small magnetic field detection by SQUID (Superconducting Quantum Interference Devices).

The possible devices are recording read heads, magnetic guidance devices in vehicles, boats and planes (with or without GPS, i.e. Global Positioning System), brain imaging (magneto-encephalogram or MEG devices) and heart mapping (magneto-cardiogram or MCG devices) etc. The detection of the Earth magnetic field has a host of applications for instance in Petroleum or minerals exploration or in shielding used for degaussing of high performance CRT monitors.

### 2.3 Fe-based hard nanocomposite magnetic materials

Recently, isotropic nanocrystalline magnetic materials with uniaxial anisotropy have been found to have a remanence to saturation magnetization ratio above the value of  $\frac{M_r}{M_s} = 0.5$  predicted by Stoner-

Wohlfarth model. This remanence enhancement is attributed to intergrain exchange interactions [42-44] and it has been observed both in single-phase [42, 45] and nanocomposite materials consisting of a fine mixture of soft and hard phases [46-48]. Exchange coupling between the phases allows one to optimize the magnetic properties of nanocomposite magnets by combining the high magnetization due to the presence of the soft phase with the high anisotropy of the hard phase. Nanocomposite materials show the characteristic 'exchange spring' behavior, which results from the reversible rotation of the soft magnetic component for field not large enough to reverse the hard magnetic phase [48]. Kueller and Hawig [48] has provided theoretical basis on exchange spring behavior of  $\text{Fe}_3\text{B}/\text{Nd}_2\text{Fe}_4\text{B}$  based alloy. A brief review on theoretical aspect has been presented below.

The theoretical limit for the maximum energy product of a given magnetic material can be represented by the following equation [48],

$$(\text{BH})_{\text{max}} \leq \frac{J_s^2}{4\mu_0} \quad (1)$$

Thus equation (1) leads to the idea that maximum energy product  $(BH)_{max}$  depends on its saturation polarization  $J_s = \mu_0 M_s$ . Other conditions which also govern the value of maximum energy product are  $B_r = J_s$  which requires that the solid ferromagnetic material, i.e., packing fraction  $p = 1$ , alignment of easy axes parallel to the field axis and critical fields for irreversible magnetization reversal (nucleation fields)

$H_n \geq \frac{J_s}{2\mu_0} \geq \frac{M_s}{2}$ . In order to fulfill the condition of equation (1) it is required that the material should

possess a high magnetocrystalline anisotropy  $K \gg \frac{J_s^2}{4\mu_0}$ . The magnitude of the ratio  $\frac{K}{J_s^2 / 4\mu_0}$

$= \frac{4K}{(\mu_0 M_s^2)}$  characterizes the basic magnetic behavior of the material. When the ratio  $\gg 1$ , the behavior is

dominated by magnetocrystalline anisotropy and when the ratio  $\ll 1$ , the behavior is governed by magnetostatic energy. Former materials are called hard magnetic materials while the latter are soft magnetic materials.

Most of the hard magnetic materials possess saturation magnetization lower than for many common soft magnetic materials whereas the coercivity of hard magnetic materials may exceed the value of  $M_s/2$  necessary to reach the limit of the equation (1). Therefore, it seems to be very suitable to consider composite materials of two suitably dispersed and mutually exchange-coupled phases, one of which is of the hard phase providing high enough nucleation field for irreversible magnetization reversal and the other is a soft phase with  $M_s$  as high as possible, in order to attain a high average saturation magnetization.

Further the hard phase materials contain about 25 wt.% or more of a rare earth material. This attributes to the high price and leads to the problem of chemical instability. Most of the soft phase materials are much less reactive and inexpensive. Therefore, a composite material of soft and hard phase is inexpensive and less corrosive since the resulting composition becomes rare earth deficient and soft phase envelops the hard phase regions in order to prevent their corrosion. Kneller and Hawig [48] have theoretically estimated the critical dimensions of the phases and discuss corresponding models of microstructure. On that basis they have typically derived magnetic properties of such composites.

### 2.3.1 Microstructure

In order to derive a rough estimate of the corresponding critical dimension of the phases let us consider one-dimensional model in Fig. 2.3 consisting of a sequence along x axis of alternating hard (k phase) and soft phase (m phase) regions of widths  $2b_k$  and  $2b_m$  respectively, which are crystallographically coherent and exchange coupled through the phase boundaries [48]. The magnetocrystalline anisotropy is assumed to be uniaxial (for simplicity) in both phases, with both easy axes being parallel to the z-axis and perpendicular to x. The anisotropy energy density depends on the angle  $\phi$  between  $\vec{M}$  and the easy axis as

$$E_k = K \sin^2 \phi \quad (2)$$

where  $K > 0$ . As per the definition mentioned earlier it may be mentioned that the ratio of the hard phase  $k_k = \frac{4K_k}{\mu_0 M_{sk}^2} \gg 1$  and that for the soft phase,  $k_m = \frac{4K_m}{\mu_0 M_{sm}^2} \ll 1$ . The ratio  $\frac{k_k}{k_m}$  is of the order  $10^2$  to  $10^3$ , according to Table 1. This is due mainly to the magnitude of the ratio  $\frac{K_k}{K_m}$  of the order of  $10^2$ . The values of  $M_{sm}$  and  $M_{sk}$  are mostly of the same order of magnitude, with the ratio  $\frac{M_{sm}^2}{M_{sk}^2}$  not exceeding 10 in practical cases.

The exchange energy density may be written in the form

$$E_A = A \left( \frac{d\psi}{dx} \right)^2 \quad (3)$$

where  $A$  is a constant of the order  $10^{11}$  J/m at room temperature, but depends on the Curie temperature  $T_C$  and temperature  $T$  as  $A \propto T_C \left[ \frac{M_s(T)}{M(0)} \right]^2$ , and  $\psi$  is for the present model the angle in the  $yz$  plane between  $M_i$  and the  $z$  axis. With these quantities, the energy per unit area of a  $180^\circ$  Bloch wall in a homogenous material may be written approximately as

$$\gamma \approx \delta K + \delta A \left( \frac{\pi}{\delta^2} \right) \quad (4)$$

where  $\delta$  is the wall thickness. In equilibrium,  $\gamma(\delta)$  has a minimum ( $d\gamma/d\delta = 0$ ), from where the equilibrium quantities  $\delta_0, \gamma_0$  are obtained:

$$\delta_0 \approx \pi \left( \frac{A}{K} \right)^{1/2} \quad (5)$$

$$\gamma_0 \approx 2\pi(A.K)^{1/2} \quad (6)$$

Critical dimensions for a high-energy magnetization reversal in the one-dimensional system in Fig. 2.3 are obtained from a consideration of the reversal process. Let us assume that the hard phase has a reasonable

thickness,  $b_k \approx \delta_0 = \pi \left( \frac{A}{K} \right)^{1/2}$  corresponding to about its critical thickness. Starting from the saturation

remanence along the easy direction  $+z$  in Fig. 2.3(a) when the reverse field  $\vec{H}$  is increased progressively, the magnetization will invariably begin to change reversibly in the soft phase. It should be noted at this

point that since  $K_m \ll K_k$  therefore,  $b_m \approx \delta_{0m} = \pi \left( \frac{A_m}{K_m} \right)^{1/2}$ . In this condition, two equilibrium  $180^\circ$  walls

will form reversibly in  $m$ -phase in Fig. 2.3(b). When  $\vec{H}$  is further increased in Fig. 2.3(c), these walls will be reversibly compressed towards the  $k$ -phase boundary, and the energy density in these walls will

Table 2.1 Room temperature values of magnetic properties of some magnetically hard (k-type) and some magnetically soft (m-type) materials [48].

Category	Material	Crystal Symmetry	$T_c$ (°C/K)	$M_s$ ( $10^6$ A / m)	K ( $10^6$ J/m <sup>3</sup> )	$\kappa = \frac{4K}{\mu_0 M_s^2}$	$H_A$ ( $10^6$ A/m)	$\mu_0 H_A$ (T)	$J_s$ (T)	$\frac{J_s^2}{4\mu_0}$ ( $10^5$ J/m <sup>3</sup> )
k-typed hard ( $\kappa \gg 1$ ) $H_A = \frac{2K}{\mu_0 M_s}$	BaO.6Fe <sub>2</sub> O <sub>3</sub>	hex	450/723	0.38	0.32	7.2	1.35	1.7	0.47	0.45
	MnB <sub>1</sub>	tetr	360/633	0.58	1.16	9.2	2.94	3.7	0.72	1.3
	Nd <sub>2</sub> Fe <sub>14</sub> B	tetr	312/585	1.25	9.4	19	12	15.1	1.57	4.9
	Co <sub>5</sub> Sm	hex	730/1003	0.84	11.9	54	23	28.6	1.05	2.2
(k ≈ 1) $\frac{M_s}{2} / \frac{2K}{\mu_0 M_s}$ m-type soft ( $\kappa \ll 1$ ) $H_A = \frac{M_s}{2}$	Co	hex	1120/1393	1.40	0.53	0.84	0.70/0.60	0.88/0.75	1.76	6.2
	α-Fe	cub	760/1043	1.70	0.047	0.05	0.85	1.06	2.13	9.0
	Fe <sub>23</sub> B <sub>6</sub>	cub	425/698	1.35	0.01	0.03	0.67	0.86	1.70	5.7
	Fe <sub>3</sub> B	tetr	510/783	1.28	≈0.2	0.39	0.64	0.80	1.60	5.1

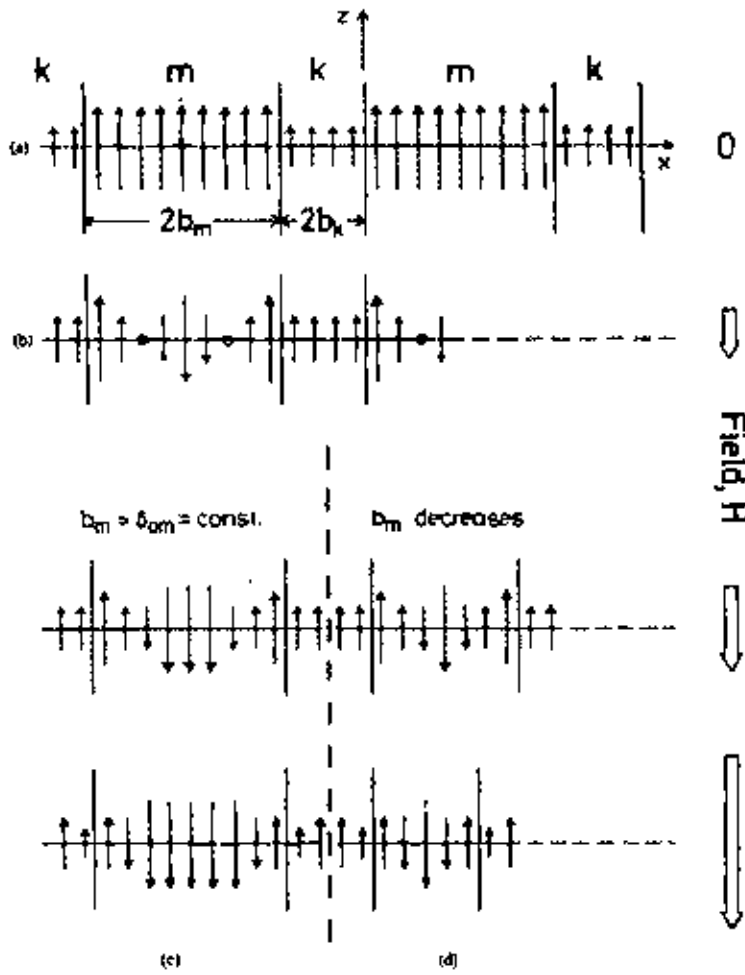


Fig. 2.3. Schematic one-dimensional model of the microstructure and micromagnetic structure of the exchange-coupled composite material as a basis for the calculation of the critical dimensions of the phase regions [48].

increase above its equilibrium value. The magnetization in the k-phase  $\bar{M}_{sk}$  remains essentially unchanged, as  $K_k \gg K_m$ . This process will continue until the energy density in the soft phase,  $E_{\gamma m}$  approaches the equilibrium energy density of the hard phase  $E_{\gamma k}$ . In this case, the wall will invade into the k-phase, thus leading to irreversible magnetization reversal of both the m and k phase regions. The corresponding critical field  $H_{co}$  is lower than the anisotropy field of the k-phase  $H_{co} < H_{Ak} = \frac{2K_k}{M_{sk}}$ , yet it will have about the same order of magnitude.

The coercive field  $H_{CM}$  is defined by  $M(H_{CM}) = 0$  and is much smaller,  $H_{CM} \ll H_{co}$ , as  $M_{sm} > M_{sk}$  and also because it has been assumed that  $b_m \gg b_k$  and thus the demagnetization curve  $M_i(H = 0)$  and  $M(H_{CM}) = 0$  is completely reversible. If  $b_m$  is now reduced to values  $b_m < \delta$ ,  $H_{co}$  remains unchanged, but  $H_{CM}$  increases because, for  $H < H_{co}$ , the thickness of the  $180^\circ$  walls in the m-phase is essentially confined to  $\delta_m \approx b_m < \delta_{om}$ . Hence the critical width of the m-phase  $b_{cm}$  giving the maximum coercivity is determined in the following way: For small  $\delta_m$  ( $\delta_m \ll \delta_{om}$ ) from equation 4,  $\gamma_m(\delta_m) \approx \delta_m A_m \left( \frac{\pi}{\delta_m} \right)^2$ , from where the energy density is,  $E_{\gamma m} = \frac{\gamma_m}{\delta_m} \approx A_m \left( \frac{\pi}{\delta_m} \right)^2$ . Inserting the result in  $\delta_m = b_{cm}$  yields the critical dimension of the m phase:

$$b_{cm} \approx \pi \left( \frac{A_m}{2K_k} \right)^{1/2} \quad (7)$$

With representative values  $A_m = 10^{11}$  J/m,  $K_k = 2 \times 10^6$  J/m<sup>3</sup>, one gets for  $b_{cm} \approx 5$  nm. For the k-phase a critical thickness cannot be derived theoretically. For practical purposes it seems reasonable to take  $b_{ck}$  about equal to the equilibrium wall thickness in the k-phase  $b_{ck} = \delta_{ck} = \pi \left( \frac{A_k}{K_k} \right)^{1/2}$ , as has been assumed initially. Since mostly  $A_k < A_m$  on account of the generally low Curie temperatures of the k-materials, this gives for  $b_{ck}$  about the same magnitude as  $b_{cm}$ :

$$b_{ck} \approx b_{cm} \quad (8)$$

### 2.3.2 Magnetic Behavior

According to the foregoing analysis, the demagnetization curve after previous saturation of such a material will be reversible in reverse fields  $H < H_{co}$ , i.e. before the magnetization of the k-phase begins to switch, as is illustrated schematically in Fig. 2.4(a) and 2.4(b). At  $H < H_{co}$ , the material has unidirectional anisotropy on account of exchange coupling between the two phases. For a given pair of phases, the reversible range in  $M$ ,  $\Delta M_{rev}$ , depends on the volume fraction of the hard phase,  $v_k$  (i.e. the soft phase  $v_m =$



1 -  $v_k$ , respectively), on the ratio  $\frac{M_{sm}}{M_{sk}}$ , and on the lateral dimension of the m-phase  $b_m$ . At fixed  $v_k$  and

$\frac{M_{sm}}{M_{sk}}$ ,  $\Delta M_{rev}$  is smallest for  $b_m \approx b_{cm}$  in the optimum microstructure of Fig. 2.4(a). The value of  $\Delta M_{rev}$

increases as  $b_m > b_{cm}$  in the overaged state of Fig. 2.4(b) because  $H_{n0}$  remains constant. At large  $v_{0b}$ ,  $v_{cm} \approx 0.8$ , for example,  $\Delta M_{rev}$  may well exceed the saturation remanence  $\Delta M_{rev} > M_r$ .

It is for this specific and quite typical magnetic behavior, in a sense resembling a mechanical spring, that such magnets have been termed exchange spring. Their striking reversibility in conjunction with a high remanence and high coercivity distinguishes them uniquely from the conventional single ferromagnetic phase permanent magnets, where the demagnetization curve reflect essentially the distribution of the critical switch field and therefore mainly reversible in Fig. 2.4(a).

In order to further illustrate these features, some minor loops are drawn in Fig. 2.4(a)-(c), as they will be obtained upon reducing to zero and re-increasing the field at various points along the demagnetization curve. The recoil permeability  $\mu_r$  of an exchange spring magnet is expected to be about 5 times as large as that of a conventional magnet with equal coercive field and saturation magnetization. For the general shape of the demagnetization curve  $M(H)$ , it is immediately obvious from the exchange spring mechanism that an optimum microstructure ( $b_m \approx b_{cm}$ ) will yield a "normal" convex  $M(H)$  curve of Fig. 2.4(a) between  $M_r$  and  $M = 0$ , similar to a conventional permanent magnet of Fig. 2.4(c). Whereas an overaged microstructure ( $b_m \gg b_{cm}$ ) must lead to a quite characteristic shape of the demagnetization curve being concave throughout between  $M_r$  and  $M_s$  in the reverse direction. In any case, the exchange coupling between the phases produces a shape of the saturation loop like that of a uniform material showing indication of the presence of two phases with extreme different hardness. If there were no exchange coupling, one would get a constricted loop as in Fig. 2.4(d).

### 2.3.3 Technological Realization

Essential condition for the microstructure, which leads to the exchange spring behavior of such materials are a fine and regular dispersion of phases and exchange coupling between the soft and hard phase regions, which implies the crystallographically coherent formation of two phases with generally different structures. Continuous decomposition of a metastable supersaturated phase that has crystallized from a glassy state leads to such condition. Thus the materials with the desired properties may be produced by liquid quenching of a suitable alloy to the glassy state and subsequent heating of the glass. Coehoorn et al. [49-50] first reported that liquid quenching and subsequent heating of alloys in the vicinity of  $Nd_4Fe_{77}B_{19}$  leads to remarkable permanent magnetic properties, which possess coercivity of around 280 kA/m (3.5 kOe) and  $(BH)_{max}$  of around 95 kJ/m<sup>3</sup> (11.9 MGOe) and unusually high remanent ratio greater than 0.5.

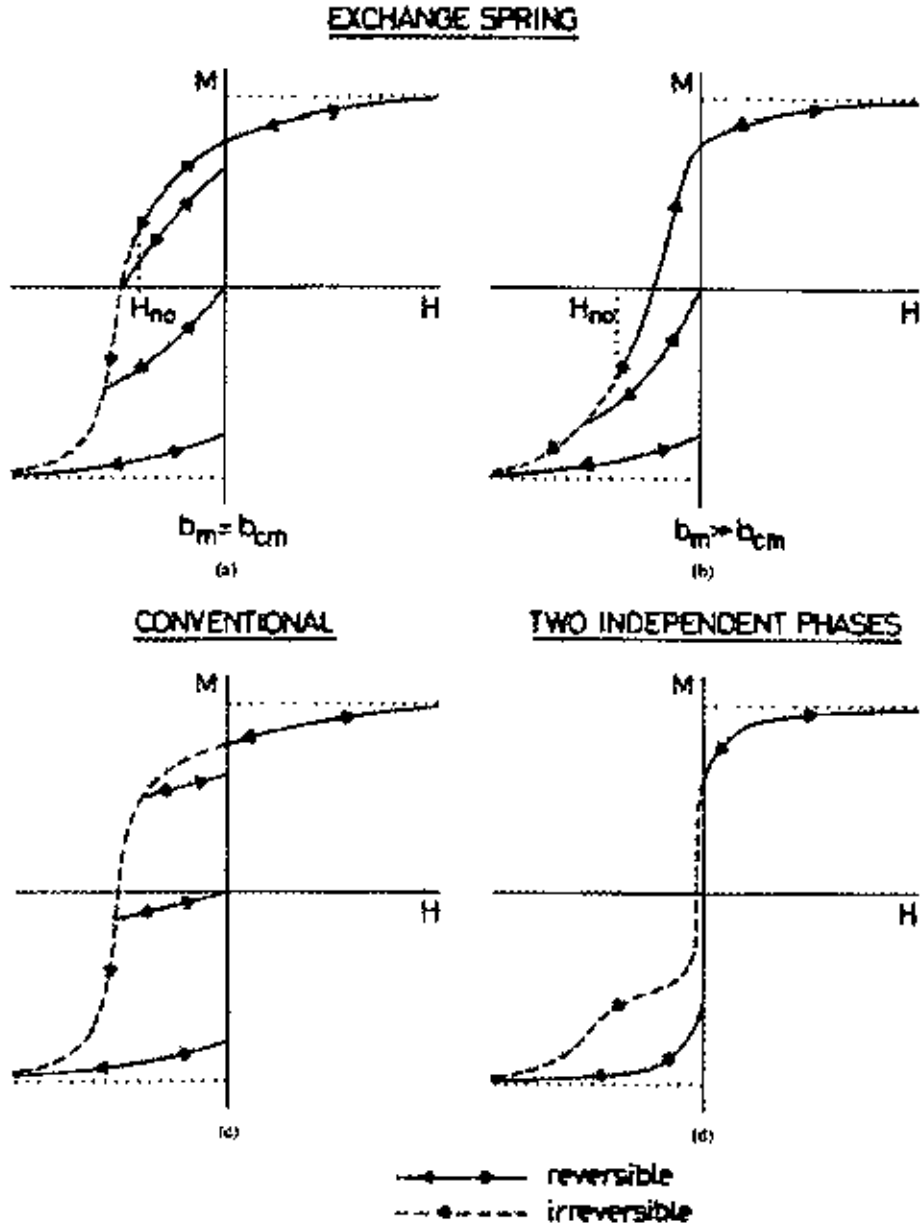


Fig. 2.4. Typical demagnetization curves  $M(H)$  (schematic) (a) Exchange-spring magnet with optimum microstructure (b) with overaged microstructure (c) Conventional single ferromagnetic phase magnet (d) Mixture of two independent ferromagnetic phases with largely different hardness (constricted loop) [48].

The material was found to consist of 85% soft magnetic phase namely 73%  $\text{Fe}_3\text{B}$  and 12%  $\alpha\text{-Fe}$  and only 15% hard phase namely  $\text{Nd}_2\text{Fe}_{14}\text{B}$ . Kneller and Hawig [48] studied alloys of similar composition  $\text{Nd}_{3.8}\text{Fe}_{77.2}\text{B}_{19}$ , which they have called as alloy (A) and  $\text{Nd}_{3.1}\text{Fe}_{73.1}\text{B}_{18}\text{Si}_1\text{B}_{3.9}$ , which they have called as alloy (B) and confirmed the study of Coehoorn et al. [49] Kneller and Hawig [48] paid particular attention to the structural development during heating of the glass by continuous X-ray structural analysis technique using dynamic temperature X-ray diffraction (DTXD).

The study of DTXD analysis of the crystallization process of alloy (A) by Kneller and Hawig [48] have revealed that the phases present in the optimum magnetic state  $\alpha\text{-Fe}$ ,  $\text{Fe}_3\text{B}$  and  $\text{Nd}_2\text{Fe}_{14}\text{B}$  do not emerge directly from the glassy state. The glassy state crystallize completely in the metastable  $\text{Cr}_{23}\text{C}_6$ -type phase namely  $\text{Fe}_{23}\text{B}_6$ . Very broad and therefore barely detectable reflections seem to result from its supersaturation with the comparatively large Nd atoms. Almost immediately after crystallization, the  $\text{Fe}_{23}\text{B}_6$  phase decomposes first and to the most part into  $\text{Fe}_3\text{B}$  and some  $\alpha\text{-Fe}$  and finally, at a somewhat higher temperature  $\text{Nd}_2\text{Fe}_{14}\text{B}$ . None of the phases,  $\text{Fe}_3\text{B}$  and  $\alpha\text{-Fe}$ , dissolve Nd. Therefore, supersaturation of Nd in the remaining  $\text{Fe}_{23}\text{B}_6$  further increases and transform into  $\text{Nd}_2\text{Fe}_{14}\text{B}$ . Since all of these three phases develop from a common crystalline  $\text{Fe}_{23}\text{B}_6$  matrix they are crystallographically coherent.

A departure from ideal exchange-spring behavior is signaled by multiphase magnetic reversal and irreversible magnetic changes that are evident at intermediate magnetic fields. These changes may be monitored via the major demagnetization curve. Analysis of the demagnetization curve yields the exchange-bias field  $H_{\text{ex}}$  and the irreversible magnetic field  $H_{\text{ir}}$ . The reorientation of the soft layer is characterized by  $H_{\text{ex}}$ . For  $H < H_{\text{ex}}$  the magnetization of the soft layer remains parallel to that of the hard layer and for  $H_{\text{ir}} > H > H_{\text{ex}}$  soft layer moments rotate away from the hard layer alignment direction, lowering the magnetization component along that direction. The irreversible magnetic field  $H_{\text{ir}}$  describes the reverse field magnitude that causes the hard phase reversal.

Reversible and irreversible component of the magnetization change as a function of the reverse field can be determined by analyzing the dc demagnetization curve  $M(H)$  between the saturation remanence  $M_r$  and

the reverse saturation  $-M_s$ , which gives the curve  $D(H) \equiv \left[ \frac{M_r - M_d(H)}{2M_r} \right] = -\frac{\Delta M_{\text{irreversible}}}{2M_r}$  versus  $H$ . The

irreversible portion is described by the dc field demagnetization remanence  $M_d(H)$  being the remanence acquired after saturation in one direction and subsequent application of a dc field  $H$  in the opposite

direction. The derivative  $\frac{dD(H)}{dH} = f(H_n)$  is the distribution function of critical field  $H_n$  for irreversible

magnetization reversals.

The reversible and irreversible components of the magnetization provide further insights as the material is cycled through the hysteresis loop. These components can be obtained from the recoil curve, which results from the successive removal to remanence and re-application of an increasingly negative demagnetization

field from the major demagnetization curve. In exchange spring system, any magnetization not recovered during a recoil measurement – the irreversible magnetization change – consists of a portion of the system that has already permanently switched polarity at a given reverse field. The steepness of the recoil curve, or the recoil susceptibility, characterizes the ease of remagnetization or “springness” of that portion of the system undergoing rotation during recoil. Kneller and Hawig [48] note that exchange-spring magnets have recoil susceptibilities five times greater than those found in conventional sintered magnets. Additionally, in contrast to recoil curves obtained from sintered permanent magnets, it is often noted that recoil curves measured from nanocrystalline magnetic materials are open, indicating the amount of materials reversing during the recoil.

In the general case, fully reversible exchange-spring behavior may persist until application of a critical negative field that causes irreversible changes in the magnetic polarization, with larger critical fields associated with a stronger exchange-spring response. These irreversible changes will be manifested as a departure from the ideal recoil remanence ratio of unity and produce recoil loops of varied area. As this critical negative field signals incoherent magnetic reversal in the system, it will be referred to as the “breakdown” field [51, 52]. At this field the system is no longer fully exchange coupled throughout the volume. Quantitative analysis of the areas enclosed by the recoil curves thus provides information about the interactions inherent to exchange-spring systems. Harland et. al. [51] reported that the development of the area of the recoil curve with reverse field and temperature provides information about the breakdown in coherence of the magnetic reversal is signaled by the appearance of open recoil loops. The recoil loops widen as individual decoupled regions of the nanocrystalline materials are driven around mini hysteresis loops during the course of the demagnetization and remagnetization processes.

## **Chapter 3**

### **Experimentals**

### 3.1 Melt spin system

Amorphous alloys in the form of ribbons have been prepared by single roller melt-spinning technique in air. Melt spin system presented in Fig. 3.1 is a small laboratory system, especially designed for production of amorphous and microcrystalline ribbons. Melting of material is performed by a high frequency generator with water-cooled induction coil. Molten material flows through a slot on a fast rotating copper wheel. The melt is quenched with a cooling rate of more than  $10^6$  K/s, which solidifies in an amorphous structure.

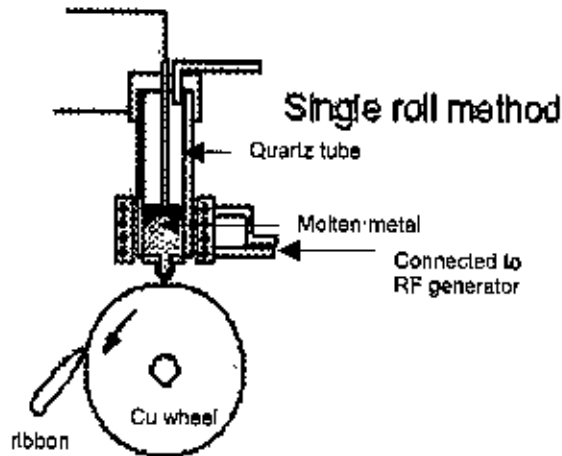


Fig. 3.1. Schematic diagram of melt spin system.

#### 3.1.1 Preparation of Fe and Co-based soft magnetic ribbon by melt spin system

The composition of Fe and Co-based soft magnetic materials are  $\text{Fe}_{73}\text{Cu}_1\text{Nb}_{3.5}\text{Si}_{14}\text{B}_{8.5}$ ,  $\text{Fe}_{73.5}\text{Cu}_{0.6}\text{Nb}_{2.4}\text{Si}_{13}\text{B}_{8.5}$ ,  $\text{Fe}_{73.5}\text{Cu}_1\text{Ta}_3\text{Si}_{13.5}\text{B}_9$ ,  $\text{Co}_{68}\text{Fe}_4\text{Ni}_1\text{Si}_{13}\text{B}_{12}$ ,  $\text{Co}_{67}\text{Fe}_4\text{Ni}_2\text{Si}_{15}\text{B}_{12}$ ,  $\text{Co}_{67}\text{Fe}_4\text{Mo}_2\text{Si}_{15}\text{B}_{12}$ . The purity and origin of the constituent elements are Fe (99.98%), Cu (99.9%), Nb (99.8%), Ta (99.8%), B (99.5%) and Si (99.9%) as obtained from Johnson Matthey (Alfa Aesar Inc.) Co (99.8%) of Chempur Feinchemikalien. Constituent elements of the alloys have been weighed in the correct proportion and collected into a quartz tube. The tube has been evacuated by a diffusion pump up to a pressure of  $10^{-6}$  mbar. Ingots of each composition were prepared using induction melting associated with melt-spin machine. The ingots are then inserted into another quartz tube. An orifice in the dimension of 6 mm width and 1 mm thickness has been prepared at the closed-end of this tube. Ingots are then melted using induction melting up to the melting point of all the constituents. Appropriate temperature of the melt has been assumed from the color of the melt by eye-estimation. The melt is then purged using Ar pressure to produce ribbon on an average 6 mm width and 20-25  $\mu\text{m}$  thickness.

### 3.1.2 Preparation of Fe-based hard magnetic ribbon by melt spin system

Exchange spring alloys of the composition of  $(\text{NdPr})_x\text{Fe}_{71}\text{Co}_5\text{Cu}_{0.5}\text{Nb}_1\text{B}_{18.5}$ ,  $\text{Nd}_4\text{Fe}_{73.5}\text{Co}_5\text{Hf}_{0.5}\text{Ga}_{0.5}\text{B}_{18.5}$ ,  $\text{Nd}_3\text{Tb}_1\text{Fe}_{76}\text{Cu}_{0.5}\text{Nb}_1\text{B}_{18.5}$  were prepared in the form of ribbons using melt-spin machine. The purity and origin of the constituent elements were Fe (99.98%), Cu (99+%), Nb (99.8%), B (99.5%), Si (99.9%), Nd (99.9%), Pr (99.9%), Tb (99.9%), Hf (99.9%), Ga (99.9%), Cr (99.9%) from Johnson Matthey (Alfa Aesar) and Co (99.8%) from Chempur Feinchemikalien. Constituent elements in the correct proportions were mixed and melted in the arc-melting furnace under vacuum of  $10^{-6}$  mbar pressure. In order to homogenize perfectly, the alloys were melted three times. The ingots were then poured into a quartz tube having an orifice diameter of 1 mm. Quartz tube was placed inside an induction coil associated with machine. A steel casing covers whole assembly of single roller melt-spin machine. In the beginning the chamber inside the casing was flashed by Ar gas three times. The chamber was then filled with Ar gas. The alloy ingots were then melted by induction melting. Appropriate temperature of the melt was assumed from the color by eye estimation. When the color of the melt was appropriate amorphous ribbons were obtained in Ar atmosphere by purging the melt using Ar pressure. Wheel speed of single roller melt spin machine was around 25 m/s. The resulting ribbons were heat treated in an evacuated quartz tube of  $10^{-5}$  mbar pressure at different temperatures and times to observe the effect of annealing condition on the magnetic properties.

## 3.2 Thermal Analysis Techniques

Thermal analysis comprises of a group of techniques in which a physical property of a substance is measured as a function of temperature, while the substance is subjected to a controlled temperature programme. In differential thermal analysis, the temperature difference that develops between a sample and an inert reference material is measured, when both are subjected to identical heat treatments. The related technique of differential scanning calorimetry relies on differences in energy required to maintain the sample and reference at an identical temperature.

### 3.2.1 Differential Thermal Analysis (DTA)

DTA involves heating or cooling a test sample and an inert reference under identical conditions, while recording any temperature difference between the sample and reference. This differential temperature is then plotted against time, or against temperature. Changes in the sample, which lead to the absorption or evolution of heat, can be detected relative to the inert reference. Differential temperatures can also arise between two inert samples when their response to the applied heat treatment is not identical. DTA can therefore be used to study thermal properties and phase changes which do not lead to a change in enthalpy. The baseline of the DTA curve should then exhibit discontinuities at the transition temperatures and the slope of the curve at any point will depend on the microstructural constitution at that temperature.

A DTA curve can be used as a fingerprint for identification purposes, for example, in the study of clays where the structural similarity of different forms renders diffraction experiments difficult to interpret. The area under a DTA peak can be related to the enthalpy change and is not affected by the heat capacity of the sample. DTA may be defined formally as a technique for recording the difference in temperature between a substance and a reference material against either time or temperature as the two specimens are subjected to identical temperature regimes in an environment heated or cooled at a controlled rate.

### *Apparatus*

The key features of a differential thermal analysis kit are as follows (Fig. 3.2): sample holder comprising thermocouples, sample containers and a ceramic or metallic block, furnace, temperature programmer, recording system. The essential requirements of the furnace are that it should provide a stable and sufficiently large hot-zone and must be able to respond rapidly to commands from the temperature programmer. A temperature programmer is essential in order to obtain constant heating rates. The recording system must have a low inertia to faithfully reproduce variations in the experimental set-up.

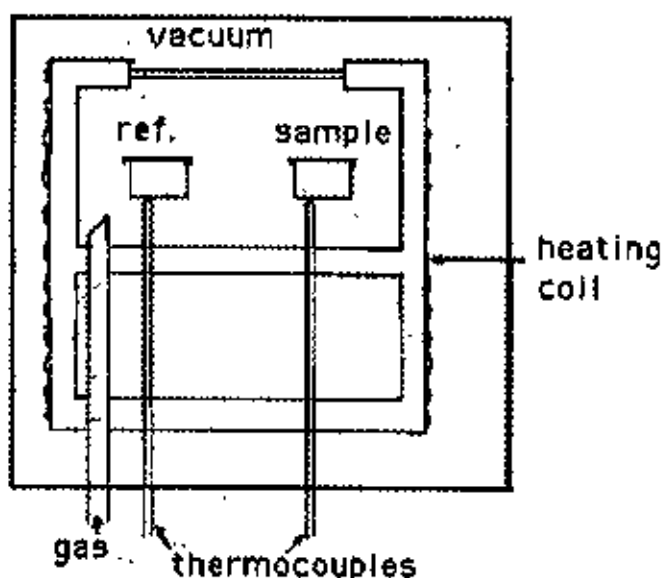


Fig. 3.2. Schematic illustration of a DTA cell.

The sample holder assembly consists of a thermocouple each for the sample and reference, surrounded by a block to ensure an even heat distribution. The sample is contained in a small crucible designed with an indentation on the base to ensure a snug fit over the thermocouple bead. The crucible may be made of materials such as pyrex, silica, nickel or platinum, depending on the temperature and nature of the tests involved. The thermocouples should not be placed in direct contact with the sample to avoid contamination and degradation, although sensitivity may be compromised. Metallic blocks are less prone



to base-line drift when compared with ceramics which contain porosity. On the other hand, their high thermal conductivity leads to smaller DTA peaks.

The sample assembly is isolated against electrical interference from the furnace wiring with an earthed sheath, often made of platinum-coated ceramic material. The sheath can also be used to contain the sample region within a controlled atmosphere or a vacuum.

During experiments at temperatures problems are encountered in transferring heat uniformly away from the specimen. These may be mitigated by using thermocouples in the form of flat discs to ensure optimum thermal contact with the now flat-bottomed sample container, made of aluminium or platinum foil. To ensure reproducibility, it is then necessary to ensure that the thermocouple and container are consistently located with respect to each other.

### *Experimental Factors*

Care is necessary in selecting the experimental parameters. For example, the effects of specimen environment, composition, size and surface to volume ratio all affect powder decomposition reactions, whereas these particular variables may not affect solid state phase changes. Experiments are frequently performed on powders so the resulting data may not be representative of bulk samples, where transformations may be controlled by the build up of strain energy. The packing state of any powder sample becomes important in decomposition reactions and can lead to large variations between apparently identical samples.

In some circumstances, the rate of heat evolution may be high enough to saturate the response capability of the measuring system; it is better then to dilute the test sample with inert material. For the measurement of phase transformation temperatures, it is advisable to ensure that the peak temperature does not vary with sample size. The shape of a DTA peak does depend on sample weight and the heating rate used. The influence of heating rate on the peak shape and disposition can be used to advantage in the study of decomposition reactions, but for kinetic analysis it is important to minimize thermal gradients by reducing specimen size or heating rate.

### *Interpretation and Presentation of Data*

A simple DTA curve may consist of linear portions displaced from the abscissa because the heat capacities and thermal conductivities of the test and reference samples are not identical, and of peaks corresponding to the evolution or absorption of heat following physical or chemical changes in the test sample.

There are difficulties with the measurement of transition temperatures using DTA curves. The onset of the DTA peak in principle gives the start-temperature, but there may be temperature lags depending on the location of the thermocouple with respect to the reference and test samples or the DTA block. It is wise to calibrate the apparatus with materials of precisely known melting points. The peak area (A), which is

related to enthalpy changes in the test sample, is that enclosed between the peak and the interpolated baseline. When the differential thermocouples are in thermal, but not in physical contact with the test and reference materials, it can be shown that  $A$  is given by,  $A = \frac{mq}{gK}$ , where  $m$  is the sample mass,  $q$  is the enthalpy change per unit mass,  $g$  is a measured shape factor and  $K$  is the thermal conductivity of sample. With porous, compacted or heaped samples, the gas filling the pores can alter the thermal conductivity of the atmosphere surrounding the DTA container and lead to large errors in the peak area. The situation is made worse when gases are evolved from the sample, making the thermal conductivity of the DTA-cell environment different from that used in calibration experiments.

The DTA apparatus is calibrated for enthalpy by measuring peak areas on standard samples over specified temperature ranges. The calibration should be based upon at least two different samples, conducting both heating and cooling experiments

In the present work, SEIKO TG/DTA 6300 has been used for thermal analysis. The TG/DTA is a simultaneous measurement instrument combining TG, which utilizes a horizontal differential type balance beam, with the highly flexible DTA feature. This instrument is used for reaction velocity and acceleration degradation tests, as well as analysis of the water and ash content in samples, and evaluation of decomposition, oxidation and heat resistance of samples.

The features are,

- i. As a forerunner in the balance beam mechanism, this instrument utilizes a horizontal differential type balance beam. The lightweight structure of the balance beam mechanism provides the following strong points: stability in regards to temperature fluctuations, buoyancy reduction and highly sensitive balance, as well as the ability of the differential balance to deal with disturbances such as oscillation.
- ii. Through the utilization of an automatic cooling unit, the instrument is now automatically cooled to a set temperature after measurements, which raises the effectiveness of measurements.
- iii. As with the DSC, the auto sampler is easily attached to the TG/DTA.

Temperature range is ambient to 1773 K; balance method is horizontal differential type; TG measurement range is  $\pm 200\text{mg}$ ; DTA measurement range is  $\pm 1000\mu\text{V}$ ; program rate is 0.01 to 100 K/min; gas flow rate is 0 to 1000ml/min; cooling rate is less than 15 minutes from 1273 to 323 K.

### 3.2.2 Differential scanning calorimetry (DSC)

DSC is a thermoanalytical technique in which the difference in the amount of heat required to increase the temperature of a sample and reference are measured as a function of temperature. Both the sample and reference are maintained at very nearly the same temperature throughout the experiment. Generally, the temperature program for a DSC analysis is designed such that the sample holder temperature increases linearly as a function of time. The reference sample should have a well-defined heat capacity over the

range of temperatures to be scanned. The basic principle underlying this technique is that, when the sample undergoes a physical transformation such as phase transitions, more (or less) heat will need to flow to it than the reference to maintain both at the same temperature. Whether more or less heat must flow to the sample depends on whether the process is exothermic or endothermic. For example, as a solid sample melts to a liquid it will require more heat flowing to the sample to increase its temperature at the same rate as the reference. This is due to the absorption of heat by the sample as it undergoes the endothermic phase transition from solid to liquid. Likewise, as the sample undergoes exothermic processes (such as crystallization) less heat is required to raise the sample temperature. By observing the difference in heat flow between the sample and reference, differential scanning calorimeters are able to measure the amount of heat absorbed or released during such transitions. DSC may also be used to observe more subtle phase changes, such as glass transitions. DSC is widely used in industrial settings as a quality control instrument due to its applicability in evaluating sample purity.

### **DSC Instrumentation**

A typical differential scanning calorimeter consists of two sealed pans: a sample pan and a reference pan (which is generally an empty sample pan). These pans are often covered by or composed of aluminum, which acts as a radiation shield. The two pans are heated, or cooled, uniformly while the heat flow difference between the two is monitored. This can be done at a constant temperature (isothermally), but is more commonly done by changing the temperature at a constant rate, a mode of operation also called temperature scanning.

During the determination, the instrument detects differences in the heat flow between the sample and reference. This information is sent to an output device, most often a computer, resulting in a plot of the differential heat flow between the reference and sample cell as a function of temperature. When there are no thermodynamic physical or chemical processes occurring, the heat flow difference between the sample and reference varies only slightly with temperature, and shows up as a flat, or very shallow base line on the plot. However, an exothermic or endothermic process within the sample results in a significant deviation in the difference between the two heat flows. The result is a peak in the DSC curve. Generally, the differential heat flow is calculated by subtracting the sample heat flow from the reference heat flow. When following this convention, exothermic processes will show up as positive peaks (above the baseline) while peaks resulting from endothermic processes are negative (below the baseline). The sample (in a condensed form such as powder, liquid, or crystal) is generally placed in an aluminum sample pan, which is then placed in the sample cell. The reference consists of a matched empty aluminum sample pan that is placed in the reference cell of the instrument. The sample pans are designed to have a very high thermal conductivity. Sample sizes generally range from 0.1 to 100 mg. The instrument cells are often airtight to shield the sample and reference from external thermal perturbations. This also allows experiments to be performed under variable pressures and atmospheres.

### Heat Flux DSC

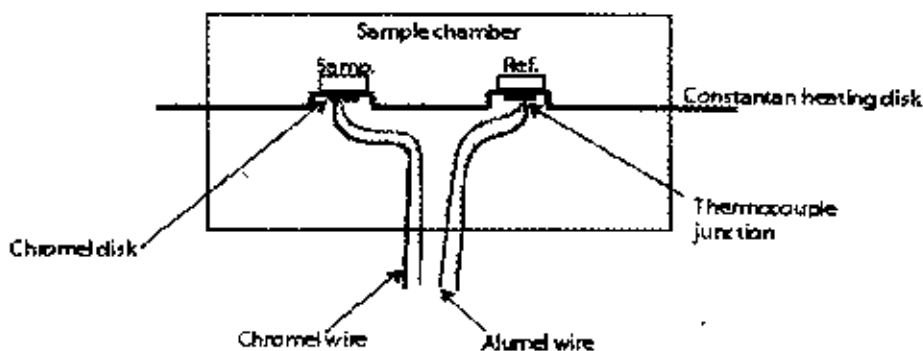


Fig. 3.3. Diagram of a heat flux differential scanning calorimeter.

There are two main types of differential scanning calorimeters: heat flux DSC and power compensation DSC. In a heat flux calorimeter, shown in Fig. 3.3, heat is transferred to the sample and reference through a disk made of the alloy constantan or in some cases, silver. The heat transported to the sample and reference is controlled while the instrument monitors the temperature difference between the two. In addition to its function in the heat transfer, this disk serves as part of the temperature-sensing unit. The sample and reference reside on raised platforms on the disk. Under each of these platforms there is a chromel (chromel is an alloy containing chromium, nickel and sometimes iron) wafer. The junction between these two alloys forms a chromel-constantan thermocouple. The signal from these sensors is then used to measure the differential heat flow. The temperature is typically monitored by chromel-alumel thermocouples attached beneath the chromel wafers.

### Power Compensated DSC

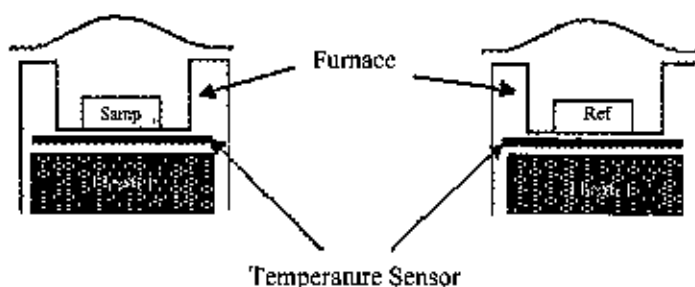


Fig. 3.4. Diagram of a power compensated differential scanning calorimeter.

In power compensated calorimeters, shown in Fig. 3.4, separate heaters are used for the sample and reference. Both the sample and reference are maintained at the same temperature while monitoring the electrical power used by their heaters. The heating elements are kept very small (weighing about 1 gram)

in order to ensure that heating, cooling, and thermal equilibration can occur as quickly as possible. The sample and reference are located above their respective heaters, and the temperatures are monitored using electronic temperature sensors located just beneath the samples. Generally platinum resistance thermometers are used due to the high melting point of platinum.

Electronically, the instruments consist of two temperature control circuits. An average temperature control circuit is used to monitor the progress of the temperature control program. This circuit is designed to assure that the temperature scanning program set by the operator is the average temperature of the sample and reference. A differential temperature control circuit is used to determine the relative temperatures of the sample and reference, and adjust the power going to the respective heaters in such a way as to maintain both at the same temperature. The output of the differential temperature control circuit is used to generate the DSC curve.

### DSC Curves

The result of a DSC experiment is a heating or cooling curve as shown in Fig. 3.5. This curve can be used to calculate enthalpies of transitions. This is done by integrating the peak corresponding to a given transition. It can be shown that the enthalpy of transition can be expressed using the following equation,  $\Delta H = KA$ , where  $\Delta H$  is the enthalpy of transition,  $K$  is the calorimetric constant, and  $A$  is the area under the curve. The calorimetric constant will vary instrument to instrument, and can be determined by analyzing a well-characterized sample with known enthalpies of transition.

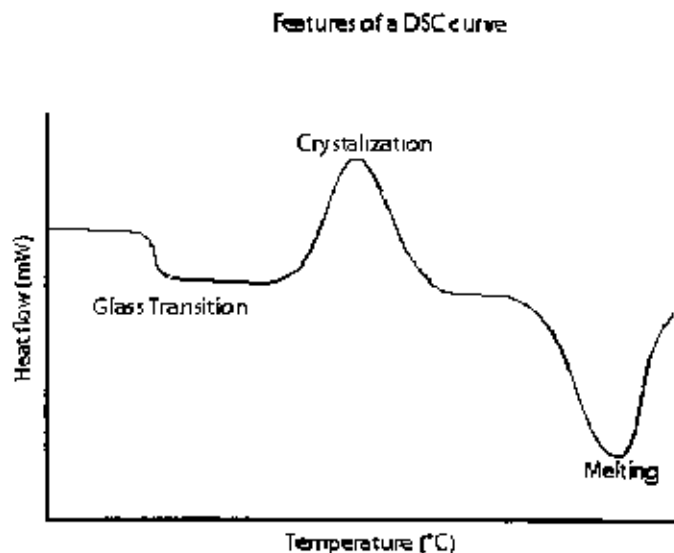


Fig. 3.5. A schematic DSC curve demonstrating appearance of several common features.

## Applications

Differential scanning calorimetry can be used to measure a number of characteristic properties of a sample. Using this technique it is possible to observe fusion and crystallization events as well as glass transition temperatures ( $T_g$ ). DSC can also be used to study oxidation, as well as other chemical reactions.

Glass transitions may occur as the temperature of an amorphous solid is increased. These transitions appear as a step in the baseline of the recorded DSC signal. This is due to the sample undergoing a change in heat capacity; no formal phase change occurs.

As the temperature increases, an amorphous solid will become less viscous. At some point the molecules may obtain enough freedom of motion to spontaneously arrange themselves into a crystalline form. This is known as the crystallization temperature. This transition from amorphous solid to crystalline solid is an exothermic process, and results in a peak in the DSC signal. As the temperature increases the sample eventually reaches its melting temperature. The melting process results in an endothermic peak in the DSC curve. The ability to determine transition temperatures and enthalpies makes DSC an invaluable tool in producing phase diagrams for various chemical systems. DSC may also be used in the study of liquid crystals. As matter transitions between solid and liquid it often goes through a third state, which displays properties of both phases. This anisotropic liquid is known as a liquid crystalline or mesomorphic state. Using DSC, it is possible to observe the small energy changes that occur as matter transitions from a solid to a liquid crystal and from a liquid crystal to an isotropic liquid. Using differential scanning calorimetry to study the oxidative stability of samples generally requires an airtight sample chamber. Usually, such tests are done isothermally (at constant temperature) by changing the atmosphere of the sample. First, the sample is brought to the desired test temperature under an inert atmosphere, usually nitrogen. Then, oxygen is added to the system. Any oxidation that occurs is observed as a deviation in the baseline. Such analyses can be used to determine the stability and optimum storage conditions for a compound.

DSC is widely used in the pharmaceutical and polymer industries. For the polymer chemist, DSC is a handy tool for studying curing processes, which allows the fine tuning of polymer properties. The cross-linking of polymer molecules that occurs in the curing process is exothermic, resulting in a positive peak in the DSC curve that usually appears soon after the glass transition.

In the pharmaceutical industry it is necessary to have well-characterized drug compounds in order to define processing parameters. For instance, if it is necessary to deliver a drug in the amorphous form, it is desirable to process the drug at temperatures below those at which crystallization can occur.

In food science research, DSC is used in conjunction with other thermal analytical techniques to determine water dynamics. Changes in water distribution may be correlated with changes in texture. Similar to material science studies, the effects of curing on confectionery products can also be analyzed.

DSC curves may also be used to evaluate drug and polymer purities. This is possible because the temperature range over which a mixture of compounds melts is dependent on their relative amounts. This effect is due to a phenomenon known as freezing point depression, which occurs when a foreign solute is

added to a solution. (Freezing point depression is what allows salt to de-ice sidewalks and antifreeze to keep vehicles running in the winter.) Consequently, less pure compounds will exhibit a broadened melting peak that begins at lower temperature than a pure compound.

SDT 2960 Simultaneous DSC – TGA measures heat flow to or from a sample as a function of temperature and time. The heat flow and temperature of the sample are monitored in comparison to the reference material. The amount of energy absorbed (endotherm) or evolved (exotherm) as the sample undergoes physical or chemical changes (e.g. melting, crystallization, curing) is measured in calories as a function of the temperature change. Any material reactions involving changes in heat capacity (e.g. glass transition) are also detected. DSC can be performed from ambient to 1773 K using this model of DSC instrument.

### 3.3 Powder Diffraction

About 95% of all solid materials can be described as crystalline. When X-rays interact with a crystalline substance (Phase), one gets a diffraction pattern. The X-ray diffraction pattern of a pure substance is, therefore, like a fingerprint of the substance. The powder diffraction method is thus ideally suited for characterization and identification of polycrystalline phases. Today about 50,000 inorganic and 25,000 organic single component, crystalline phases, diffraction patterns have been collected and stored on magnetic or optical media as standards. The main use of powder diffraction is to identify components in a sample by a search/match procedure. Furthermore, the areas under the peak are related to the amount of each phase present in the sample.

#### 3.3.1 Theoretical Considerations

In order to better convey an understanding of the fundamental principles of X-ray diffraction instruments, let us quickly look at the theory behind these systems. An electron in an alternating electromagnetic field will oscillate with the same frequency as the field. When an X-ray beam hits an atom, the electrons around the atom start to oscillate with the same frequency as the incoming beam. In almost all directions we will have destructive interference, that is, the combining waves are out of phase and there is no resultant energy leaving the solid sample. However the atoms in a crystal are arranged in a regular pattern, and in a very few directions we will have constructive interference. The waves will be in phase and there will be well-defined X-ray beams leaving the sample at various directions. Hence, a diffracted beam may be described as a beam composed of a large number of scattered rays mutually reinforcing one another.

The orientation and interplanar spacings of these planes are defined by the three integers  $h$ ,  $k$ ,  $l$  called indices. A given set of planes with indices  $h$ ,  $k$ ,  $l$  cut the  $a$ -axis of the unit cell in  $h$  sections, the  $b$  axis in  $k$  sections and the  $c$  axis in  $l$  sections. A zero indicates that the planes are parallel to the corresponding axis. For Example the 2 0 0 planes, in Fig. 3.6, cut the  $a$ -axis in half, but are parallel to the  $b$  and  $c$ - axis.

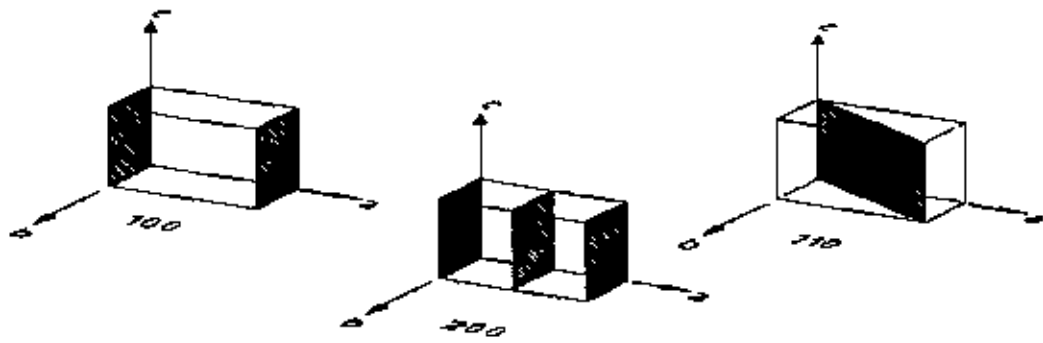


Fig. 3.6. Miller indices of different planes.

If we use the three dimensional diffraction grating as a mathematical model, the three indices  $h, k, l$  become the order of diffraction along the unit cell axes  $a, b$  and  $c$  respectively. Let us consider the theoretical model depending on what we use the terms X-ray reflection and X-ray diffraction as synonyms.

Let us consider an X-ray beam incident on a pair of parallel planes  $P1$  and  $P2$ , in Fig. 3.7, separated by an interplanar spacing  $d$ . The two parallel incident rays 1 and 2 make an angle  $\theta$  with these planes. A reflected beam of maximum intensity will result if the waves represented by 1' and 2' are in phase. The difference in path length between 1 to 1' and 2 to 2' must then be an integral number of wavelengths,  $\lambda$ . We can express this relationship mathematically in Bragg's law,  $n\lambda = 2d \sin \theta$ .

The process of reflection is described here in terms of incident and reflected (or diffracted) rays, each making an angle  $\theta$  with a fixed crystal plane. Reflections occur from planes set at angle  $\theta$  with respect to the incident beam and generates a reflected beam at an angle  $2\theta$  from the incident beam. The possible  $d$ -spacing defined by the indices  $h, k, l$  are determined by the shape of the unit cell. Rewriting Bragg's law we get,  $\sin \theta = \lambda/2d$ .

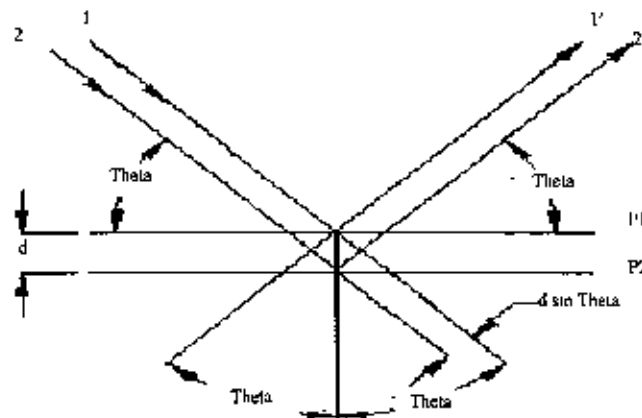


Fig. 3.7. Bragg reflection of two parallel incident rays 1 and 2.



Therefore the possible  $2\theta$  values where we can have reflections are determined by the unit cell dimensions. However, the intensities of the reflections are determined by the distribution of the electrons in the unit cell. The highest electron density are found around atoms. Therefore, the intensities depend on what kind of atoms we have and where in the unit cell they are located. Planes going through areas with high electron density will reflect strongly, planes with low electron density will give weak intensities.

### *Goniometer*

The mechanical assembly that makes up the sample holder, detector arm and associated gearing is referred to as goniometer. The working principle of a Bragg-Brentano parafocusing (if the sample was curved on the focusing circle we would have a focusing system) reflection goniometer is shown below.

The distance from the X-ray focal spot to the sample is the same as from the sample to the detector. If we drive the sample holder and the detector in a 1:2 relationship, the reflected (diffracted) beam will stay focused on the circle of constant radius. The detector moves on this circle.

For the THETA : 2-THETA goniometer, in Fig. 3.8, the X-ray tube is stationary, the sample moves by the angle THETA and the detector simultaneously moves by the angle 2-THETA. At high values of THETA small or loosely packed samples may have a tendency to fall off the sample holder.

For the THETA:THETA goniometer, in Fig. 3.9, the sample is stationary in the horizontal position, the X-ray tube and the detector both move simultaneously over the angular range THETA

### *Diffractometer Slit System*

The diffractometer slit system has been presented in Fig. 3.10. The focal spot for a standard focus X-ray tube is about 10 mm long and 1 mm wide, with a power capability of 2,000 watt, which equals to a power loading of 200 watt/mm<sup>2</sup>. Power ratings are dependent on the thermal conductivity of the target material. The maximum power loading for a Cu X-ray tube is 463 watt/mm<sup>2</sup>. This power is achieved by a long fine focus tube with a target size of 12 mm long and 0.4 mm wide. In powder diffraction the line focus or line source of the tube is normally utilized. The line source emits radiation in all directions, but in order to enhance the focusing it is necessary to limit the divergence in the direction along the line focus. This is realized by passing the incident beam through a soller slit, which contains a set of closely spaced thin metal plates. In order to maintain a constant focusing distance it is necessary to keep the sample at an angle THETA (Omega) and the detector at an angle of 2-THETA with respect to the incident beam. For a THETA:THETA goniometer the tube has to be at an angle of THETA (Omega) and the detector at an angle of THETA with respect to the sample.

### *Diffraction Spectra*

A typical diffraction spectrum consists of a plot of reflected intensities versus the detector angle  $2\theta$  or  $\theta$  depending on the goniometer configuration. The  $2\theta$  values for the peak depend on the wavelength of the

anode material of the X-ray tube. It is therefore customary to reduce a peak position to the interplanar spacing  $d$  that corresponds to the  $h, k, l$  planes that caused the reflection. The value of the  $d$ -spacing depend only on the shape of the unit cell. We get the  $d$ -spacing as a function of  $2\theta$  from Bragg's law,  $d = \lambda/2 \sin \theta$ . Each reflection is fully defined when we know the  $d$ -spacing, the intensity (area under the peak) and the indices  $h, k, l$ . If we know the  $d$ -spacing and the corresponding indices  $h, k, l$  we can calculate the dimension of the unit cell.

### **ICDD Data Base**

International Center Diffraction Data (ICDD) or formerly known as (JCPDS) Joint Committee on Powder Diffraction Standards is the organization that maintains the data base of inorganic and organic spectra's. The data base is available from the diffraction equipment manufacturers or from ICDD direct. Currently the data base is supplied either on magnetic or optical media. Two data base versions are available the PDF I and the PDF II.

The PDF I data base contains information on  $d$ -spacing, chemical formula, relative intensity, RIR quality information and routing digit. The information is stored in an ASCII format in a file called PDF1.dat. For search/match purposes most diffraction manufactures are reformatting the file in a more efficient binary format.

The PDF II data base contains full information on a particular phase including cell parameters. Scintag's newest search/match and look-up software package is using the PDF II format. Optimized data base formats, index files and high performance PC-computers make PDF II search times extremely efficient. The data base format consists of a set number and a sequence number. The set number is incremented every calendar year and the sequence number starts from 1 for every year. The yearly releases of the data base is available in September of each year.

### **3.3.2 Applications**

**Identification :** The most common use of powder (polycrystalline) diffraction is chemical analysis. This can include phase identification (search/match), investigation of high/low temperature phases, solid solutions and determination of unit cell parameters of new materials.

**Polymer crystallinity :** A polymer can be considered partly crystalline and partly amorphous. The crystalline domains act as a reinforcing grid, like the iron framework in concrete, and improves the performance over a wide range of temperature. However, too much crystallinity causes brittleness. The crystallinity parts give sharp narrow diffraction peaks and the amorphous component gives a very broad peak (halo). The ratio between these intensities can be used to calculate the amount of crystallinity in the material.

## Bragg Brentano 2 Theta:Theta Set-up

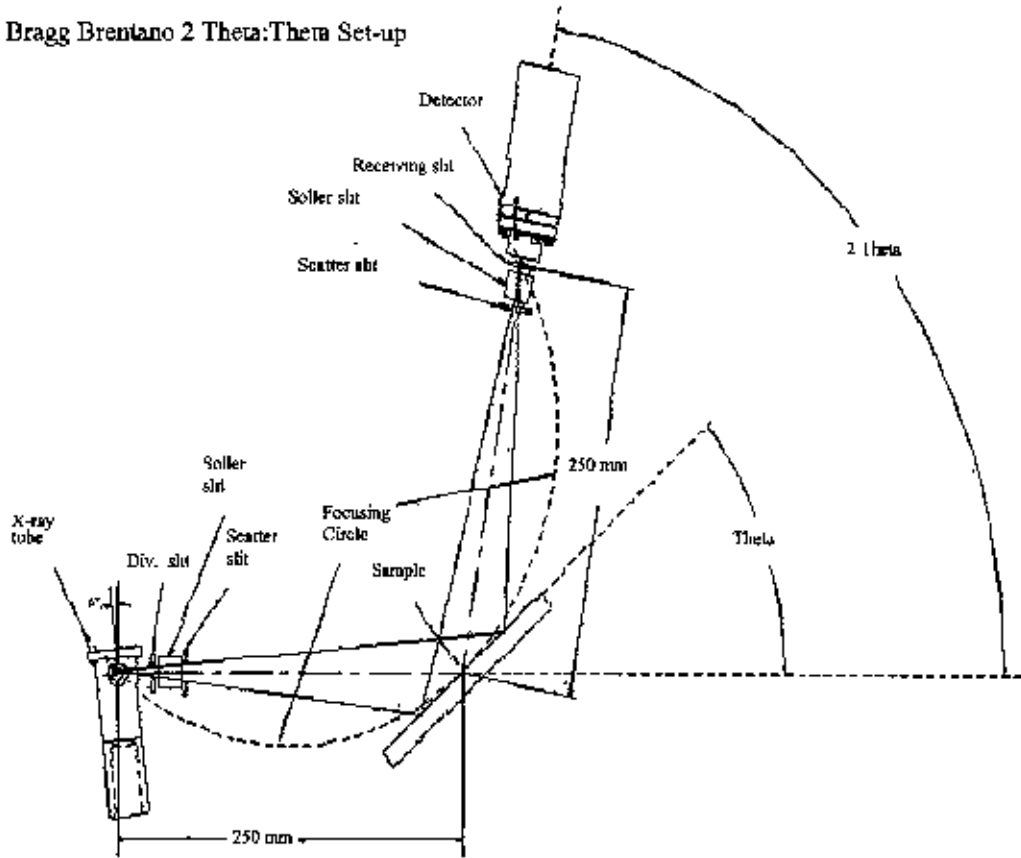


Fig. 3.8. THETA:2-THETA goniometer.

**Residual stress :** Residual stress is the stress that remains in the material after the external force that caused the stress have been removed. Stress is defined as force per unit area. Positive values indicate tensile (expansion) stress, negative values indicate a compressive stress. The deformation per unit length is called strain. The residual stress can be introduced by any mechanical, chemical or thermal process. e.g. machining, plating and welding.

The principles of stress analysis by the X-ray diffraction is based on measuring angular lattice strain distributions. That is, we choose a reflection at high 2-Theta and measure the change in the d-spacing with different orientations of the sample. Using Hooke's law the stress can be calculated from the strain distribution.

**Texture analysis :** The determination of the preferred orientation of the crystallites in polycrystalline aggregates is referred to as texture analysis, and the term texture is used as a broad synonym for preferred crystallographic orientation in the polycrystalline material, normally a single phase.

**Grain size :** When the size of the individual crystals is less than about 1000 Å, grain size can be determined from line broadening,  $B = \frac{0.9\lambda}{t \cos \theta}$  where B = broadening of diffraction line measured at half

its maximum intensity (radians) and t = diameter of crystal particle. The breadth B refers however, to the extra breadth, or broadening, due to the particle-size effect alone. If the situation is such that only particle size contributes significantly to the line width in excess of the instrumental width, and if one is only interested in the estimation of average crystallite size, the data can be interpreted in a particularly simple way. If one assumes that the line shapes are Gaussian, then the squares of the contributing width factors are additive. Thus if  $B_{inst}$  is the instrumental line width and  $B_{obs}$  the observed width, the value of  $B_d$ , the line width due to particle size broadening is given by,  $B_d^2 = B_{obs}^2 - B_{inst}^2$ .

Bragg Brentano Theta Theta Set-up

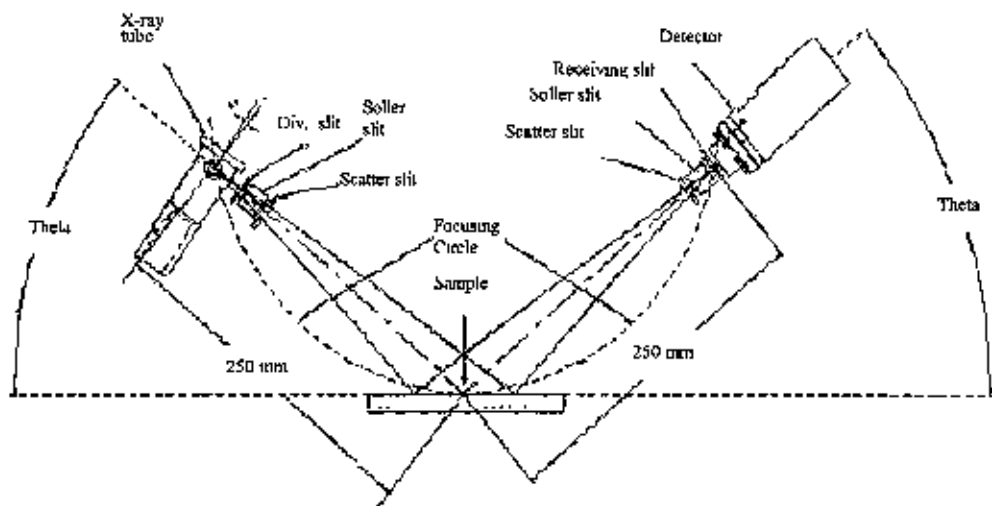


Fig. 3.9. THETA:THETA goniometer.

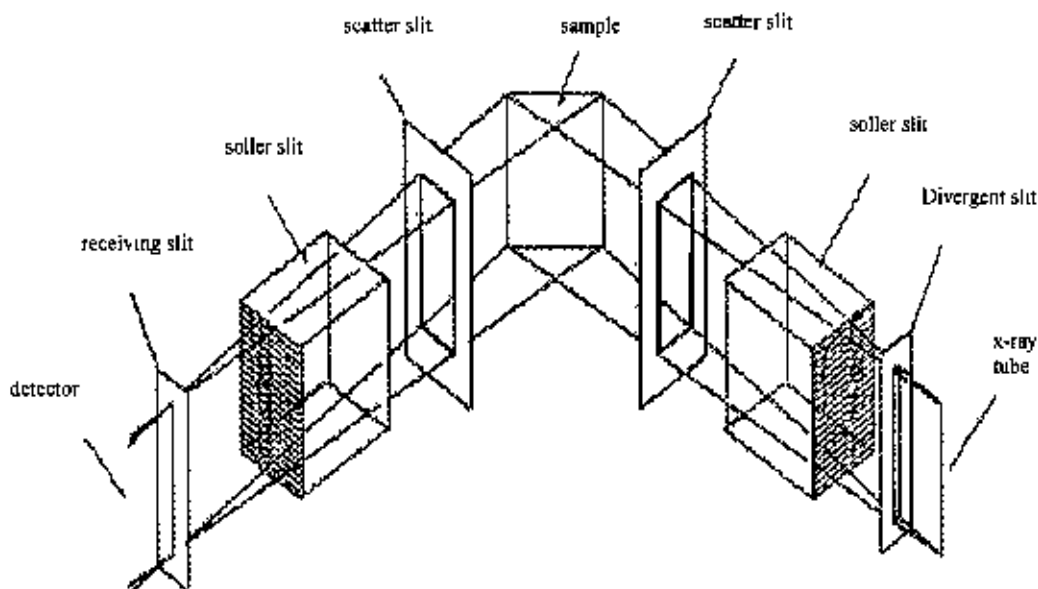


Fig. 3.10. Diffractometer Slit System.

### 3.3.3 Philips X'Pert Pro Multipurpose X-ray Diffractometer

The X'Pert PRO diffraction system utilizes a modular system approach to provide performance for applications ranging from routine characterization to in-depth research investigations. The PreFIX (Pre-aligned Fast-Interchangeable X-ray optics) concept enables the diffraction system to be reconfigured in a few minutes without the need for re-alignment to handle different types of analysis. A suite of data analysis software from Philips is available. During X-ray diffraction analysis, X-ray beams are reflected off the parallel atomic layers within a mineral over a range of diffraction angles. Because the X-ray beam has a specific wavelength, for any given 'd-spacing' (distance between adjacent atomic planes) there are only specific angles at which the exiting rays will be 'in phase' and therefore, will be picked up by the detector producing a peak on the 'diffractogram'. Just like a 'fingerprint', every mineral has its own distinct set of diffraction peaks that can be used to identify it.

The system enables us to do the analysis on phase identification and quantification, as well as crystal structure studies. The specifications of the system are:

- X-RAY SOURCES: 3 kW Copper tube
- OPTICS: Focussing and parallel PreFix optics, programmable slits, tunable diffracted beam monochromator
- DETECTORS: Xe proportional counter and solid state X'cellerator
- SAMPLE STAGES: Single sample holder, 15-sample changer

- **VARIABLE TEMPERATURE CAPABILITY:** Anton-Paar 77 - 725 K and 300 - 1475 K cameras
- **SOFTWARE AND DATABASES:** Data Collector, XPert Plus crystallographic analysis software with Rietveld capability, ProFit line profile analysis software
- **INSTRUMENT STATISTICS:** The system uses Cu  $K_{\alpha}$  radiation that has a wavelength of 1.54Å. Analyses are commonly run using a 40kV 45mA x-ray tube voltage, a 0.04° soller slit, 1° divergence and antiscatter slits, and a 1/2° (for powder) or 1/4° (for clays) receiving slit.

### 3.4 Hysteresisgraph

A hysteresisgraph or BH-Meter allows for the magnetic properties of soft magnetic materials to be measured. A schematic diagram of commercial hysteresisgraph has been presented in Fig. 3.11. A hysteresisgraph has two major functions. It produces current to produce a magnetic field, and measures voltage over time to measure magnetic induction. By determining the induction response of the test sample to the applied current, the magnetic properties of the material is determined. Most soft magnetic materials are measured using ring geometry. The advantage of a ring geometry will be discussed subsequently. Two coils of wire are wound around the sample. A current from a bi-polar power supply is passed through the primary coil to generate a magnetic field in the ring. The applied magnetic field is proportional to the current. As the sample magnetic induction changes in response to the applied magnetic field, a voltage is induced in the secondary windings. This induced voltage is integrated over time with a circuit often called a fluxmeter, as it is used in many applications to measure magnetic flux. The integrated voltage is proportional to the magnetic induction of the test samples. The current in the primary coil is determined by measuring the voltage across a resistor. Commercial hysteresisgraphs use a computer to control the applied field and measure both B and H simultaneously.

An initial BH-curve is generated by slowly increasing the applied magnetic field from zero to some value on a demagnetized sample. Initial BH-curves of a soft magnetic material are often used to model the performance of soft magnetic materials in an electro-mechanical device

#### 3.4.1 Measurement of an Initial BH-Curve

As these are important curves for magnetic design, these curves are measured using a hysteresisgraph. For accurate initial curves, the sample must be demagnetized prior to the measurement. This demagnetization can be performed either externally, or in many cases, the sample can be demagnetized by the hysteresisgraph. Residual magnetization can greatly distort the response of a soft magnetic material near zero field.

### 3.4.2 AC BH-Curve Measurements

In many applications, soft magnetic materials are subjected to cyclical magnetic field. The response of a soft magnetic material can be very complicated in this case, and is determined by both material parameter

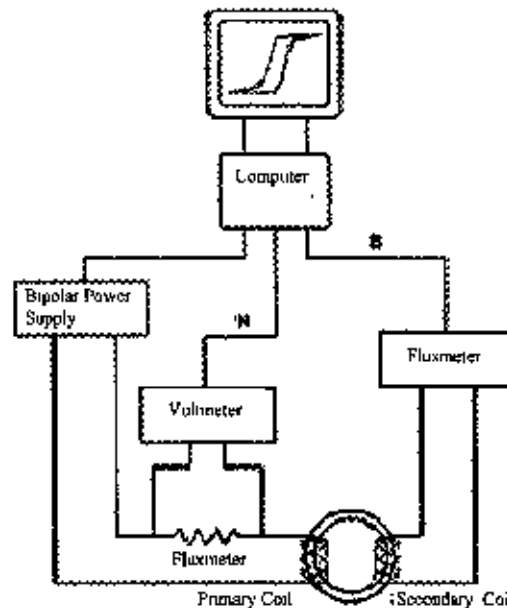


Fig. 3 11. Schematic diagram of commercial hysteresisgraph.

such as sample permeability and material geometry. It can be exceedingly difficult to make accurate predictions of material performance through computer models. Therefore, the best way to determine the performance of these materials is to measure the BH-curve under cyclical applied magnetic fields. This can be performed using a hysteresisgraph. The bi-polar power is driven at the test frequency, and the fluxmeter can measure the varying magnetic induction of the material. The resulting BH-curves are called AC BH-curves, and yield important information in regards to the material such as AC permeability and core loss. For these types of measurements, it is important that the hysteresisgraph components have the appropriate frequency response to measure the AC BH-curve properly.

### 3.4.3 Materials Geometries

**Ring Geometry:** The ideal sample geometry of soft magnetic materials is a ring. This shape is preferable because a ring shape eliminates factors that can distort the magnetic test results. The main source of distortion of test data on soft magnetic materials is usually from air gaps present in the magnetic test circuit. These air gaps lower the apparent permeability of the material, and can be difficult to control.

As a ring geometry is continuous path, the magnetic circuit is closed, without any air gaps that cause distortions. In addition, the magnetic path length, which is required to convert the applied current in the sense windings into applied magnetic field is easy to calculate an unambiguous for ring samples.

In many cases, block or rod samples can be machined into a ring specimen for the most accurate magnetic measurements. If this machining process is on a sample, a technique that produces minimal cold working the material is preferred such as wire EDM or laser cutting.

In ring shaped samples, primary windings are wound on the ring to generate a magnetic field in the sample via applied current to the primary windings. A secondary coil is also wound onto the ring to inductively measure the magnetic induction of the sample.

**Squares, Rectangles, and Other Closed Geometries :** In some cases, the soft magnetic material specimen is a rectangular or square geometry, which does not lend itself to be machined into a ring. In these instances, accurate magnetic measurements can still be performed, since the sample geometry creates a closed magnetic circuit. For these measurements, primary and secondary coils are wound onto the sample, as with ring measurements. The magnetic path length of the test circuit must be either determined or known in order to convert the applied primary current into applied magnetic field.

**Testing Epstein Strips – the Epstein Frame:** Epstein strips, which are 3 cm × 25-30 cm long strips, are the overwhelming sample geometry in which core loss of electrical steels and laminations are measured. The strips are measured in a test fixture called an Epstein Frame, which basically reproduces the primary and secondary windings one would use to test a ring sample. Diagrams of an Epstein frame are shown in Fig. 3.12.

An Epstein frame consists of four primary coils, or H-coils, which magnetize the samples. A multiple of four strips are used for the test, which are inserted into the H-coil in interlocking fashion. Inside each H-coil of the Epstein frame is a set of two coils, wired in series, which measure the magnetic induction of the sample. One of the coils, called the B-sense coil, is positioned so the Epstein frame strips fit inside of it. The other coil, called the H-compensation coil, is in series with the B-sense coil. The H-compensation coil does not measure any properties of the material. Instead, it is used to compensate the applied magnetic field from distorting the results.

In the B-sensing coil, a voltage is induced due to both the magnetization of the sample, which is of interest, and distorts the measured curve. In order to compensate for this distortion due to the applied magnetic field, the H-compensation coil, which cancels the induced voltage in the B-sense coil due to the applied magnetic field. In this way, only the material properties of the Epstein strips are measured.

**Testing Individual Strip Samples :** Instead of several Epstein strips, some soft magnetic material are evaluated using a single strip of material. This has advantages from a sample preparation point of view, especially with very low carbon steels, which can be difficult to cut in Epstein strips. For these measurements, a single strip fixture is used, as shown in Fig. 3.13. A single strip fixture consists of a magnetic flux return path, to complete the magnetic path. The strip sample is gently clamped down to the



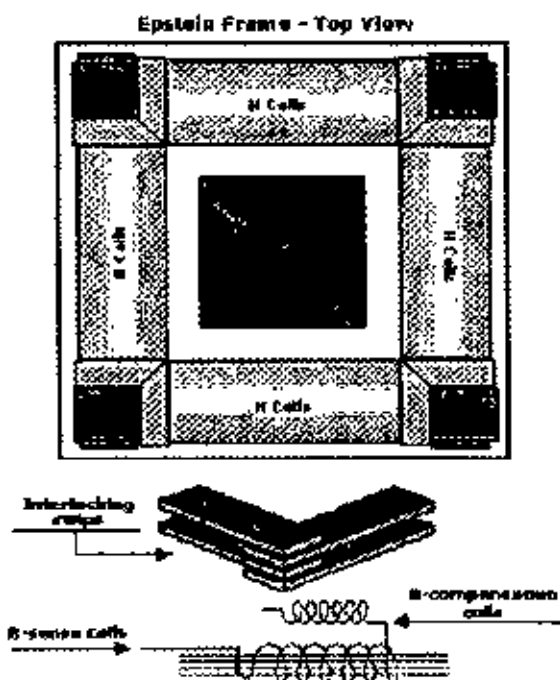


Fig 3.12. Standard Epstein frame.

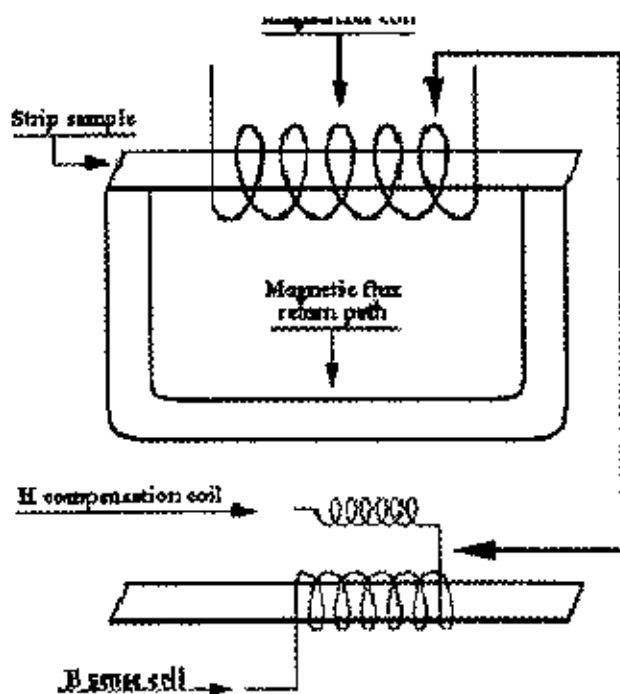


Fig. 3.13. Testing individual strip sample.

ends of the yolk. A compensated coil assembly sits inside magnetizer coil, similar to this assembly used in Epstein frame. As single strip measurements are less labor intensive than Epstein frame measurements, this suggests that test time can be reduced in using single strip fixtures to measure core loss.

Finally, it is also possible to measure single strip samples in a single strip fixture with no magnetic return path. This constitutes an open magnetic circuit measurement, but has many advantages for quality control purposes. First, elimination of the magnetic return path significantly reduces the cost of the fixture. Secondly, test time is reduced, as the strip samples do not need to be clamped down to any yolk. And finally, an open loop single strip fixture can accommodate a wider variety of sample dimensions. For quality assurance purposes such as evaluating an annealing process, it may be disadvantageous to use an open loop single strip fixture.

### 3.4.4 AMH-20 Low Frequency Automatic Hysteresisgraph System

Figure 3.14(a) shows the simplified block diagram of the AMH-20 Low Frequency Automatic Hysteresisgraph System. Output from the AMH-20 is illustrated in Figure (b). The computer-controlled function generator and power amplifier combination drive the primary winding. The primary current is measured using a non-inductive precision series resistor. The applied magnetic field,  $H$ , which magnetize the sample, is calculated from the primary current using the equation :

$$H = \frac{\pi NI}{2.5L} \quad (1)$$

Where,  $N$  = Number of primary turns,  $L$  = Magnetic path length of sample,  $H$  = Maximum desired  $H$  drive (Oersteds),  $I$  = Maximum drive current (Amperes)

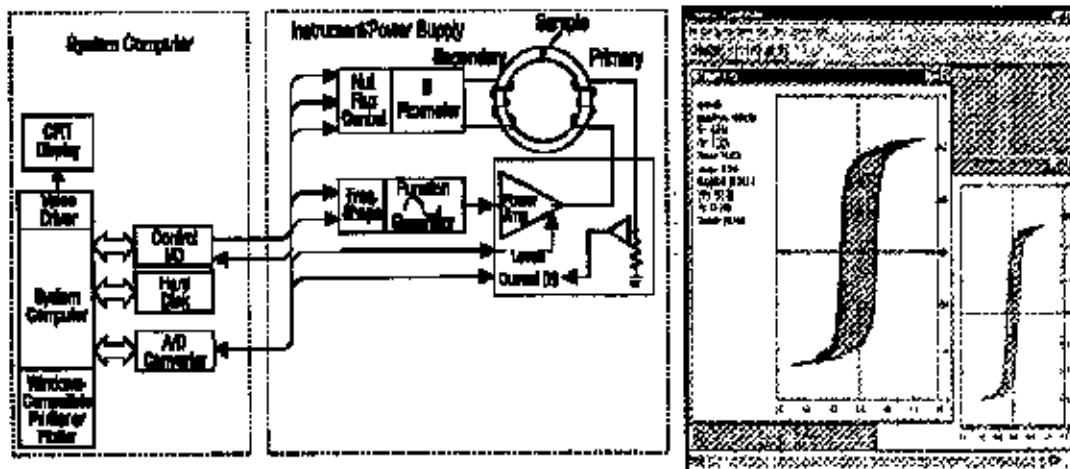


Fig. 3.14. (a) Walker Scientific AMH-20 Low Frequency Automatic Hysteresisgraph System for Soft Magnetic Materials. (b) AMH-20 Output.

The magnetic flux induced in the sample under test is measured using a computer-controlled integrating fluxmeter attached to the secondary windings. The induced flux  $\Phi$  resulting from the variation of the magnetic field (H), generates a voltage (e) in the secondary winding equal to

$$e = NK_1 \frac{d\Phi}{dt} \quad (2)$$

Therefore:

$$\Phi = \frac{1}{K_1 N} \int e dt \quad (3)$$

Where,  $\Phi$  = total flux induced in the test sample by the driving magnetic field (H),  $dt$  = time differential,  $N$  = number of secondary turns,  $K_1 = 10^{-8}$  for cgs-emu system, or  $K_1 = 1$  for S. I. System.

The integrating fluxmeter is the preferred method of measuring induced magnetic flux when the H field is being varied at frequencies from DC (typically 0.01 Hz) to 10 kHz. The common method for implementing an electronic integrator consists of a dc amplifier with resistive-capacitive feedback, and based on :

$$E = \frac{1}{RC} \int e dt \quad (4)$$

Where,  $E$  = Amplifier output voltage,  $V$ ,  $R$  = Input resistance of the integrator in the secondary circuit,  $\Omega$ ,  $C$  = Feedback capacitance,  $F$

Combining Equations (3) and (4):

$$\Phi = \frac{ERC}{K_1 N} \text{ or } E = \frac{\Phi NK_1}{RC} \quad (5)$$

### 3.5 Vibrating sample magnetometer (VSM)

The vibrating sample magnetometer has become a widely used instrument for determining magnetic properties of a large variety of materials: diamagnetics, paramagnetics, ferromagnetics, ferrimagnetics and antiferromagnetics. This experimental technique was invented in 1956 by Simon Foner of the MIT. It has a flexible design and combines high sensitivity with ease of sample mounting and exchange. Samples may be interchange rapidly even at any operating temperature. Measurements of magnetic moments as small as  $5 \times 10^{-5}$  emu are possible in magnetic fields from zero to 9 Tesla (or higher). Maximum applied fields of 2-3 Tesla or 9 Tesla are reached using conventional laboratory electromagnets and superconducting solenoids, respectively. Vibrating sample magnetometers normally operate over a temperature range of 2.0 to 1050 K. Powders, bulk and thin films can be measured and studied.

### 3.5.1 Principle

If a sample of any material is placed in a uniform magnetic field, created between the poles of an electromagnet, a dipole moment will be induced. If the sample vibrates with sinusoidal motion a sinusoidal electrical signal can be induced in suitable placed pick-up coils. The signal has the same frequency of vibration and its amplitude will be proportional to the magnetic moment, amplitude, and relative position with respect to the pick-up coils system. Fig. 3.15 shows the block diagram of vibrating sample magnetometer.

The sample is fixed to a small sample holder located at the end of a sample rod mounted in an electromechanical transducer. The transducer is driven by a power amplifier which itself is driven by an oscillator at a frequency of 90 Hertz. So, the sample vibrates along the Z axis perpendicular to the magnetizing field. The latter induced a signal in the pick-up coil system that is fed to a differential amplifier. The output of the differential amplifier is subsequently fed into a tuned amplifier and an internal lock-in amplifier that receives a reference signal supplied by the oscillator.

The output of this lock-in amplifier, or the output of the magnetometer itself, is a DC signal proportional to the magnetic moment of the sample being studied. The electromechanical transducer can move along

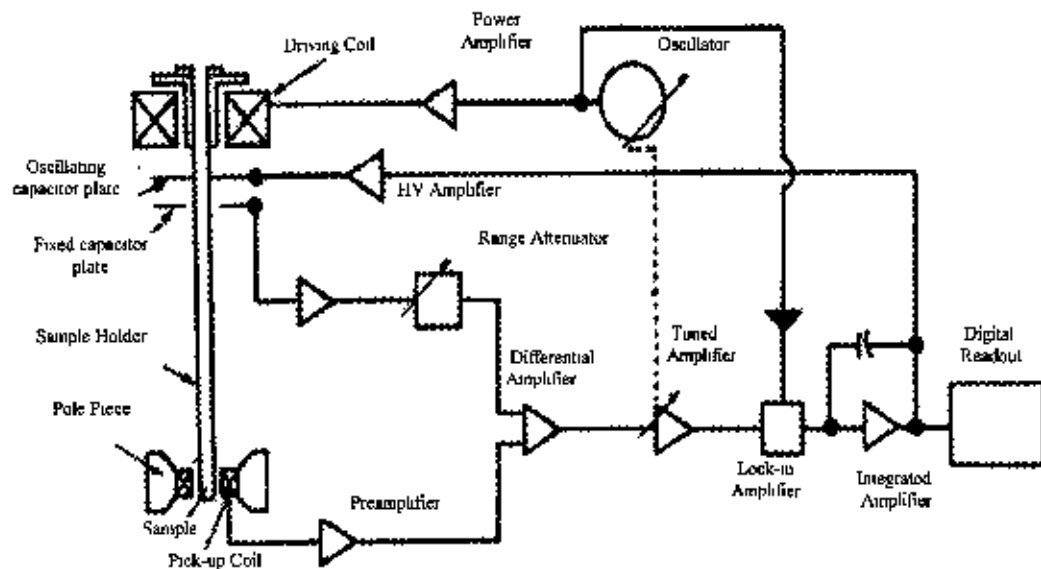


Fig 3.15 Block diagram of vibrating sample magnetometer.

X, Y and Z directions in order to find the saddle point. Calibration of the vibrating sample magnetometer is done by measuring the signal of a pure Ni standard of known saturation magnetic moment placed in the saddle point. The basic instrument includes the electromechanical system and the electronic system (including a personal computer). Laboratory electromagnets or superconducting coils of various maximum field strengths may be used. For ultra-high magnetic fields a cryogen-free magnets can be also

used. For the characterization of soft magnetic materials a pair of Helmholtz coils may be also used. As accessories a high temperature oven assembly and a liquid Helium cryostat is also used.

Technical specifications of VSM (typical figures).

Maximum sensitivity:  $5 \times 10^{-5}$  emu

Calibrated ranges from 100 to 0.01 emu full scale.

Stability of output signal: 0.05 % of full scale per day.

Absolute accuracy: better than 2 %

Angular variation of H: full 360° rotation ~ 0.5°

Maximum sample size: 7 mm.

Operating temperature range: 2.0 K to 1050 K

### 3.5.2 Applications

Using a vibrating sample magnetometer one can measure the DC magnetic moment as a function of temperature, magnetic field, angle and time. So, it allows to perform susceptibility and magnetization studies. Some of the most common measurements done are: hysteresis loops, susceptibility or saturation magnetization as a function of temperature (thermomagnetic analysis), magnetization curves as a function of angle (anisotropy), and magnetization as a function of time.

### 3.5.3 DMS 880 VSM

The DMS Vibrating Sample Magnetometer (VSM) is a computer-controlled measurement system capable of characterizing a wide variety of magnetic samples. Its reliability, user friendliness, and ability to measure both high and low coercivity materials make it the standard measurement system used by almost all hard disk manufacturers and magnetic research facilities.

DMS 880 VSM system supports all known magnetic measurements such as Hysteresis and Minor Loops, IRM and DCD Remanence Loops, Delta M and Henkel Plots, and Angular and AC Remanence Loops. Any series of measurements can be run without user intervention, using the flexible EasyVSM software.

#### Key Features

- Maximum field: 1.5 T
- Temperature control: 77K ~ 1000K
- Field resolution: better than 0.01 Oe
- Field control: stepped field control in conjunction with Digital Signal Averaging

**High Accuracy :** The high precision stepped field control used in conjunction with Digital Signal Averaging leads to increased accuracy of the measured graphs and measurement parameters, while at the

same time facilitating measurements on soft magnetic samples with a field resolution better than 0.01 Oe. Since the field is stepped rather than swept, there is higher accuracy in the field setting and a more precise determination of the coercivity and many other magnetic parameters. The number of data points can be defined by the user. This allows for greater accuracy in areas where detailed data is required or changes in signal expected.

**Flexible Options (Three Systems in One) :** DMS offers a unique combination system including Torque and/or Magneto-Resistance (MR) options, which can be added to the VSM without increasing the system footprint and are less expensive. The torque option measures the torque of materials as a function of rotation angle and applied field, resulting in Anisotropy data. The MR option measures the resistance of thin film samples as a function of both magnetic field, temperature and angle.

**Fast and Easy to Use :** A unique sample vibrating mechanism makes sample mounting and alignment fast and convenient. Using *EasyVSM*, samples can quickly and easily be aligned properly to maximize the measurement efficiency. The precise alignment techniques provide for excellent accuracy and repeatability. *EasyVSM* software calculates and displays the results required even when performing complex measurements. *EasyVSM* can be used by researchers who want to specify the parameters in their experiments, as well as through Operator menus when lower levels of control are needed or wanted. The powerful data analysis software has many options, including automatic subtraction of background signals and the calculation of up to 6- different test parameters. The optional temperature control is extremely fast, reducing typical measurement time to a few minutes per temperature setting.

### 3.6 SQUID magnetometers

A SQUID (Superconducting Quantum Interference Device) is the most sensitive available device for measuring magnetization. Based on this sensitive device the so-called 'SQUID magnetometers' have been developed. SQUID magnetometers are used to characterize materials when the highest detection sensitivity over a broad temperature range and using applied magnetic fields up to several Tesla is needed. Nowadays, this instrument is widely used worldwide in research laboratories. The system is designed to measure the magnetic moment of a sample, from which the magnetization and magnetic susceptibility can be obtained. Therefore, SQUID magnetometers are versatile instruments that perform both, DC and AC magnetic moment measurement.

SQUID magnetometers are classified within the flux methods of measuring magnetization of a sample. Fig. 3.16 illustrates schematically its principle: the measurement of the flux change through a pick-up coil system with a SQUID. This signal is proportional to the magnetic moment of a sample, which is magnetized by the magnetic field produced by a superconducting magnet.

### 3.6.1 Basic Components

The main components of a SQUID magnetometer are: (a) superconducting magnet (that must be acquired together its programmable bipolar power supply); (b) superconducting detection coil which is coupled inductively to the sample; (c) a SQUID connected to the detection coil; (d) superconducting magnetic shield. In the following a description of each one is given:

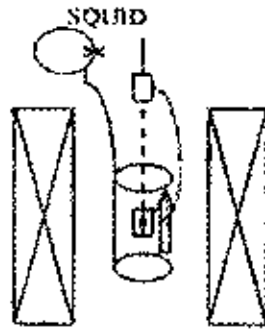


Fig. 3.16. SQUID magnetometer principle.

**Superconducting magnet :** A superconducting magnet is a solenoid made of superconducting wire. Fig. 3.17 shows a cut away view of a typical superconducting magnet used in a SQUID magnetometer. This solenoid must be kept at liquid helium temperature in a liquid-helium dewar. The uniform magnetic field is produced along the axial cylindrical bore of the coil. Currently, superconducting solenoids that produce magnetic fields in the range 5-18 Tesla are commercially available. To operate a superconducting magnet requires an appropriate programmable bipolar power supply.

**Superconducting detection coil :** This is a single piece of superconducting wire configured as a second-order gradiometer (Fig. 3.18). This pick-up coil system is placed in the uniform magnetic field region of the solenoidal superconducting magnet.

**SQUID :** High sensitivity is possible because this device responds to a fraction of the flux quantum. The SQUID device is usually a thin film that functions as a extremely sensitive current-to-voltage-converter. A measurement is done in this equipment by moving the sample through the second-order gradiometer. Hence, the magnetic moment of the sample induces an electric current in the pick-up coil system. A change in the magnetic flux in these coils changes the persistent current in the detection circuit. So, the change in the current in the detection coils produce variation in the SQUID output voltage proportional to the magnetic moment of sample.

**Superconducting magnetic shield :** Superconducting magnetic shield is used to shield the SQUID sensor from the fluctuations of the ambient magnetic field of the place where the magnetometer is located and from the large magnetic field produced by the superconducting magnet.

**Applications :** Using this kind of equipment one can measure: (a) The real and imaginary components of the AC magnetic susceptibility as a function of frequency, temperature, AC magnetic field amplitude and

DC magnetic field value. (b) The DC magnetic moment as a function of temperature, DC magnetic field, and time. Using a specially designed sample holder the magnetic moment as a function of angle can also be measured.

High sensitivity is needed when samples with low intrinsic magnetic moment or low mass are measured. In thin films, for instance, the mass may be smaller than 1 microgram. These materials are therefore difficult to characterize using an extraction or vibrating sample magnetometer but not with a SQUID

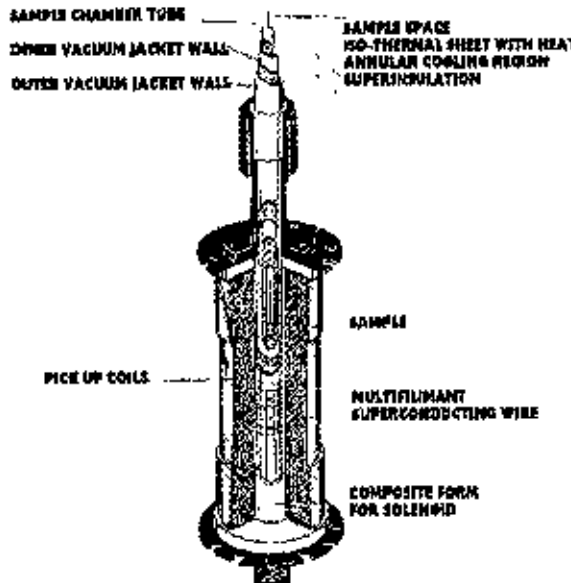


Fig. 3.17. Cut view of a typical superconducting pick-up coils.

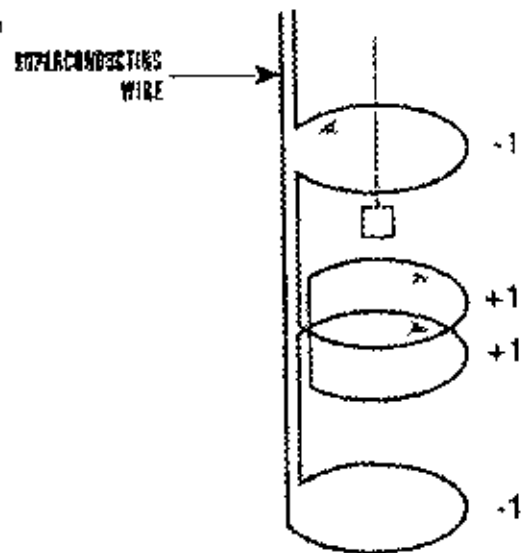


Fig. 3.18. Second-order gradiometer magnet.

magnetometer. Also for measurements of magnetic viscosity in permanent magnets, where small changes of magnetization as a function of time must be recorded, a SQUID magnetometers is the best choice.

### 3.6.2 The Features of MPMS XL

**Improved sensitivity :** The MPMS XL features the new reciprocating sample measurement system. Unlike DC measurements where the sample is moved through the coils in discrete steps the RSO measurements are performed using a servo motor which rapidly oscillates the sample, as shown in Fig. 3.19. These measurements have a sensitivity of  $5 \times 10^{-9}$  EMU.

A shaft encoder on the servo motor records the position of the sample synchronous with the SQUID signal. The data received is fitted to an ideal dipole moment response. To ensure this assumption is applicable, samples need to be small: the calibration sample is a cylinder of 3 mm diameter and 3 mm height. Samples of this size or smaller match an ideal point dipole to an accuracy of approximately 0.1%.

RSO measurements can be made in one of two configurations: Center or Maximum slope. Center scans use large oscillations (2 to 3 cm) around the center point of the pickup coils. These scans take a long time



but the sample always remains properly located and a large number of measurements are recorded. These give the most accurate readings.

The Maximum Slope method oscillates the sample over a small region (2 mm) at the most linear part of the SQUID response (as shown in Figure 3.19). The smaller amplitude makes measurements quicker and prevents the sample being subjected to significant magnetic field variation, however it also makes the measurement less accurate and susceptible to drift in the sample position.

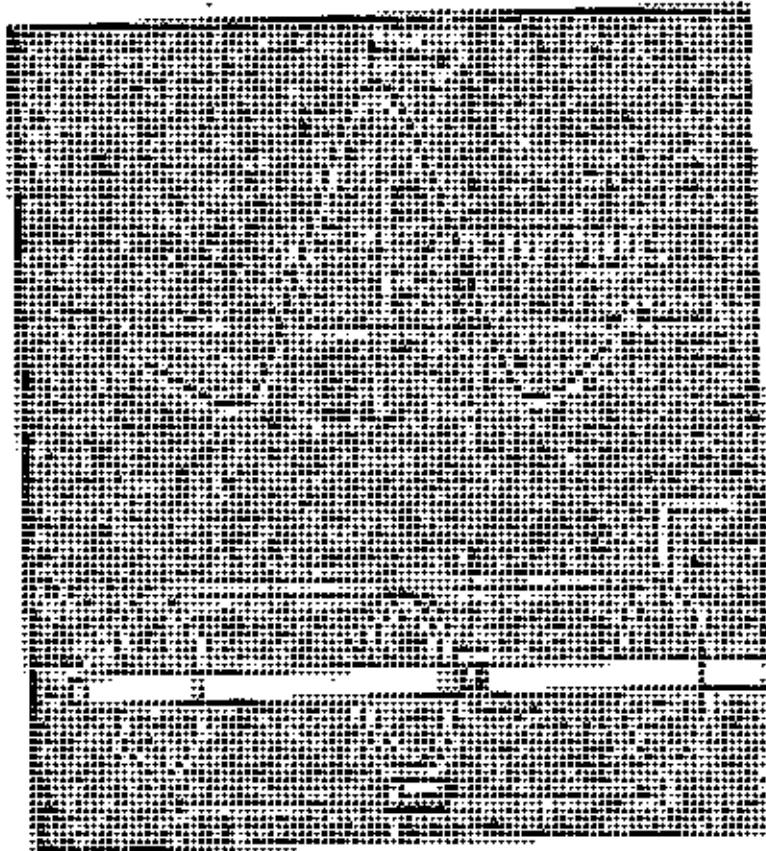


Figure 3.19. Illustration of an RSO measurement with a small amplitude. (a) shows the ideal SQUID response for a dipole and (b) shows the movement of the sample within the SQUID pickup coils.

**Extended Low Temperature Capability :** The MPMS XL features significant improvements in the temperature control system. Utilizing a new design for the helium flow impedance, the MPMS XL has the capability to operate continuously at temperatures below 4.2 K for indefinite periods of time - completely removing time limitations for making measurements in this temperature regime. The new MPMS XL eliminates the operations associated with filling and recycling the He reservoir. Thus, the system solves the traditional problems of temperature instability and hysteresis associated with rapid boil off of liquid helium when warming through 4.2 K. The results are smooth monotonic transitions

across 4.2 K during both warming and cooling temperature sweeps. All these capabilities are fully automated for precise systems control and user-friendly operation.

**Enhanced Thermometry and Temperature Sweep Operation :** In addition to a redesigned impedance system, the MPMS XL uses a new thermometer design for improved temperature accuracy and precise thermal control. The new thermometry, designed and developed at Quantum Design, is installed in close proximity to the sample within the sensitive coil detection region. This improved design is combined with new temperature control capabilities to provide more accurate measurements of the sample chamber, even under extreme temperature changes.

The new Temperature Sweep mode of operation provides MPMS XL users with the ability to take magnetic measurements while sweeping the system temperature at a controlled rate – automatically – with no manual intervention. This mode provides a controlled, monotonic change in temperature during a measurement sequence at rates up to 10 K/min. Measurements of temperature dependence over large temperature ranges, which previously required time consuming temperature stabilization, can now be made quickly and precisely using Temperature Sweep Mode.

**Software Control / Automation :** A new software interface completes the flexibility and usability of the MPMS XL. Running under Microsoft Windows the state-of-the-art MPMS MultiVu software interface provides a level of control for system operation, graphics and data analysis previously unavailable. With MultiVu, simultaneously viewing data files in multiple formats is easily accomplished. Similarly, display of multiple graphs allows for easy comparison of results from different experiments. Operationally, MultiVu is a valuable tool in setting up and editing several measurement protocol files simultaneously.

### 3.6.3 Specifications

#### *Reciprocating Sample Measurement System*

Features:

- New servo powered, shaft encoded transport allows precision oscillating sample motion
- New sample rod with low thermal expansion and radial sample centring features
- New high precision data acquisition electronics, including a digital signal processor
- New MPMS software revision including a digital signal processor.
- New MPMS software revision, including support for all Reciprocating Sample Features:
  - SQUID signal analysis phase locked to sample motion.
  - Support of longitudinal and transverse measurement axes.
  - Sample centring methods
  - Support all measurements with new sample transport (AC, DC, Reciprocating Samples)
- 16 measurement ranges from  $10^{-5}$  emu to 5 emu
- Frequency ranges: 0.5-4.0 Hz

- Oscillation amplitude range: 0.5 to 50 mm p-p
- Max. DC scan length: 87 mm
- Relative sensitivity : Max. of  $< 1 \times 10^{-8}$  emu or 0.1 % (0 – 2,500 Oe)
- Upgrade available for all basic MPMS systems

### ***Continuous Low Temperature Control and Enhanced Thermometry***

#### **Features:**

- New dual impedance design allows continuous operation below 4.2 K
- New sample space thermometry improves temperature control
- Transition through 4.2 K requires no <sup>4</sup>He reservoir refilling and recycling (no pot fill)
- New MPMS software revision for all continuous Low Temperature features
- Temperature stability:  $\pm 0.5\%$  (1.9-4.2 K)
- Include temperature Sweep feature. Sweep rate range : 0.001-10 K/min
- Upgrade available for all basic MPMS systems.

#### **Configurations**

The MPMS XL is offered in two high homogeneity magnet configurations – MPMS XL 5 (5 Tesla) and MPMS XL 7 (7 Tesla). Each system includes:

- Reciprocating Sample Measurement System
- Continuous Low Temperature Control / Temperature Sweep
- MPMS MultiVu Software Interface

### **3.7 Initial Permeability measurements**

Frequency and temperature dependence of real ( $\mu'$ ) and imaginary part ( $\mu''$ ) of complex initial permeability of the as cast and annealed ribbons have been measured using a laboratory built furnace and Wayne Kerr 3255 B inductance and HP 4192A impedance analyzer with continuous heating rate of  $\approx 5$  K / min with very low applied ac field of  $\approx 10^3$  Oe. From this measurement, Curie temperature,  $T_c$ , of the as cast amorphous phase have been determined. In addition to the measurement of Curie temperature, temperature dependence of initial permeability at different stages of crystallization has been studied for Fe-based soft nanocomposite magnetic materials. Frequency, annealing temperature and annealing time dependence of complex initial permeability of the amorphous and the annealed samples provide wide information about material property of soft nanocomposite magnetic materials.

Wayne Kerr 3255 B inductance and HP 4192A impedance analyzer provide the value of inductance, L and loss factor,  $D = \tan \delta$ . From inductance the value of real part of complex initial permeability,  $\mu'$  can be

obtained by using the relation,  $\mu' = \frac{L}{L_0}$ . Here, L is the inductance of the toroid and  $L_0$  is the inductance of the coil of same geometric shape of vacuum.  $L_0$  is determined by using the relation,  $L_0 = \frac{\mu_0 N^2 S}{\pi d}$  where  $S = \frac{m}{\pi \rho d}$ . In these two equations  $\mu_0$  is the permeability of the vacuum, N is the number of turns, S is the cross-sectional area of the toroid, d is the average diameter and  $\rho$  is the density of the material. The imaginary part of complex initial permeability can be determined by using the relation,  $\tan \delta = \frac{\mu''}{\mu'}$ .

### 3.7.1 Inductance Analyzer

The 3255B Precision Magnetics Analyzer provides 2-terminal measurement of inductors and transformers over the frequency range 20 Hz to 500 kHz. DC resistance measurements are performed at a drive level of 100 mV. The drive level for AC measurements can be varied from 1 mV to 10 V rms. Automatic level control (ALC) can maintain the drive level at the component. During AC measurements the 3255B can supply a DC bias current which is variable between 1 mA and 1 A and when used with external 3265B DC bias units, up to 125 A DC bias current is available.

The analyzer's measurement, display and control facilities include:

- Spot frequency measurements;
- Multi-frequency measurements at a number of user-defined frequencies;
- Display of actual measurement values;
- Output of measurement results to an Epson-compatible printer;
- Sorting of components into bins according to their measured value and/or minor term (option)

All the above functions can be selected via manual front panel control or remote control via the GPIB interface for fully-automated high-speed testing.

Self calibration is performed to set calibration constants for signal processing elements in the measurement hardware and signal generation system, and to compensate for components, which drifted with time. To maintain full specified accuracy it should be run at least every three months. To measure the inductance of a component the analyzer should be powered up with the test leads or fixture connected to the front panel BNC connectors. The analyzer should be operated in Measurement Mode. The component to be measured is connected to the test leads or fixture. The measurement may be performed as single shot mode for single measurement or repetitive mode for continuous measurement.

### 3.7.2 Impedance Analyzer

The Hewlett Packard 4192A LF Impedance Analyzer can measure eleven impedance parameters - absolute value of impedance ( $|Z|$ ), absolute value of admittance ( $|Y|$ ), phase angle ( $\theta$ ), resistance (R),

reactance (X), conductance (G), susceptance (B), inductance (L), capacitance (C), dissipation factor (D) and quality factor (Q). Measurement range of  $|Z|/R/X$  is 0.1 m $\Omega$  to 1.2999 M $\Omega$ ;  $|Y|/G/B$  is 1 ns to 12.999 s;  $\theta$  is -180.00° to +180.00°; L is 0.01 mH to 1 000 kH; C is 0.1 pF to 100.0 mF; Dis 0.0001 to 19.999; Q is 0.1 to 1999.9. All have a basic accuracy of 0.1% and resolution of 4½ digits. Number of display digits dependence on measuring frequency and OSC level setting.

The 4192A can provide measuring frequency, OSC level, and dc bias voltage equivalent to actual operating conditions. The sweep capabilities of the built-in frequency synthesizer and dc bias source permits quick and accurate measurements. The built-in frequency synthesizer can be set to measuring frequency within the range from 5 Hz to 13 MHz with 1mHz maximum resolution. OSC level is variable from 5 mV to 1.1 Vrms with 1 mV resolution. The internal dc bias voltage source provides  $\pm 35$  V in 10 mV increments. Measuring frequency or dc bias voltage can be automatically or manually swept in either direction. OSC level can be manually swept in either direction in 1 mV increments (5mV for levels above 100 mV). Actual test voltage across or test signal current through the device under test is also measured. Thus the 4192A can evaluate components and circuits under a wide variety of measurements conditions.



## **Chapter 4**

### ***Results and Discussions on Fe-based soft nanocomposites***

#### 4.1 Structural and Magnetic Properties of $\text{Fe}_{73}\text{Cu}_1\text{Nb}_{3.5}\text{Si}_{14}\text{B}_{8.5}$

Kinetics of crystallization of different crystalline phases has been studied by using differential thermal analysis DTA diagrams of  $\text{Fe}_{73}\text{Cu}_1\text{Nb}_{3.5}\text{Si}_{14}\text{B}_{8.5}$  amorphous ribbon measured in nitrogen atmosphere with continuous heating rate of 10–50 K/min is shown in Fig. 4.1.1 and DTA curves of the samples in the as-cast and annealed condition has been presented in Fig. 4.1.2. In Fig. 4.1.1, two exothermic peaks in the curve indicate two distinct crystallization temperatures, the first one corresponds to the crystallization of  $\alpha\text{-Fe}(\text{Si})$  phase and the second one is related to the crystallization of iron boride. It is observed that the crystallization of each phase has occurred over a wide range of temperatures and that the peak temperature shifts to higher values with the increase of heating rate. Activation energy of crystallization of  $\alpha\text{-Fe}(\text{Si})$  and iron boride phases have been evaluated using Kissinger's plots [1] presented in Fig. 4.1.3 and 4.1.4 and found to be 3.71 and 4.71 eV respectively.

In Fig. 4.1.2, DTA curves of as cast and samples annealed at 798 and 818 K for 20 minutes have been presented. It is observed that the enthalpy of crystallization of bcc phase, which is proportional to the area under corresponding peak decreases with the increase of annealing temperature due to increased fraction of crystalline phase in pre-annealed samples. Thus, the calculated volume fraction of  $\alpha\text{-Fe}(\text{Si})$  phase can

be derived from  $\frac{\Delta H_{\text{as-cast}} - \Delta H_{\text{anneal}}}{\Delta H_{\text{as-cast}}}$ , where  $\Delta H$  is the enthalpy of crystallization in the corresponding

state. The calculated volume fraction of  $\alpha\text{-Fe}(\text{Si})$  phase for sample annealed at 798 K is around 81% and for sample annealed at 818 K is around 89%.

In Fig. 4.1.5, x-ray diffraction spectra of as-cast and annealed samples at different annealing temperatures have been presented. X-ray diffraction results show that no crystalline phases are detected below 773 K, with the appearance of broader diffused pattern, which is characteristic to amorphous material. For the samples annealed at or above 773 K, peaks corresponding to crystalline phases appear, which have been identified as bcc  $\alpha\text{-Fe}(\text{Si})$  solid solution produced in the amorphous matrix. With the increase of annealing temperature the peaks become narrower with higher intensity indicating that the crystalline volume fraction has increased. Iron boride phase is detected in the samples annealed at 973 K.

In Fig. 4.1.6, the lattice parameters and Si content of  $\alpha\text{-Fe}(\text{Si})$  nanograins dispersed in the surrounding amorphous matrix have been presented for various annealed samples in the temperature range between 773 and 973 K. With the increase of annealing temperature lattice parameter decreases until 923 K beyond which it increases. The lattice parameter of  $\alpha\text{-Fe}(\text{Si})$  phases are always smaller than that of pure Fe, the value of which is 2.866 Å. Thus it can be assumed that the decrease of lattice parameter is due to the contraction of  $\alpha\text{-Fe}$  lattice as a result of diffusion of the silicon with smaller atomic size into the iron lattice with larger atomic size forming a substitutional solid solution during the crystallization process to form  $\alpha\text{-Fe}(\text{Si})$ .

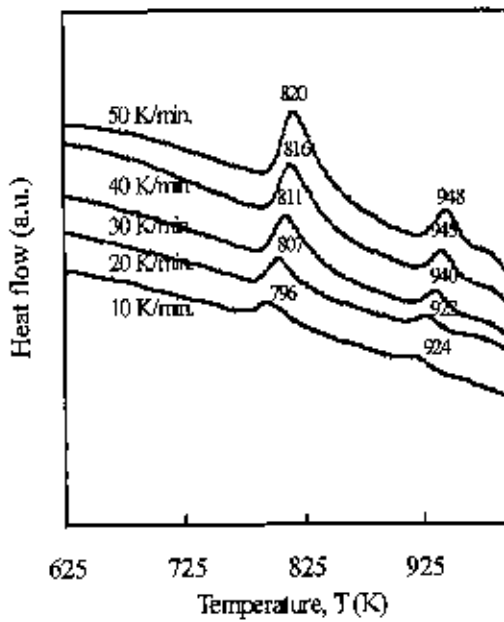


Fig. 4.1.1. Differential thermal analysis curves of as-cast amorphous ribbons of at different heating rate.

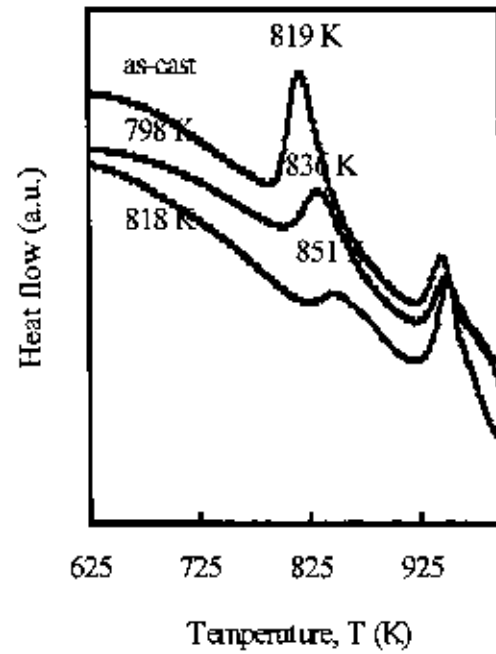


Fig. 4.1.2. Differential thermal analysis curves of as-cast and annealed samples at the heating rate of 50K/min.

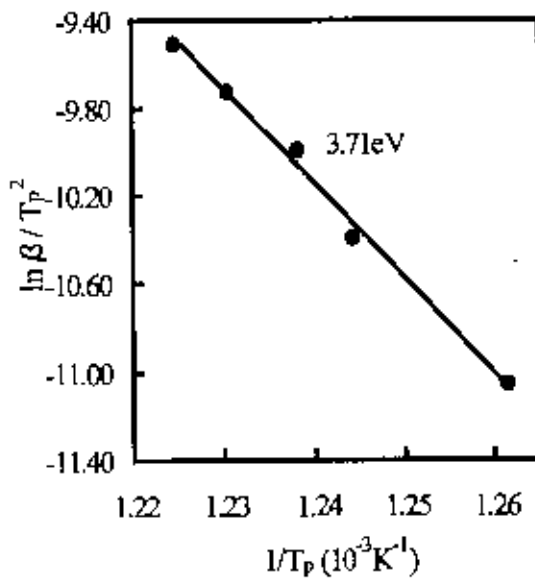


Fig. 4.1.3. Kissinger's plot to determine the activation energy of Fe(Si) phase.

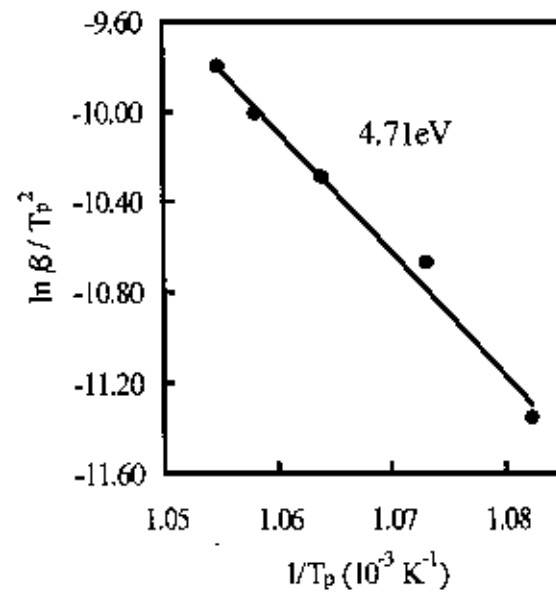


Fig. 4.1.4. Kissinger's plot to determine the activation energy of iron boride phase.



From the established quantitative relationship between lattice parameter ( $a$ ) and Si content (%Si) of Fe-Si alloys  $\%Si = -467.19a + 1342.8$  [2], Si contents of  $\alpha$ -Fe(Si) nanograins have been determined and shown in Fig. 4.1.6. The Si content of  $\alpha$ -Fe(Si) increases with the increase of annealing temperature attaining a maximum value of about 21 at.% at 923 K beyond which it starts decreasing. When the samples are annealed above 923 K, an increase of lattice parameter with subsequent decrease of Si content indicates that recrystallization of  $\alpha$ -Fe(Si) grains has taken place and that during recrystallization silicon diffuses out of the  $\alpha$ -Fe(Si) grains. This result is compatible with those reported for similar composition [3].

In Fig. 4.1.7, the mean grain size of the nanograins determined from the X-ray fundamental line (110) using the Scherrer's formula has been presented. The grain size increases gradually up to 828 K and then attains a limiting value of 12 nm until 923 K. An abrupt increase above 923 K is noticed attaining a value of 32 nm. Our result corresponds well with the reported results of Rubinstein et. al. [4]. The formation of this particular nanostructure is ascribed to combined effects of Cu and Nb and their low solubility in iron.

In Fig. 4.1.8, temperature dependence of real part of the initial permeability of the as-cast and samples annealed at 798 and 818 K have been presented. For the as-cast sample, permeability passes through a maximum just before a sharp fall to near zero with the manifestation of Hopkinson effect characterizing the ferro-paramagnetic transition at 597 K compatible with the reported results. Practically the accurate determination of  $T_c$  of the amorphous materials is really difficult due to irreversible components of the structural relaxation like long-range internal stress, topological and chemical short-range order. This structural relaxation without destroying the amorphous state may influence  $T_c$ . Therefore during the measurement of  $T_c$  the heating rate has been adjusted in such a way that no substantial relaxation takes place. From the variation of  $\mu'$  with temperature for the toroidal samples annealed at 798 and 818 K, Curie temperature of residual amorphous matrix determined from the maximum value of  $\frac{d\mu'}{dt}$  are 563 K and

553 K for the sample annealed at 798 K and 818 K respectively. Another feature, which can be observed from Fig. 4.1.8 is that as the annealing temperature is above the crystallization temperature i.e. 798 and 818 K, the sharpness of the fall to lower values of permeability is smeared out with the appearance of a tail in the high temperature region. These results are in good agreement with those previously reported for the FINEMET composition [5].

From the results of the temperature dependence of permeability for samples annealed at 798 and 818 K, the grain coupling is largely but not completely interrupted above the Curie temperature of the amorphous matrix. A system, in which the magnetic coupling between particles is significant and prevents superparamagnetic relaxations, has been termed superferromagnetism by S. Mørup [6]. The precise coupling mechanism for this type of behavior at  $T > T_c^{am}$  may be explained in terms of exchange penetration through the thin, paramagnetic intergranular layer and / or dipolar interactions [7]. With further increase of temperature sharp increase in permeability takes place and subsequently falls to zero

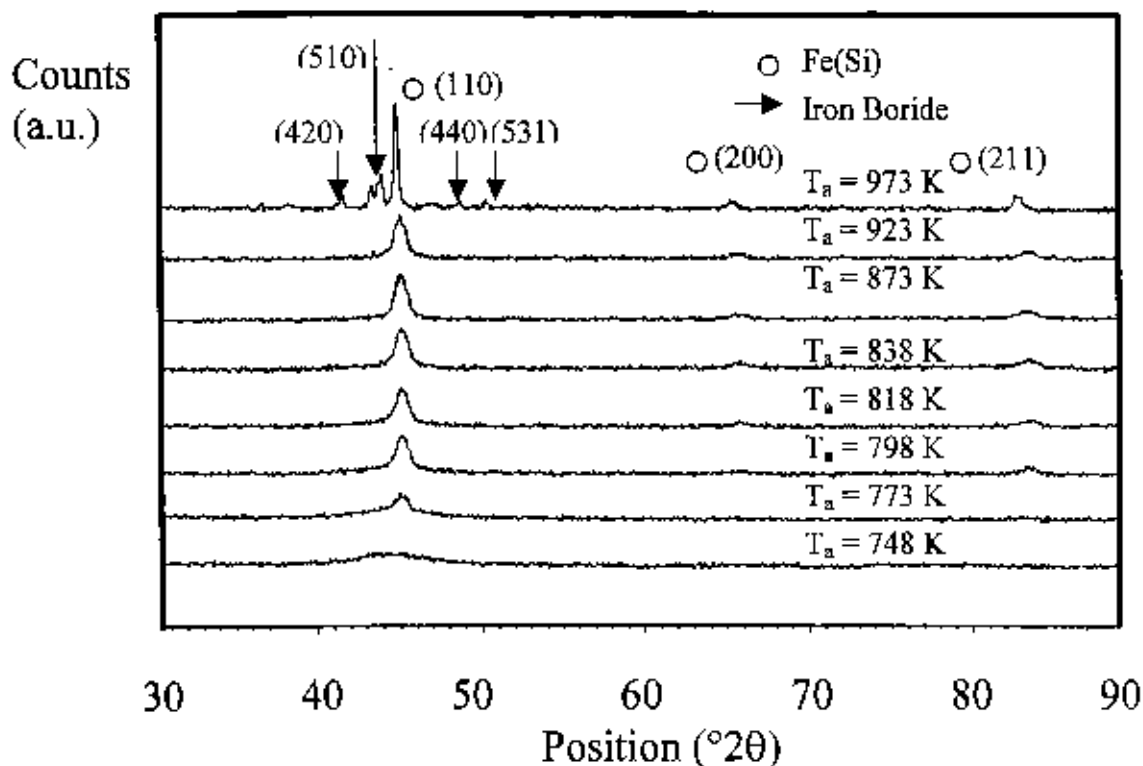


Fig. 4.1.5. X-ray diffraction patterns of the amorphous and annealed samples at different annealing temperature for 1 hour.

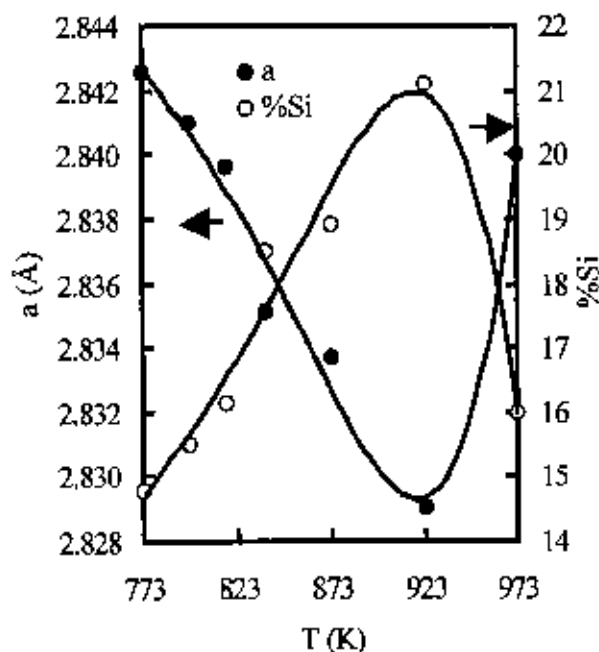


Fig. 4.1.6. Variation of lattice parameter,  $a$  and silicon content, %Si of Fe(Si) nanograins.

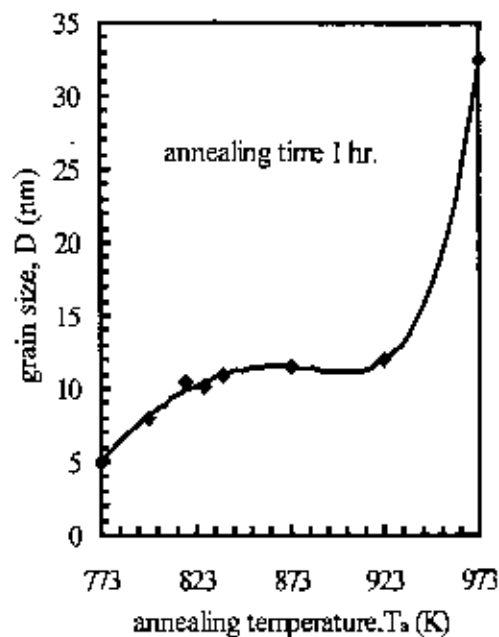


Fig. 4.1.7. Variation of grain size of  $\alpha$ -Fe(Si) phase with annealing temperature

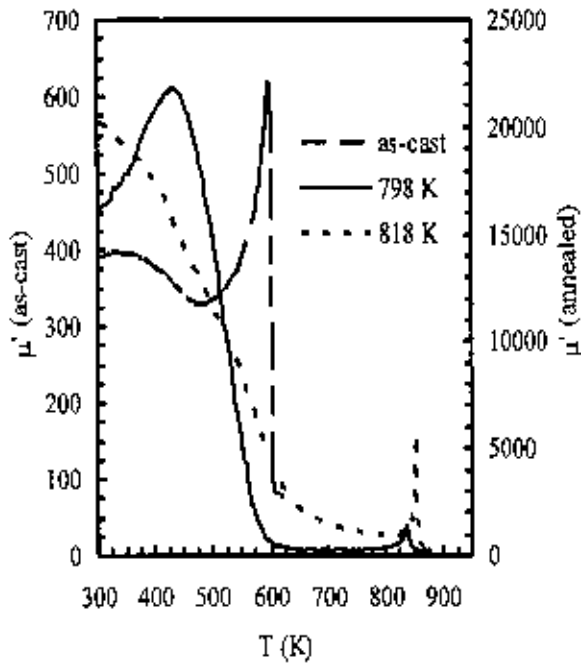


Fig. 4.1.8. Variation of real part initial permeability,  $\mu'$  with measuring temperature for as-cast and annealed samples.

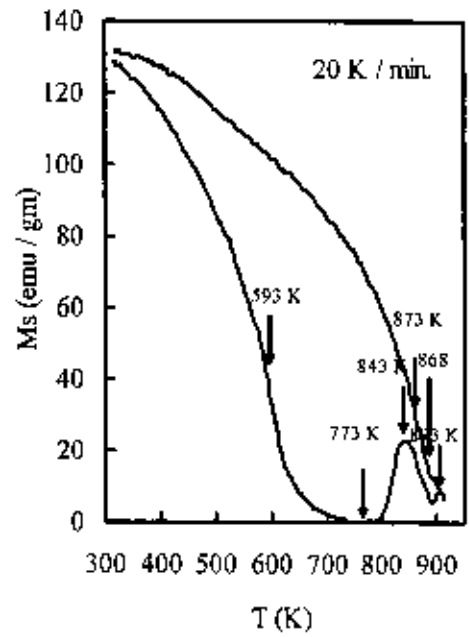


Fig. 4.1.9. Variation of saturation magnetization with temperature with an applied field of 1 Tesla.

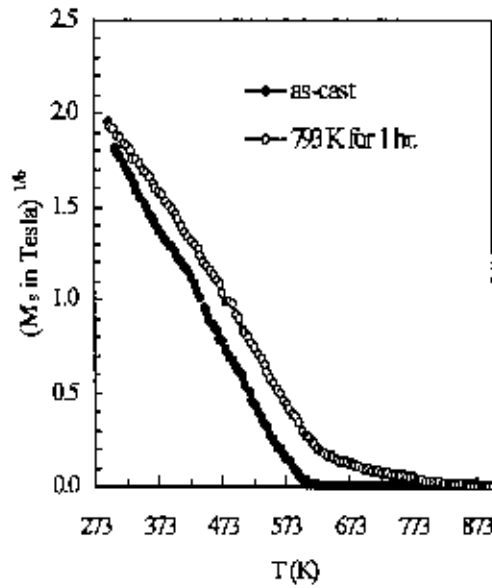


Fig. 4.1.10. Variation of  $M_s^{1/2}$  with temperature.

due to the decrease of the average anisotropy of the nanograins with a retaining value of magnetization [8]. It is noteworthy that the temperature corresponding to the increase of permeability at higher measuring temperature coincided with the temperature at which coercivity vanishes [9]. This temperature shifts to higher value from 837 to 853 K as the annealing temperature increases from 798 to 818 K i.e. with the increase of volume fraction of the crystallite, which may be attributed to the decrease of the thickness of the amorphous grain boundary favoring the interaction between the nanograins compatible with the previous observation [5] and is limited by the Curie temperature of bcc Fe(Si) nanograins

In Fig. 4.1.9, temperature dependence of saturation magnetization,  $M_s$ , has been presented, which has been measured in an applied field of 1 Tesla at a heating rate of 20 K/min. Field cooled curve has also been presented in the same figure. The characteristic feature of the curve is,  $M_s$  decreases with temperature and passes through ferro-paramagnetic transition at the Curie temperature. The Curie temperature has been estimated from the maxima of the rate of change of saturation magnetization and found to be 593 K. From the figure it can be observed that the onset of crystallization temperature is 773 K, which has good correlation with DSC measurements such as 783 K for the heating rate of 20 K/min (Fig. 6). Magnetization passes through a maximum at the temperature of around 843 K. Magnetization again decreases with temperature to a very low value beyond the Curie temperature of  $\alpha$ -Fe(Si) phase which is around 868 K. Magnetization again increases corresponding to the formation of boride phase at 893 K and then falls. From the cooling curve the Curie temperature of Fe(Si) phase has been estimated as 873 K.

In Fig. 4.1.10, temperature dependence of  $M_s^{1/b}$  has been presented for as-cast and sample annealed at 793 K for 1 hr. The temperature dependence of saturation magnetization  $M_s(T)$  of a single-phase ferromagnet

can be described by [10],  $M_s(T) = M_0 \left(1 - \frac{T}{T_c}\right)^{1/b}$  where, b is a critical exponent close to the Heisenberg

value 0.36. Anomaly in  $M_s(T)$  due to structural details can be detected from the deviation of  $M_s^{1/b}$  vs. T plot from linearity. From Fig. 4.1.10 it can be observed that the amorphous sample closely follows the above equation with a Curie temperature of  $T_c = 598$  K. The  $M_s^{1/b}$  vs T curve for the nanocrystalline material shows a distinct change of slope at about 613 K. Such behavior is common for two-phase magnetic material.

In Fig. 4.1.11, x-ray diffraction spectra of as cast and annealed samples at 818 K with varying annealing time have been presented. The evolution of crystalline phase appears with the annealing time of 5 minutes and onward and have been identified as bcc  $\alpha$ -Fe(Si) using standard software.

In Fig. 4.1.12 the lattice parameters of various samples annealed at 818 K with varying annealing time have been presented. With the increase of annealing time lattice parameter decreases. The lattice parameters of all the bcc  $\alpha$ -Fe(Si) phase are smaller than the lattice parameter of pure Fe (2.8664 Å). Thus it can be assumed that the decrease of lattice parameter is due to the increase of silicon content in the  $\alpha$ -Fe(Si) grains as the annealing time increases due to the contraction of Fe lattice.

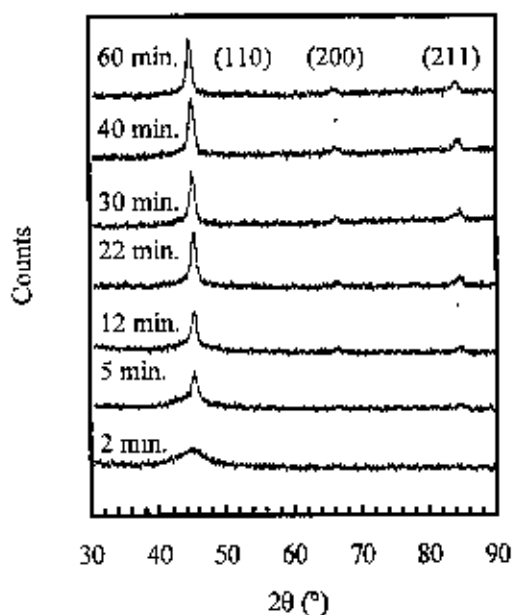


Fig. 4.1.11. X-ray diffraction pattern of  $\text{Fe}_{73}\text{Cu}_1\text{Nb}_{3.5}\text{Si}_{14}\text{B}_{8.5}$  annealed at 818 K for different annealing time.

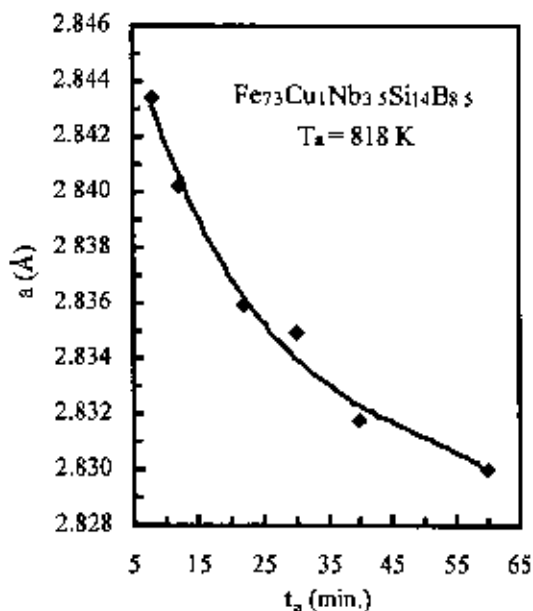


Fig. 4.1.12. Annealing time,  $t_a$  dependence of lattice parameter,  $a$ .

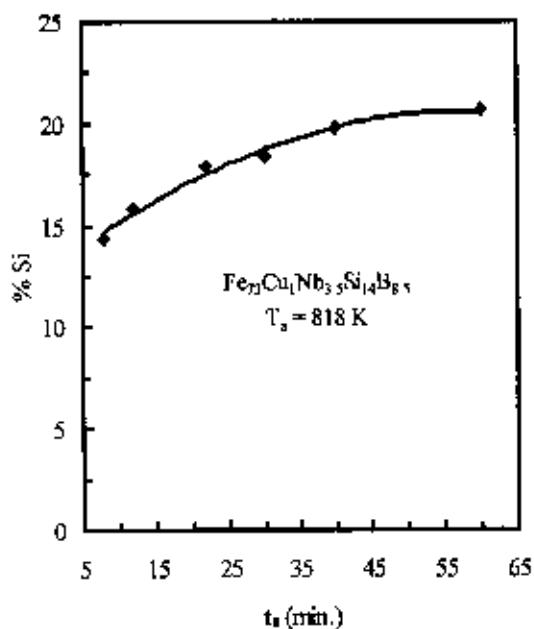


Fig. 4.1.13 Annealing time,  $t_a$  dependence of silicon content.

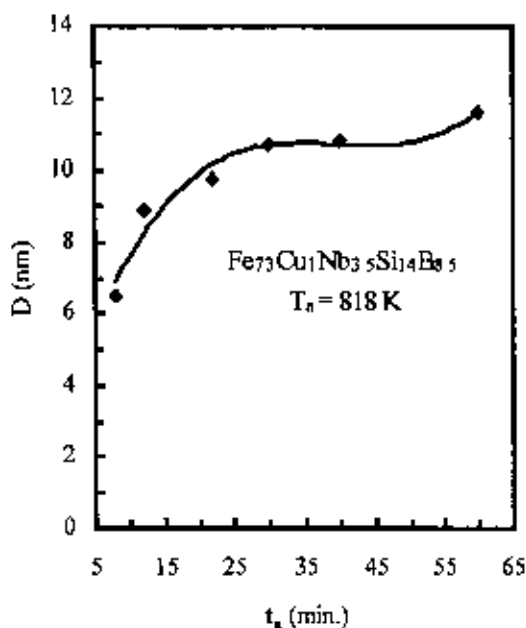


Fig. 4.1.14 Annealing time,  $t_a$  dependence of grain size,  $D$ .

1045244

Using the relationship between lattice parameter and Si content in Fe-Si alloys, Si content in the Fe(Si) nanograins has been determined and presented in Fig. 4.1.13. Silicon content in the  $\alpha$ -Fe(Si) grains increases with increasing annealing time attaining a value of  $\approx 21$  at.% for 60 minutes annealing at 818 K.

In Fig. 4.1.14, the mean grain size of the  $\alpha$ -Fe(Si) nanograins using the Scherrer's formula has been presented. The grain size increases with increasing annealing time attaining a limiting value of  $\approx 11$  nm in 24 minutes and remains almost constant up to 60 minutes of annealing. It may be attributed to the combined effect of Cu and Nb elements, where, Cu increases the nucleation density and Nb inhibits the grain growth resulting in homogeneous distribution of nanograins in the surrounding amorphous matrix.

In Fig. 4.1.15(a) annealing temperature dependence of initial permeability for 1 hour annealing time has been presented. Enhancement of permeability by two orders of magnitude has been observed for the sample annealed at 828 K. Dependence of  $\mu'$  upon annealing temperature is similar to the later compositions and hence it will be described later. The increase of the real part of complex initial permeability measured at 1 kHz as a function of cumulative annealing time for the annealing temperature of 818 K has been presented in Fig. 4.1.15(b). The increase of  $\mu'$  is very steep initially for the annealing time of 5 minutes. The highest value of  $\mu'$  around 31000 was attained for the annealing time of 22 minutes. As the annealing time is increased further by only 2 minutes the value of  $\mu'$  drops to 24000. Upon further increase of annealing time the value of  $\mu'$  does not vary significantly up to 60 minutes annealing time maintaining a plateau value of 26000 – 23000. It has been demonstrated that when a sample is annealed for cumulative time, the effect of induced anisotropies become dominant and the permeability is significantly reduced [12]. From the comparison of two figures it can be observed that the permeability enhancement with short time annealing is more effective than long time annealing at the same temperature. While the value of  $\mu'$  is around 17000 for the  $T_a = 818$  K for 1 hour holding time obtained from  $\mu'$  vs.  $T_a$  curve presented in the inset of Fig. 4.1.15 (b),  $\mu'$  attains a value of around 31000 within 22 minutes. This shows that long time annealing has some effect of induced anisotropy, which reduces the value of  $\mu'$  significantly.

In Fig. 4.1.16, frequency dependence of complex permeability has been presented for as cast sample and the sample annealed at 823 K for 10 minutes. A steep increase of  $\mu'$  by two orders of magnitude from around 320 for the amorphous ribbons to 37000 by annealing the same at 823 K for 10 minutes is observed. The loss component represented by  $\mu''$  has also been presented for both the samples in Fig. 4.1.16. The loss component of the complex permeability,  $\mu''$ , increases much faster for the amorphous ribbons than the annealed one with increasing frequency and passes through a maximum caused due to the resonance effect which shifts to lower frequency for the annealed samples with high permeability than that of amorphous one as expected. The loss factor,  $\tan \delta = \frac{\mu''}{\mu'}$  is high for the amorphous ribbon and a sharp increase with increasing frequency is observed which may be attributed to the internal stresses created



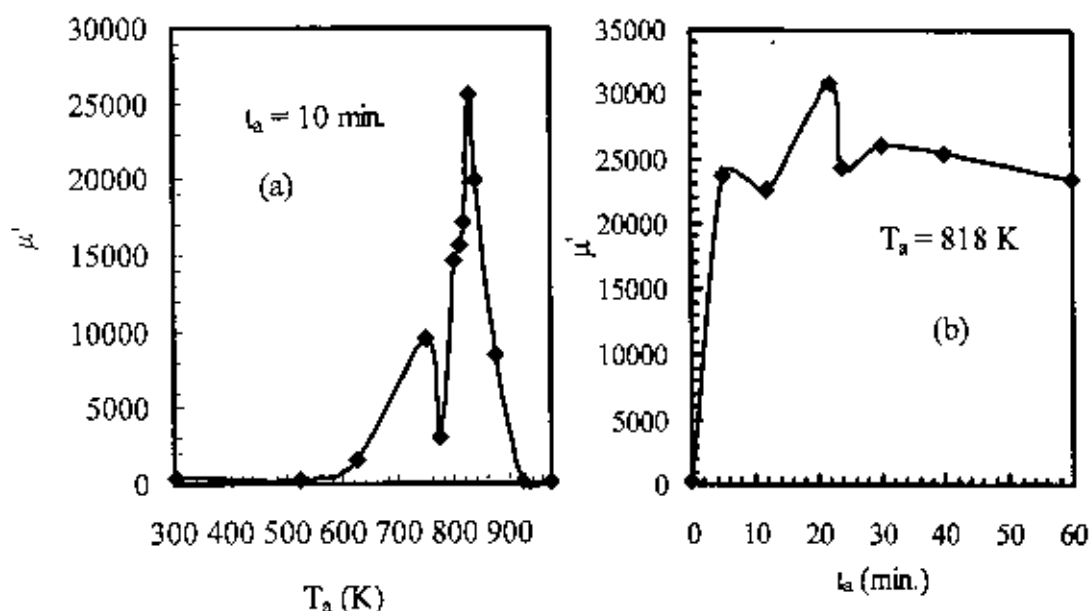


Fig. 4.1.15. (a) annealing temperature dependence of initial permeability annealed for 1 hr. at 1 kHz; (b) Annealing time dependence of initial permeability at the annealing temperature of 818 K at 1 kHz.

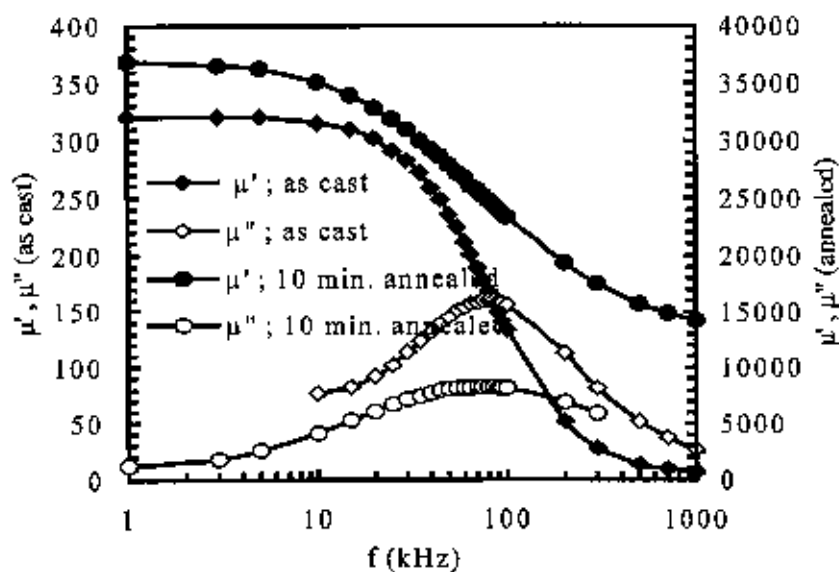


Fig. 4.1.16. Frequency dependence of real,  $\mu'$  and imaginary part,  $\mu''$ , of complex initial permeability for as-cast and annealed samples at 823 K for 10 minutes.

Table 4.1 The values of saturation magnetization at different annealing temperature and time.

annealing temperature, $T_a$ (K)	annealing time, $t_a$ (min.)	saturation magnetization (emu / g)
as cast	-	128.1
623	60	130.1
723	30	134.3
793	10	137
823	10	133.3
823	15	131.1



during rapid solidification. At low frequency, the magnetic losses are controlled by hysteresis caused due to irreversible magnetization process and at higher frequency loss is governed by eddy current. The relative loss factor,  $\frac{\mu''}{\mu' \delta}$  has been reduced by three orders of magnitude for the optimum annealed sample than for the as cast sample. This very high initial permeability and extremely low magnetic losses of the optimized nanocrystalline alloys are due to the drastic reduction in the local anisotropy randomly averaged out by the exchange interactions due to the formation of nanometric grains smaller than the ferromagnetic exchange length.

The coupling between the nanograins mediated by amorphous matrix is of paramount importance for the magnetic softening of these materials, which depends not only on the nanometric grains but more importantly on the composition, thickness and amount of the intervening amorphous phase. It is a prerequisite for the ferromagnetic grains to be strongly exchange coupled to maintain good soft magnetic properties. For longer annealing time amorphous matrix is enriched with Nb which makes a magnetically weaker grain boundary and hence reduce the exchange coupling between the nanograins. Therefore, optimization of magnetic properties of the nanocrystalline alloys need more detailed study on the effect of heat treatment as a function of temperature and time.

The saturation magnetization,  $M_s$ , of the amorphous and annealed samples measured with a VSM at room temperature are shown in Table 4.1. Amorphous alloys are basically metastable materials. Hence structural relaxation can occur even though the alloys remain amorphous when they are annealed at temperature well below the crystallization temperature. Saturation magnetization, increases for the amorphous  $Fe_{73}Cu_1Nb_{3.5}Si_{14}B_{8.5}$  when annealed below the crystallization temperature for a longer time or close to the crystallization temperature for a shorter time. Saturation magnetization,  $M_s$ , however decreases when annealed up to the advanced crystallized state [13, 14]. Saturation magnetization increase gradually with the increase of annealing temperature up to 793 K. However,  $M_s$  decreases when annealed at 823 K. Maximum value of saturation magnetization is attained for the sample annealed at 793 K for 10 minutes, which corresponds to the temperature of early stage of nanocrystallization. The increase in  $M_s$  until the early stage of crystallization can be attributed to the irreversible structural relaxation and varying degrees of chemical disorder [13]. The decrease in  $M_s$  for the sample annealed at 823 K for 10 minutes corresponds to the optimum nanocrystallized state with high volume fraction of  $\alpha$ -Fe(Si) nanograins is interpreted as due to enrichment of nanograins with Si by diffusion resulting in a decrease of magnetic moment of Fe and the enrichment of the residual amorphous phase with Nb.

#### 4.2 Structural and Magnetic Properties of $Fe_{73.5}Cu_1Ta_3Si_{13.5}B_9$

DTA measurements of as-cast samples in nitrogen atmosphere with continuous heating rate of 10 – 50 K/min is shown in Fig. 4.2.1 and for as-cast and annealed samples with the heating rate of 20 K/min have been presented in Fig. 4.2.2. The exothermic peak corresponds to the crystallization of  $\alpha$ -Fe(Si) and iron

boride phases respectively. The activation energy of crystallization of  $\alpha$ -Fe(Si) and iron boride phases have been evaluated using Kissinger's plot of  $\ln \frac{\beta}{T_p^2}$  vs.  $\frac{1}{T_p}$  presented in Fig. 4.2.3 and Fig. 4.2.4 [1]

where  $\beta$  is the heating rate (10-50 K/min in this experiment) and  $T_p$  is the peak temperature of  $\alpha$ -Fe(Si) and iron boride phases for each of the heating rate. The activation energy of crystallization of  $\alpha$ -Fe(Si) and iron boride phases are found to be 3.50 and 4.15 eV respectively. In Fig. 4.2.2, DTA curves of as cast samples and samples annealed at 773, 798 and 818 K for 20 minutes have been presented. The volume fraction estimated from the comparison of DTA curves of as-cast and annealed samples has been found to be 39% for 773 K, 68% for 798 K and 84% for 818 K.

In Fig. 4.2.5, lattice parameter of various annealed samples in the temperature range between 773 and 973 K has been presented. With the increase of annealing temperature lattice parameter decreases up to  $T_a = 848$  K. For the annealing temperature of 873 K and above, increase of lattice parameter is observed. The lattice parameters of  $\alpha$ -Fe(Si) phases are smaller than pure Fe, the value of which is 2.866 Å. When the annealing temperature is below 848 K the decrease of lattice parameter is due to the contraction of  $\alpha$ -Fe lattice as a result of diffusion of the silicon with smaller atomic size into the iron lattice with larger atomic size forming a substitutional solid solution during the crystallization process to form  $\alpha$ -Fe(Si). When the annealing temperature is above 848 K some of the Si diffuses out of the  $\alpha$ -Fe(Si) lattice and therefore the value of lattice parameter increases again.

From the established quantitative relationship between lattice parameter and Si content in Fe-Si alloys [2], Si contents of Fe(Si) nanograins have been determined and shown in Fig. 4.2.6. It is observed from Fig. 4.2.6 that the Si content of  $\alpha$ -Fe(Si) increases with the increase of annealing temperature attaining a maximum value of about 20.5 at.% at 848 K beyond which it starts decreasing. This maximum value of 20.5 at.% Si is compatible with 21 at.% Si obtained by Mössbauer study [15]. An increase of lattice parameter with subsequent decrease of Si content beyond 848 K indicates that recrystallization of  $\alpha$ -Fe(Si) grains has taken place. This result is compatible with those reported for similar composition [3].

In Fig. 4.2.7, the mean grain size of the nanograins determined from the X-ray fundamental line (110) using the Scherrer's formula has been presented. The grain size increases gradually up to 848 K and then attains a limiting value of 10 to 12 nm until 923 K. An abrupt increase of grain size above 923 K is noticed attaining a value of 26 nm at 973 K. Our result corresponds well with the reported results of Rubinstein et. al. [4]. The formation of this particular nanostructure is ascribed to the combined effects of Cu and Ta and their low solubility in iron.

In order to correlate the microstructural features on the soft magnetic properties of the alloys under study, magnetic initial permeability of the toroidal shaped samples annealed at different temperatures are measured with very low field. Magnetic properties of the soft magnetic materials are mainly determined

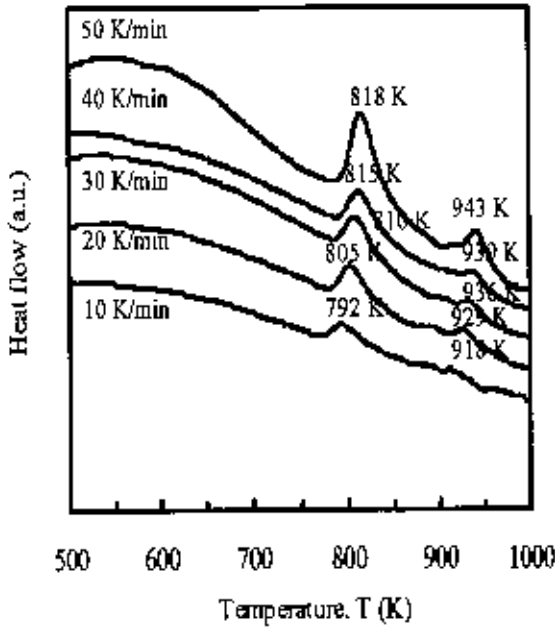


Fig. 4.2.1 DTA curves of amorphous ribbons at different heating rate of 10,20,30,40 and 50 K/min from below to above.

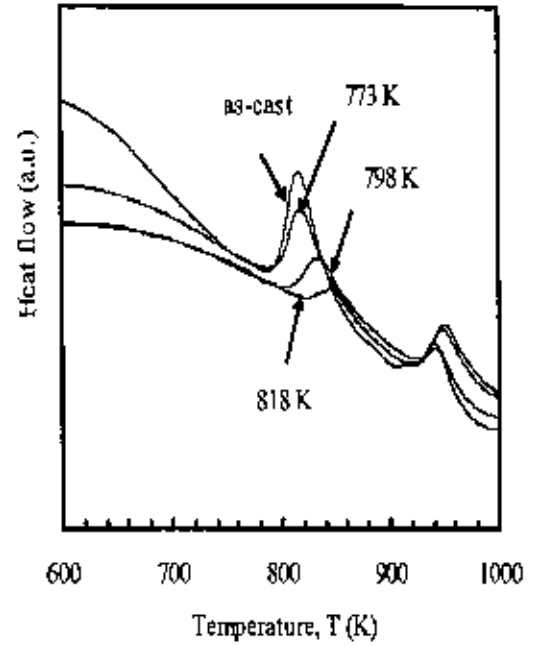


Fig. 4.2.2 DTA curves of as-cast and samples annealed at 773, 798, 818 K.

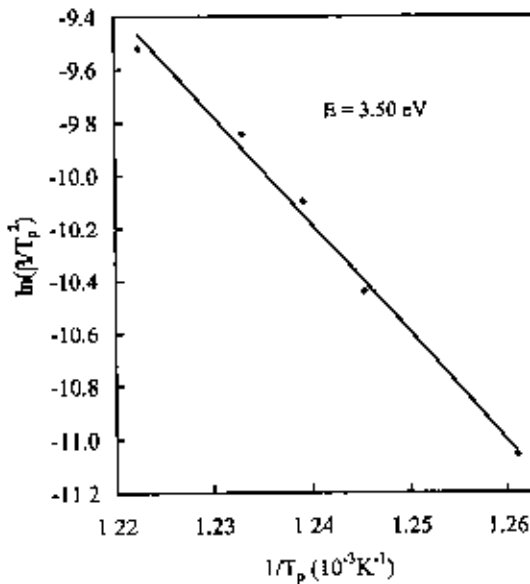


Fig. 4.2.3. Kissinger plot for the determination of the activation energy for the formation of Fe(Si) phase in  $\text{Fe}_{73.5}\text{Cu}_1\text{Ta}_3\text{Si}_{13.5}\text{B}_9$ .

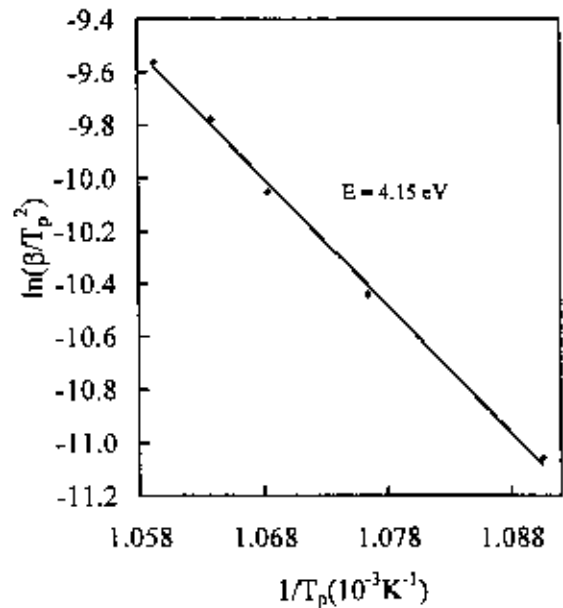


Fig. 4.2.4. Kissinger plot for the determination of activation energy for the formation of  $\text{Fe}_2\text{B}$  phase in  $\text{Fe}_{73.5}\text{Cu}_1\text{Ta}_3\text{Si}_{13.5}\text{B}_9$ .

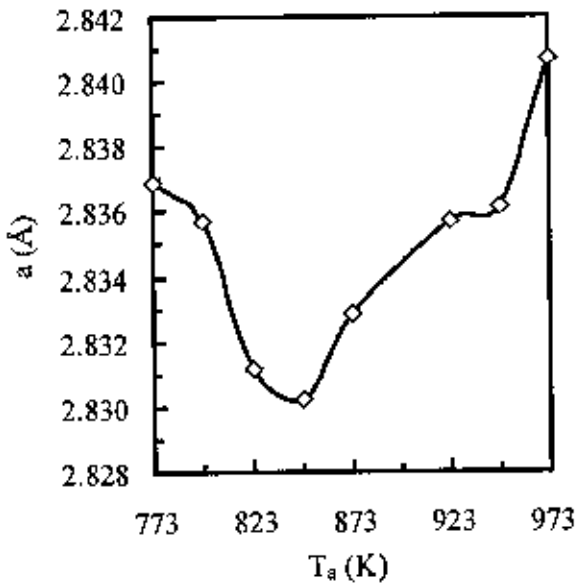


Fig. 4.2.5. Variation of lattice parameter,  $a$  with the annealing temperature  $T_a$ .



Fig. 4.2.6. Variation of silicon content with annealing temperature,  $T_a$ .

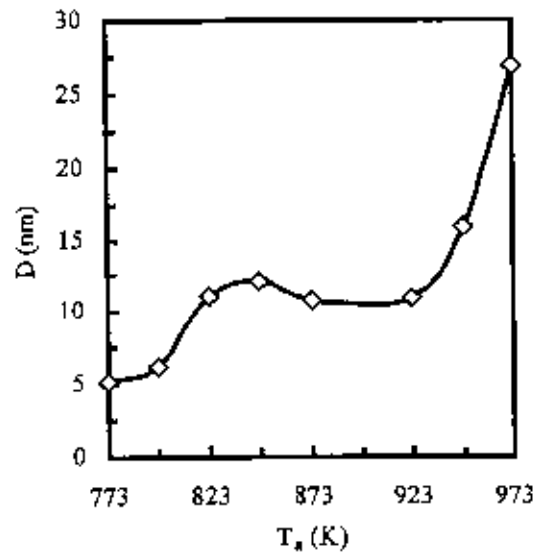


Fig. 4.2.7. Variation of grain size,  $D$  with annealing temperature,  $T_a$ .



by the domain wall mobility especially in the range of reversible magnetization. In Fig. 4.2.8, the real part of the complex initial permeability  $\mu'$  up to  $f = 500$  kHz has been presented for as cast and annealed samples. The general characteristic of the curves is that  $\mu'$  remains fairly constant up to some critical frequency characterized by the onset of resonance connected with the loss component. At critical frequencies,  $\mu'$  drop rapidly. The low frequency value of  $\mu'$  generally increases with the increase of annealing temperature. In association with the higher value of low frequency permeability, the frequency at which resonance occurs appears at a lower frequency. This shows that the high permeability ribbons can be used as core materials only in a limited frequency range. This trend of increase of low frequency permeability is observed up to the annealing temperature of 823 K. For the annealing temperature of 848 K the low frequency permeability decreases and for 873 K it drops to a very low value.

In Fig. 4.2.9, the real part of the complex initial permeability  $\mu'$  has been presented as a function of annealing temperature  $T_a$  at a fixed frequency of 1 kHz. The curve reveals strong dependence of initial permeability upon annealing temperature. When annealed at temperatures below the onset of crystallization, an increase of initial permeability with annealing temperature was observed due to irreversible structural relaxation of the amorphous matrix i.e. stress relief, increase of packing density by annealing out micro-voids and changing the degree of chemical disorder. At the annealing temperature of 760 K, the permeability drops to a lower value. This is the temperature around which initiation of crystallization takes place. The decrease of permeability may be attributed to the new stresses developed in the matrix by the growing crystallites, which act as pinning centers for the domain walls constraining the domain wall mobility as well as weak intergranular magnetic coupling since the growing crystallites are far apart from each other representing small volume fraction that cannot be exchange coupled and the anisotropy cannot be averaged. Further increase of annealing temperature leads to the increase of permeability due to the increased volume fraction of  $\alpha$ -Fe(Si) nanograins coupled via exchange interaction resulting in a reduction of anisotropy energy. An enhancement of initial permeability by two orders of magnitude was observed for the annealing temperature of 823 K. For the annealing temperature above 823 K,  $\mu'$  drops to lower value drastically. The probable reason might be the evolution of boride phase, which will be shown later. This leads to the increase of anisotropy energy to a high value, which essentially reduces the local exchange correlation length weakening the intergranular magnetic coupling as a result of which magnetic hardening takes place. This could not be detected by X-ray diffraction since the amount of boride phase is extremely low [9].

In Fig. 4.2.10, temperature dependence of real part of the initial permeability of the as cast amorphous ribbon and the samples annealed at 673 – 748 K at the interval of 25 K has been presented. For the samples annealed at 673 – 723 K permeability passes through a maximum followed by a sharp fall passing through Curie temperature of the sample. However, for the sample annealed at 748 K the sharpness of the fall is relatively smeared out which might be an indication of initiation of nucleation since no crystalline

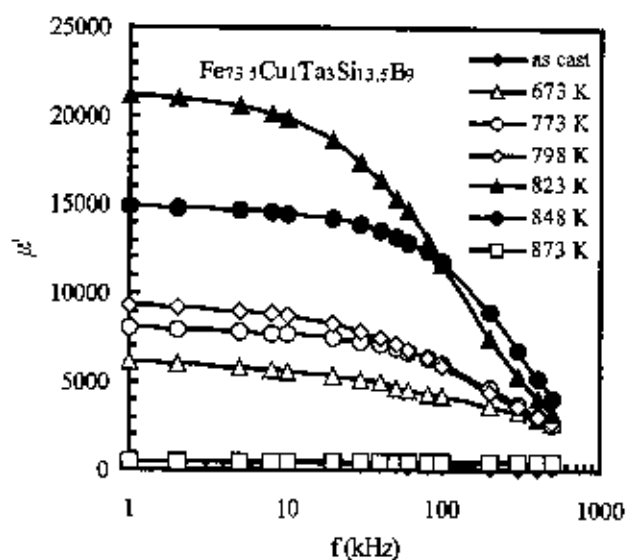


Fig. 4.2.8. Frequency dependence of  $\mu'$  at different annealing temperatures.

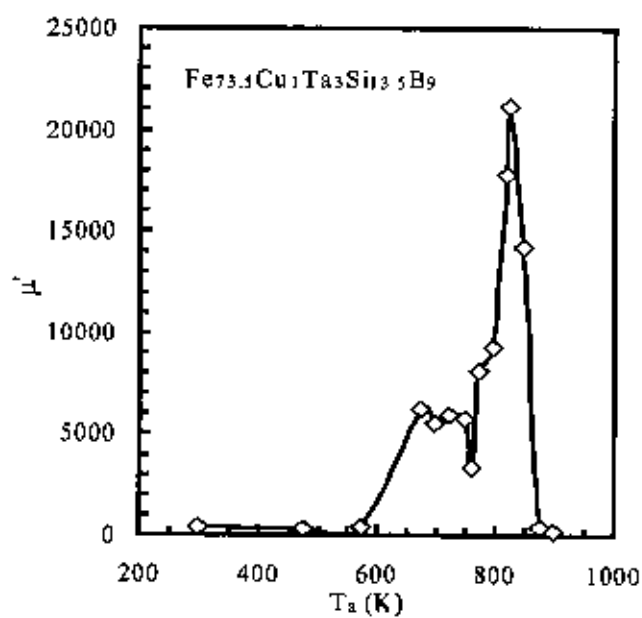


Fig. 4.2.9. Variation of  $\mu'$  with annealing temperature,  $T_a$ .

phase could be detected for this annealing temperature by X-ray diffraction. During the measurement of  $T_c$  the heating rate has been adjusted in such a way that no substantial relaxation takes place. However, the Curie temperature estimated from the curves presented in Fig. 4.2.10 for the as-cast and annealed samples in the amorphous state has been given in Table 4.2.

In Fig. 4.2.11, the variation of  $\mu'$  with temperature for the toroid samples annealed at 773 – 848 K has been presented. As it has been observed for earlier composition, in Fig. 4.2.11, when the annealing temperature is increased above the crystallization temperature, the sharpness of the fall to lower values of permeability is progressively smeared out with the appearance of a tail in the high temperature region. These results are in good agreement with those previously reported for the FINEMET composition [5]. Curie temperature of residual amorphous matrix determined from derivative of  $\mu'$  vs  $T$  curves has been presented in Table 4.2.

From Table 4.2 it can be observed that the Curie temperature of the as cast amorphous ribbon is 610 K. Enhancement of Curie temperature occurs when the sample is annealed in the temperature range of 673 – 748 K. From X-ray diffraction no crystalline phase was observed up to the annealing temperature of 748 K. Enhancement of Curie temperature occurs because of irreversible structural relaxation as mentioned above. Further from the analysis of the Mössbauer spectra for the quenched and annealed samples below the crystallization temperature it has been observed that this treatment leads to the increase in packing density of atoms [16]. Increase in packing density of atoms might have significant contribution in the enhancement of Curie temperature in the amorphous state. Above the crystallization temperature, Curie temperature of the amorphous matrix decreases significantly. The probable reason of decreasing the Curie temperature of the amorphous phase when annealed at and above the crystallization temperature is that the amorphous matrix is depleted with iron and the relative amount of Ta in the amorphous matrix increases, which weakens the exchange interaction resulting in a decrease of Curie temperature of the amorphous matrix.

At higher measuring temperatures above  $T_c^{am}$ , permeability value decreases to very low value. Franco et al. [5] have demonstrated super-paramagnetic behavior is a general feature of these nanocrystalline alloys. The practical requisite for observing superparamagnetic relaxation in the nanocrystalline alloys is the absence of interactions between nanograins in the residual amorphous matrix. At  $T > T_c^{am}$  very low value of permeability for the sample annealed at 773 K suggests that superparamagnetic type of behavior may be present below this temperature presented in Fig. 4.2.11 where the exchange interaction between the nanograins mainly occurs via sufficiently thick paramagnetic interfacial amorphous matrix in which the nanocrystallites possessing high magnetic moments are dispersed. When the measuring temperature approaches the Curie temperature of the intergranular amorphous phase, which is much lower than that of nanograins ( $\approx 873$  K), the exchange coupling between the crystallites is largely reduced. As a consequence the initial permeability drops down to a very low value.

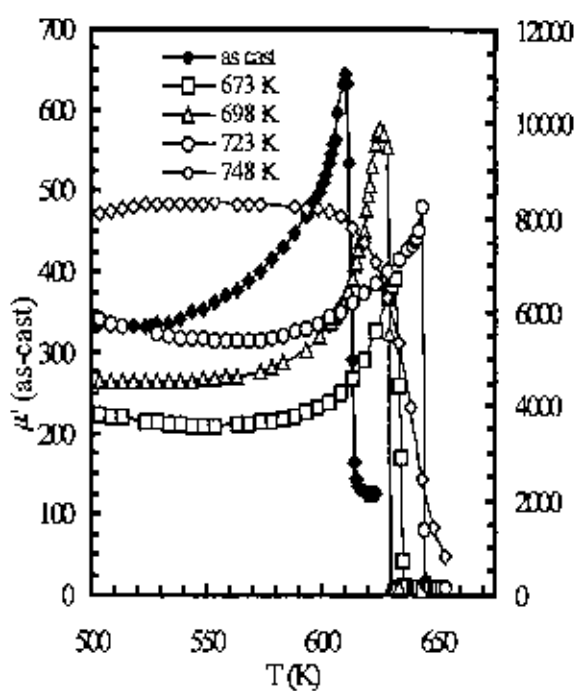


Fig. 4.2.10. Temperature dependence of  $\mu'$  of as cast and annealed sample in the amorphous relaxed state.

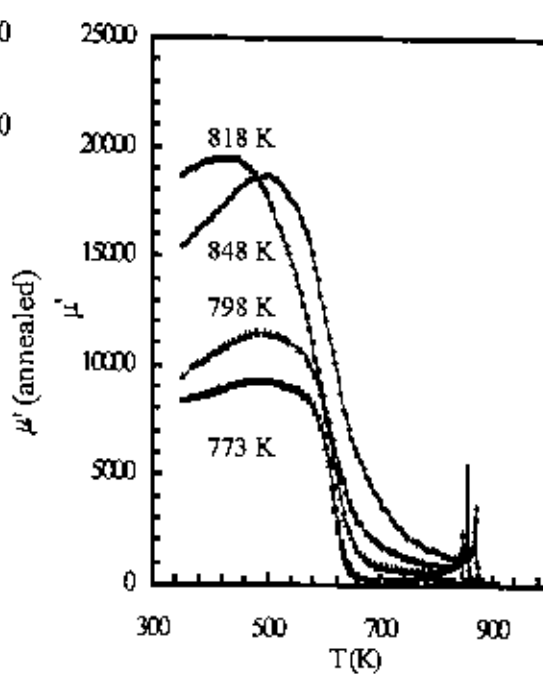


Fig. 4.2.11. Temperature dependence of  $\mu'$  in the nanocrystalline state.

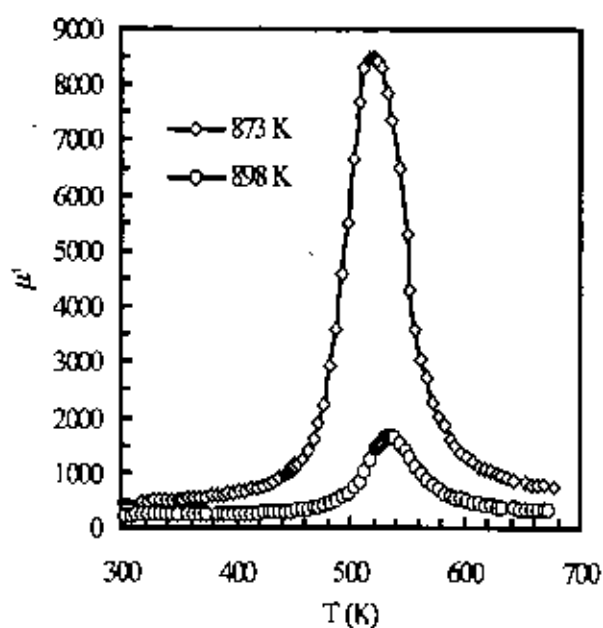


Fig. 4.2.12 Temperature dependence of  $\mu'$  after the evolution of  $\text{Fe}_2\text{B}$ .



Table 4.2 Annealing temperature,  $T_a$  dependence of the Curie temperature of amorphous matrix  $T_c^m$ .

Annealing Temperature, $T_a$ (K)	Curie Temperature, $T_c^m$ (K)
as cast	610
673	632
698	627
723	643
748	638
773	623
798	608
818	578
848	588

From the results of the temperature dependence of permeability for samples annealed above 773 K, the grain coupling is largely but not completely interrupted above  $T_c^{sm}$  and still persists to higher value of permeability compared to the sample annealed at 773 K. This type of behavior where superparamagnetic relaxations have been prevented due to higher volume fraction of Fe(Si) nanograins resulting in increased interaction between them, has been termed superferromagnetism by S. Mørup [6], in which case, the coupling mechanism has been explained in terms of exchange penetration through the thin, paramagnetic intergranular layer and / or dipolar interactions [7].

With further increase of measuring temperature superparamagnetic transition takes place with the manifestation of a sharp increase in permeability and subsequent fall to zero due to the decrease of the average anisotropy of the nanograins with a retaining value of magnetization [8]. It is noteworthy that the temperature corresponding to the increase of permeability at higher measuring temperature coincided with the temperature at which coercivity vanishes [9]. This temperature shifts to higher value from 791 K to 869 K as the annealing temperature increases from 773 K to 848 K i.e. with the increase of volume fraction of the crystallite, which may be attributed due to the decrease of the thickness of the amorphous grain boundary favoring the interaction between the nanograins compatible with the previous observation [5] and is limited by the Curie temperature of the bcc Fe(Si) nanograins.

In Fig. 4.2.12, the variation of real part initial permeability  $\mu'$  with temperature has been presented for samples annealed at 873 K and 898 K. From Fig. 4.2.9, it can be observed that the value of  $\mu'$  has dropped to a very low value for the annealing temperature of 873 K. It has been reported earlier that this fall of  $\mu'$  to a very low value might occur due to the evolution of boride phase at higher  $T_a$  of 873 K. In our experiment the presence of boride phase could not be detected by X-ray diffraction. Since the anisotropy constant  $K_1$  of  $Fe_2B$  ( $430 \text{ kJ} / \text{m}^3$ ) is five order of magnitude higher than the average anisotropy  $\langle K \rangle$  of  $\alpha$ -Fe(Si) nanograins ( $4 \text{ J} / \text{m}^3$ ), minor evolution of  $Fe_2B$  phase can cause significant damage to exchange interaction [9]. Temperature dependence of  $\mu'$  reveals the presence of  $Fe_2B$ , which was not possible to detect by X-ray diffraction. Since  $K_1$  of  $Fe_2B$  passes from negative to positive value at 523 K, a dramatic rise of  $\mu'$  from 440 at room temperature to 8400 at 523 K for the samples annealed at 873 K is evidenced. However, for the sample annealed at 898 K the value of  $\mu'$  rises from 220 at room temperature to 1600 at 537 K.

In Fig. 4.2.13, temperature dependence of saturation magnetization,  $M_s$ , has been presented, which has been measured in an applied field of 1 Tesla at a heating rate of 20 K/min. Field cooled curve has also been presented in the same figure. The characteristic feature of the curve shows that,  $M_s$  decreases with temperature and passes through ferro-paramagnetic transition at the Curie temperature. Curie temperature has been estimated from rate of change of saturation magnetization and found to be 611 K, which has an excellent compatibility with temperature dependence of permeability, the value of which has been presented in Table 4.2. Magnetization remains near zero until 785 K, where increase in magnetization

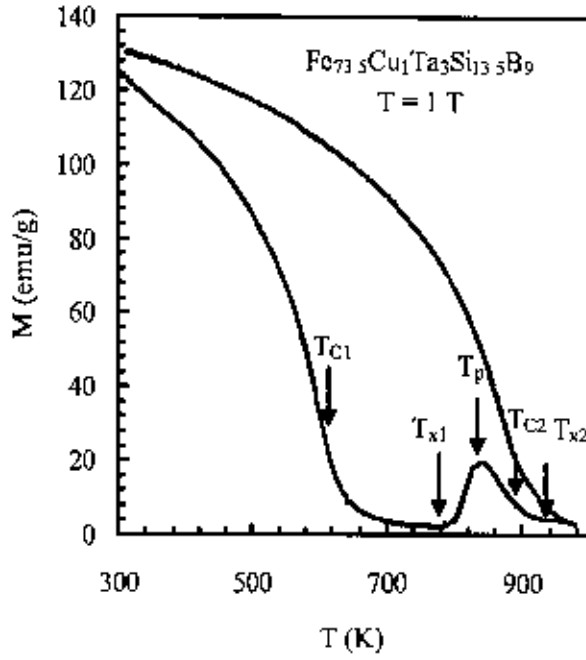


Fig. 4.2.13. Variation of saturation magnetization of  $\text{Fe}_{73.5}\text{Cu}_1\text{Ta}_3\text{Si}_{13.5}\text{B}_9$  alloy with temperature.

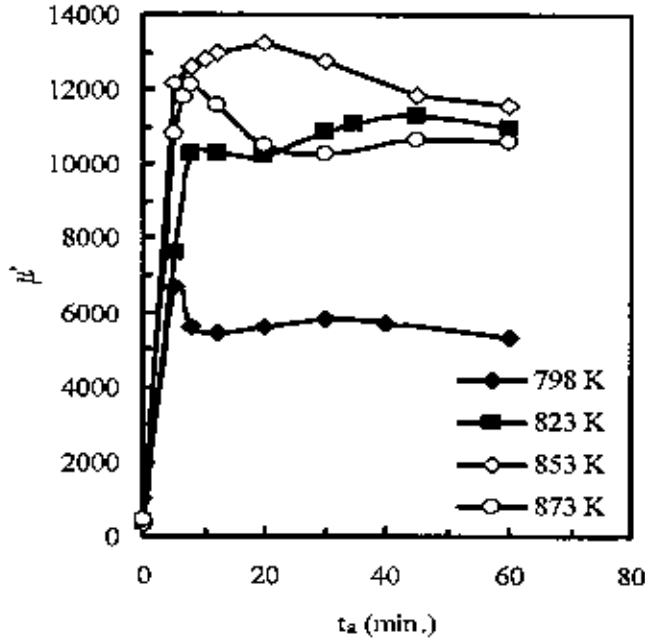


Fig. 4.2.14 Variation of  $\mu'$  with annealing time at different annealing temperature.

is related to the evolution of ferromagnetic  $\alpha$ -Fe(Si) phase formed in the paramagnetic amorphous matrix. The crystallization temperature corresponds well with the DTA measurements, which is around 783 K for the heating rate of 20 K/min. as observed from Fig. 4.1.1. The onset of crystallization has been observed at 773 K from X-ray diffraction. Magnetization passes through a maximum at the temperature of around 842 K. Magnetization again decreases with temperature to a very low value beyond the Curie temperature of Fe(Si) phase which is around 890 K. At a temperature about 932 K slight increase of magnetization is observed due to the crystallization of iron boride phase, which is compatible with the second peak of DTA curve at the heating rate of 20 K/min as presented in Fig. 4.1.1. Field cooled magnetization during cooling passes through a para-ferro magnetic transition at the Curie temperature of  $\alpha$ -Fe(Si) phase, which is around 896 K.

In Fig. 4.2.14, the value of  $\mu'$  has been presented as a function of cumulative annealing time for different annealing temperatures. For all the temperatures, the maximum value of  $\mu'$  is attained within 5-8 minutes. Further increase of annealing time lowers the value of  $\mu'$ . It has been demonstrated that when a sample is annealed for cumulative time, the effect of induced anisotropies become dominant and the permeability is significantly reduced [12].

#### 4.3 Structural and Magnetic Properties of $\text{Fe}_{75.5}\text{Cu}_{0.6}\text{Nb}_{2.4}\text{Si}_{13}\text{B}_{1.5}$

Phase transition and kinetics of crystallization of different crystalline phases has been studied by using differential scanning calorimetry. DSC curves of  $\text{Fe}_{75.5}\text{Cu}_{0.6}\text{Nb}_{2.4}\text{Si}_{13}\text{B}_{1.5}$  ribbons in the as-cast and annealed condition has been obtained by carrying out the measurement in nitrogen atmosphere with continuous heating rate of 20 K/min and presented in Fig. 4.3.1. Curves presented in the figure shows exothermic peaks in which the first one represents the formation of  $\alpha$ -Fe(Si) phase and the second peak represents the formation of iron boride. Leu and Chin [17] pointed out the use of the DTA apparatus for estimating the crystallization fraction  $\chi_t = \frac{\Delta H_a - \Delta H_t}{\Delta H_a}$ , where,  $\Delta H_a$  and  $\Delta H_t$  are the crystallization

enthalpy of the as-cast alloy and of the alloy annealed for a time  $t$ , respectively. Thus, the volume fraction of  $\alpha$ -Fe(Si) phase was determined using above equation considering first peak of DSC curves at different annealing temperature and presented in Table 4.3. This shows progressive increase of volume fraction of  $\alpha$ -Fe(Si) phase with the increase of annealing temperature. Activation energy of crystallization of  $\alpha$ -Fe(Si) phase is 2.9 eV and iron boride 3.7 eV obtained from Kissinger' plot [1] presented in Fig. 4.3.2 and 4.3.3. Activation energy of crystallization of different crystalline phases is much lower than the activation energy of crystallization for earlier compositions. Lower content of grain growth inhibiting element such as Nb might be the probable reason for lower activation energy of crystallization.

When the sample is annealed above the crystallization temperature nanocrystalline grain of  $\alpha$ -Fe(Si) is formed from amorphous precursor. The grain size determined by using the Scherrer's formula is presented

Table 4.3. Effect of annealing on structural and magnetic properties of  $\text{Fe}_{75}\text{Cu}_{0.6}\text{Nb}_{2.4}\text{Si}_{13}\text{B}_{8.5}$ .

Annealing temperature, $T_a$ (K)	Lattice parameter, $a$ (Å)	Silicon content (%Si)	Grain size (nm)	Volume fraction of $\alpha\text{-Fe}(\text{Si})$	Saturation magnetization, $M_s$ (emu / g)
as-cast	-	-	-	-	158
773	2.8472	12.616	10.574	0.665	163
793	2.8433	14.439	10.936	0.904	165
803	2.8425	14.812	11.771	0.971	164

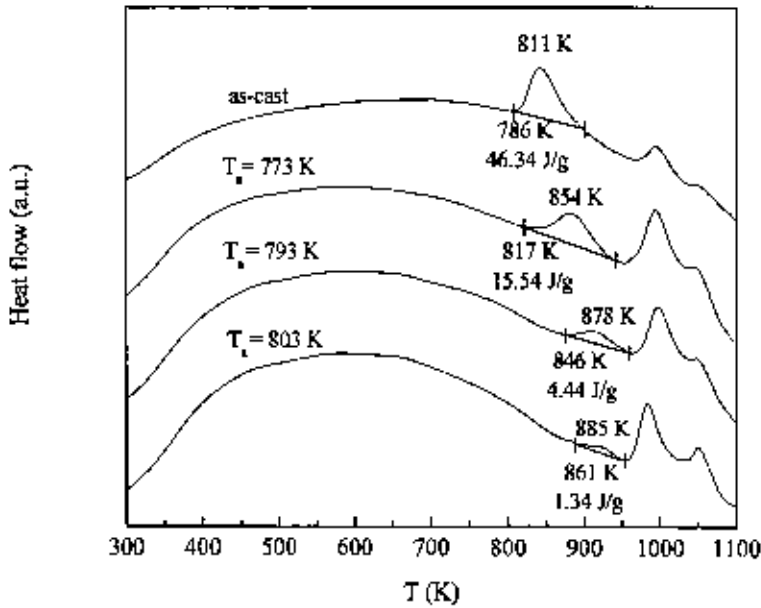


Fig. 4.3.1. DSC curves of as-cast and annealed samples at different heating rates of 20 K/min.

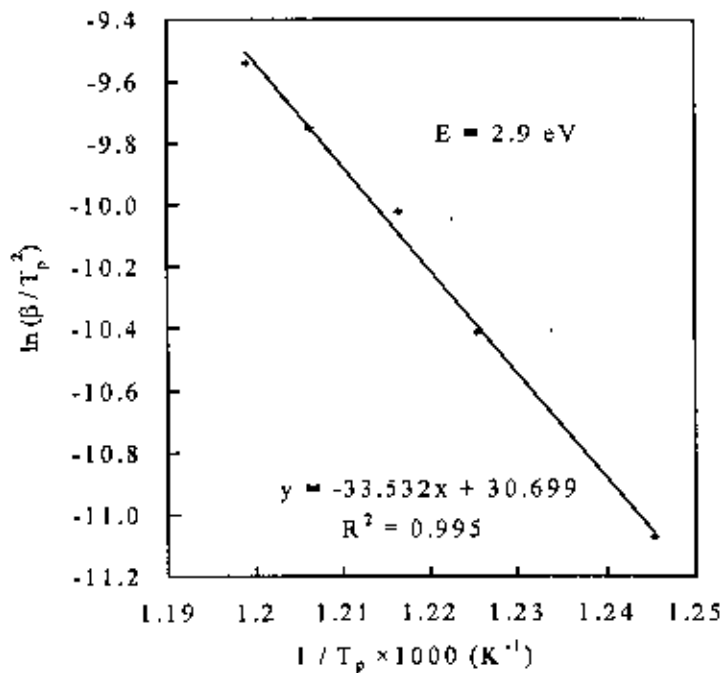


Fig. 4.3.2. Kissinger plot for the determination of activation energy of crystallization of  $\alpha\text{-Fe(Si)}$  phase.

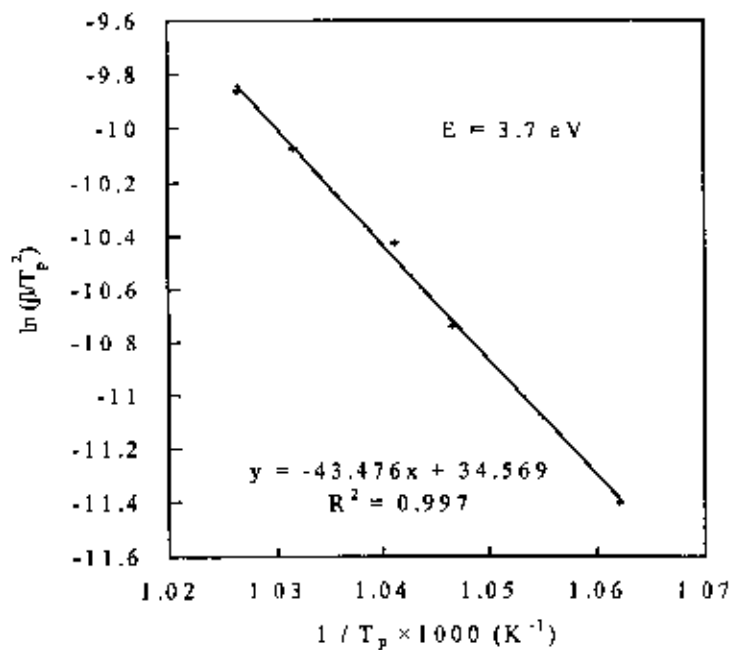


Fig. 4.3.3. Kissinger plot for the determination of activation energy of crystallization of iron boride phase.

in Table 4.3. The silicon content of  $\alpha$ -Fe(Si) nanograins have been determined from the established quantitative relationship [3] between lattice parameter and silicon content of  $\alpha$ -Fe(Si) and presented in Table 4.3. The lattice parameter of  $\alpha$ -Fe(Si) nanograins decreases with the increase of annealing temperature due to diffusion of Si into  $\alpha$ -Fe(Si) nanograins resulting in an increase of Si content. Grain size increases with the increase of annealing temperature of the order of 10-12 nm, which is very suitable for the exchange coupling through residual amorphous matrix [9]. The results correspond well to those of the previous results [17].

In Fig. 4.3.4, temperature dependence of real part of the initial permeability of the as-cast amorphous ribbon and the samples annealed at 698 – 748 K has been presented. For as-cast and samples annealed at 698 and 723 K, permeability passes through a maximum followed by a sharp fall with the manifestation of Hopkinson effect. However, for the sample annealed at 748 K sharpness of the fall is relatively smeared out. As described earlier, this is due to the loss of homogeneity of sample due to initiation of crystallization as observed in an earlier study [19]. Permeability is still much lower for this annealing temperature compared to the advanced crystalline stage presented later. The Curie temperature estimated from the curves presented in Fig. 4.3.4 for as-cast and annealed samples in the amorphous state has been presented in Table 4.4.

In Fig. 4.3.5, the variation of  $\mu'$  with temperature annealed at 773 – 853 K has been presented. When the annealing temperature is increased above the crystallization temperature, sharpness of the fall to lower values of permeability is progressively smeared out. These results are in good agreement with those previously reported for the Finemet composition [5]. Average Curie temperature of residual amorphous matrix, which is concentration wise inhomogeneous has been determined from the maximum value of  $\frac{d\mu'}{dt}$  curves and presented in Table 4.4. In Table 4.4, enhancement of Curie temperature compared to the

Curie temperature of as-cast sample occurs, when the sample is annealed in the temperature range of 698 – 748 K. From x-ray diffraction and DSC results it has been observed that no crystalline phase forms up to the annealing temperature of 748 K. Enhancement of Curie temperature occurs because of irreversible structural relaxation as mentioned above. Further, from the analysis of the Mössbauer spectra for the quenched and annealed samples below the crystallization temperature it has been observed that this treatment leads to the increase of packing density of atoms [16]. Increase of packing density of atoms might have significant contribution to the enhancement of Curie temperature in the amorphous state. Above the crystallization temperature, average Curie temperature of the inhomogeneous amorphous matrix decreases significantly. The probable reason of decreasing the average Curie temperature of the inhomogeneous residual amorphous phase when annealed at and above the crystallization temperature is that the amorphous matrix is depleted with iron and the relative amount of Nb in the amorphous matrix increases, which weakens the exchange interaction resulting in a decrease of Curie temperature of the amorphous matrix [9].

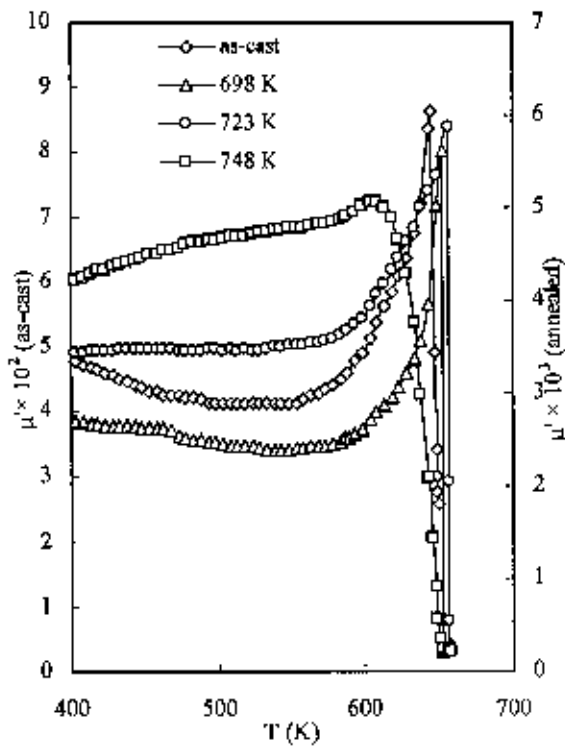


Fig. 4.3.4 Variation of initial permeability,  $\mu'$  with temperature for samples with different annealing temperatures in the amorphous state of the material.

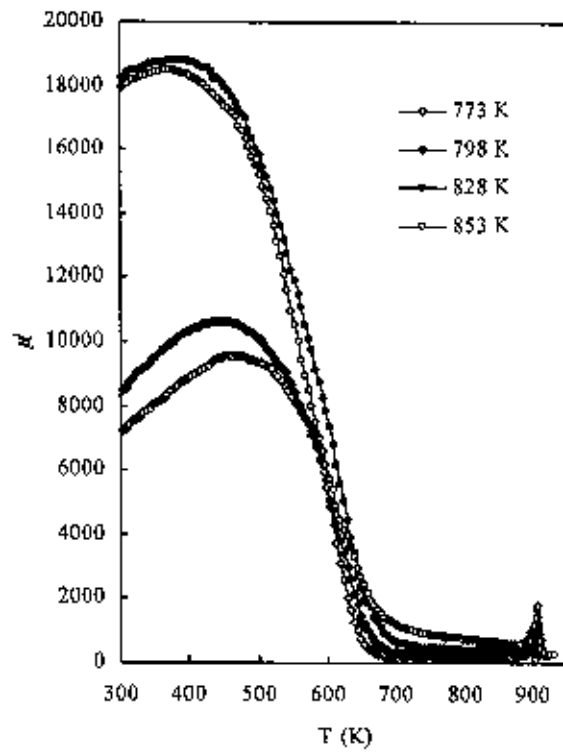


Fig. 4.3.5. Variation of initial permeability,  $\mu'$  with temperature for samples with different annealing temperatures in the nanocrystalline state of the material.

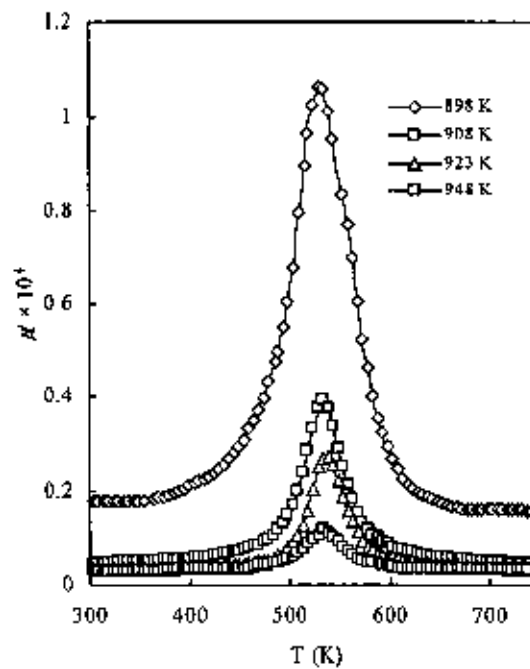


Fig. 4.3.6. Variation of initial permeability,  $\mu'$  with temperature for samples with different annealing temperatures after the evolution of iron boride phase



Table 4.4. Effect of annealing on the Curie temperature of amorphous phase of  $Fe_{73.5}Cu_{0.6}Nb_{2.4}Si_{13}B_{8.5}$ .

Crystalline state	Annealing temperature, $T_a$ (K)	Curie Temperature of amorphous phase, $T_c^{am}$ (K)
Amorphous state	as-cast	644
	698	651
	723	657
	748	650
Nanocrystalline state	773	613
	798	598
	828	578
	853	543

At higher measuring temperatures above  $T_c^{ani}$  in Fig. 4.3.5, initial permeability drops to a very low value. However the value of initial permeability in this region increases with the increase of annealing temperature. This is the region where superparamagnetic and/or superferromagnetic behavior is observed depending upon size and volumetric fraction of crystalline phases and separation between the crystallites as has been reported earlier [5, 6]. The practical requisite for observing superparamagnetic relaxation in the nanocrystalline alloys is the absence of exchange interactions between nanograins in the residual amorphous matrix. Presence of superparamagnetic behavior has to be confirmed by fitting magnetization as a function of  $\frac{M_s H}{T}$  curves to a Langevin function. These measurements are beyond the scope of present study.

For the sample annealed around 773 K where initiation of crystallization takes place as observed from DSC measurements in Fig. 4.3.1, exchange interaction between the nanograins mainly occurs via sufficiently thick interfacial amorphous matrix in which the nanocrystallites are dispersed. When the measuring temperature approaches the Curie temperature of the intergranular amorphous phase, which is much lower than that of  $\alpha$ -Fe(Si) nanograins ( $T_c > 873$  K), the exchange coupling between the crystallites is largely reduced. As a consequence the initial permeability drops down to a very low value.

For higher annealing temperature in Fig. 4.3.5, when  $T > T_c^{ani}$ , the grain coupling is largely but not completely interrupted above  $T_c^{ani}$  and still persists to higher value of permeability compared to the sample annealed at 773 K exhibiting the magnetic coupling between particles is significant. As pointed out earlier, precise coupling mechanism may be explained in terms of exchange penetration through thin paramagnetic intergranular layer and / or dipolar interactions [9]. Fig. 4.3.5 reveals that the interaction between the nanograins is progressively increased as the volume fraction of the crystallites is increased with higher annealing temperature.

With further increase of measuring temperature a sharp increase in permeability is observed similar to previous compositions due to the decrease of the average anisotropy of the nanograins [8]. This temperature shifts to higher value from 898 K to 903 K as the annealing temperature increases from 773 K to 853 K i.e. with the increase of volume fraction of the crystallite, which may be attributed to the decrease of the thickness of the amorphous grain boundary favoring the interaction between the nanograins compatible with the previous observations [5] which is limited by the Curie temperature of the bcc Fe(Si) nanograins.

In Fig. 4.3.6, the variation of real part of initial permeability  $\mu'$  with temperature has been presented for samples annealed at 898, 908, 923 and 948 K. It has been found from DSC curves that this is the temperature range of the evolution of boride phase. Minor evolution of  $Fe_2B$  can cause significant damage to exchange interaction because at room temperature the anisotropy constant  $K_1$  of  $Fe_2B$  ( $430 \text{ kJ} / \text{m}^3$ ) is

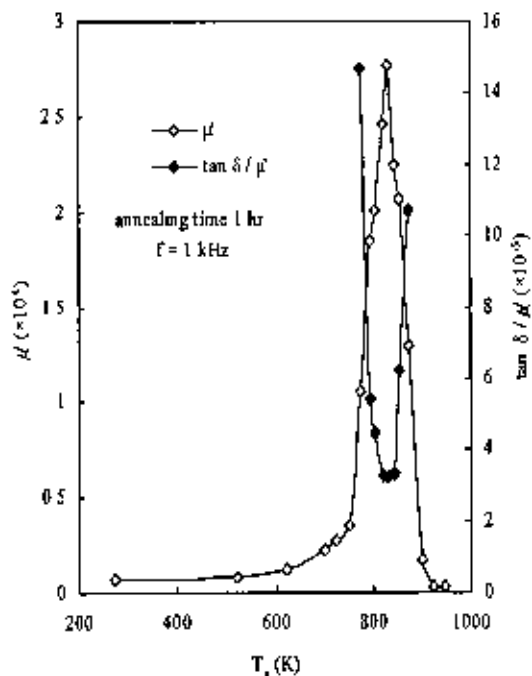


Fig. 4.3.7. Variation of initial permeability,  $\mu'$  and loss factor,  $\tan \delta / \mu'$  with annealing temperature at  $f = 1$  kHz.

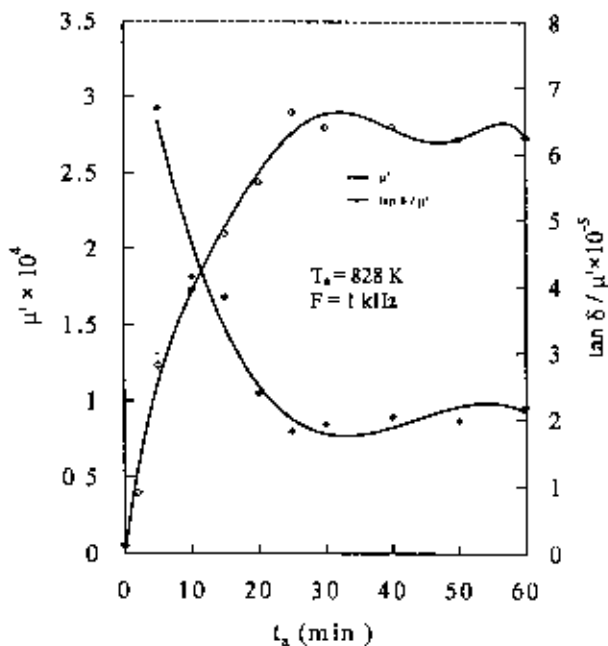


Fig. 4.3.8. Variation of initial permeability,  $\mu'$  and loss factor,  $\tan \delta / \mu'$  with annealing time for the annealing temperature of 828 K.

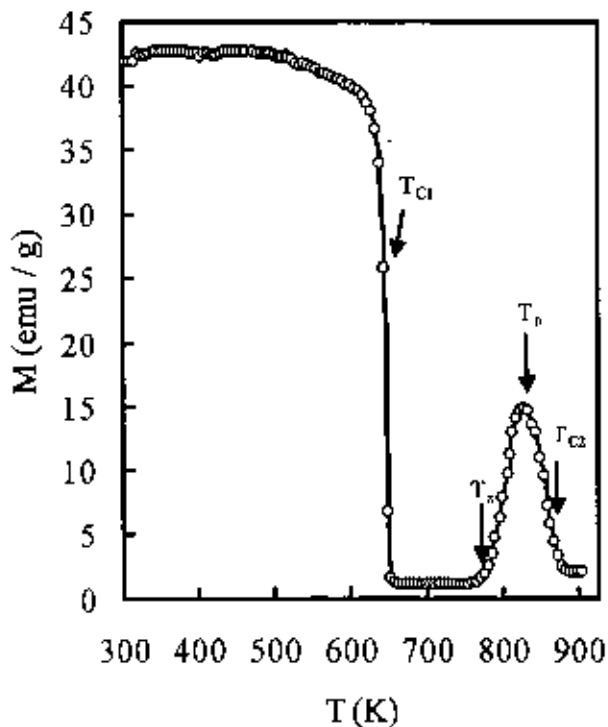


Fig. 4.3.9. Temperature dependence of magnetization,  $M$  of as-cast sample with an applied field of 20 Oe.

five order of magnitude higher than the average anisotropy  $\langle K \rangle$  of  $\alpha$ -Fe(Si) nanograins ( $4 \text{ J/m}^3$ ) [9]. The anisotropy constant  $K_1$  of  $\text{Fe}_2\text{B}$  passes from negative to positive value having  $K_1 = 0$  at 523 K. Therefore, in our study a steep rise of  $\mu'$  is observed around this temperature due to the zero anisotropy of iron boride phase when the sample has been annealed at 898 K [9]. However, for the samples annealed at 908, 923 and 948 K the increase of  $\mu'$  around 533 K is substantially reduced. The peak value of  $\mu'$  progressively decreases with increasing annealing temperature, probably due to the evolution of some complex phases.

Initial permeability,  $\mu'$  and relative loss factor,  $\frac{\tan \delta}{\mu'}$  has been presented as a function of annealing

temperature  $T_a$  at a fixed frequency of 1 kHz and presented in Fig. 4.3.7. When annealed at temperatures below the onset of crystallization i.e. 748 K, an increase of initial permeability with annealing temperature was observed due to irreversible structural relaxation of the amorphous matrix i.e. stress relief, increase of packing density by annealing out micro-voids and changing the degree of chemical disorder. Further increase of annealing temperature leads to a sharp increase of permeability due to crystallization of  $\alpha$ -Fe(Si) phase and increased volume fraction of nanograins coupled via exchange interaction resulting in a reduction of anisotropy energy. An enhancement of initial permeability by two orders of magnitude was observed for the annealing temperature of 843 K. The relative loss factor  $\frac{\tan \delta}{\mu'}$  decreases up to an order

of  $10^{-5}$  at this temperature. Beyond this temperature  $\mu'$  drops to lower value drastically and  $\frac{\tan \delta}{\mu'}$

increases. Evolution of boride phase leads to the increase of anisotropy to a high value that essentially reduces the local exchange correlation length weakening the intergranular magnetic coupling as a result of which magnetic hardening takes place [9].

The increase of initial permeability,  $\mu'$  and loss factor,  $\frac{\tan \delta}{\mu'}$  measured at room temperature as a function

of cumulative annealing time has been presented in Fig. 4.3.8, for the annealing temperature of 828 K at 1 kHz. The value of  $\mu'$  increases monotonically up to 25 min attaining a maximum value while  $\frac{\tan \delta}{\mu'}$

decreases to an order of  $\sim 10^{-5}$ . Upon further increase of annealing time the value of  $\mu'$  and  $\frac{\tan \delta}{\mu'}$  does not

vary significantly maintaining a plateau value. Long time annealing has the effect of induced anisotropy, which reduces the value of  $\mu'$  to some extent [12].

Temperature dependence of magnetization,  $M$ , is presented in Fig. 4.3.9, which has been measured with an applied field of 20 Oe at a heating rate of 20 K/min. The characteristic feature of the curve is that  $M$  decreases with temperature and passes through ferro-paramagnetic transition at Curie temperature  $T_c = 643 \text{ K}$  and have coincided with  $T_c = 644 \text{ K}$  measured from  $\mu'$  vs.  $T$  curve. Onset of crystallization temperature of  $\alpha$ -Fe(Si) takes place at  $T_s = 774 \text{ K}$ . Magnetization passes through a maximum at the

temperature of around 833 K and then decreases with temperature to a very low value beyond the Curie temperature of  $\alpha$ -Fe(Si) phase of around 878 K.

Saturation magnetization has been measured for as-cast and samples annealed at 773, 793 and 803 K with a maximum field of about 13.5 kOe and presented in Table 1. In the as-cast condition the value of saturation magnetization,  $M_s$ , is about 158 emu / g (1.47 Tesla), which increases to 165 emu / g (1.53 Tesla) with the increase of annealing temperature and then decreases slightly at  $T_a = 803$  K as shown in Table 1. The increase in  $M_s$  can be attributed to the irreversible structural relaxation and varying degree of chemical disorder [14]. In our experiment, higher value of  $M_s$  than conventional FINEMET composition is possibly due to increased amount of Fe content in our composition. Butvino et. al. [20] have reported induction as 1.47 Tesla to 1.10 Tesla of FeCuNbSiB alloys in the as-cast condition with the variation of relative amount of constituent elements at 7.5Oe (600 A/m).

## **Chapter 5**

***Results and Discussions on Co-based soft  
nanocomposites***

### 5.1 Structural and Magnetic Properties of $\text{Co}_{69}\text{Fe}_4\text{Ni}_1\text{Si}_{15}\text{B}_{12}$

Kinetics of crystallization of  $\text{Co}_{69}\text{Fe}_4\text{Ni}_1\text{Si}_{15}\text{B}_{12}$  has been studied by differential scanning calorimetry (DSC) in nitrogen atmosphere with continuous heating rate of 10-50 K/min. DSC curves presented in Fig. 5.1.1 shows exothermic peaks, which represent the formation of crystalline phases. For the heating rate of 10 K/min, the initiation of crystallization is around 813 K and the process of crystallization is completed at 833 K while the peak temperature is 821 K. This indicates that no crystalline phase is formed below 813 K and the crystallization process is completed within a narrow range of temperature. For higher heating rates the phase transition temperatures shift towards the higher values. The activation energy of crystallization presented in Fig. 5.1.2 is 4.29 eV.

X-ray diffraction patterns of as-cast and sample annealed at 693 K for 1 hr. have been observed and presented in Fig. 5.1.3. X-ray diffraction patterns of both as-cast and annealed samples presented in Fig. 5.1.3 show that the samples are in the amorphous state with broad diffused patterns. This corresponds well with the DSC diagrams, which shows that there is no crystallization at 693 K.

Fig. 5.1.4 shows the temperature dependence of magnetization measured with an applied field of 20 Oe and heating rate of 10 K/min. The characteristic feature of the curve is that magnetization decreases with temperature and passes through magnetic phase transition at the Curie temperature. The Curie temperature has been estimated to be 503 K from the maxima of the rate of change of magnetization with temperature.

In Fig. 5.1.5, the real part of the complex initial permeability  $\mu'$  up to  $f = 10$  MHz has been presented for as-cast and annealed samples. The results refer to isothermal annealing time of 60 min. The magnetic properties of the soft magnetic materials are mainly determined by the domain wall mobility especially in the range of reversible magnetization. The measurement of permeability was performed with toroidal shaped samples at room temperature with an ac field of amplitude  $10^{-3}$  Oe. The value of initial permeability at 1 kHz for the toroids increase with the increase of annealing temperature up to 693 K. The stability of  $\mu'$  with frequency is better for the samples, which possess lower value of permeability. The samples, which possess high value of  $\mu'$  are applicable only at low frequency. The losses indicated by the  $\mu''$  curves are maximum at the frequency at which  $\mu'$  has fallen to half the value of the value of  $\mu'$  of  $f = 1$  kHz. The  $\mu''$  curve is very asymmetrical with a large tail towards the high frequencies.

In Fig. 5.1.6, annealing temperature dependence of real part permeability,  $\mu'$  and relative loss factor  $\frac{\tan \delta}{\mu'}$  have been presented for the frequency of 1 kHz. The initial permeability value increases gradually with annealing temperature up to 573 K, beyond which  $\mu'$  increases abruptly up to the annealing temperature of 693 K and attains a maximum value of  $63 \times 10^3$ . At this annealing temperature the value of relative loss factor  $\frac{\tan \delta}{\mu'}$  is the lowest of the order of  $10^{-6}$ . Beyond the annealing temperature of 693 K,

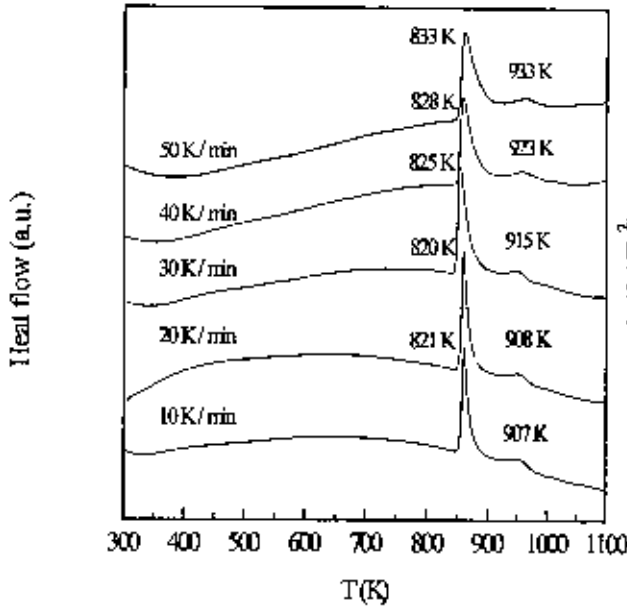


Fig. 5.1.1. DSC traces of as-cast sample of  $\text{Co}_{68}\text{Fe}_4\text{Ni}_1\text{Si}_{15}\text{B}_{12}$  for different heating rate.

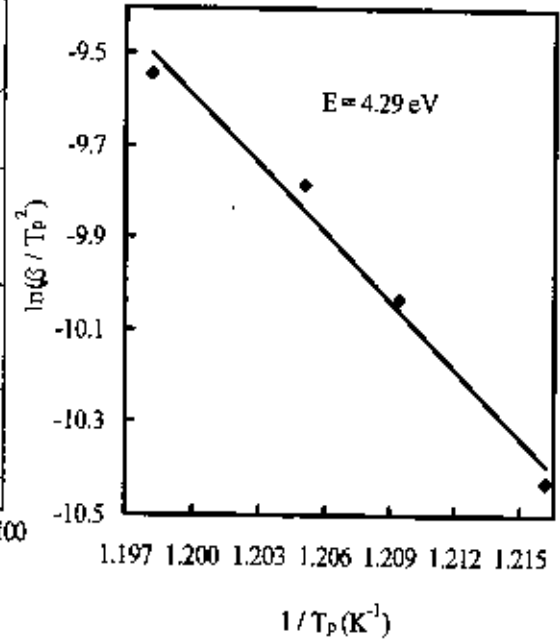


Fig. 5.1.2. Kissinger's plot for the determination of activation energy of crystallization.

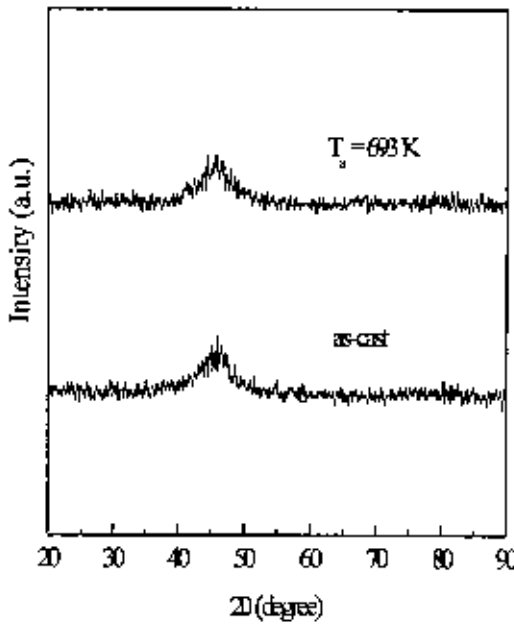


Fig. 5.1.3. X-ray diffraction patterns of as-cast and sample annealed at 693 K for 1 hr.

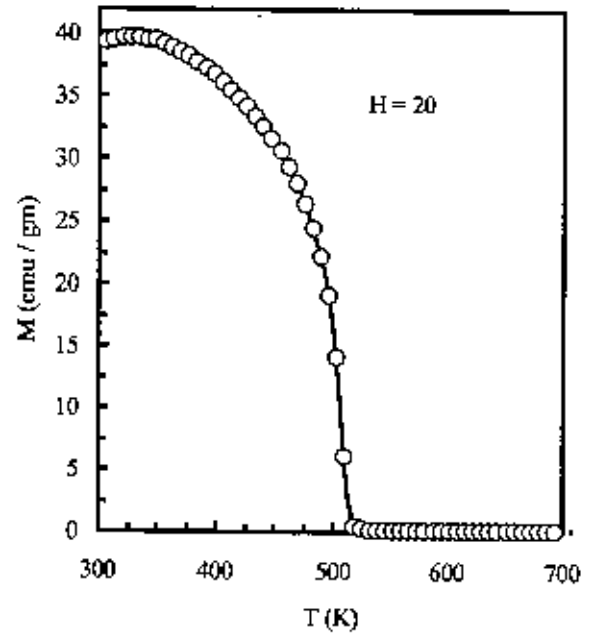


Fig. 5.1.4. Temperature dependence of magnetization with the applied field of 20 Oe and heating rate of 10 K/min.



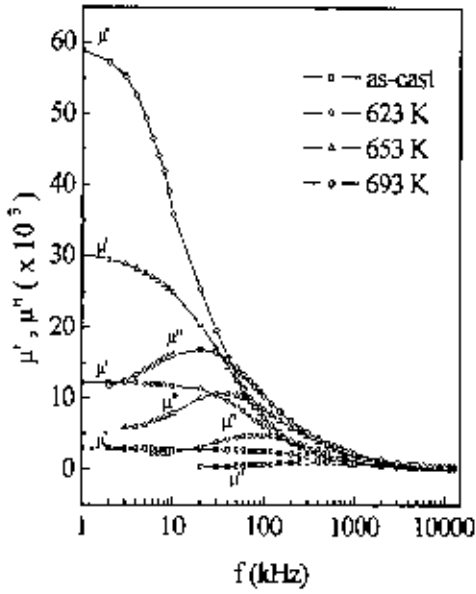


Fig. 5.1.5 Variation of real ( $\mu'$ ) and imaginary ( $\mu''$ ) part of initial permeability of as-cast and annealed samples.

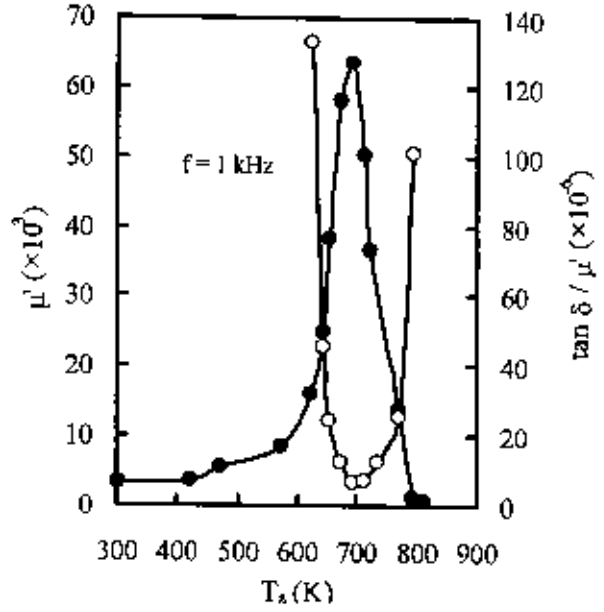


Fig. 5.1.6. Variation of initial permeability,  $\mu'$  (solid symbol) and relative loss factor  $\tan \delta / \mu'$  (open symbol) with annealing temperature,  $T_a$ .

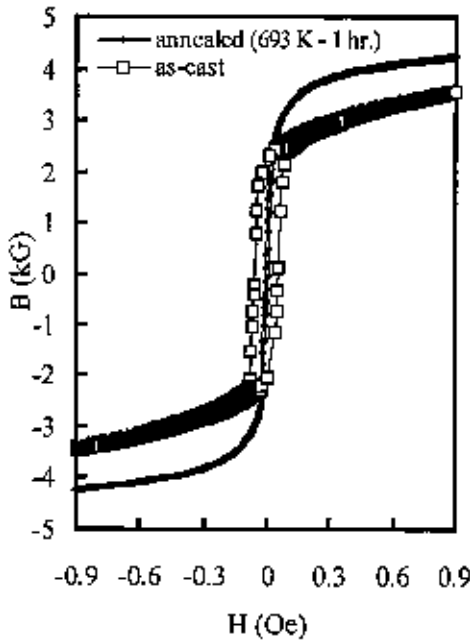


Fig. 5.1.7. Hysteresis loop of as-cast and sample annealed at 693 K for 1 hr.

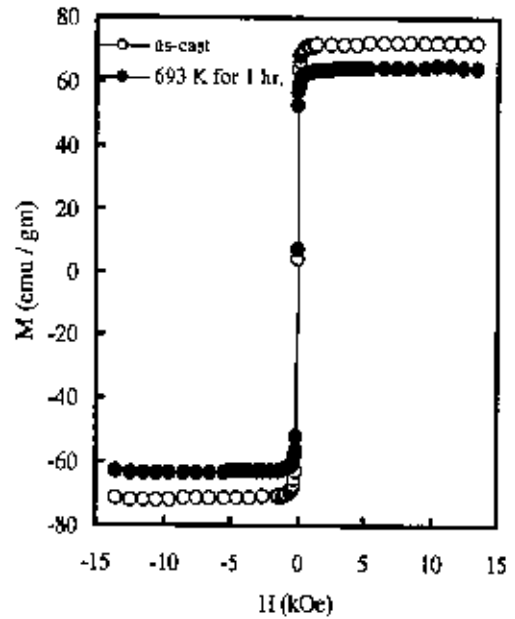


Fig. 5.1.8. M-H curves of as-cast and sample annealed at 693 K for 1 hr.

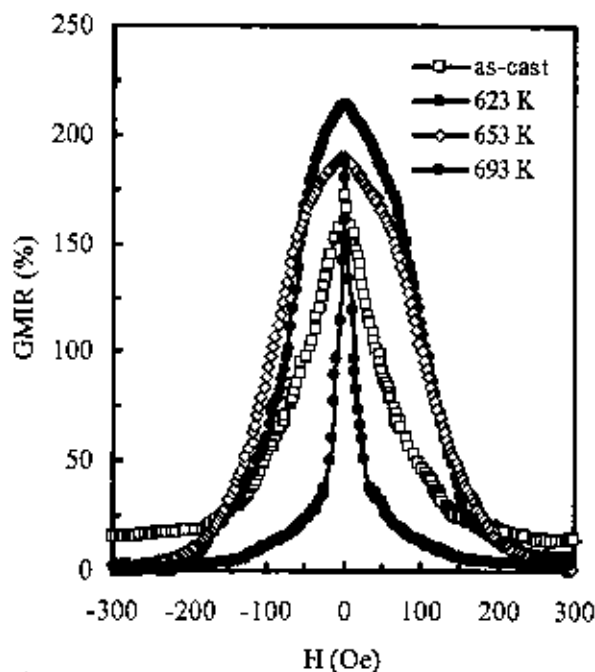


Fig. 5.1.9 (a). Field dependence of GMIR for as-cast and annealed samples.

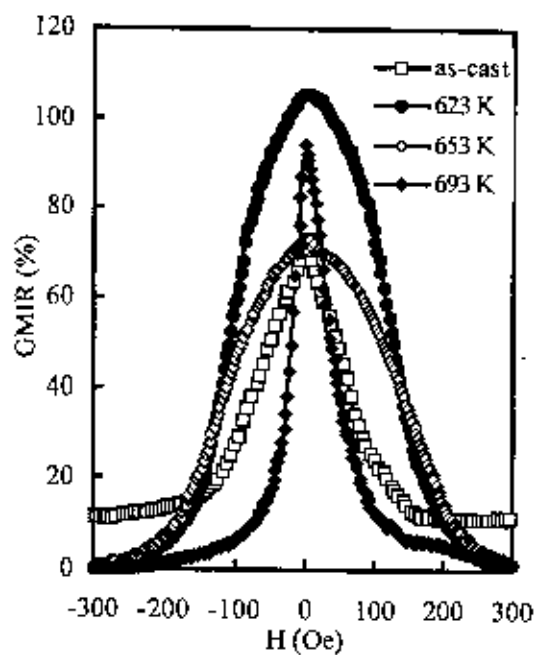


Fig. 5.1.9 (b). Field dependence of GMIR of as-cast and annealed samples at 6 MHz.

Table 5.1.  $(GMIR)_{max}$  and sensitivity of field dependence of GMIR for different annealing conditions.

Frequency (MHz)	annealing temperature (K)	$(GMIR)_{max}$ (%)	$\frac{d(GMIR)}{dH}$ (up to 30Oe) (%/Oe)
4.5	as-cast	172	1.712
	623 K	213	0.501
	653 K	186	0.504
	693 K	186	4.376
6.0	as-cast	73	0.511
	623 K	106	0.131
	653 K	73	0.122
	693 K	94	1.207

$\mu'$  decreases rapidly in association with an abrupt increase of relative loss factor. Extraordinary increase in  $\mu'$  at this annealing temperature is due to structural relaxation by relieving internal stress.

The nature of hysteresis loop of as-cast and annealed sample has been analyzed for the frequency of 0.2 Hz and presented in Fig. 5.1.7. The sample has been annealed at 693 K for 1 hr. at which highest  $\mu'$  has been obtained. Hysteresis loop of annealed sample exhibits extraordinary low coercivity compared to as-cast sample. The coercivity of the as-cast sample is 0.051 Oe and annealed sample 0.01 Oe.

In order to determine  $M_s$  for the as-cast and samples annealed at 693 K for 1 hr., field dependence of magnetization has been measured up to  $H = 13.5$  kOe and presented in Fig. 5.1.8. For as-cast and annealed sample the value of saturation magnetization is 72.3 emu / gm and 64.5 emu / gm respectively.

In Fig. 5.1.9(a) and 5.1.9(b), field dependence of magneto-impedance ratio (MIR) has been presented for as-cast and annealed samples at 623, 653, and 693 K for 1 hr at the frequency of 4.5 and 6 MHz. The sample dimension has been chosen as, length = 5 mm and width = 0.3 mm. The magneto-impedance ratio

(MIR) is defined as  $MIR(\%) = 1 - \left| \frac{Z(H_{dc})}{Z(H_{max})} \right|$ , where  $H_{max}$  is the external dc magnetic field for obtaining

the saturation value of magneto-impedance. For the present work, the value of  $H_{max}$  is 300 Oe. The curves reveal strong field dependence of MIR for both as-cast and annealed samples. The parameters that characterize the GMI efficiency are the maximum value of GMIR and maximum field sensitivity expressed by the slope of the field dependence of magneto-impedance ratio according to ref. [1]. Maximum value of MIR and slope of the field dependence of MIR up to 30 Oe has been obtained for as-cast and annealed samples and presented in Table 5.1 for 4.5 and 6 MHz. For higher frequency of 6 MHz the peak values are lower for as-cast and annealed samples than for 4.5 MHz. At higher frequencies, eddy currents heavily damp domain wall movements and only magnetization rotation are responsible for magnetic permeability. This reduces the GMI effect substantially. In Table 5.1, maximum field sensitivity has been exhibited by the sample annealed at 693 K for 1 hr in both the cases. It is observed from Fig. 5.1.6 and 5.1.7 that the sample annealed at 693 K for 1 hr is extraordinarily soft in which maximum permeability and very low coercivity have been obtained. The higher sensitivity of field dependence of MIR originates from ultrasoft magnetic properties at this annealing temperature due mainly to the structural relaxation. The higher sensitivity of field dependence of MIR is a pre-requisite condition for extremely low field sensors, which allows a very sensitive detection of the magnetic field, especially around  $H \sim 0$ .

## 5.2 Structural and Magnetic Properties of $Co_{63}Fe_4Ni_2Si_{15}B_{12}$

DSC curves presented in Fig. 5.2.1 shows exothermic peaks, which represent the formation of crystalline phases. For the heating rate of 10 K/min, the initiation of crystallization is around 808 K and the process of crystallization is completed at 843 K while the peak temperature is 815 K. This indicates that no

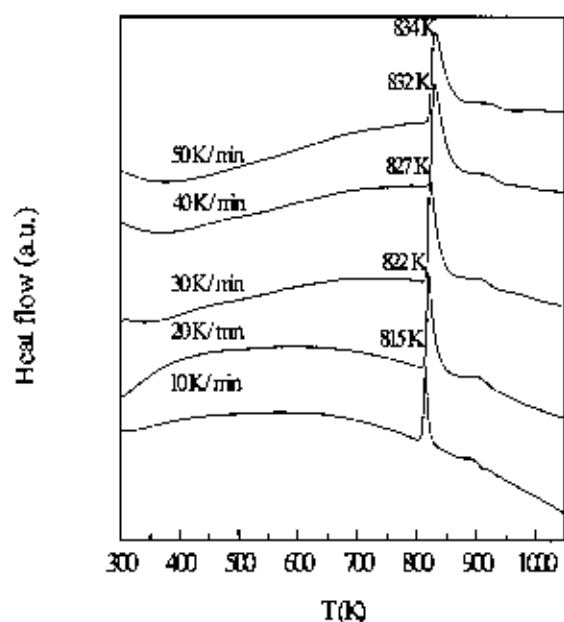


Fig. 5.2.1. DSC traces of as-cast sample of  $\text{Co}_{67}\text{Fe}_4\text{Ni}_2\text{Si}_{15}\text{B}_{12}$  for different heating rates.

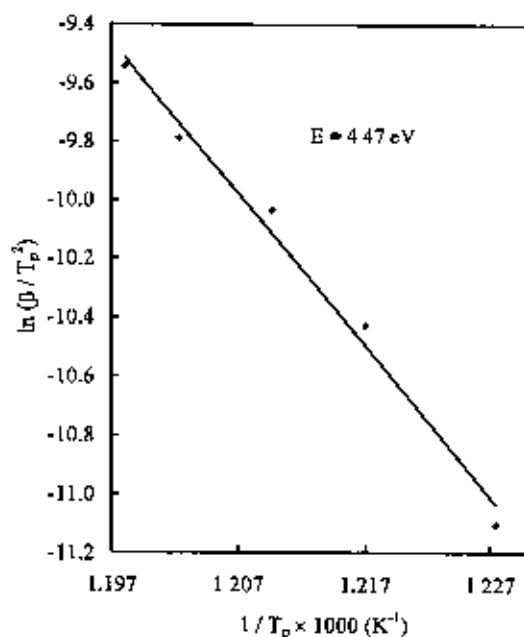


Fig. 5.2.2. Kissinger's plot for the determination of activation energy of crystallization.

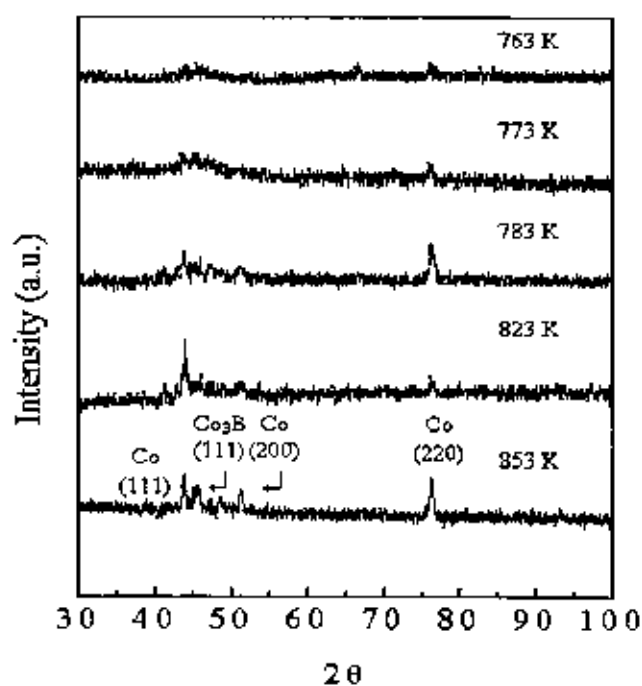


Fig. 5.2.3. XRD patterns of as-cast and annealed sample of  $\text{Co}_{67}\text{Fe}_4\text{Ni}_2\text{Si}_{15}\text{B}_{12}$ .

crystalline phase is formed below 808 K and the crystallization process is completed within a narrow range of temperature. For higher heating rates the phase transition temperature shift towards the higher values. Activation energy of crystallization found as 4.47 eV obtained by using Kissinger's plot presented in Fig. 5.2.2

In an attempt to identify crystalline phases, X-ray diffraction studies has been performed for samples annealed at different temperatures and X-ray diffraction patterns are presented in Fig. 5.2.3 For the annealing temperature of 853 K where the crystallization is in the advanced stage, the phases are identified by using standard software. The phases are fcc-Co and  $\text{Co}_3\text{B}$ . Similar phases have been identified in ref. [2] by using TEM. Nucleation of these crystalline phases have been initiated at much lower temperature and for the annealing temperature of 763 K some of the similar phases just appeared with very small grain size of about 2 nm which has been determined by TEM in ref. [3] under similar condition of annealing.

Fig. 5.2.4 shows the temperature dependence of magnetization measured with an applied field of 20 Oe and heating rate of 10 K/min. Magnetization decreases with temperature and passes through magnetic phase transition at the Curie temperature. The Curie temperature has been estimated to be 545 K from the maxima of the rate of change of magnetization with temperature.

In Fig. 5.2.5, the real part of the complex initial permeability  $\mu'$  up to  $f = 10$  MHz has been presented for as-cast and annealed samples. The results refer to isothermal annealing time of 30 min. The magnetic properties of the soft magnetic materials are mainly determined by the domain wall mobility especially in the range of reversible magnetization. The measurement of permeability was performed with toroidal shaped samples at room temperature with an ac field of amplitude  $10^{-3}$  Oe. The value of initial permeability at 1 kHz for the toroids increases with the increase of annealing temperature. The stability of  $\mu'$  with frequency is better for the samples, which possess lower value of permeability. The losses indicated by the imaginary part of initial permeability,  $\mu''$  curves are maximum at the frequency at which  $\mu'$  has fallen to half the value of  $\mu'$  (at 1 kHz). The  $\mu''$  curve is asymmetrical with a large tail towards the high frequencies.

In Fig. 5.2.6, annealing temperature dependence of real part permeability,  $\mu'$  and relative loss factor  $\frac{\tan \delta}{\mu'}$  have been presented for the frequency of 1 kHz in order to demonstrate the evolution of magnetic

softness with annealing. The initial permeability value increases gradually with annealing temperature up to 673 K, beyond which  $\mu'$  increases abruptly up to the annealing temperature of 693 K and attains a maximum of  $36 \times 10^3$ . At this annealing temperature, relative loss factor  $\frac{\tan \delta}{\mu'}$  is of the order of  $10^{-6}$ .

The extraordinary increase in  $\mu'$  at this annealing temperature is due to the structural relaxation by relieving internal stresses. Beyond the annealing temperature of 693 K,  $\mu'$  decreases rapidly. At the annealing temperature of 723 K, permeability drops down to lower value. This might be the temperature

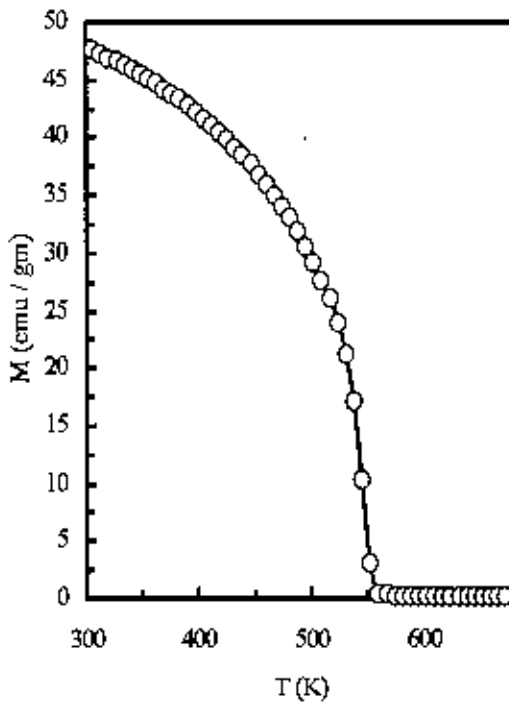


Fig. 5.2.4. Temperature dependence of magnetization of as-cast sample of  $\text{Co}_7\text{Fe}_4\text{Ni}_2\text{Si}_{15}\text{B}_{12}$  with a heating rate of 10 K/min.

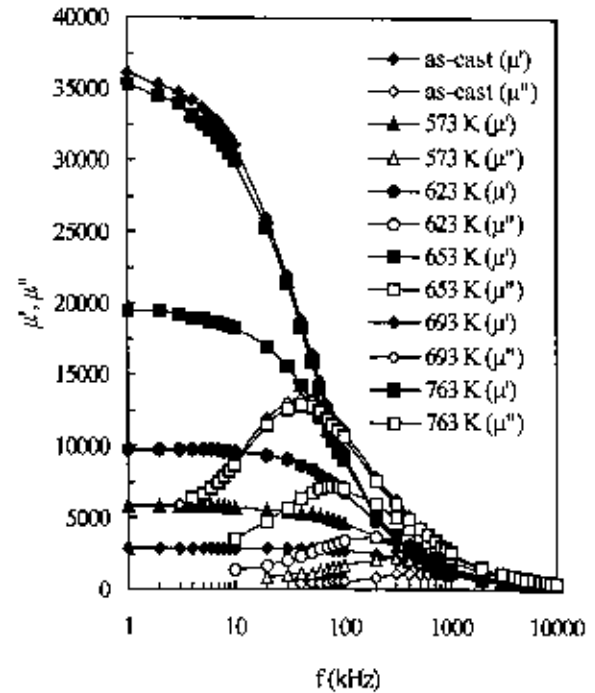


Fig. 5.2.5. Frequency dependence real and imaginary part of initial permeability ( $\mu'$ ,  $\mu''$ ) of as-cast and annealed sample of  $\text{Co}_7\text{Fe}_4\text{Ni}_2\text{Si}_{15}\text{B}_{12}$ .

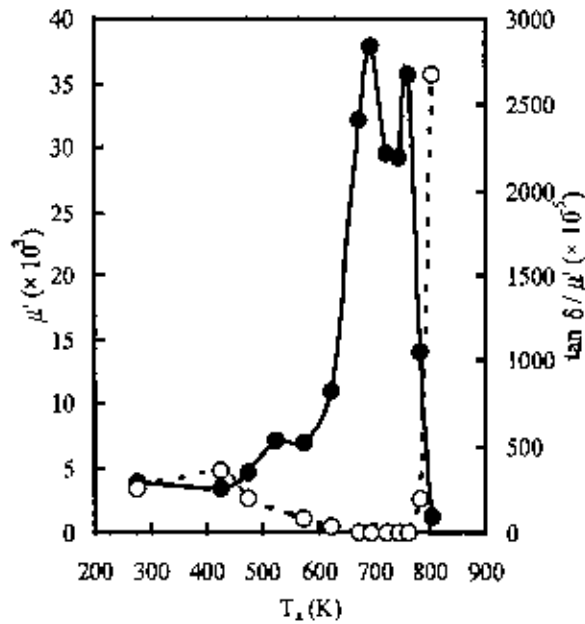


Fig. 5.2.6. Variation of real part initial permeability  $\mu'$  (solid symbol) and relative loss factor  $\tan \delta/\mu'$  (open symbol) with annealing temperature,  $T_a$ .

around which initiation of crystallization takes place. The decrease of permeability may be attributed to the stresses developed in the amorphous matrix by the growing crystallites [3]. This act as pinning centre for the domain wall mobility. The increase of  $\mu'$  at 763 K is associated with the formation of nanogram of the phases identified by X-ray diffraction in this study and correlated with the observation of TEM [3]. Buttino et. Al. [3] found that grains with 2 nm are embedded in a residual amorphous matrix under similar condition of annealing. For higher annealing temperature devitrification is completed with increasingly coarser microstructure as a result of which permeability decreases.

Nature of hysteresis loop of as-cast and annealed sample has been analyzed at room temperature for the frequency of 0.2 Hz and presented in Fig. 5.2.7. Sample has been annealed at 693 K for 30 min at which highest value of  $\mu'$  has been obtained. Hysteresis loop of annealed sample exhibits extraordinary low  $H_c$  compared to as-cast sample. The  $H_c$  of the as-cast sample is 0.134 Oe and annealed sample 0.017 Oe

In order to determine  $M_s$  for the as-cast and samples annealed at 693 K for 30 min, field dependence of magnetization has been measured at room temperature up to  $H = 13.5$  kOe and presented in Fig. 5.2.8. For as-cast and annealed samples the values of  $M_s$  are 74 emu / gm and 69 emu / gm respectively.

In Fig. 5.2.9(a) and 5.2.9(b), field dependence of magneto-impedance ratio (MIR) has been presented for as-cast and samples annealed at 573, 623 and 653 K for 30 min at the frequency of 4.5 and 6 MHz. The sample dimension has been chosen as, length = 5 mm and width = 0.3 mm. The magneto-impedance ratio

(MIR) is defined as  $MIR(\%) = 1 - \frac{|Z(H_{dc})|}{|Z(H_{max})|}$ , where  $H_{max}$  is the external dc magnetic field for obtaining

the saturation value of magneto-impedance. For the present work, the value of  $H_{max}$  is 300 Oe. The curves reveal strong field dependence of MIR for both as-cast and annealed samples. Maximum values of MIR for as-cast and annealed samples are presented in Table 5.2 for 4.5 and 6 MHz. It can be observed from Fig. 5.2.9 (a) and (b) and Table 5.2 that peak value of MIR is lower for the frequency of 6 MHz than for 4.5 MHz for all the as-cast and annealed samples. At higher frequencies eddy currents heavily damp domain wall movements and only magnetization rotation are responsible for magnetic permeability. This reduces the GMI effect substantially. Another aspect of GMI curves is hysteresis character in the peak. The GMI curve for this sample shows two-peaks located near the anisotropy field as has been observed in previous studies [4-6]. Hysteretic GMI appears on the field value to which the magnetic hysteresis takes place showing that it is correlated with the change of magnetization process [4]. When dc applied field is larger than anisotropy field it overcomes the domain wall pinning forces. Therefore, reversible rotational processes contribute to magnetization processes and to the reversible magneto-impedance behavior. When the dc applied field is smaller than the anisotropy field, magnetization process is governed by domain wall motion, which leads to the typical hysteresis of magnetization curve. GMI hysteretic behavior in Fig. 5.2.9 (a) and (b) is related to this change of magnetization process and seems to be connected to existence of irreversible domain wall displacement.

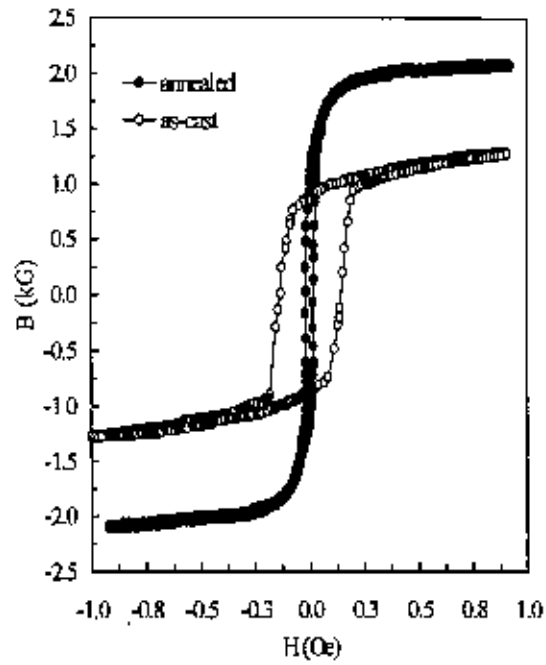


Fig 5.2.7. B-H loop of as-cast and sample annealed at 693 K for 30 minutes.

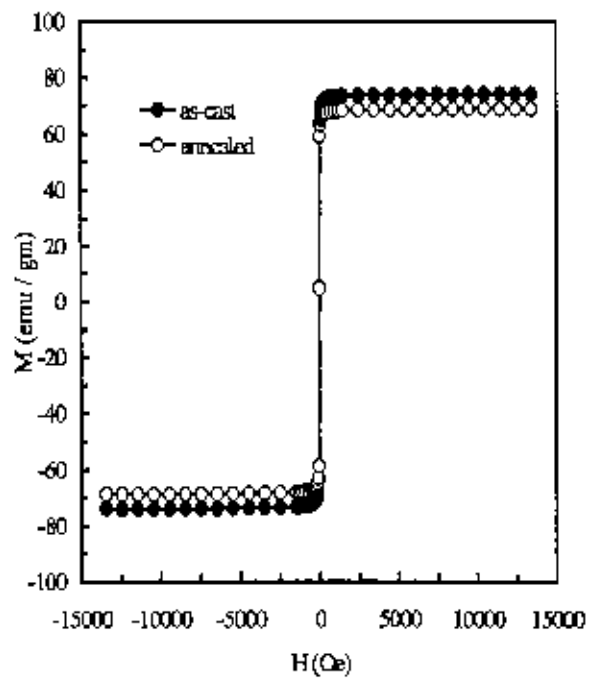


Fig. 5.2.8. M-H curve of as-cast and sample annealed at 693 K for 30 minutes.



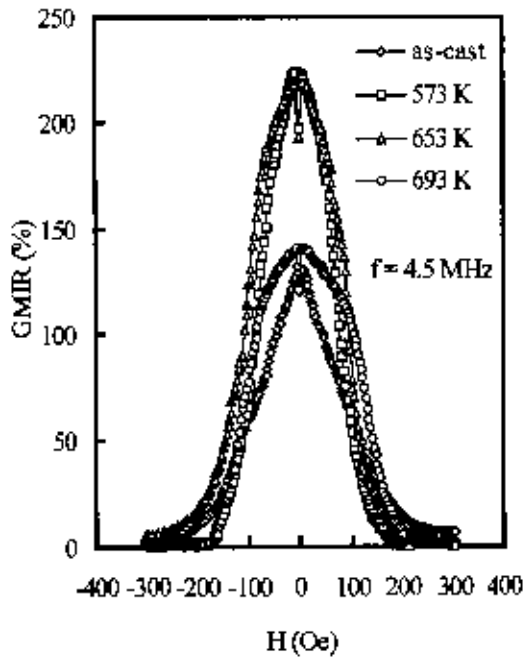


Fig. 5.2.9(a). Field dependence of GMIR(%) of as-cast and annealed sample at different temperatures for 30 minutes at 4.5 MHz.

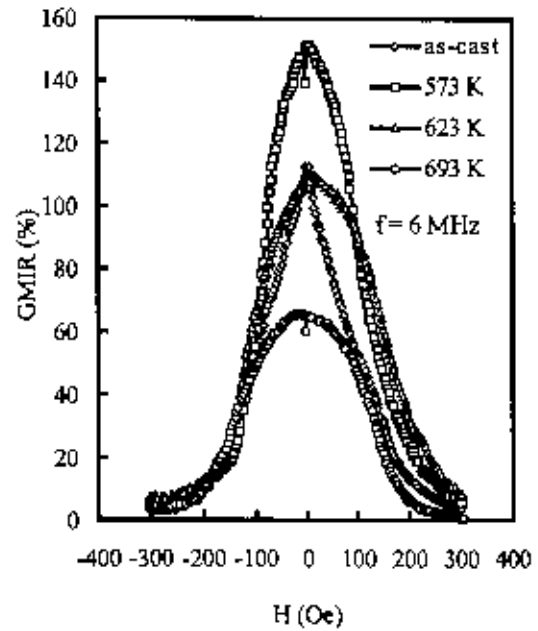


Fig. 5.2.9(b). Field dependence of GMIR(%) of as-cast and annealed sample at different temperatures for 30 minutes at 6 MHz.

Table 5.2.  $(MIR)_{max}$  for different annealing conditions at 4.5 and 6 MHz.

$f$ (MHz)	$T_a$ (K)	$(MIR)_{max}$ (%)
4.5	as-cast	132
	573 K	223
	623 K	217
	693 K	140
6.0	as-cast	112
	573 K	151
	623 K	109
	693 K	65

Hysteretic effect of field dependence magneto-impedance can be exploited as a practical tool to study induced anisotropics and magnetization process.

### 5.3 Structural and Magnetic Properties of $\text{Co}_{67}\text{Fe}_4\text{Mo}_7\text{Si}_{15}\text{B}_{12}$

DTA curves presented in Fig. 5.3.1 shows exothermic peaks, which represent the formation of crystalline phases. For the heating rate of 10 K/min, the initiation of crystallization is around 791 K, the peak temperature is 800 K and the process of crystallization is completed at 803 K. This indicates that the crystallization process is completed within a narrow range of temperature. For higher heating rates the phase transition temperature shift towards the higher values. Activation energy of crystallization has been found as 5.43 eV.

In an attempt to identify crystalline phases, x-ray diffraction study has been performed for samples annealed at different temperatures. X-ray diffraction patterns of the samples annealed at 773 and 823 K for 30 minutes are presented in Fig 5.3.2. For the annealing temperature of 823 K where the crystallization is in the advanced stage, the phases are identified by using standard software. The phases are fcc-Co and  $\text{Co}_2\text{B}$  as obtained by Betancourt et. al. [2] using TEM and electron diffraction studies. Nucleation of these crystalline phases have been initiated at much lower temperature and for the annealing temperature of 773 K some of the phases just appeared with very small grain size. As mentioned before for the previous composition, Buttno et. al. has determined the grain size of about 2 nm by using TEM [3] in the similar condition of heat treatment. Below the annealing temperature of 773 K the sample is in the amorphous state with broad diffused pattern, which is characteristic to the amorphous state of the material. In Fig. 5.3.3, the real part of the complex initial permeability  $\mu'$  up to  $f = 10$  MHz has been presented for as-cast and annealed samples. The results refer to isothermal annealing time of 30 min. The magnetic properties of the soft magnetic materials are mainly determined by the domain wall mobility especially in the range of reversible magnetization. The measurement of permeability was performed with toroidal shaped samples at room temperature with an ac field of  $\approx 10^3$  Oe. The value of initial permeability at 1 kHz for the toroids increase with the increase of annealing temperature up to 773 K. The stability of  $\mu'$  with frequency is better for the samples, which possess lower value of permeability. The losses indicated by the imaginary part of initial permeability,  $\mu''$  curves are maximum at the frequency at which  $\mu'$  has fallen to half the value of  $\mu'$  (at  $f = 1$  kHz). The  $\mu''$  curve is very asymmetrical with a large tail towards the high frequencies. The maxima of  $\mu''$  curve shift towards lower frequency for higher value of  $\mu'$  (at  $f = 1$  kHz).

In Fig. 5.3.4, annealing temperature dependence of real part permeability,  $\mu'$  and relative loss factor,  $\frac{\tan \delta}{\mu'}$  have been presented for  $f = 1$  kHz in order to demonstrate evolution of magnetic softness with annealing treatment. Initial permeability value increases gradually with annealing temperature up to 673K,

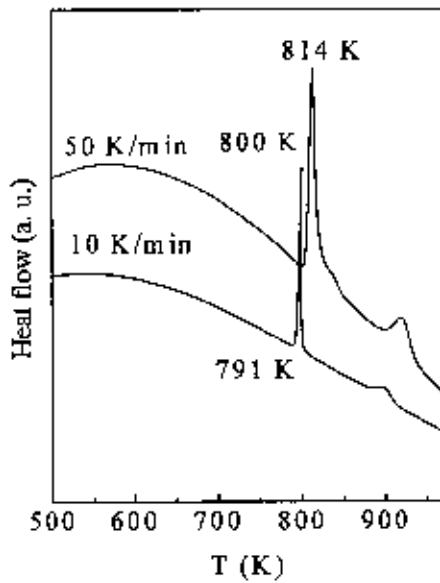


Fig. 5.3.1. DTA curves of  $\text{Co}_{67}\text{Fe}_4\text{Mo}_2\text{Si}_{15}\text{B}_{12}$  in the as-cast condition for the heating rate 10 and 50 K/min.

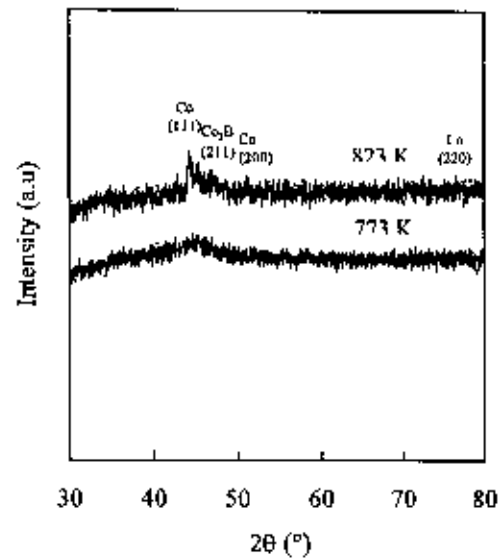


Fig. 5.3.2. X-ray diffraction patterns of  $\text{Co}_{67}\text{Fe}_4\text{Mo}_2\text{Si}_{15}\text{B}_{12}$  annealed at the initial stage of crystallization temperature 773 K and advanced stage of crystallization temperature 823 K.

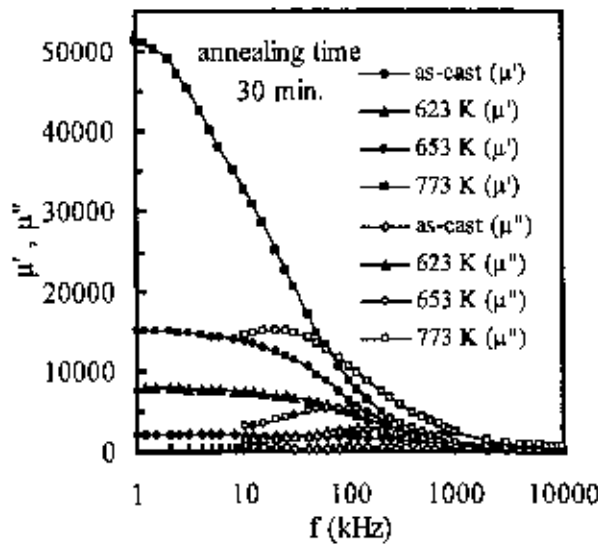


Fig. 5.3.3 Frequency spectrum of real and imaginary part of permeability ( $\mu'$ ,  $\mu''$ ) of  $\text{Co}_{67}\text{Fe}_4\text{Mo}_2\text{Si}_{15}\text{B}_{12}$  in the as-cast and annealed condition.

beyond which  $\mu'$  increases abruptly up to the annealing temperature of 753 K and attains a value of  $3.4 \times 10^3$ . The extraordinary increase in  $\mu'$  at this annealing temperature is due to the structural relaxation by relieving internal stresses. At the annealing temperature of 763 K, the permeability drops down to a lower value. This is the temperature around which initiation of crystallization takes place. The decrease of permeability may be attributed to the stresses developed in the amorphous matrix by the growing crystallites [3], which act as pinning centre for the domain wall mobility. For the annealing temperature of 773 K,  $\mu'$  attains a value of about  $5.1 \times 10^4$  while the relative loss factor,  $\tan \delta/\mu'$  decreases to a value of about  $9 \times 10^{-6}$ . The increase of  $\mu'$  and decrease of relative loss factor,  $\tan \delta/\mu'$  at 773 K is associated with the formation of nanograin of the phases identified by X-ray diffraction in this study. It has been correlated with the observation of TEM by Butino et. al. [3] where they have found grains with size 2 nm appears to be embedded in a residual amorphous matrix at the early stage of crystallization similar to the previous composition. This is also compatible with the phase transition temperature obtained from differential thermal analysis. Devitrification proceeds with increasingly coarser microstructure for higher annealing temperature as a result of which permeability decreases.

In Fig. 5.3.5, temperature dependence of permeability has been presented in the as-cast condition in order to determine Curie temperature of the sample. Shape of the curve is characterized by Hopkinson effect, which passes through a maximum just before a sharp fall. Curie temperature has been estimated as 540 K.

In Fig. 5.3.6, field dependence of magneto-impedance ratio (MIR) has been presented for as-cast and samples annealed at 573, 623, 653 and 693 K for 30 minutes at the frequency of 4.5 MHz. Sample dimension has been chosen as, length = 5mm and width = 0.3 mm. The curves reveal strong field dependence of MIR for both as-cast and annealed samples. Magneto-impedance ratio is maximum for the annealing temperature of 653 K. For higher annealing temperature of 693 K maximum value of magneto-impedance ratio decreases to a very low value. Changes in the pre-existing anisotropy direction due to rearrangement of atom pairs [3] reduced the GMI effect substantially. Another aspect of GMI curves is hysteresis character in the peak. The GMI curve for this sample shows two symmetrical peaks located near the anisotropy field as has been observed in previous studies [4-7]. It has been reported in the previous studies that the hysteretic GMI appears on the field value to which the magnetic hysteresis takes place showing that it is correlated with the change of magnetization process. When dc applied field is larger than anisotropy field it overcomes the domain wall pinning forces. Therefore, reversible rotational processes contribute to magnetization processes and to the reversible magneto-impedance behavior. When the dc applied field is smaller than the anisotropy field magnetization process is also governed by domain wall motion, which leads to the typical hysteresis of magnetization curve. The GMI hysteretic behavior observed in Fig. 5.3.6 is related to this change of the magnetization process and seems to be connected to the existence of irreversible domain wall displacement.

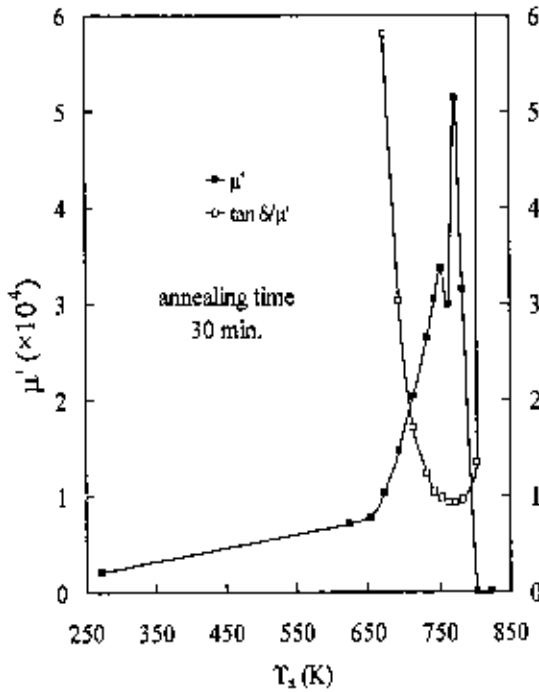


Fig. 5.3.4. Annealing temperature dependence of initial permeability ( $\mu'$ ) and relative loss factor ( $\tan \delta / \mu'$ ) of  $\text{Co}_{67}\text{Fe}_4\text{Mo}_2\text{Si}_{15}\text{B}_{12}$ .

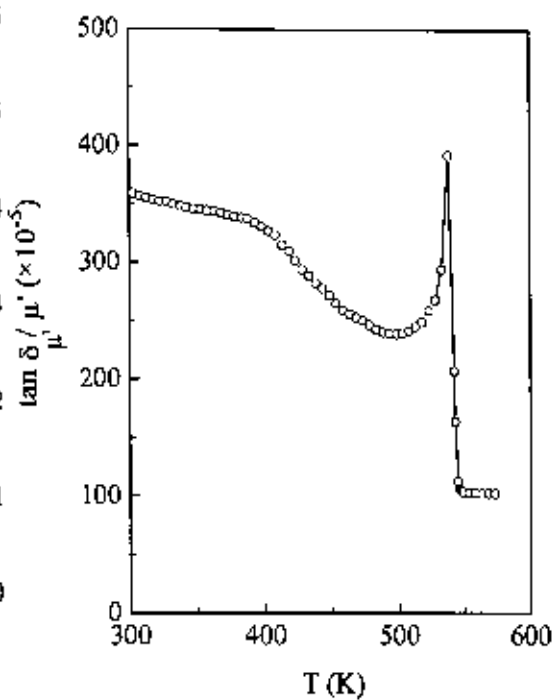


Fig. 5.3.5. Variation of initial permeability,  $\mu'$  with temperature in the as-cast condition.

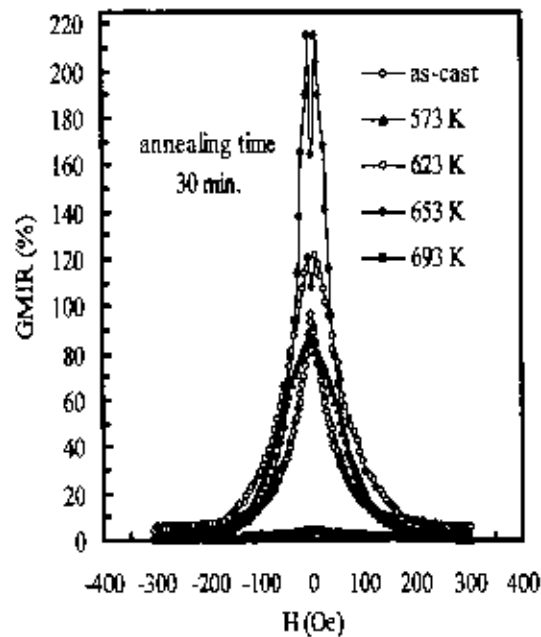


Fig. 5.3.6. Field dependence of magneto-impedance ratio of as-cast and annealed samples of  $\text{Co}_{67}\text{Fe}_4\text{Mo}_2\text{Si}_{15}\text{B}_{12}$ .

## **Chapter 6**

**Results and Discussions on Fe-based  
hard nanocomposites**

### 6.1 Structural and Magnetic Properties of $(\text{NdPr})_4\text{Fe}_{71}\text{Co}_5\text{Cu}_{0.5}\text{Nb}_1\text{B}_{18.5}$

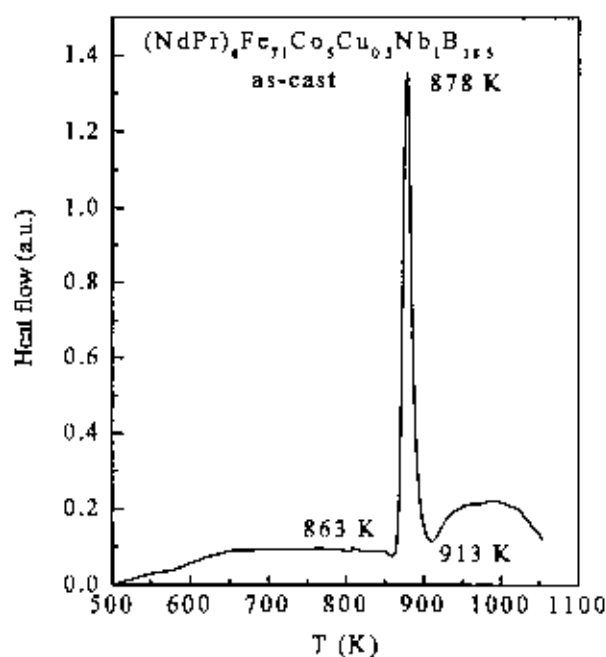
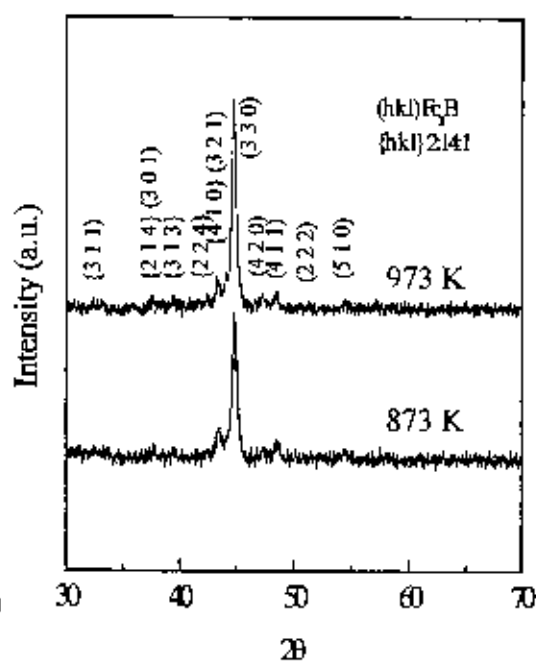
Crystallization temperature of  $(\text{NdPr})_4\text{Fe}_{71}\text{Co}_5\text{Cu}_{0.5}\text{Nb}_1\text{B}_{18.5}$  was identified by differential scanning calorimetry (DSC). The DSC trace shown in Fig. 6.1.1 has been measured on a sample in the as-cast condition by carrying out measurement in nitrogen atmosphere with a continuous heating rate of 20 K/min. The curve shows a single exothermic peak, which represents the formation of both soft and hard phases within a narrow range of temperature. Li et. al. [1] has obtained similar single exothermic peak of  $\alpha\text{-Fe/Nd}_2\text{Fe}_{14}\text{B}$  based sample. According to Fig. 6.1.1, initiation of crystallization occurs at 863 K, peak temperature is at 878 K and the crystallization process is completed around 913 K.

X-ray diffraction patterns for the samples annealed at 873 and 973 K are shown in Fig. 6.1.2. The major phases have been identified as  $\text{Fe}_3\text{B}$  and 2:14:1 phases. Any diffraction peaks from a probable  $\alpha\text{-Fe}$  phase were not detected but might be present in small amount. Majority of the Co atoms are dissolved with Fe forming  $(\text{NdPr})_2(\text{FeCo})_{14}\text{B}$  with a smaller proportions in  $\text{Fe}_3\text{B}$  [2, 3]. The grain size of the soft phase ( $\text{Fe}_3\text{B}$ ) has been determined by using Scherrer's formula from FWHM of highest intensity peak (3 3 0) for samples of different annealing conditions and presented in Table 6.1. It can be noticed in Table 6.1 that there is stability in the grain size in certain annealing temperature range and time. This stability of grain size may be attributed to the simultaneous addition of Cu and Nb in the present composition. Cho et.al. [2] has found that simultaneous addition of Cu, Mo and Co refined grain size as observed by TEM which enhanced the value of coercivity compared to the samples without these additives and resulted in more uniform change of coercivity with annealing temperature.

Hysteresis loops obtained at different temperatures and time have been presented in Fig. 6.1.3(a) and (b). In Fig. 6.1.3(a) y-axis values have been normalized by the maximum value of saturation magnetization of the sample annealed at 853 K for 10 minutes and in Fig. 6.1.3(b) y-axis values have been normalized by the saturation magnetization value of the sample annealed at 923 K of 3 minutes. The values of saturation magnetization, coercivity, remanent ratio, and maximum energy product derived from the hysteresis loops have been presented in Table 6.1. While varying annealing temperature and time, coercivity, remanent ratio and maximum energy product increase with the increase of annealing temperature at first, remains almost constant and then decreases. In Fig. 6.1.3(a), there is no change in the shape of the hysteresis loops, which are convex like single-phase permanent magnet up to the annealing temperature of 933 K. For the annealing temperature of 973 K shape of the hysteresis loop is characteristic to the sample in the over-annealed condition [4]. In Fig. 6.1.3(b), where annealing time has been varied for the annealing temperature of 923 K, there is a change in the shape of the hysteresis loops at 3 minutes and 20 minutes. For the sample annealed at 923 K for 3 minutes crystallization is not completed and there remains some metastable phase, which hinders exchange interaction. For the samples annealed at 923 K for 20 minutes the sample is over-annealed which has been manifested in the shape of the hysteresis loop.

Table 6.1 Hysteresis loop parameters for  $(\text{NdPr})_4\text{Fe}_{71}\text{Co}_5\text{Cu}_0.5\text{Nb}_1\text{B}_{18.5}$ 

Annealing temperature K	Annealing time Min.	$M_s$ emu/g	$H_c$ kOe	$M_r/M_s$	$(\text{BH})_{\text{max}}$ MGOe	Grain size of $\text{Fe}_3\text{B}$ nm
853	10	152	-	-	-	14
873	10	148	3.56	0.705	9.73	16
893	10	150	3.66	0.718	11.07	17
903	10	148	3.87	0.741	11.01	17
913	10	151	4.08	0.716	11.06	17
923	10	147	3.98	0.747	10.82	17
933	10	146	3.77	0.720	8.66	20
973	10	149	3.18	0.689	5.20	20
923	1	145	-	-	-	-
923	3	147	3.06	0.706	5.51	16
923	5	146	3.98	0.749	9.84	17
923	10	146	3.98	0.747	10.8	17
923	20	147	3.30	0.703	6.07	20

Fig. 6.1.1 DSC trace of  $(\text{NdPr})_4\text{Fe}_{71}\text{Co}_5\text{Cu}_{0.5}\text{Nb}_1\text{B}_{18.5}$  in the as-cast condition with a heating rate of 20 K/min.Fig. 6.1.2 X-ray diffraction patterns of  $(\text{NdPr})_4\text{Fe}_{71}\text{Co}_5\text{Cu}_{0.5}\text{Nb}_1\text{B}_{18.5}$  for the samples annealed at 873 and 973 K for 10 minutes.



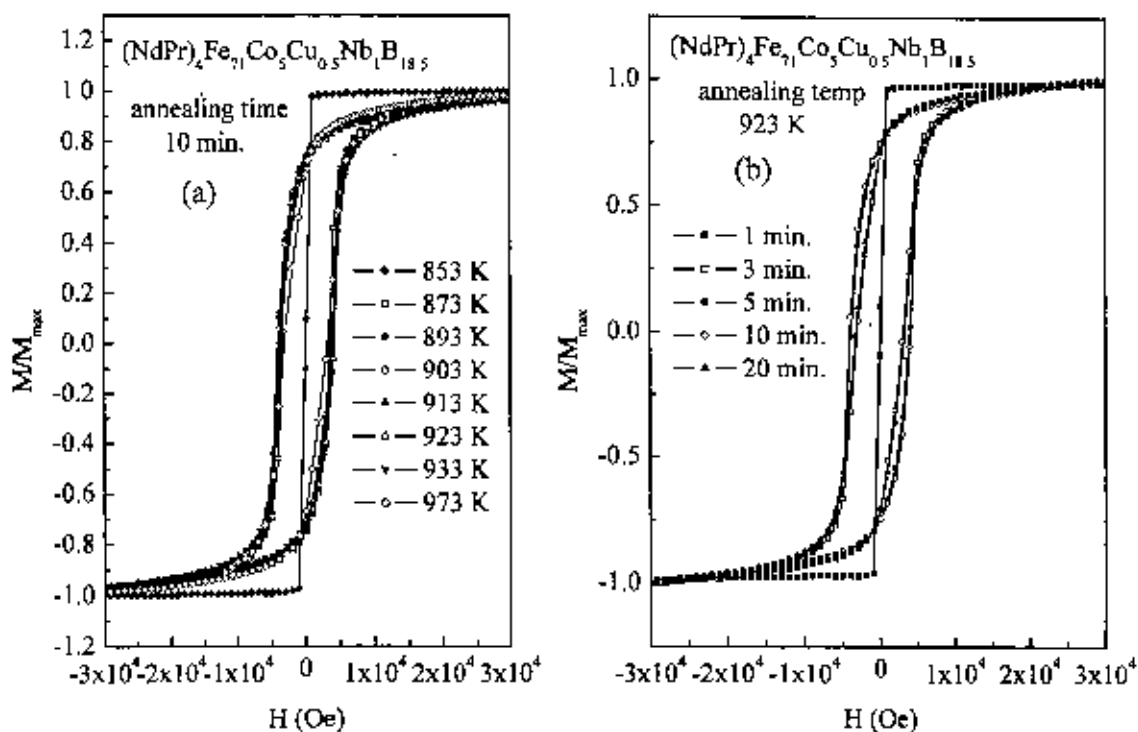


Fig. 6.1.3. Annealing temperature and annealing time dependence of hysteresis loops.

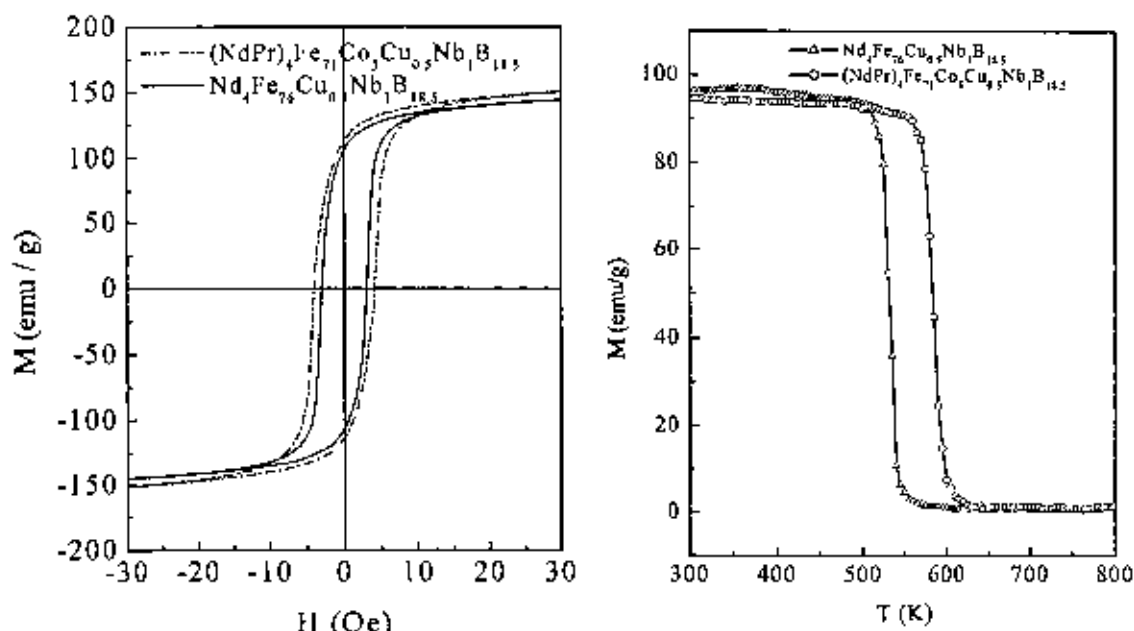


Fig. 6.1.4. Hysteresis loops of samples of compositions  $(\text{NdPr})_4\text{Fe}_{71}\text{Co}_5\text{Cu}_{0.5}\text{Nb}_1\text{B}_{18.5}$  and  $\text{Nd}_4\text{Fe}_{76}\text{Cu}_{0.5}\text{Nb}_1\text{B}_{18.5}$ .

Fig. 6.1.5. Temperature dependence of magnetization of  $(\text{NdPr})_4\text{Fe}_{71}\text{Co}_5\text{Cu}_{0.5}\text{Nb}_1\text{B}_{18.5}$  and  $\text{Nd}_4\text{Fe}_{76}\text{Cu}_{0.5}\text{Nb}_1\text{B}_{18.5}$  with an applied field of 100 Oe and heating rate of 20 K/min.

In Fig. 6.1.4, hysteresis loops of samples of compositions  $(\text{NdPr})_4\text{Fe}_{71}\text{Co}_5\text{Cu}_{0.5}\text{Nb}_1\text{B}_{18.5}$  and  $\text{Nd}_4\text{Fe}_{76}\text{Cu}_{0.5}\text{Nb}_1\text{B}_{18.5}$  have been presented. It is seen from Table 6.1.1 that the highest value of coercivity of  $(\text{NdPr})_4\text{Fe}_{71}\text{Co}_5\text{Cu}_{0.5}\text{Nb}_1\text{B}_{18.5}$  has been obtained for the sample annealed at 913 K for 10 minutes. In Fig. 6.1.4, the sample of composition  $\text{Nd}_4\text{Fe}_{76}\text{Cu}_{0.5}\text{Nb}_1\text{B}_{18.5}$  annealed at the same temperature i.e. 913 K for 10 minutes have been presented for comparison. Coercivity, remanent ratio and maximum energy product of  $\text{Nd}_4\text{Fe}_{76}\text{Cu}_{0.5}\text{Nb}_1\text{B}_{18.5}$  are 3.06 kOe, 0.731 and 8.62 MGOe respectively, while for  $(\text{NdPr})_4\text{Fe}_{71}\text{Co}_5\text{Cu}_{0.5}\text{Nb}_1\text{B}_{18.5}$  are 4.08 kOe, 0.716 and 11.06 MGOe.

In Fig. 6.1.5, temperature dependence of magnetization has been presented with an applied field of 100 Oe and at a heating rate of 20 K/run for  $(\text{NdPr})_4\text{Fe}_{71}\text{Co}_5\text{Cu}_{0.5}\text{Nb}_1\text{B}_{18.5}$  and  $\text{Nd}_4\text{Fe}_{76}\text{Cu}_{0.5}\text{Nb}_1\text{B}_{18.5}$ . The characteristic feature of the curves is that the magnetization remains constant up to a certain temperature followed by an abrupt decrease in its value passing through ferro-paramagnetic transition at the Curie temperature. The Curie temperature has been estimated from the rate of change of magnetization and found as 585 K for  $(\text{NdPr})_4\text{Fe}_{71}\text{Co}_5\text{Cu}_{0.5}\text{Nb}_1\text{B}_{18.5}$  and 535 K for  $\text{Nd}_4\text{Fe}_{76}\text{Cu}_{0.5}\text{Nb}_1\text{B}_{18.5}$ .

Figs. 6.1.6 (a) and (b) show room temperature (300 K) hysteresis loops and some minor recoil loops along the demagnetization branch for the samples annealed at 873 and 973 K i.e. in the initial and over-annealed condition. In Fig. 6.1.7, the area of the recoil loops normalized to the area of half of the major hysteresis loop are plotted as a function of the reverse field  $H_r$ . The areas have been extracted by numerical integration of the recoil curves of Fig. 6.1.6. Below the critical field, the magnetic moment when returning to the demagnetizing field is very close to the starting value. The sample annealed at 873 K for 10 minutes shows a narrow recoil area peak compared to the samples annealed at 973 K. The development of the loop area is due to the decoupling of the magnetic moment between hard and soft phase [5]. The recoil area shows a pronounced maximum at the field where the largest number of hard phase grains switch magnetization direction. These fields are quoted in the figure and amounts to 3500 and 4200 Oe for the samples annealed at 873 and 973 K respectively. As pointed out by Kang et. al. [5], the peak in the recoil area is coincident with the coercivity of the hard component while the departure from zero recoil area at low reverse fields corresponds to the inter-phase exchange field,  $H_{ex}$ . It is to be noted that for the sample annealed at 873 K for 10 minutes the peak value is very close to the coercivity value presented in Table 6.1.1 whereas the peak value for the sample annealed at 973 K exceeds the coercivity value obtained from the hysteresis loop for this sample and presented in Table 6.1.1. It is known from the literature [4] that for over-annealed sample the critical field where the onset of irreversible change of magnetization in the hard phase takes place exceeds the apparent coercive field obtained from the hysteresis loop.

In Fig. 6.1.8, the reduced quantity  $D(H) = \frac{M_r - M_d(H)}{2M_r} = -\frac{\Delta M_{\text{revers}}(H)}{2M_r}$  is plotted vs.  $H_r$ , where  $M_d(H)$

is the dc field demagnetization remanence i.e. the remanence acquired after saturation in one direction and subsequent application of a dc field  $H_r$  in the opposite direction and  $M_r$  is the saturation remanence. The curves of Fig. 6.1.8 provide information about the stability of the reversible state and the critical field

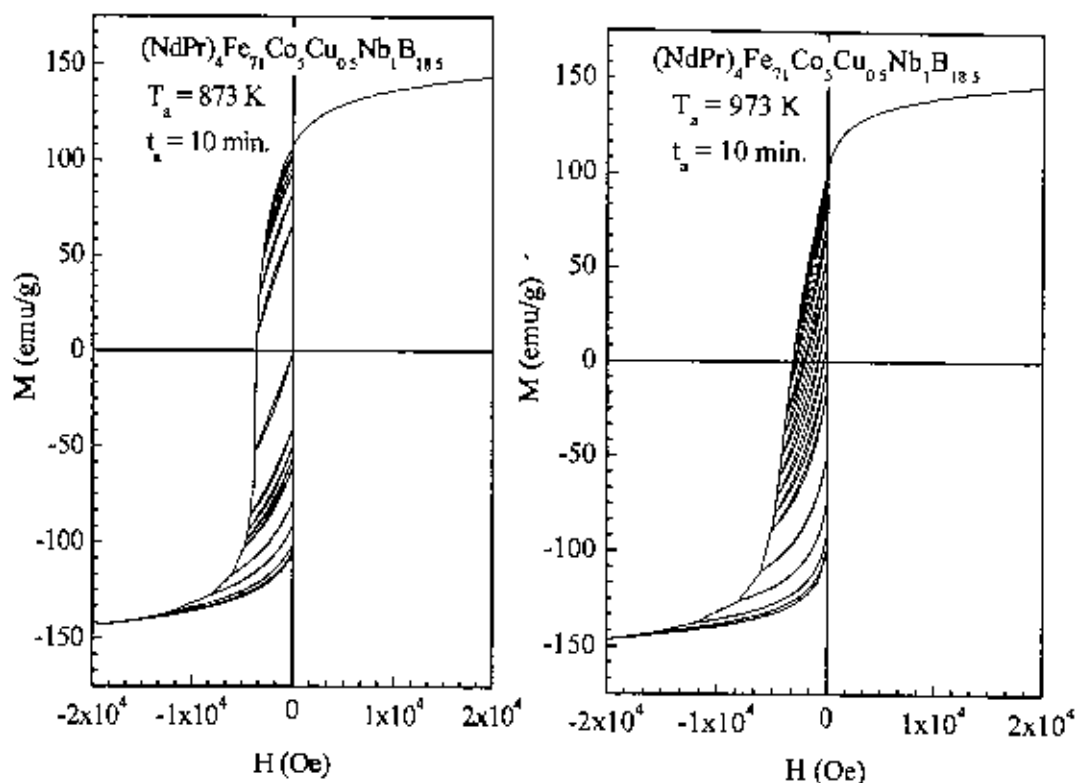


Fig. 6.1.6. Recoil hysteresis loops for samples annealed at 873 and 973 K for 10 minutes.

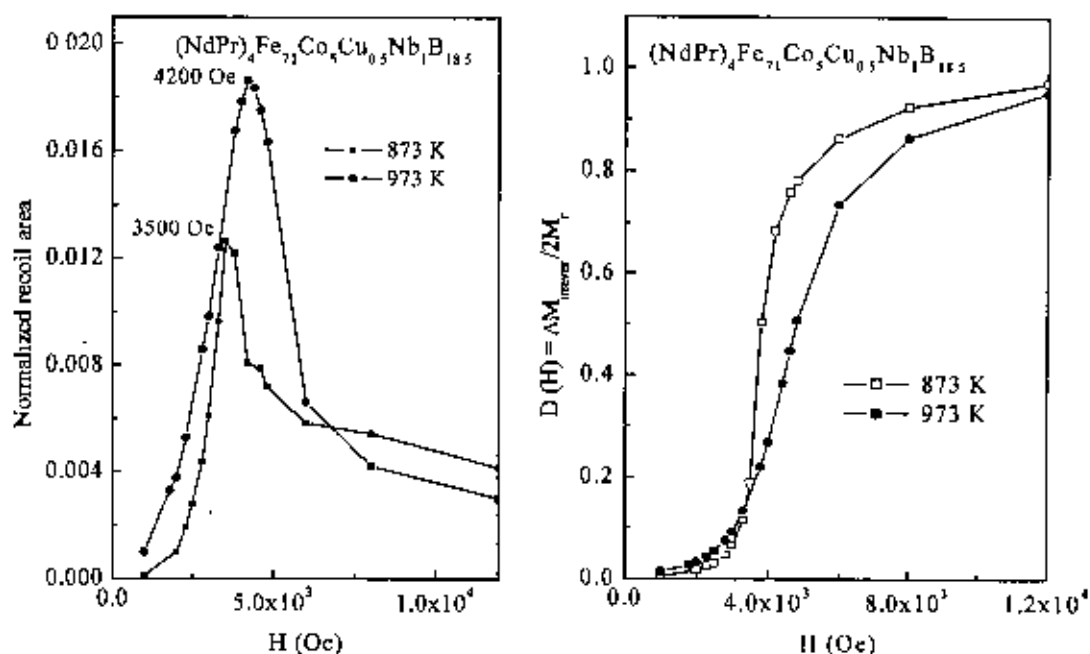


Fig. 6.1.7. Recoil loop area as a function of reverse field for annealed samples.

Fig. 6.1.8. Measurements of the irreversible portion  $D(H) = -\Delta M_{\text{irrev}}(H)/2M_r$  versus  $H$  for the samples annealed at 873, 903 and 973 K.

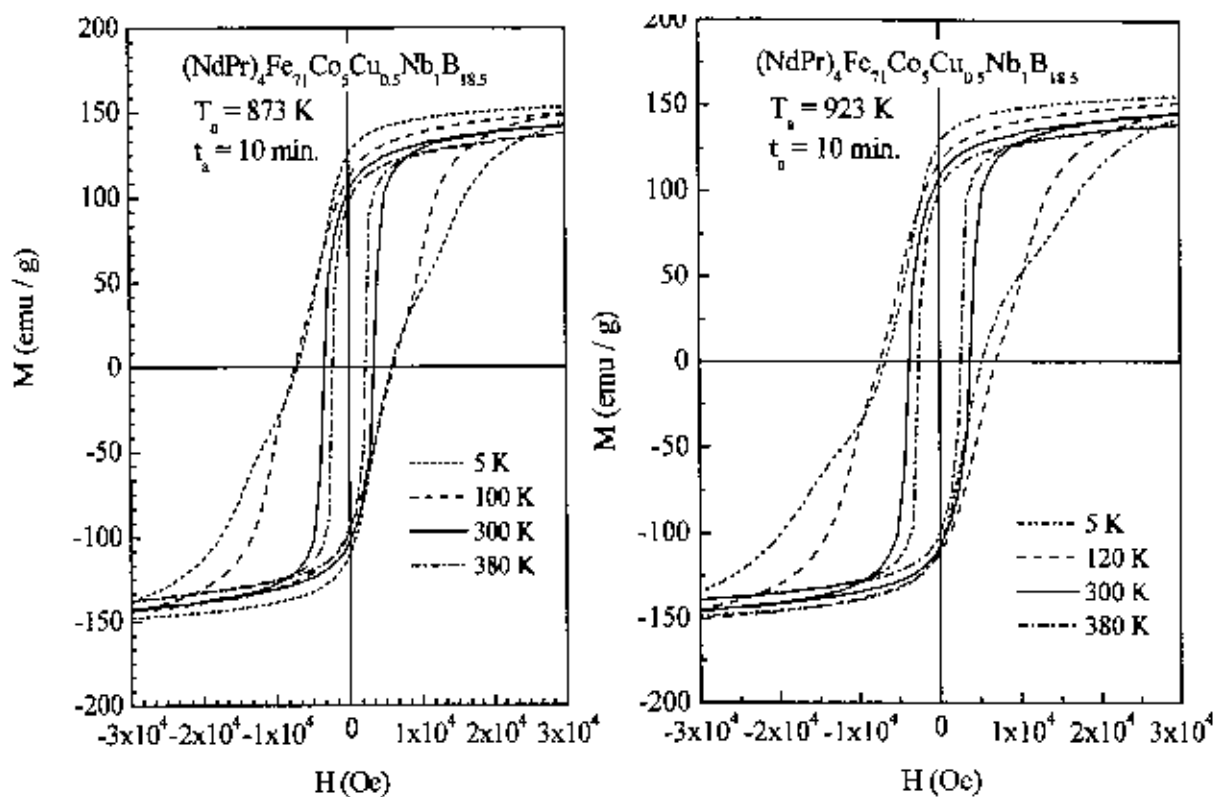


Fig. 6.1.9. Temperature dependence of hysteresis loops for samples annealed at 873 and 923 K for 10 minutes.

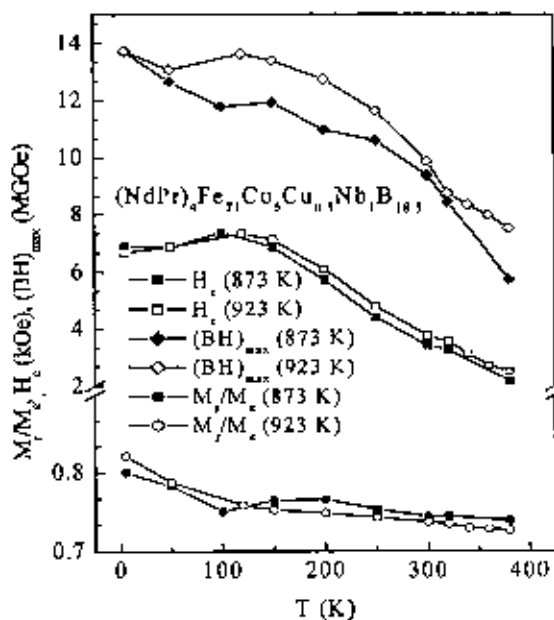


Fig. 6.1.10. Temperature dependence of hysteresis loop parameters for samples annealed at 873 and 923 K for 10 minutes.

of irreversible changes of the magnetization. For the sample annealed at 873 K, the  $D(H)$  versus  $H$  curve is characterized by relatively sharp change of  $D(H)$  at the critical field whereas for the samples annealed at 973 K the change is more gradual. Below the critical field of around 3000 Oe, change in  $\Delta M_{\text{revers}}$  is small and magnetization almost return to the remanent configuration when the field is decreased back to zero.

Temperature dependence of the hysteresis loop has been measured in the temperature range of 5 to 380 K for the sample annealed at 873 and 923 K. Some representative hysteresis loops are shown in Fig. 6.1.9 and derived hysteresis loop parameters at different temperatures are plotted in Fig. 6.1.10. Shape of the hysteresis loop changes at 100 K and below, which is related to a spin re-orientation in the hard phase that occurs at low temperatures. From studies of powdered and single crystalline  $\text{Nd}_2\text{Fe}_{14}\text{B}$ , Givord et. al. [6, 7] found that at temperatures below 135 K there is an angle  $\theta$  between the easy magnetization direction and the  $c$ -axis that progressively increases and amounts to about  $30^\circ$  at low temperatures. In ref. [8] it was observed that the hysteresis loop for  $\text{Nd}_2\text{Fe}_{14}\text{B}/\alpha\text{-Fe}$  becomes constricted below the spin reorientation temperature, i.e. with the decrease of temperature the magnetization curve becomes more discontinuous at low field. The curves presented in Fig 6.1.9 shows a change in the shape of the hysteresis loop at 100 K and lower temperatures, which agree with previous measurements [6, 7, 8]. It is to be noted that extent of discontinuity at low field is weaker for the composition under present study than in ref [8]. The reason might be Nd has been replaced by Pr  $\text{Pr}_2\text{Fe}_{14}\text{B}$  does not exhibit low temperature spin reorientation [6, 9].

In Fig. 6.1.10, temperature dependence of the coercivity,  $H_c$ , the remanent ratio,  $M_r/M_s$  and maximum energy product,  $(BH)_{\text{max}}$  are plotted. Curves for both the samples show similar behavior. The coercivity increases with decreasing temperature down to about 150 K. Below 150 K there is a decrease of the slope of  $H_c(T)$  and below 100 K there is a slight decrease. The decrease of the coercivity at low temperatures is related to the spin reorientation. This behavior of  $H_c(T)$  may be compared with that reported in ref. [9] in which a stronger decay of the coercivity at low temperatures is observed. This difference may be due to the partial substitution of Nd by Pr in our alloy composition. The temperature dependence of remanent ratio,  $\frac{M_r}{M_s}$  is also governed by the temperature dependence of anisotropy field. The value of  $M_r/M_s$

decreases with the increase of temperature because of easier domain wall motion due to the reduction of the anisotropy field at higher temperature. Temperature dependence of maximum energy product,  $(BH)_{\text{max}}$  also decreases with the increase of temperature due to the reduction of anisotropy field for both samples.

## 6.2 Structural and Magnetic Properties of $\text{Nd}_4\text{Fe}_{73.5}\text{Co}_3\text{Hf}_{0.5}\text{Ga}_{0.5}\text{B}_{18.5}$

Hysteresis loops of the samples have been measured at room temperature for the samples annealed at different temperatures and time to observe the variation of magnetic properties with annealing condition. Variations of hysteresis loops with annealing temperatures have been presented in Fig. 6.2.1(a) for the annealing time of 10 minutes. Hysteresis loop parameters obtained from Fig. 6.2.1(a) have been presented

in Table 6.2. With the variation of annealing temperature it has been found that the sample is magnetically very soft at 873 K. At 903 K small amount of coercivity,  $H_c$  has developed. At 923 K for 10 minutes the values of  $H_c$  and  $(BH)_{max}$  are maximum. Thus, the variations of hysteresis loops have been measured at this annealing temperature for different annealing time and presented in Fig. 6.2.1(b). Hysteresis loop parameters obtained from Fig. 6.2.1(b) are also presented in Table 6.2. All the samples possess very high remanent ratio. The highest value of  $H_c$  around 2.62 kOe and  $(BH)_{max}$  around 11.05 MGOe have been found at 923 K for 5 minutes. For higher annealing times the value of  $H_c$  and  $(BH)_{max}$  decrease.

Samples annealed at 923 K for 5, 10 and 20 minutes have been studied in order to see the effect of optimum and over-annealed condition on the magnetic properties. X-ray diffraction patterns at the annealing temperature of 923 K for 5, 10 and 20 minutes have been presented in Fig. 6.2.2. Phases have been identified as  $Fe_3B$  and 2:14:1 phases and indexed in Fig. 6.2.2. Probable soft phase  $\alpha$ -Fe is not noticeable for the annealing times of 5 and 10 minutes. Small amount  $\alpha$ -Fe is present for the annealing time of 20 minutes. Majority of the Co is dissolved with Fe forming  $Nd_2(FeCo)_{14}B$  with a smaller proportion in  $Fe_3B$  [2, 3]. Grain size of the soft phase,  $Fe_3B$  has been determined by using Scherrer's formula from line broadening of fundamental peak. The grain size has been obtained as 23 nm for the sample annealed for 5 minutes, 25 nm for the sample annealed for 10 minutes and 24 nm for the sample annealed for 20 minutes. With the increase of annealing time relative amount of soft phase increases than hard phase manifested by the relative intensity of hard and soft phase in the XRD patterns.

In Fig. 6.2.3 (a), (b) and (c), dc demagnetization curves after previous saturation in the opposite direction and some minor recoil loops along the demagnetization curve has been presented at 923 K for 5, 10 and 20 minutes of annealing. In Fig. 6.2.3, area of the recoil loops are small having high recoil permeability. Harland et. al. [10] have mentioned that the development of the area of the recoil curve with reverse field and temperature provides information about the breakdown of exchange coupling of  $Nd_2Fe_{14}B / \alpha$ -Fe nanocomposites. Thus it can be observed in Fig. 6.2.3 that there is an evolution of recoil loop area with the increase of reverse field and recoil loop area is maximum at coercive field for which recoil loop does not trace major demagnetization curve. The recoil loop area normalized to the area of half of the major hysteresis loop has been presented in Fig. 6.2.4 as a function of reverse field. In Fig. 6.2.4, sample annealed at 923 K for 5 minutes shows a narrow recoil area peak compared to the sample annealed for 10 and 20 min, which is an indication of greater exchange-spring character for the annealing condition of 923 K for 5 minutes. The peak in the recoil area is coincident with the coercivity of the hard component while the departure from zero recoil area at low reverse fields corresponds with the interphase exchange field,  $H_{ex}$  [5]. In Fig. 6.2.4, the peak value of the sample annealed at 5 minutes is 2500 Oe. The peak value of the sample annealed for 10 and 20 minutes is 2300 Oe. The areas of the recoil loops in Fig. 6.2.4 progressively increase with the increase of annealing time.

Table 6.2. Hysteresis loop parameters of  $\text{Nd}_4\text{Fe}_{73.5}\text{Co}_3\text{Hf}_{0.5}\text{Ga}_{0.5}\text{B}_{18.5}$  with the variation of annealing temperature and time.

Annealing temp (K)	Annealing time (min.)	$M_s$ (emu/g)	$M_r$ (emu/g)	$H_c$ (Oe)	$M_r/M_s$	$(BH)_{\text{max}}$ (MGOe)
873	10	154	-	-	-	-
903	10	152	116	363	0.76	-
923	10	154	123	2425	0.80	9.38
933	10	155	121	2410	0.78	8.82
953	10	155	116	2380	0.75	7.37
923	3	154	125	2016	0.81	8.39
923	5	154	127	2622	0.82	11.05
923	10	154	123	2425	0.80	9.38
923	15	152	123	2425	0.81	9.48
923	20	153	115	2228	0.75	6.38

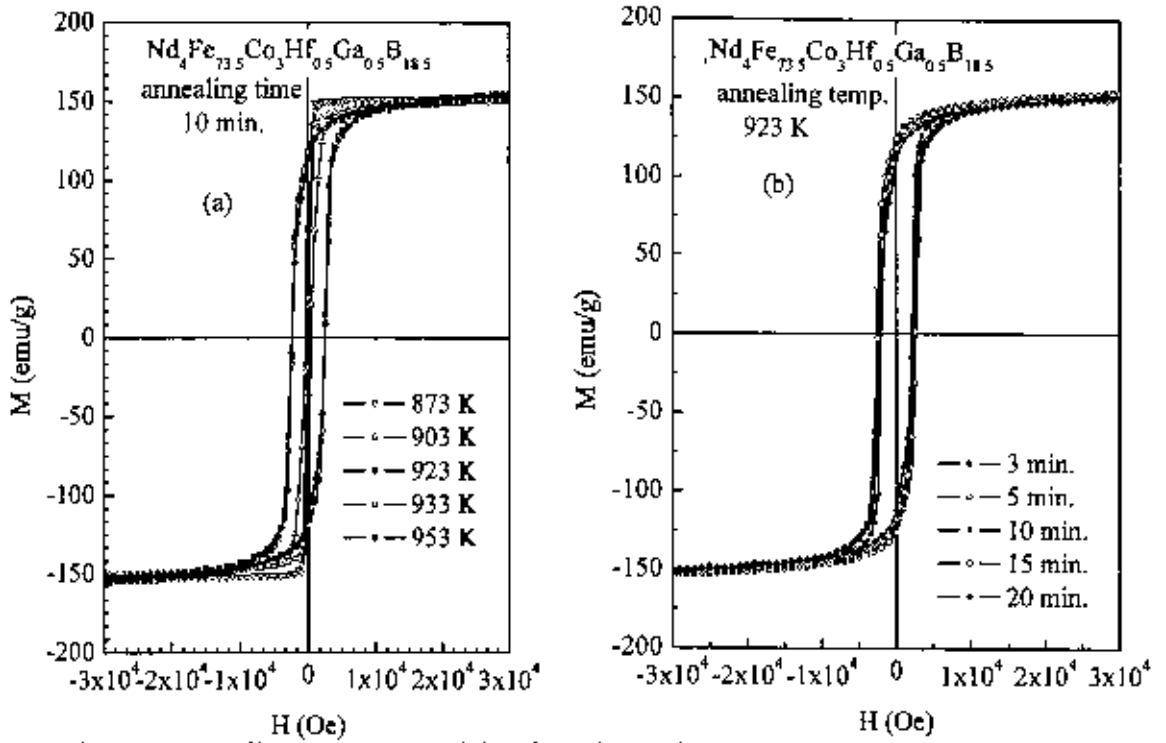


Fig. 6.2.1 Annealing temperature and time dependence of hysteresis loops of  $\text{Nd}_4\text{Fe}_{73.5}\text{Co}_3\text{Hf}_{0.5}\text{Ga}_{0.5}\text{B}_{18.5}$ .

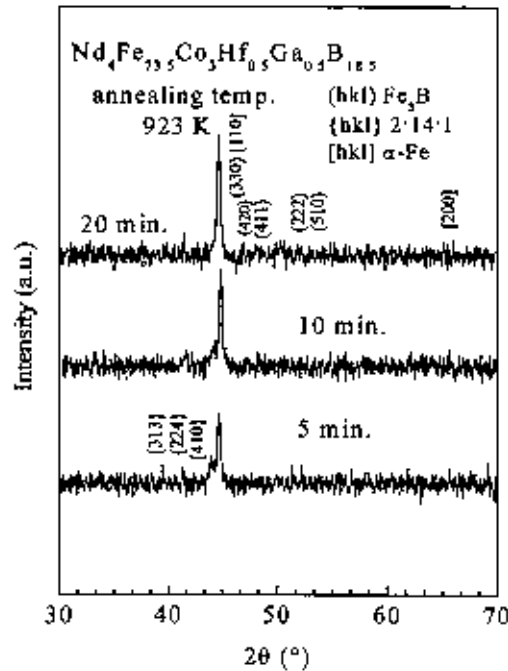


Fig. 6.2.2 X-ray diffraction patterns of  $\text{Nd}_4\text{Fe}_{73.5}\text{Co}_3\text{Hf}_{0.5}\text{Ga}_{0.5}\text{B}_{18.5}$  annealed at 923 K for 5, 10 and 20 minutes.



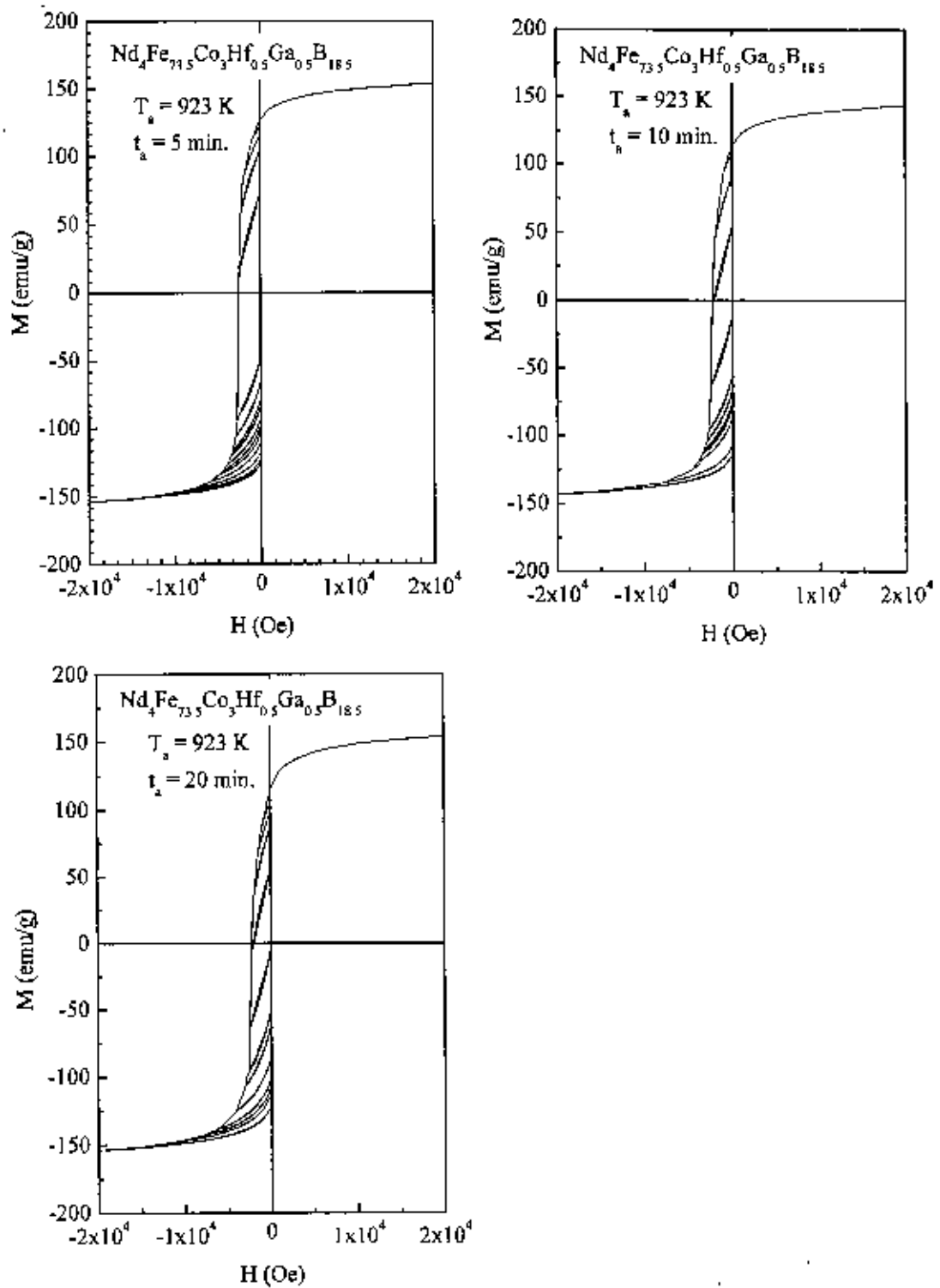


Fig. 6.2.3. Recoil hysteresis loops for samples annealed at 923 K for 5, 10 and 20 minutes.

In Fig. 6.2.5, the irreversible component of magnetization represented by,

$$D(H) = \frac{M_r - M_d(H)}{2M_r} = -\frac{\Delta M_{\text{irrever.}}(H)}{2M_r}$$

versus reverse field has been presented. In this expression,  $M_r$  is the saturation remanence and  $M_d(H)$  is the dc field demagnetization remanence. In Fig. 6.2.5, the value of  $D(H)$  changes gradually up to the critical field followed by an abrupt change of  $D(H)$  at the critical field. The change is relatively sharper at the critical field for the sample annealed at 923 K for 5 minutes whereas for the samples annealed for 10 and 20 minutes the change is relatively gradual.

Temperature dependence of hysteresis loops have been measured in the temperature range of 5 to 380 K for the samples annealed at 923 K for 5 and 20 minutes with a maximum applied field of 2 Tesla. Some of the representative hysteresis loops have been presented in Fig 6.2.6 (a) and (b) while the hysteresis loops parameters for all the measured data have been presented in Fig. 6.2.7. At lower temperatures, for both the samples, field dependence of magnetization shows discontinuous behavior at low fields. Hadjipanayis et. al. [8, 9] have reported similar discontinuity at low field at the temperature below 135 K, i.e. the spin reorientation temperature of  $\text{Nd}_2\text{Fe}_{14}\text{B}$ . Givord et. al. [6, 7] has found that the easy axis of magnetization is located at  $30^\circ$  from c-axis below 135 K. From temperature dependence of angle  $\theta$  between the easy magnetization direction and the c-axis they have found that the magnetization direction progressively reorients towards the c-direction, which is of easy magnetization direction with the increase of temperature above 135 K. The curves presented in Fig 6(a) and (b) show the variation in the shape of the hysteresis loop at temperature lower than 150 K which is consistent with the previous measurements [6-9].

In Fig. 6.2.7, temperature dependence of coercivity,  $H_c$ , remanent ratio,  $M_r/M_s$  and maximum energy product,  $(BH)_{\text{max}}$  have been presented. The coercivity generally increase with the decrease of temperature though at low temperature the increase of coercivity is large. Increase in the anisotropy field at low temperature leads to the increase of coercivity. Temperature dependence of remanent ratio,  $M_r/M_s$  is also governed by the temperature dependence of anisotropy field. The value of  $M_r/M_s$  decreases with the increase of temperature because of easy domain wall motion due to the reduction of anisotropy field at higher temperature. Above 150 K the change of  $M_r/M_s$  ratio with temperature is small. Temperature dependence of maximum energy product,  $(BH)_{\text{max}}$  generally decreases with the increase of temperature due to the reduction of anisotropy field for both samples. The change is gradual in the range of 380 to 50 K for both samples. At 5 K the change in  $(BH)_{\text{max}}$  is rather abrupt due to high squareness and coercivity at this temperature. For most of the temperatures sample annealed for 5 minutes possess higher squareness i.e.  $M_r/M_s$  and higher coercivity than the sample annealed for 20 minutes, which in turn raise the value of  $(BH)_{\text{max}}$ .

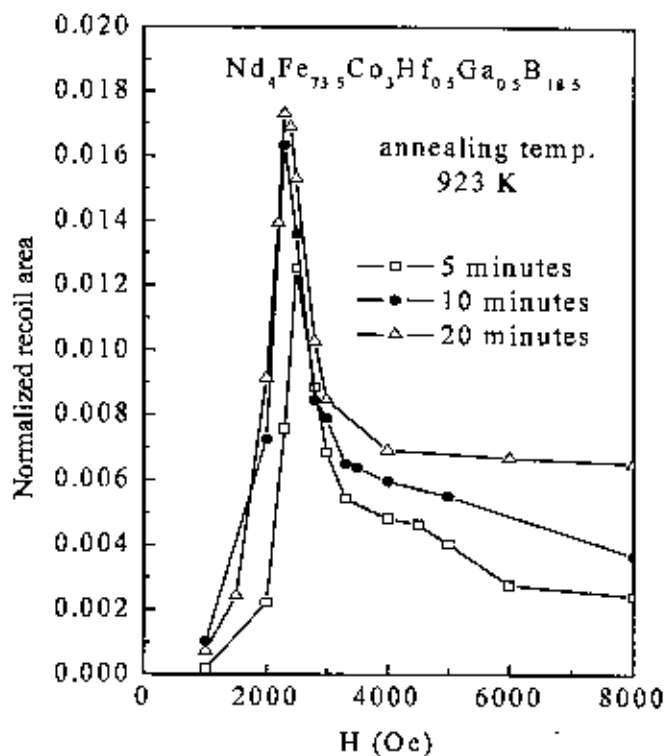


Fig. 6.2.4. Recoil loop area as a function of reverse field for annealed samples.

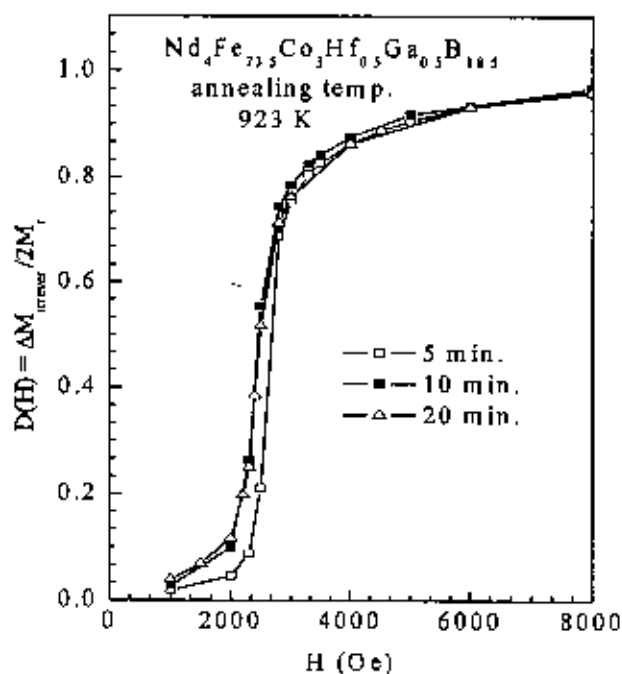


Fig. 6.2.5. Measurements of the irreversible portion  $D(H) = -\Delta M_{\text{irrev}}(H) / 2M_t$  versus  $H$  for the samples annealed at 923 K for 5, 10 and 20 minutes.

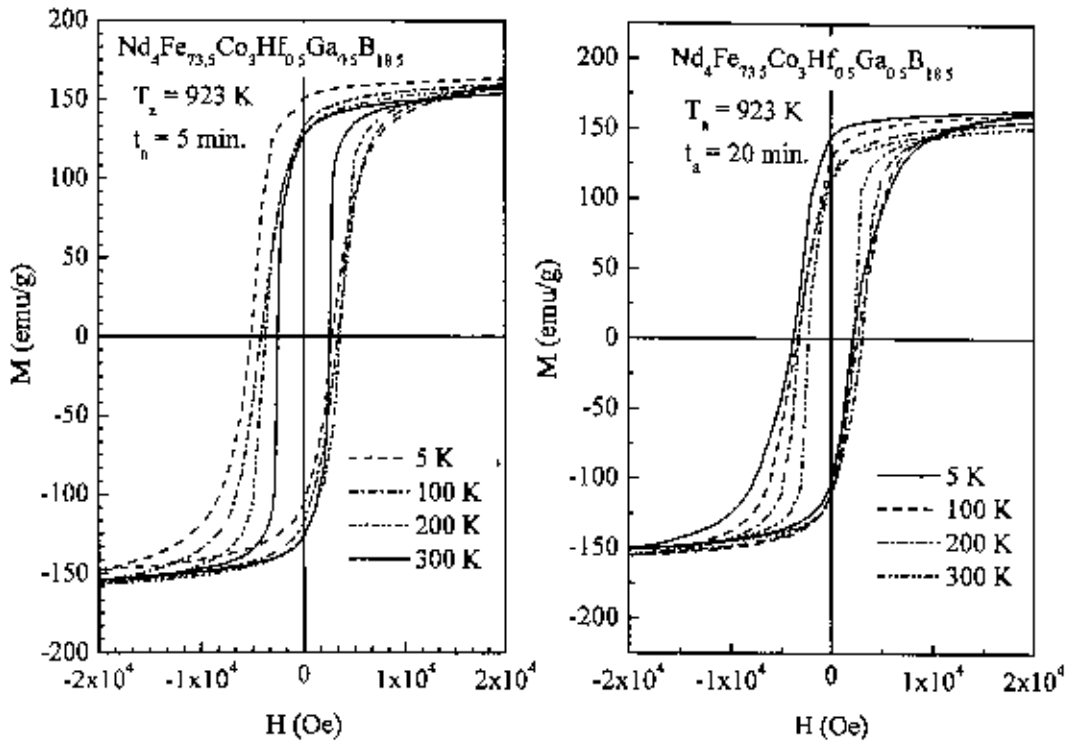


Fig. 6.2.6 Temperature dependence of hysteresis loops for samples annealed at 923 K for 5 and 20 minutes.

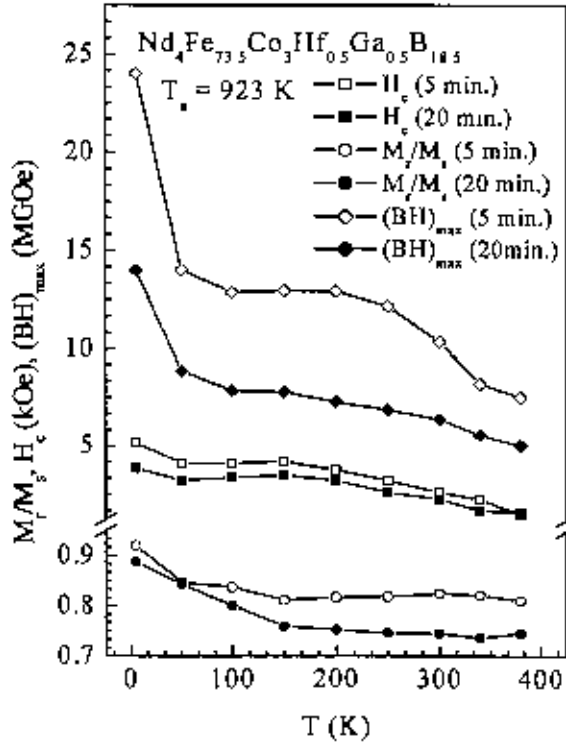


Fig. 6.2.7 Temperature dependence of hysteresis loop parameters for samples annealed at 923 K for 5 and 20 minutes.

### 6.3 Structural and Magnetic Properties of $\text{Nd}_3\text{Tb}_1\text{Fe}_{76}\text{Cu}_{0.5}\text{Nb}_1\text{B}_{18.5}$

Crystallization temperature of  $\text{Nd}_3\text{Tb}_1\text{Fe}_{76}\text{Cu}_{0.5}\text{Nb}_1\text{B}_{18.5}$  was identified by differential thermal analysis (DTA). The DTA trace shown in Fig. 6.3.1 has been measured on a sample in the as-cast condition by carrying out measurement in nitrogen atmosphere with a continuous heating rate of 20 K/min. The curve shows exothermic peaks which represents the formation of both soft and hard phases. Onset of crystallization of the first exothermic peak is at 843 K while peak temperature is at 860 K. For the second exothermic peak, the peak temperature is at 887 K. In order to determine crystallization products at different stages of crystallization X-ray diffraction studies have been performed.

X-ray diffraction patterns for the samples annealed at 853, 873, 893, and 923 K for 10 minutes are shown in Fig. 6.3.2. For the annealing temperature of 853 K, soft phase  $\text{Fe}_3\text{B}$  has formed. For the higher annealing temperature of 873 K, hard magnetic phase  $\text{Nd}_2\text{Fe}_{14}\text{B}$  has started to form though in a small amount in association with soft phase  $\text{Fe}_3\text{B}$ . At higher annealing temperature of 893 and 923 K characteristic patterns of the mixture of soft and hard phases ( $\text{Fe}_3\text{B}$  and  $\text{Nd}_2\text{Fe}_{14}\text{B}$ ) are observed. With the increase of annealing temperature grain size does not change significantly and remains on the average of 14 nm as determined from FWHM of highest intensity peak and presented in Table 6.3. But the relative amount of soft and hard phases change with the increase of annealing temperature as can be observed from the relative intensity of soft and hard phases.

Hysteresis loops obtained at different annealing temperatures have been presented in Fig. 6.3.3. In Fig. 6.3.3, y-axis values have been normalized by the maximum value of saturation magnetization. It may be noticed that saturation magnetization has not been achieved even after applying a maximum field of 3 Tesla. This is due to the high magneto-crystalline anisotropy, which is common for  $\text{R}_2\text{Fe}_{14}\text{B}$ . Values of saturation magnetization, coercivity, remanent ratio, and maximum energy product derived from the hysteresis loops have been presented in Table 6.3. While varying annealing temperature, coercivity generally increases with the increase of annealing temperature while remanent ratio decreases. Highest value of energy product about 9.43 MGOe has been obtained for the sample annealed at 923 K for 10 minutes. In Fig. 6.3.3, there is no change in the shape of the hysteresis loops, which are convex like single phase permanent magnet up to the annealing temperature of 953 K, which indicates that the material is exchange-coupled up to the annealing temperature adopted in this experiment.

In Fig. 6.3.4, hysteresis loops of samples of compositions  $\text{Nd}_3\text{Tb}_1\text{Fe}_{76}\text{Cu}_{0.5}\text{Nb}_1\text{B}_{18.5}$  and  $\text{Nd}_4\text{Fe}_{76}\text{Cu}_{0.5}\text{Nb}_1\text{B}_{18.5}$  have been presented. It is seen from Table 6.3 that the highest value of  $(\text{BH})_{\text{max}}$  of  $\text{Nd}_3\text{Tb}_1\text{Fe}_{76}\text{Cu}_{0.5}\text{Nb}_1\text{B}_{18.5}$  has been obtained for the sample annealed at 923 K for 10 minutes. In Fig. 6.3.4, the sample without Tb of composition  $\text{Nd}_4\text{Fe}_{76}\text{Cu}_{0.5}\text{Nb}_1\text{B}_{18.5}$  annealed at the same temperature i.e. 923 K for 10 minutes have been presented for comparison. Coercivity, remanent ratio and maximum energy product of  $\text{Nd}_4\text{Fe}_{76}\text{Cu}_{0.5}\text{Nb}_1\text{B}_{18.5}$  are 3.18 kOe, 0.753 and 9.21 MGOe respectively. While the Coercivity,

Table 6.3. Hysteresis loop parameters for  $\text{Nd}_7\text{Tb}_1\text{Fe}_{76}\text{Cu}_{0.5}\text{Nb}_1\text{B}_{18.5}$ .

Annealing temperature K	Annealing time min.	$M_s$ emu / g	$H_c$ kOe	$M_r/M_s$	$(BH)_{\text{max}}$ MGOe	g.s. nm
853	10	147	-	-	-	10
873	10	146	2.68	0.719	6.11	14
893	10	142	4.10	0.697	7.85	14
913	10	147	4.00	0.665	7.26	13
923	10	147	4.40	0.683	9.43	14
953	10	147	4.76	0.674	8.67	15

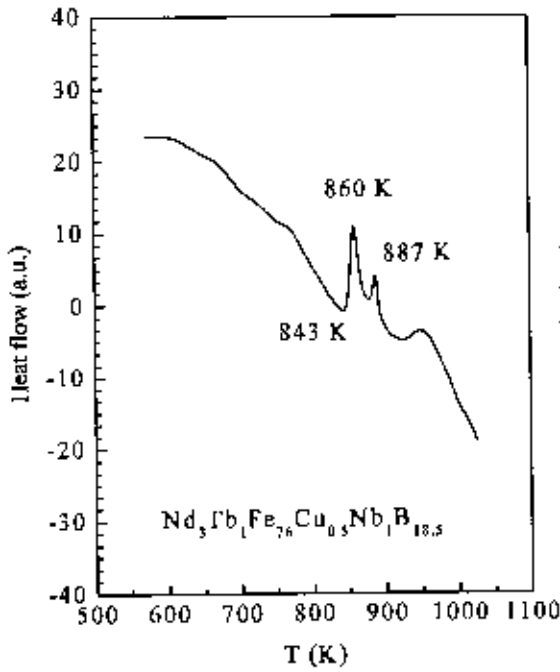


Fig. 6.3.1. DTA trace of  $\text{Nd}_3\text{Tb}_1\text{Fe}_{76}\text{Cu}_{0.5}\text{Nb}_1\text{B}_{18.5}$  in the as-cast condition with a heating rate of 20 K/min.

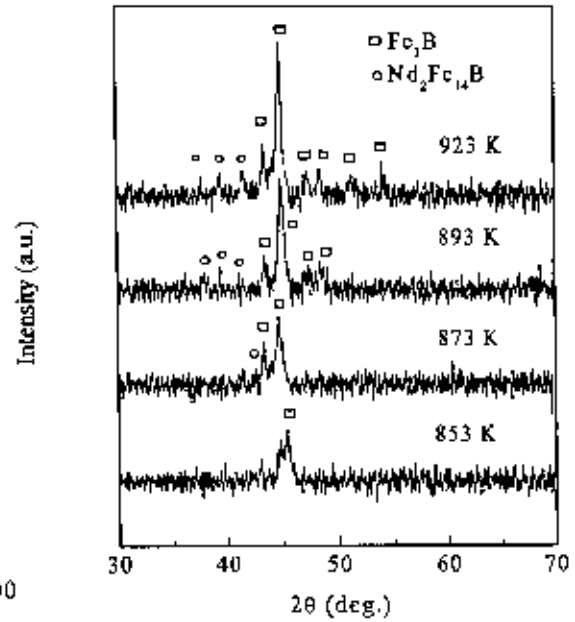


Fig. 6.3.2. X-ray diffraction pattern of  $\text{Nd}_3\text{Tb}_1\text{Fe}_{76}\text{Cu}_{0.5}\text{Nb}_1\text{B}_{18.5}$  samples in the annealed condition.

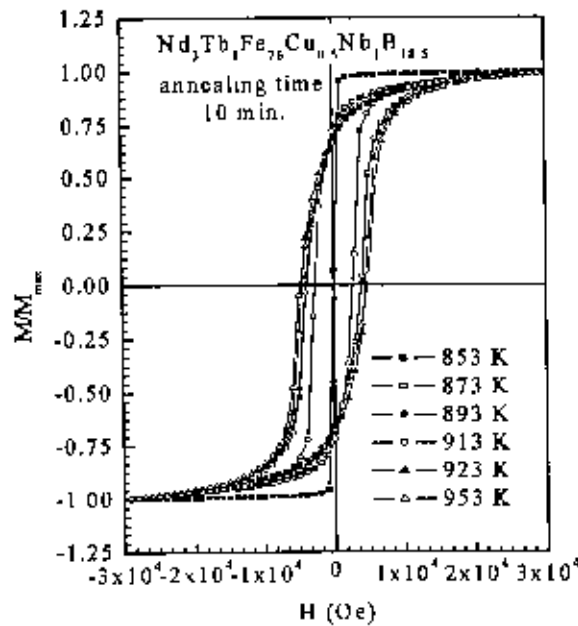


Fig. 6.3.3. Hysteresis loops of  $\text{Nd}_3\text{Tb}_1\text{Fe}_{76}\text{Cu}_{0.5}\text{Nb}_1\text{B}_{18.5}$  samples in the annealed condition at different temperatures.

remanent ratio and maximum energy product of  $\text{Nd}_3\text{Tb}_1\text{Fe}_{76}\text{Cu}_{0.5}\text{Nb}_1\text{B}_{18.5}$  are 4.40 kOe, 0.683 and 9.43 MGOe.

Though an enhancement of coercivity takes place due to the higher anisotropy field when Nd is partially substituted by Tb, remanent ratio is decreased due to antiferromagnetic coupling between rare earth and transition metal [11]. The magnetization of light rare earth (LRE) sublattice couples ferromagnetically to the magnetization of the transition metal sublattice. The opposite is true for the heavy rare earth (HRE) elements rendering these latter materials ferromagnetic. It may be pointed out here that the anisotropy field of  $\text{Nd}_2\text{Fe}_{14}\text{B}$  is 150 kOe (12 MA/m) and  $\text{Tb}_2\text{Fe}_{14}\text{B}$  is 350 kOe (28 MA/m) [11]. Combined effect of antiferromagnetic coupling between Fe and Tb and higher anisotropy field of  $\text{Tb}_2\text{Fe}_{14}\text{B}$  led to the enhancement of coercivity and reduction of remanent ratio, which in turn has resulted in lower value of maximum energy product.

In Fig. 6.3.5, temperature dependence of magnetization has been presented with an applied field of 100 Oe and at a heating rate of 20 K/min for  $\text{Nd}_3\text{Tb}_1\text{Fe}_{76}\text{Cu}_{0.5}\text{Nb}_1\text{B}_{18.5}$  and  $\text{Nd}_4\text{Fe}_{76}\text{Cu}_{0.5}\text{Nb}_1\text{B}_{18.5}$ . The characteristic feature of the curves is magnetization remains almost constant up to a certain temperature followed by an abrupt decrease in its value passing through ferro-paramagnetic transition at the Curie temperature. The Curie temperature has been estimated from the rate of change of magnetization and found as 549 K for  $\text{Nd}_3\text{Tb}_1\text{Fe}_{76}\text{Cu}_{0.5}\text{Nb}_1\text{B}_{18.5}$  and 535 K for  $\text{Nd}_4\text{Fe}_{76}\text{Cu}_{0.5}\text{Nb}_1\text{B}_{18.5}$ . Exchange in interaction between R and Fe moments enhances the Curie temperature [11].

Fig. 6.3.6 shows room temperature (300 K) hysteresis loop and some minor recoil loops along the demagnetization branch for the sample annealed at 923 K for 10 minutes. In Fig. 6.3.7, the area of the recoil loops normalized to the area of half of the major hysteresis loops are plotted as a function of the reverse field H. The areas have been extracted by numerical integration of the recoil curves of Fig. 6.3.6. The development of the loop area is due to the decoupling of the magnetic moment between hard and soft phase. In Fig. 6.3.7, the recoil area shows a pronounced maximum at the field where the largest number of hard phase grains switch magnetization direction. This field amounts to 4600 Oe for the sample annealed at 923 K for 10 minutes.

In Fig. 6.3.7, the reduced quantity  $D(H) = \frac{M_r - M_d(H)}{2M_r} = -\frac{\Delta M_{\text{revers}}(H)}{2M_r}$  is plotted vs. H, where  $M_d(H)$

is the dc field demagnetization remanence and  $M_r$  is the saturation remanence. The curves of Fig. 6.3.7 provide information about the stability of the reversible state. For the sample annealed at 923 K, the  $D(H)$  versus H curve is characterized by relatively sharp change of  $D(H)$  at the critical field where irreversible change in the hard phase is relatively large, which has been obtained from the derivative of the  $D(H)$  vs. H curve and found as 4000 Oe.

Temperature dependence of the hysteresis loop has been measured in the temperature range of 5 to 380 K for the sample annealed at 893 and 923 K. Some representative hysteresis loops are shown in Fig 6.3.8 and derived hysteresis loop parameters from all measured temperatures are plotted in Fig. 6.3.9. The shape



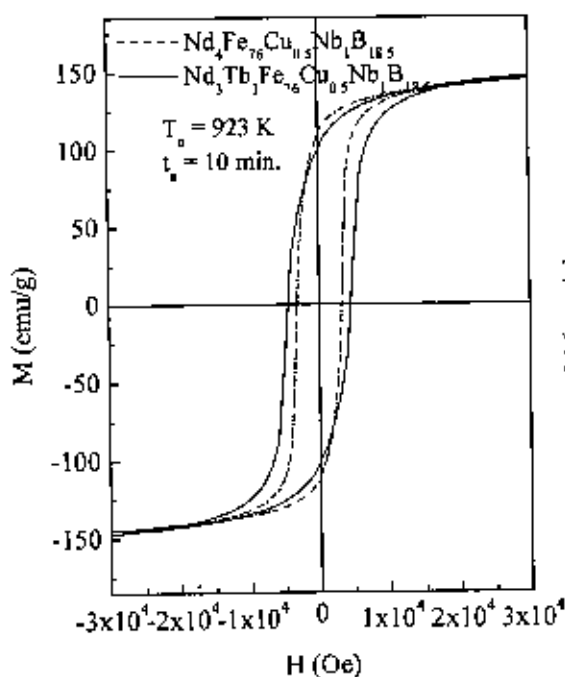


Fig. 6.3.4. Hysteresis loops of samples of compositions  $\text{Nd}_3\text{Tb}_1\text{Fe}_{76}\text{Cu}_{0.5}\text{Nb}_1\text{B}_{18.5}$  and  $\text{Nd}_4\text{Fe}_{76}\text{Cu}_{0.5}\text{Nb}_1\text{B}_{18.5}$ .

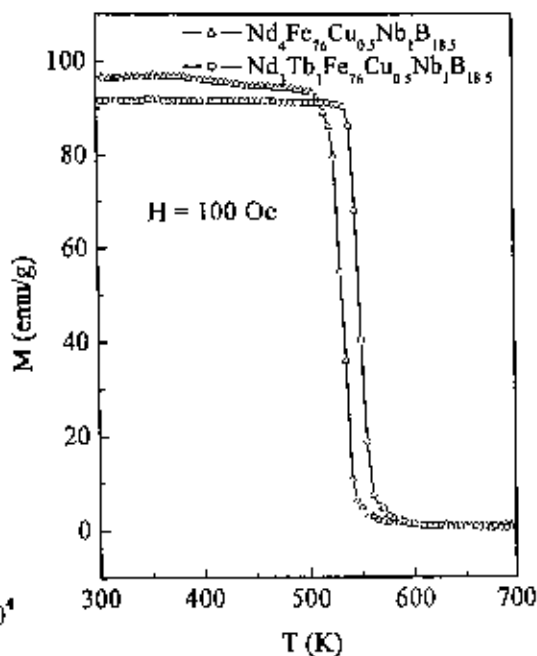


Fig. 6.3.5. Temperature dependence of magnetization of  $\text{Nd}_3\text{Tb}_1\text{Fe}_{76}\text{Cu}_{0.5}\text{Nb}_1\text{B}_{18.5}$  and  $\text{Nd}_4\text{Fe}_{76}\text{Cu}_{0.5}\text{Nb}_1\text{B}_{18.5}$  with an applied field of 100 Oe and heating rate of 20 K/min.

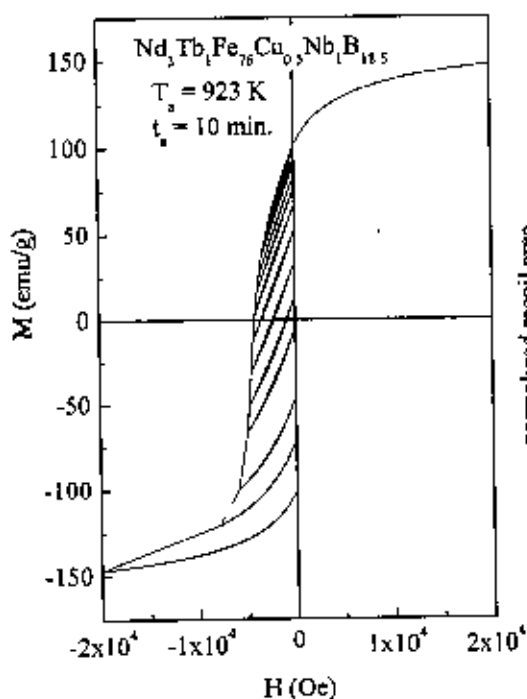


Fig. 6.3.6. Recoil hysteresis loops for  $\text{Nd}_3\text{Tb}_1\text{Fe}_{76}\text{Cu}_{0.5}\text{Nb}_1\text{B}_{18.5}$  sample annealed at 923 K for 10 min.

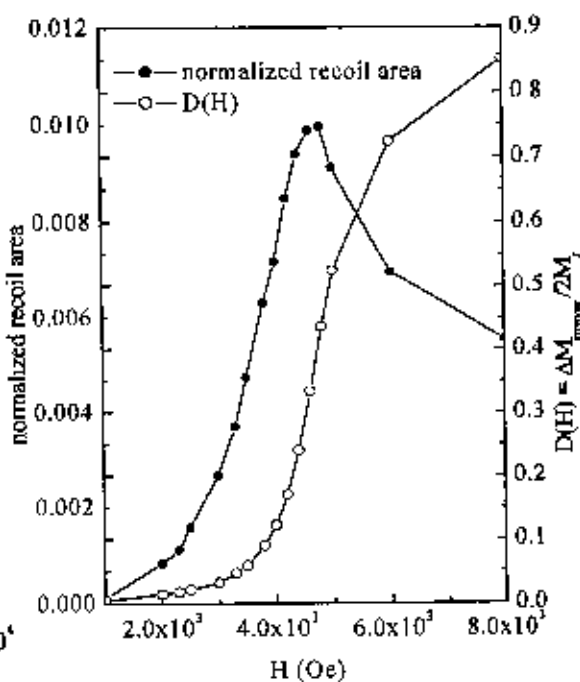


Fig. 6.3.7. Variation of irreversible component of magnetization  $D(H)$  and normalized recoil area with reverse field.

D

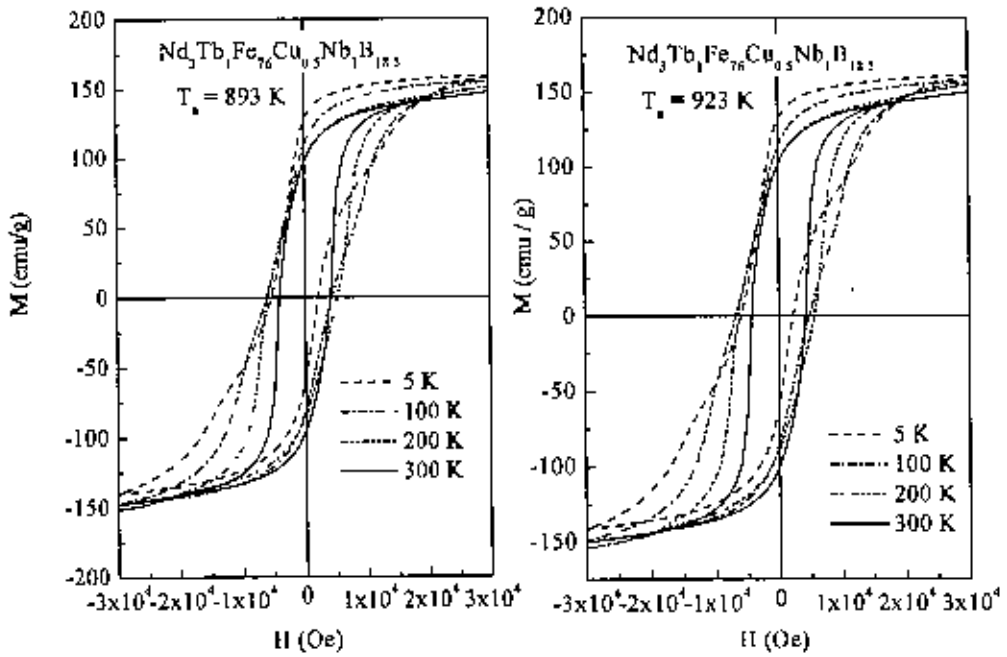


Fig. 6.3.8. Temperature dependence of hysteresis loops for samples annealed at 893 and 923 K.

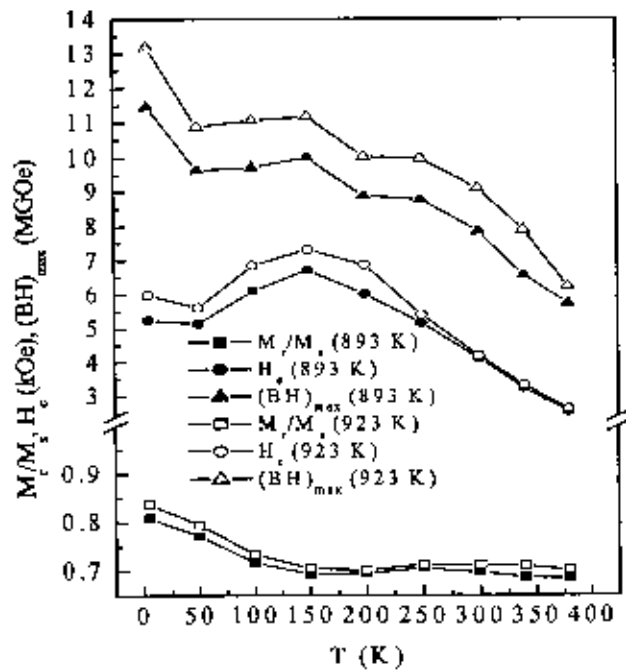


Fig. 6.3.9. Temperature dependence of hysteresis loop parameters for samples annealed at 893 and 923 K for 10 minutes

of the hysteresis loop changes below 150 K, which is related to a spin re-orientation in the hard phase that occurs at low temperatures [6, 7]. In ref. [8] it was observed that the hysteresis loop for  $\text{Nd}_2\text{Fe}_{14}\text{B}/\alpha\text{-Fe}$  becomes constricted below the spin reorientation temperature, i.e. with the decrease of temperature the magnetization curve becomes discontinuous at low field. The curves presented in Fig 6.3.8 shows a change in the shape of the hysteresis loop below 150 K, which agree with the previous measurements [6, 7, 8].

In Fig. 6.3.9, temperature dependence of the coercivity,  $H_c$ , the remanent ratio,  $\frac{M_r}{M_s}$  and maximum energy product,  $(BH)_{\text{max}}$  are plotted. Curves for both the samples show similar behavior. The coercivity increases with the decrease of temperature down to about 150 K. Below 150 K there is a change of the slope of  $H_c(T)$ . The decrease of the coercivity at low temperatures is related to the spin reorientation. This behavior of  $H_c(T)$  may be compared with that reported in ref. [9] in which a stronger decay of the coercivity at low temperatures is observed. The temperature dependence of remanent ratio,  $M_r/M_s$  and  $(BH)_{\text{max}}$  are also governed by the temperature dependence of anisotropy field which decrease with the increase of temperature because of easier domain wall motion due to the reduction of the anisotropy field at higher temperature.

## **Chapter 7**

### **Conclusions**



### Fe-based soft nanocomposite magnetic materials

Good correlation of crystallization and phase transition temperatures has been obtained between different experimental techniques of X-ray diffraction, differential thermal analysis and thermo-magnetic measurements for the alloy of composition  $\text{Fe}_{73}\text{Cu}_1\text{Nb}_{3.5}\text{Si}_{14}\text{B}_{8.5}$ ,  $\text{Fe}_{73.5}\text{Cu}_1\text{Ta}_3\text{Si}_{13.5}\text{B}_9$ ,  $\text{Fe}_{75.5}\text{Cu}_{0.6}\text{Nb}_{2.4}\text{Si}_{13}\text{B}_{8.5}$  close to original FINEMET composition. Activation energy of crystallization of different crystalline phases are sensitively dependent on Nb content having higher activation energy when Nb content is higher. Therefore, crystallization temperatures shift accordingly to higher and lower temperatures respectively for these two compositions. Whereas activation energy and crystallization temperatures of  $\text{Fe}_{73.5}\text{Cu}_1\text{Ta}_3\text{Si}_{13.5}\text{B}_9$  are close to original FINEMET.

Magnetic initial permeability of nanocrystalline / amorphous ribbon strongly depends on annealing temperatures and times. Short time annealing above the crystallization temperature leads to the improvement of soft magnetic properties and is better than that for long time annealing. The best magnetic properties have been observed for the optimized annealed condition. At lower annealing temperature, enhancement of permeability takes place due to the structural relaxation. Permeability drops to a lower value during the initiation of crystallization. An enhancement of initial permeability by two orders of magnitude was observed for the optimized annealed samples. The high permeability is attributed to the drastic decrease of effective anisotropy due to nanometric grain size effect and strong magnetic coupling. Decrease of magnetic permeability for a longer annealing time possibly is related to induced anisotropy.

Enhancement of Curie temperature was observed for samples annealed below the crystallization temperature due to structural relaxation. Curie temperature of the interfacial amorphous phase has decreased for samples annealed at and above the crystallization temperature due to the depletion of Fe and increase of relative amount of Nb/Ta in the residual amorphous phase. Temperature dependence of real part of initial permeability of the annealed samples between the annealing temperature of 773 and 848 K exhibits decoupling of magnetic moment between nanograins via residual amorphous matrix at  $T > T_c^*$  since residual amorphous matrix becomes paramagnetic within which ferromagnetic nanograins are embedded. When volume fraction of  $\alpha\text{-Fe}(\text{Si})$  nanograins are increased, dipolar and/or exchange interaction between nanograins via paramagnetic residual amorphous matrix would lead to finite value of permeability, which increases with the increase of the volume fraction of  $\alpha\text{-Fe}(\text{Si})$  nanograins. When the annealing temperature is increased further the temperature dependence of permeability is governed by the presence of iron boride phase. This experiment has been exploited as a practical tool for the identification of iron boride phase, which is difficult to identify by other phase identification techniques.

### Co-based soft nanocomposite magnetic materials

Magnetic softening and its correlation with giant magneto-impedance (GMI) effect have been investigated for  $\text{Co}_{68}\text{Fe}_4\text{Ni}_1\text{Si}_{15}\text{B}_{12}$  subjected to different annealing temperatures. In the as-cast condition the Curie

temperature of the sample is 503 K and saturation magnetization is 72.3 emu / gm. Very high value of initial permeability around  $59 \times 10^3$  and low value of relative loss factor around  $10^{-6}$  have been obtained for the annealing temperature of 693 K for 1 hr. The sensitivity of field dependence of the ratio of giant magneto-impedance (GMIR) for this annealing temperature is the highest at a current driving frequency of 4.5 MHz. From the X-ray diffraction and DSC results it has been observed that at the annealing temperature of 693 K for 1 hr. the ribbon is in fully amorphous state. The extraordinary soft magnetic properties at this annealing temperature are mainly due to the structural relaxation, which determines the profile of field dependence of GMIR.

Co-based amorphous alloys of compositions  $\text{Co}_{67}\text{Fe}_4\text{Ni}_2\text{Si}_{15}\text{B}_{12}$  and  $\text{Co}_{67}\text{Fe}_4\text{Mo}_7\text{Si}_{15}\text{B}_{12}$  exhibit superior soft magnetic properties after appropriate annealing at the initiation of crystallization temperature of the amorphous phase. It is to be noted that the annealing of the previous composition,  $\text{Co}_{68}\text{Fe}_4\text{Ni}_1\text{Si}_{15}\text{B}_{12}$  in the similar condition led to deterioration of soft magnetic properties. An extraordinary increase of initial permeability had occurred due to relaxation of the amorphous matrix. Ultra-soft magnetic properties for  $\text{Co}_{67}\text{Fe}_4\text{Ni}_2\text{Si}_{15}\text{B}_{12}$  and  $\text{Co}_{67}\text{Fe}_4\text{Mo}_7\text{Si}_{15}\text{B}_{12}$  manifested by enhanced initial permeability,  $\mu'$  is of the order of  $\sim 10^4$  and reduction of relative loss factor,  $\frac{\tan \delta}{\mu'}$  is of the order of  $\sim 10^{-6}$ , which have been achieved at

optimized annealing condition of respective compositions. This has been achieved because at this stage local anisotropy is averaged out by exchange coupling between nanograins embedded in the residual amorphous matrix. Field dependence of magneto-impedance measured for as-cast and annealed samples at current driving frequency of 4.5 MHz are around 220%. Field dependence of magneto-impedance show hysteresis at low field for both the compositions, which is related to the changes in the magnetization process of the sample.

#### Fe-based hard nanocomposite magnetic materials

Simultaneous additions of Cu and Nb in  $(\text{NdPr})_4\text{Fe}_{71}\text{Co}_5\text{Cu}_{0.5}\text{Nb}_1\text{B}_{18.5}$  gave rise to a stability of grain size of  $\text{Fe}_3\text{B}$ , which stabilized the hysteresis loop parameters for a wide range of annealing temperature. Reversible and irreversible magnetization behavior has been examined for  $(\text{NdPr})_4\text{Fe}_{71}\text{Co}_5\text{Cu}_{0.5}\text{Nb}_1\text{B}_{18.5}$  annealed at 873 and 973 K for 10 minutes by using recoil hysteresis and DCD technique. Recoil hysteresis loops are steep having small recoil area, which is a characteristic to exchange coupled system. For sample annealed at 873 K, the values of  $H_c$  have been found as 7.28 and 3.36 kOe at 5 and 300 K respectively. The values of  $(\text{BH})_{\text{max}}$  at 5 and 300 K are 13.72 and 9.39 MGOe and remanent ratios are 0.8 and 0.74 respectively.

The sample of composition  $\text{Nd}_4\text{Fe}_{73.5}\text{Co}_2\text{Hf}_{0.5}\text{Ga}_{0.5}\text{B}_{18.5}$  possesses high remanent ratio of around 0.82 and coercivity 2.62 kOe in the optimum annealing condition. The value of maximum energy product in the optimum annealing condition has been obtained as 11.05 MGOe using an applied field of 3 Tesla. Recoil hysteresis loops are steep and recoil loop areas are small, which indicates higher degree of reversibility for

the samples annealed at 923 K for 5, 10 and 20 minutes of annealing. However, areas of the recoil loops are progressively increased with the increase of annealing time. At the critical field i.e. at the field where onset of irreversibility takes place, the area enclosed by the recoil loop is maximum and recoil loop does not trace the major demagnetization curve. Temperature dependence of hysteresis curves exhibit variation in shape around the spin reorientation temperature of 135 K where field dependence of magnetization is discontinuous.

A partial substitution of Nd by Tb led to the enhancement of coercive field up to a value of 4.76 kOe for the sample annealed at 953 K for 10 minutes. Highest value of energy product of Tb-substituted  $(\text{Nd,Tb})_2\text{Fe}_{14}\text{B}/\text{Fe}_3\text{B}$  nanocomposite ribbons of the composition of  $\text{Nd}_3\text{Tb}_1\text{Fe}_{76}\text{Cu}_{0.5}\text{Nb}_1\text{B}_{12.5}$  is about 9.43 MGOe obtained for the sample annealed at 923 K for 10 minutes. Recoil hysteresis loops have been measured along the major demagnetization curve to observe reversible behavior of magnetization for the sample annealed at 923 K for 10 minutes. Temperature dependence of coercivity, remanent ratio and maximum energy product have been measured for the sample annealed at 893 and 923 K for 10 minutes. At 5 K, coercivity and energy product of the sample annealed at 893 K for 10 minutes found to be 5.2 kOe and 11.5 MGOe respectively. Whereas, coercivity and energy product of the sample annealed at 923 K for 10 minutes found to be 6 kOe and 13.1 MGOe respectively.

In conclusion it may be stated that when the grain size is reduced to submicron level, which is well below the exchange correlation length, the sample is exchange-biased which helps to tailor the material for the achievement of enhanced values of magnetic properties. Evolution of nanograins of different phases with magnetic properties are well synchronized. Thus, qualitative increment of soft and hard magnetic properties are observed for nanometric grain size, which has been achieved by controlled thermal treatment for different kind of compositions of soft and hard nanocomposite systems.

*References for Chapter 1*

- [1] Herzer, G. "Grain structure and magnetism of nanocrystalline ferromagnets" *IEEE Trans. Magn.* 25 (1989) 3327-3329; Herzer, G. "Grain size dependence of coercivity and permeability in nanocrystalline ferromagnets" *IEEE Trans. Magn.* 26 (1990) 1397-1402.
- [2] Buttino, G., Cecchetti, A., Poppi, M. "Magnetic softening and nanocrystallization in amorphous Co-rich alloys" *J. Magn. Magn. Mat.* 172 (1997) 147-152.
- [3] Betancourt, I., Jiménez, M., Aburto, S., Marquina, V., Gómez, R., Marquina, M. L., Ridaura, R., Mika, M., Valenzuela, R. "Nanocrystallization studies in Co-rich amorphous alloys" *J. Magn. Magn. Mat.* 140-144 (1995) 459-460.
- [4] Kneller, E. F. and Hawig, R. "The exchange-spring magnet: a new material principle for permanent magnets" *IEEE Trans. Magn.* 27 (1991) 3588-3600.
- [5] Kang, K., Lewis, L. H., Jiang, J. S. and Bader, S. D. "Recoil hysteresis of Sm-Co/Fe exchange-spring bilayers" *J. Appl. Phys.* 98 (2005) 113906(1)-(6).





## References for Chapter 2

- [1] Yoshizawa, Y., Oguma, S. and Yamauchi, K. "New Fe-based soft magnetic alloys composed of ultrafine grain structure" *J. Appl. Phys.* 64 (1988) 6044-6046.
- [2] Herzer, G. *Handbook of Magnetic Materials*, K. H. J. Buschow (ed.), Elsevier Science, Amsterdam, 1997, p. 417.
- [3] Kubrt, C. and Schultz, L. "Formation and magnetic properties of nanocrystalline mechanically alloyed Fe-Co and Fe-Ni" *J. Appl. Phys.* 73 (1993) 6588-6590.
- [4] Kulik, T., Horubala, T. and Matyja, H. "Flash annealing nanocrystallization of Fe-Si-B-based glasses" *Mater. Sci. Eng. A* 157 (1992) 107-112.
- [5] Hono, K., Hiraga, K., Wang, Q., Inoue, A. and Sakurai, R. *Acta Metall. Mater.* 40 (1992) 2137.
- [6] Hono, K. and Sakurai, T. "Atom probe studies of nanostructured alloys" *Appl. Surf. Sci.* 87-88 (1995) 166-178.
- [7] Ayers, J. D., Harris, V. G., Spague, J. A. and Blan, W. T. "On the role of Cu and Nb in the formation of nanocrystals in amorphous  $Fe_{71.5}Nb_3Cu_1Si_{13.5}B_9$ " *Appl. Phys. Lett.* 64 (1994) 974-976.
- [8] Köster, U., Schönemann, U., Blank-Bewerdorff, M., Brauer, S., Sutton, M. and Stephenson, G. B. "Nanocrystalline materials by crystallization of metal-metalloid glasses" *Mater. Sci. Eng. A* 133 (1991) 611-615.
- [9] Kataoka, N., Matsunaga, T., Inoue, A. and Masumoto, T. "Soft Magnetic Properties of bcc Fe-Au-X-Si-B (X=Early Transition Metal) Alloys with Fine Grain Structure" *Mater. Trans. JIM* 30 (1989) 947-950.
- [10] Yoshizawa, Y. and Yamauchi, K. "Magnetic properties of Fe-Cu-M-Si-B (M = Cr, V, Mo, Nb, Ta, W) alloys" *Mater. Sci. Eng. A* 133 (1991) 176-179.
- [11] Müller, M. and Matern, N. "The influence of refractory element additions on the magnetic properties and on the crystallization behaviour of nanocrystalline soft magnetic Fe-B-Si-Cu alloys" *J. Magn. Magn. Mater.* 136 (1994) 79-87.
- [12] Schäfer, R., Hubert, A. and Hezer, G. "Domain observation on nanocrystalline material" *J. Appl. Phys.* 69 (1991) 5325-5327.
- [13] Alben, R., Becker, J. J. and Chi, M. C. "Random anisotropy in amorphous ferromagnets" *J. Appl. Phys.* 49 (1978), 1653-1658.
- [14] Herzer, G. "Grain structure and magnetism of nanocrystalline ferromagnets" *IEEE Trans. Magn.* 25 (1989) 3327-3329; Herzer, G. "Grain size dependence of coercivity and permeability in nanocrystalline ferromagnets" *IEEE Trans. Magn.* 26 (1990) 1397-1402.
- [15] Herzer, G. "Magnetization process in nanocrystalline ferromagnets" *Mat. Sci. Eng. A* 133 (1991) 1-5.
- [16] Herzer, G. "Nanocrystalline soft magnetic materials" *J. Magn. Magn. Mat.* 157/158 (1996) 133-136.
- [17] Slawska-Waniewska, A., Gutowski, M., Lachowicz, H., Kulik, T. and Matyja, H. "Superparamagnetism in a nanocrystalline Fe-based metallic glass" *Phys. Rev. B.* 46 (1992) 14594-14597.
- [18] del Riego, L., El Ghannami, M., Dominguez, M., Conde, C. F., Conde, A. "Superparamagnetic behaviour of a nanocrystalline Fe(CrMo)SiBCuNb alloy" *J. Magn. Magn. Mat.* 196-197 (1999) 201-203.
- [19] Franco, V., Conde, C. F., Conde, A., Kiss, L. F. "Superparamagnetic behaviour in an  $Fe_{76}Cu_1Nb_3Si_{10.5}B_{9.5}$  alloy" *J. Magn. Magn. Mater.* 215-216 (2000) 400-403.
- [20] Kulik, T. and Hernando, A. "Magnetic properties of two-phase nanocrystalline alloy determined by anisotropy and exchange interactions through amorphous matrix" *J. Magn. Magn. Mater.* 138 (1994) 270-280.
- [21] Hernando, A. and Kulik, T. "Exchange interactions through amorphous paramagnetic layers in ferromagnetic nanocrystals" *Phys. Rev. B.* 49 (1994) 7064-7067.
- [22] Slawska-Waniewska, A., Kuzminski, M., Gutowski, M. and Lachowicz, H. K. *IEEE Trans. Magn.*, 29 (1993) 2628.
- [23] Buttino, G. Cecchetti, A. Poppi, M. "Magnetic softening and nanocrystallization in amorphous Co-rich alloys." *J. Magn. Magn. Mat.* 172 (1997) 147-152.

- [24] Quintana, P. Amano, E. Valenzuela, R. Irvine, J. T. S. "Effects of nanocrystallization upon the soft magnetic properties of Co-based amorphous alloys" *J. Appl. Phys.* 75 (1994) 6940-6942
- [25] Lee, H. Kim, Y. K. Kim, Y. B. "Soft Magnetic Properties of Co-Based Amorphous Alloy by Two-Step Cooling Method" *Phys. Stat. Sol. (a)* 189(3) (2002) 1073-1076
- [26] Bordin, G. Buttino, G. Cecchetti, A. Cecchetti, M. Poppi, M. "Influence of the structural instabilities on the anisotropy fields in Co-based amorphous alloys" *J. Magn. Magn. Mat* 153 (1996) 285-292.
- [27] Berancourt, I. Jiménez, M. Aburto, S. Marquina, V. Gómez, R. Marquina, M. L. Ridaura, R. Mika, M. Valenzuela, R. "Nanocrystallization studies in Co-rich amorphous alloys." *J. Magn. Magn. Mat* 140-144 (1995) 459-460.
- [28] D. Atkinson and P. T. Squire, "Phenomenological model for magnetoimpedance in soft ferromagnets" *J. Appl. Phys.* 83 (1998) 6569-6571.
- [29] Knobel, M. and Pirota, K. R. "Giant magnetoimpedance. concepts and recent progress" *J. Mag. Mag. Mater.* 242-245 (2002) 33-40.
- [30] R. Valenzuela, M. Knobel, M. Vazquez and A. Hernando, "An alternative approach to giant magnetoimpedance phenomena in amorphous ferromagnetic wires" *J. Appl. Phys.*, 78 (1995) 5189-5191.
- [31] Panina, L. V. and Mohri, K. "Magneto-impedance effect in amorphous wires" *Appl. Phys. Lett.* 65 (1994) 1189-1191.
- [32] Beach, R. S. and A. E. Berkowitz, "Giant magnetic field dependent impedance of amorphous FeCoSiB wire" *Appl. Phys. Lett.* 64 (1994) 3652-3654.
- [33] Machado, F. L., da Silva, B. L., Rezende, S. M. and Martins, C. S. "Giant ac magnetoimpedance in the soft ferromagnet  $Co_{70}Fe_{4}Si_{13}B_{10}$ " *J. Appl. Phys.* 75 (1994) 6563-6565.
- [34] Beach, R. S. and Berkowitz, A. E. "Sensitive field and frequency-dependent impedance spectra of amorphous FeCoSiB wire and ribbon (invited)." *J. Appl. Phys.* 76 (1994) 6209-6213.
- [35] Hu, J., Zhang, L., Qin, H., Wang, Y., Wang, Z. and Zhou, S. X. "Giant magnetoimpedance and permeability in CoFeNiSiB amorphous ribbon" *J. Phys. D: Appl. Phys.* 33(5) (2000) L45-L47.
- [36] Panina, L. V., Mohri, K., Bushida, K. and Noda, M. "Giant magneto-impedance and magneto-inductive effects in amorphous alloys (invited)" *J. Appl. Phys.* 76(10) (1994) 6198-6203.
- [37] Sommer, R. L. and Chien, C. L. "Role of magnetic anisotropy in the magnetoimpedance effect in amorphous alloys" *Appl. Phys. Lett.* 67 (6) (1995) 857-859
- [38] Kraus, L. and Knobel, M., Kane, S. N., Chiriac, H. "Influence of Joule heating on magnetostriction and giant magnetoimpedance effect in a glass covered CoFeSiB microwire" *J. Appl. Phys.* 85(8) (1999) 5435-5437.
- [39] Panina, L. V., Mohri, K. and Makhnovskiy, D. P. "Mechanism of asymmetrical magnetoimpedance in amorphous wires" *J. Appl. Phys.* 85(8) (1999) 5444-5446.
- [40] Pirota, K. R., Sartorelli, M. L., Knobel, M., Gutiérrez, J., Barandiarán, J. M. "Influence of induced anisotropy and magnetostriction on the giant magnetoimpedance effect and its aftereffect in soft magnetic amorphous ribbons" *J. Mag. Mag. Mat.* 202 (1999) 431-444.
- [41] Sinnecker, J. P., Tiberto, P., Kurlyandskaia, G. V., Sinnecker, E. H. C. P., Vázquez, M. "Hysteretic giant magneto impedance" *J. Appl. Phys.* 84(10) (1998) 5814-5816.
- [42] Hadjipanayis, G. C. and Gong, W. "Magnetic hysteresis in melt-spun Nd-Fe-Al-B-Si alloys with high remanence" *J. Appl. Phys.* 64 (1988) 5559-5561.
- [43] Schrefl, T., Fidler, J. and Kronmüller, H. "Remanence and coercivity in isotropic nanocrystalline permanent magnets" *Phys. Rev. B* 49 (1994) 6100-6110.
- [44] Manaf, A., Leonowicz, M., Davies, H. A. and Buckley, R. A. "Effect of grain size and microstructure on magnetic properties of rapidly solidified  $Fe_{82}Nd_{13}B_{4}S$  alloy" *J. Appl. Phys.* 70 (1991) 6366-6368.
- [45] Coehoorn, R., de Mooij, D. B., Duchateau, J. P. W. B. and Buschow, K. H. J. *J. de Phys.* 49 (1988) 669.
- [46] Manaf, A., Buckley, R. A., and Davies, H. A. "New nanocrystalline high-remnance Nd-Fe-B alloys by rapid solidification" *J. Magn. Magn. Mater.* 128 (1993) 302-306.
- [47] Withwanawasam, L., Hadjipanayis, G. C. and Hause, R. F. "Enhanced remanence in isotropic Fe-rich melt-spun Nd-Fe-B ribbons" *J. Appl. Phys.* 75 (1994) 6646-6648.

- [48] Kneller, E. F. and Hawig, R. "The exchange-spring magnet: a new material principle for permanent magnets." *IEEE Trans. Magn.* 27 (1991) 3588.
- [49] Coehoorn, R., de Mooij, D. B. and de Waard, C. "Meltspun permanent magnet materials containing  $Fe_3B$  as the main phase" *J. Magn. Magn. Mater.* 80 (1989) 101-104.
- [50] Buschow, K. H. J., de Mooij, D. B. and Coehoorn, R. "Metastable ferromagnetic materials for permanent magnets" *J. Less Common Metals* 145 (1988) 601-611.
- [51] Harland, C. L., Lewis, L. H., Chen, Z. and Ma, B. M. "Exchange coupling and recoil loop area in  $Nd_2Fe_{14}B$  nanocrystalline alloys" *J. Magn. Mag. Mater.* 271 (2004) 53-62.
- [52] Kang, K., Lewis, L. H., Jiang, J. S. and Badtr, S. D. "Recoil hysteresis of Sm-Co/Fe exchange-spring bilayers" *J. Appl. Phys.* 98 (2005) 113906(1)- 113906(7).

- [1] Kissinger, H. E. "Reaction Kinetics in Differential Thermal Analysis" *Analyt. Chem.* 29 (1957) 1702-1706.
- [2] Buzoroth, R. M. *Ferromagnetism*, (D. Van Nostrand Company, Inc. Princeton, New Jersey) p. 74 (1964)
- [3] Franco, V., Conde, C. F., Conde, A. "Changes in magnetic anisotropy distribution during structural evolution of  $Fe_{70}Si_{10.5}B_{9.5}Cu_1Nb_3$ " *J. Magn. Magn. Mat.* 185 (1998) 353-359.
- [4] Rubinstein, M., Harris, V. G., Lubitz, P. "Ferromagnetic resonance in nanocrystalline  $Fe_{73.5}Cu_1Nb_3Si_{13.5}B_9$  (Finemet)" *J. Magn. Magn. Mat.* 234 (2001) 306-312.
- [5] Franco, V., Conde, C. F., Conde, A., Kiss, L. F. "Superparamagnetic behaviour in an  $Fe_{70}Cu_1Nb_3Si_{10.5}B_{9.5}$  alloy" *J. Magn. Magn. Mater.* 215-216 (2000) 400-403
- [6] Mørup, S., Christensen, P. H. and Clausen, B. S. "Magnetic hyperfine splitting in superparamagnetic particles in external magnetic fields" *J. Magn. Magn. Mat.* 68 (1987) 160-170.
- [7] Lachowicz, H. K. and Slawska-Waniewska, A. "Coexistence of various magnetic phases in nanocrystalline Fe-based metallic glasses" *J. Magn. Magn. Mat.* 133 (1994) 238-242.
- [8] Pfeiffer, H. and Schüppel, W. *J. Magn. Magn. Mat.* "Temperature dependence of the magnetization in fine particle systems and the Hopkinson effect. Application to barium ferrite powders" 130 (1994) 92-98.
- [9] Herzer, G. *Handbook of Magnetic Materials*, Vol. 10, ed. K. H. J. Buschow (Elsevier Science B. V.) p. 417 (1997).
- [10] Herzer, G. "Grain structure and magnetism of nanocrystalline ferromagnets" *IEEE Trans. Magn.* 25 (1989) 3327-3329; Herzer, G. "Grain size dependence of coercivity and permeability in nanocrystalline ferromagnets" *IEEE Trans. Magn.* 26 (1990) 1397-1402.
- [11] He, K. Y., Sui, M. L., Liu, Y. and Zhao, B. F. "A structural investigation of a  $Fe_{73.5}Cu_1Nb_3Si_{13.5}B_9$  nanocrystalline soft magnetic material" *J. Appl. Phys.*, 75(7) (1994) 3684-3686.
- [12] Knobel, M., Sinnecker, J. P., Saenger, J. F., Sato Turtelli, R. "Initial magnetic permeability during the development of the nanocrystalline state in amorphous ribbons" *J. Mag. Mag. Mater.* 133 (1994) 255-258.
- [13] Berkowitz, A. E., Walter, J. L., Wall, K. F. "Magnetic Properties of Amorphous Particles Produced by Spark Erosion" *Phys. Rev. Lett.* 46 (1981) 1484-1487.
- [14] Lovas, A., Kiss, L.F., Balogh, I. "Saturation magnetization and a morphous Curie point changes during the early stage of amorphous-nanocrystalline transformation of a FINEMET-type alloy" *J. Mag. Mag. Mater.*, 215-216 (2000) 463-465.
- [15] Brzozka, K., Slawska-Waniewska, A., Gawronski, M., Jezuita, K. and Lachowicz, H. K. "Evolution of Mössbauer spectra with nanocrystallite content in  $Fe_{73.5}Cu_1Nb_3-Si_{13.5}B_9$  alloys" *J. Magn. Magn. Mat.* 140-144 (1995) 481.
- [16] Olzewski, A., Zbrozyczky, J., Olzewski, J., Ciurzyńska, W. H., Fukunaga, H., Narita, K., Wystocki, B., Hasiak, M., *J. Mag. Mag. Mater.* 215-216 (2000) 422.
- [17] Leu, M. S. and Chin, T. S. *MRS Symposium Proceedings*, "Quantitative crystallization and nano-grain size distribution studies of a nanocrystalline alloy" 577 (1999) 557-562.
- [18] Varga, L. K., Bakos, É., Kisdi-Kosztó, É., Zsoldos, É., Kiss, L. F. "Time and temperature dependence of nanocrystalline structure formation in a Finemet-type amorphous alloy" *J. Magn. Magn. Mater.* 133 (1994) 280-282.
- [19] Hakim, M. A. and Hoque, S. M. "Effect of structural parameters on soft magnetic properties of two phase nanocrystalline alloy of  $Fe_{73.5}Cu_1Ta_3Si_{13.5}B_9$ " *J. Magn. Magn. Mat.* 284 (2004) 395
- [20] Butvinová, B., Vlasák, G., Butvin, P., Illeková, E. "Magnetic properties and dilatation of  $FeNbCuBSi$  alloys" *Acta Phy. Slov.* 51(1) (2001) 1-7.

*References for Chapter 5*

- [1] Hauser, H., Kraus, L., Rípka, P. "Giant magnetoimpedance sensors" IEEE Instrum. Meas. Mag. 4 (2001), 28-32.
- [2] Betancourt, I., Jiménez, M., Aburto, S., Marquina, V., Gómez, R., Marquina, M. L., Ridaura, R., Mika, M., Valenzuela, R. "Nanocrystallization studies in Co-rich amorphous alloys" J. Magn. Magn. Mat. 140-144 (1995) 459-460.
- [3] Buttino, G., Cecchetti, A., Poppi, M. "Magnetic softening and nanocrystallization in amorphous Co-rich alloys" J. Magn. Magn. Mat. 172 (1997) 147-152.
- [4] Sinnecker, J. P., Tiberio, P., Kurlyandskaja, G. V., Sinnecker, E. H. C. P., Vázquez, M. and Hernando, A. "Hysteretic giant magneto impedance" J. Appl. Phys. 84(10) (1998) 5814-5816.
- [5] Panina, L. V., Mohri, K., Uchiyama, T., Noda, M. "Giant magneto-impedance in Co-rich amorphous wires and films" IEEE Trans. Magn. 31(2) (1995) 1249-1260.
- [6] Sommer, R. L. and Chien, C. L. "Role of magnetic anisotropy in the magnetoimpedance effect in amorphous alloys" Appl. Phys. Lett. 67(6) (1995) 857-859.
- [7] Hu, J., Zhang, L., Qm, H., Wang, Y., Zhou, S. X. "Giant magnetoimpedance and permeability in CoFeNiSiB amorphous ribbon" J. Phys. D : Appl. Phys. 33(5) (2000) L45-L47

### References for Chapter 6

- [1] Li, S. D., Sun, W. S. and Quan, M. X. "Crystallization and magnetic properties of melt-spun two-phase nanocrystalline Nd-Fe-B alloy" *Mat Lett.* 30 (1997) 351-355
- [2] Cho, Y. S., Kim, Y. B., Kim, C. S. and Kim, T. S. "Magnetic properties of new Nd-Fe-B nanocrystalline with  $\alpha$ -Fe as main phase" *IEEE Trans. Magn.* 32 (1996) 1964-1966.
- [3] Jurczyk, M., Collocott, S. J., Dunlop, J. B. and Gwan, P. B. "Magnetic properties of nanocomposite  $(Nd,Dy)_2(Fe, Co, Zr)_{14}B$  and  $Nd(Fe,Mo)_{12}N_x$  materials with an excess of Fe" *J. Phys. D:Appl Phys.* 29 (1996) 2284-2289.
- [4] Kneller, E. F. and Hawig, R. "The exchange-spring magnet: a new material principle for permanent magnets" *IEEE Trans. Magn.* 27 (1991) 3588-3600.
- [5] Kang, K., Lewis, L. H., Jiang, J. S. and Bader, S. D. "Recoil hysteresis of Sm-Co/Fe exchange-spring bilayers" *J. Appl. Phys.* 98 (2005) 113906(1)-(6).
- [6] Givord, D., Tenaud, P. and Viadieu, T. "Analysis of hysteresis loops in Nd-Fe-B sintered magnets" *J. Appl. Phys.* 60 (1986) 3263-3265.
- [7] Givord, D., Li, H. S. and Perrier, R. "Magnetic properties of  $Y_2Fe_{14}B$  and  $Nd_2Fe_{14}B$  single crystals" *Solid State Com.* 51 (1984) 857-860.
- [8] Hadjipanayis, G. C., Hall, C., Kim, A. *IEEE Trans. Magn.* "Temperature dependence of magnetic hysteresis in melt-spun and sintered Nd-Fe-B magnets" *MAG-23* (1987) 2533.
- [9] Hadjipanayis, G. C., Withanawasam, L. and Krause, R. F. "Nanocomposite  $R_2Fe_{14}B/\alpha$ -Fe permanent magnets" *IEEE Trans. Magn.* 31 (1995) 3596.
- [10] Harland, C. L., Lewis, L. H., Chen, Z. and Ma, B. M. "Exchange coupling and recoil loop areas in  $Nd_2Fe_{14}B$  nanocrystalline alloys" *J. Magn. Mag. Mater.* 271 (2004) 53-62.
- [11] Sagawa, M., Fujimura, S., Yamamoto, H., Matsuura, Y. "Permanent magnet materials based on the rare earth-ion-boron tetragonal compounds" *IEEE Trans. Magn. Mag-20* (1984) 1584-1589.

**List of Publications Related to This Thesis Work**

**International Refereed Journals**

1. M. A. Hakim and S. Manjura Hoque, "Effect of structural parameters on soft magnetic properties of two phase nanocrystalline alloy of  $Fe_{73.5}Cu_1Ta_3Si_{13.5}B_9$ ," J. Mag. Mag. Mat., Vol. 284, p. 395, 2004.
2. S. Manjura Hoque, M. A. Hakim, F. A. Khan and N. Chau, "Ultra-soft magnetic properties of devitrified  $Fe_{73.5}Cu_{0.6}Nb_{2.4}Si_{13}B_{8.3}$  alloy." Materials Chemistry and Physics, 101 (2007) 112.
3. S. Manjura Hoque, M. A. Hakim and F. A. Khan, "Magnetic softening and giant magneto-impedance effect of  $Co_{68}Fe_4Ni_1Si_{15}B_{12}$ ." Physica Status Solidi, 203 (2), (2005), 336-342.
4. S. Manjura Hoque, M. A. Hakim, F. A. Khan, "Enhanced initial permeability and magneto-impedance ratio of  $Co_{67}Fe_4Mo_2Si_{15}B_{12}$ ." Materials Letters 61 (2007) 1227.
5. S. Manjura Hoque, M. A. Hakim, F. A. Khan, "Structural and Magnetic Characterization of  $Co_{67}Fe_4Ni_2Si_{15}B_{12}$ " Physica B 390 (2007) 245.
6. S. Manjura Hoque, F. A. Khan and M. A. Hakim, "Exchange Spring Behavior of Nanocrystalline  $(NdPr)_4Fe_{71}Co_5Cu_{0.5}Nb_1B_{18.5}$ " Physica Status Solidi 204 (2007) 2461.
7. S. Manjura Hoque, M. A. Hakim, F. A. Khan and N. H. Dan, "Effect of Tb substitution on the magnetic properties of exchange-biased  $Nd_2Fe_{14}B/Fe_3B$ " J. Mater Sci. 42 (2007) 9415.
8. S. Manjura Hoque, M. A. Hakim, F. A. Khan and N. H. Nghi "Recoil Hysteresis and Temperature Dependence of Coercivity of  $Nd_4Fe_{73.5}Co_3Hf_{0.5}Ga_{0.5}B_{18.5}$ " Physica Status Solidi (in press) February 2007.

**National Refereed Journal**

9. S. Manjura Hoque, M. A. Hakim, F. A. Khan, M. A. Gafur, "Nanocrystalline Structure formation in  $Fe_{73.5}Cu_1Ta_3Si_{13.5}B_9$  Alloy Studied by Differential Thermal Analysis, Thermomagnetic Measurements and X-ray Diffraction" Nuclear Science and Applications Vol. 14(1), p. 61, 2005.
10. S. Manjura Hoque and M. A. Hakim, "Study of the hard nanocomposite  $R_2Fe_{14}B/Fe$  exchange coupled magnets." J. Bang. Acad. Sci. (accepted) April, 2005.
11. S. Manjura Hoque, M. A. Hakim, F. A. Khan and N. Chau, "Nanocrystalline Structure Formation of Fe-based Metallic Glass by Devitrification Followed by Appropriate Annealing" Nuclear Science and Applications Vol. 15(2), p. 8, 2006.
12. S. Manjura Hoque, M. A. Hakim, F. Alam Khan and M. A. Gafur, "Crystallization behavior and magnetic softness of devitrified Fe-based metallic glasses" Proceedings of 9<sup>th</sup> Asia Pacific Physics Conference, Hanoi 2004.
13. M. A. Hakim, S. Manjura Hoque, F. A. Khan, M. A. Gafur, "Structural characterization and thermomagnetic measurements of  $Fe_{73}Cu_1Nb_{3.5}Si_{14}B_{4.5}$ ." Nuclear Science and Applications Vol. 15(2), p. 75, 2006.

**Conference Reports**

1. **S. Manjura Hoque**, M. A. Hakim, F. A. Khan and N. Chau "Nanocrystalline structure formation of Fe-based metallic glass by densification" Regional Physics Conference, Feb 11-13, 2006, AECD, Bangladesh.
2. **S. Manjura Hoque**, M. A. Hakim and F. A. Khan "Effect of Exchange Spring Mechanism in Soft and Hard Nanocomposite  $(\text{NdPr})_4\text{Fe}_{71}\text{Co}_5\text{Cu}_{0.5}\text{Nb}_1\text{B}_{18.5}$ " Annual Conference of Bangladesh Physical Society, 4-5 May, 2007, Dhaka, Bangladesh.
3. **S. Manjura Hoque**, M. A. Hakim and F. A. Khan, "Recoil Hysteresis and Temperature Dependence of Magnetic Properties of Exchange-Biased  $(\text{NdPr})_4\text{Fe}_{71}\text{Co}_5\text{Cu}_{0.5}\text{Nb}_1\text{B}_{18.5}$  Nanocomposite Alloys" Diamond Jubilee symposium, 2-7 July, 2007, Indian Institute of Science, Bangalore, India.

**Seminars**

1. **S. Manjura Hoque**, "Exchange-biased  $\text{R}_2\text{Fe}_{14}\text{B}/\text{Fe}_3\text{B}$  based nanocomposite alloys" Physics New Auditorium, Mokarram Hussain Science Building, Dhaka University, 23 May, 2007.
2. **S. Manjura Hoque**, "Effect of Exchange Spring Mechanism in Soft and Hard Nanocomposite Alloys" Bangladesh University of Engineering and Technology, June, 2007.
3. **S. Manjura Hoque**, "Fe-based soft nanocomposite magnetic materials" Bangladesh University of Engineering and Technology, August, 2007.





ELSEVIER

Available online at [www.sciencedirect.com](http://www.sciencedirect.com)

SCIENCE @ DIRECT<sup>®</sup>

Journal of Magnetism and Magnetic Materials 284 (2004) 395–402

Journal of  
magnetism  
and  
magnetic  
materials

[www.elsevier.com/locate/jmmm](http://www.elsevier.com/locate/jmmm)

## Effect of structural parameters on soft magnetic properties of two phase nanocrystalline alloy of $\text{Fe}_{73.5}\text{Cu}_1\text{Ta}_3\text{Si}_{13.5}\text{B}_9$

M.A. Hakim\*, S. Manjura Hoque

*Magnetic Materials Division, Atomic Energy Centre, 4 Kazi Nazrul Islam Avenue, P.O. Box 164, Dhaka 1000, Bangladesh*

Received 11 May 2004, received in revised form 21 June 2004

Available online 29 July 2004

### Abstract

The rapidly quenched  $\text{Fe}_{73.5}\text{Cu}_1\text{Ta}_3\text{Si}_{13.5}\text{B}_9$  alloy has been annealed in a controlled way in the temperature range 400–700°C for 1 h in order to study the effect of structural parameters such as lattice parameter, grain size and silicon content of the nanocrystalline Fe(Si) grains on the initial permeability. Temperature and frequency dependence of initial permeability of amorphous and devitrified toroid shaped samples have been measured. Enhancement of Curie temperature of the amorphous alloys has been observed due to the irreversible structural relaxation. With the appearance of nanocrystalline phase the Curie temperature of the residual amorphous phase gradually decreases with the increase of annealing temperature. Temperature dependence of permeability of annealed samples in the temperature range of 500–575°C exhibits superparamagnetic and superferromagnetic behavior depending upon the volume fraction of nanograins.

© 2004 Elsevier B.V. All rights reserved.

PACS: 75.50.Tt

**Keyword:** Finemet; Nanocrystalline structure; Superparamagnetism; Superferromagnetism; Amorphous alloys

### 1. Introduction

A new class of Fe-based alloys exhibiting superior soft magnetic properties has been discovered for the first time by Yoshizawa et al [1]. Nanocrystalline phase evolving from amorphous

precursor by controlled annealing develops the unique properties with combination of the low losses, high permeability and near zero magnetostriction. The major requirements for superior soft magnetic properties are high initial permeability and extremely low coercivity, which is governed by a low or vanishing magnetocrystalline anisotropy. The anisotropy constant,  $K_1$  for  $\alpha\text{-Fe(Si)}$ , the constituent phase of  $\text{Fe}_{73.5}\text{Cu}_1\text{Ta}_3\text{Si}_{13.5}\text{B}_9$  is about  $8\text{ kJ/m}^3$ , which is by far too large to explain by

\*Corresponding author. Tel.: +880-2-8626603; fax: +880-2-8617946

E-mail address: [hakimaec@yahoo.com](mailto:hakimaec@yahoo.com) (M.A. Hakim).

# Ultra-soft magnetic properties of devitrified $\text{Fe}_{75.5}\text{Cu}_{0.6}\text{Nb}_{2.4}\text{Si}_{13}\text{B}_{8.5}$ alloy

S. Manjura Hoque<sup>a,\*</sup>, M.A. Hakim<sup>a</sup>, F.A. Khan<sup>b</sup>, N. Chau<sup>c</sup>

<sup>a</sup> Magnetic Materials Division, Atomic Energy Centre, P.O. Box 164, Dhaka 1000, Bangladesh

<sup>b</sup> Department of Physics, Bangladesh University of Engineering and Technology, Dhaka 1000, Bangladesh

<sup>c</sup> Centre for Materials Science, Hanoi University of Technology, Hanoi, Vietnam

Received 3 October 2005; received in revised form 23 January 2006; accepted 20 February 2006

## Abstract

Temperature dependence of real part initial permeability ( $\mu'$ ) of  $\text{Fe}_{75.5}\text{Cu}_{0.6}\text{Nb}_{2.4}\text{Si}_{13}\text{B}_{8.5}$  has been measured with different crystalline state of the material. Enhanced value of initial permeability by two orders of magnitude and very low value of relative loss factor of the order of  $10^{-5}$  has been observed with the variation of annealing temperature and time, which shows that Fe-based alloys of this composition with lower Cu and Nb content also bears ultra-soft magnetic properties like conventional FINEMET. The results have been correlated with the volume fraction of amorphous and crystalline phases obtained by differential scanning calorimetry. Temperature dependence of initial permeability curve for the annealing temperature,  $T_a < 475^\circ\text{C}$ , is characterized by the single amorphous phase. The curve is characterized by the two-phase structure for  $475^\circ\text{C} < T_a < 625^\circ\text{C}$ . The curve is characterized by presence of iron boride phase for  $T_a > 625^\circ\text{C}$ .

© 2006 Elsevier B.V. All rights reserved.

PACS: 75.50 Tt

Keywords: Finemet; Nanostructured materials; Magnetization; Differential scanning calorimetry; Initial permeability

## 1. Introduction

In the devitrified condition of  $\text{Fe}_{75.5}\text{Cu}_{0.6}\text{Nb}_{2.4}\text{Si}_{13}\text{B}_{8.5}$ , small crystallites are exchange coupled through residual amorphous matrix resulting in magnetic softening which leads to a steep increase of permeability with decreasing grain size [1,2]. The crucial role of exchange interaction is clearly evident in the temperature dependence of permeability of these two-phase alloys if the measuring temperature exceeds the Curie temperature of the amorphous matrix ( $T > T_c^{\text{am}}$ ) where the residual amorphous matrix becomes paramagnetic. For  $T > T_c^{\text{am}}$ , superparamagnetic/superferromagnetic behavior has been reported by several authors [3–6] depending on the volume fraction of crystallites controlled by annealing temperature, distance between the crystallites and thickness of intergranular layer of the paramagnetic amorphous matrix.

The aim of our present study is to observe magnetic softness characterized by initial permeability of devitrified  $\text{Fe}_{75.5}\text{Cu}_{0.6}\text{Nb}_{2.4}\text{Si}_{13}\text{B}_{8.5}$  and to study temperature dependence of initial permeability with different volume fraction by con-

trolled annealing. In our present work, phase transition temperatures and kinetics of crystallization of  $\text{Fe}_{75.5}\text{Cu}_{0.6}\text{Nb}_{2.4}\text{Si}_{13}\text{B}_{8.5}$  has been studied by differential scanning calorimetry. Temperature dependence of permeability has been measured in the amorphous and nanocrystalline state with different volume fraction of amorphous and nanocrystalline phases. Differential scanning calorimetry and temperature dependence of magnetization has been performed in order to study phase transition temperatures and kinetics of crystallization. Annealing temperature and annealing time dependence of initial permeability has been measured to observe extent of magnetic softness.

## 2. Experimental

Ribbons of composition  $\text{Fe}_{75.5}\text{Cu}_{0.6}\text{Nb}_{2.4}\text{Si}_{13}\text{B}_{8.5}$  have been prepared by rapid solidification technology with a dimension of 10 mm width and 25  $\mu\text{m}$  thickness. The purity of the material is Fe (99.98%), Cu (99.4%), Nb (99.8%), B (99.5%) and Si (99.9%) as obtained from Johnson Mathey (Alfa Aesar Inc.). Amorphosity of the ribbon and nanocrystalline structure has been studied by Bruker D5005 X-ray diffractometer, Germany with Cu K $\alpha$  radiation. Crystallization behavior has been performed using 2960 SDT Differential Scanning Calorimetry, USA. Temperature dependence of magnetization has been performed using 880 DMS Vibrating Sample Magnetometer, USA. Measurement of temperature dependence of initial permeability has been carried out by laboratory built furnace and Wayne Kerr 3255 B Impedance Analyzer.

\* Corresponding author. Tel.: +880 2 8626603; fax: +880 2 8617946.  
E-mail address: [manjura.hoque@yahoo.com](mailto:manjura.hoque@yahoo.com) (S. Manjura Hoque).

## Magnetic softening and giant magneto-impedance effect of $\text{Co}_{68}\text{Fe}_4\text{Ni}_1\text{Si}_{15}\text{B}_{12}$

S. Manjura Hoque<sup>1,1</sup>, M. A. Hakim<sup>1</sup>, and F. A. Khan<sup>2</sup>

<sup>1</sup> Magnetic Materials Division, Atomic Energy Centre, P.O. Box 164, Dhaka 1000, Bangladesh

<sup>2</sup> Department of Physics, Bangladesh University of Engineering and Technology, Bangladesh

Received 5 April 2005, revised 27 September 2005, accepted 28 October 2005

Published online 23 December 2005

PACS 75.50.Bb, 75.50.Kj, 75.60.Nc

Magnetic softening and its correlation with the giant magneto-impedance effect have been investigated for  $\text{Co}_{68}\text{Fe}_4\text{Ni}_1\text{Si}_{15}\text{B}_{12}$  subjected to different annealing temperatures. In the as-cast condition the Curie temperature is 230 °C and the saturation magnetization is 72.3 emu/g. A very high value of initial permeability of around  $59 \times 10^3$  and a low value of relative loss factor of the order of  $10^{-6}$  have been obtained for samples annealed at 420 °C for 1 h. The sensitivity of the field dependence of the giant magneto-impedance ratio (GMIR) for this annealing temperature is higher than that for as-cast and other annealed samples. From X-ray diffraction and differential scanning calorimetry results it has been found that for samples annealed at 420 °C for 1 h the ribbon is in a fully amorphous state. The extraordinary soft magnetic properties at this annealing temperature are mainly due to the structural relaxation, which determines the profile of the field dependence of the GMIR.

© 2006 WILEY-VCH Verlag GmbH & Co. KGaA, Weinheim

### 1 Introduction

Magneto-impedance (MI) consists of a change of total impedance of a magnetic conductor under the application of a static magnetic field  $H_{dc}$ . When an ac current flows through a material, it generates a transverse magnetic field. At low frequencies of 1–10 kHz, the change in the transverse magnetization generates an additional inductive voltage across the conductor which can be expressed as  $V = RI + V_L$ , where  $R$  is the resistance and  $V_L$  is the magneto-inductive voltage. MI can be written as  $Z = R + j\omega\mu I$ , where the imaginary part is given by the ratio of magnetic flux to ac current and the field-dependent MI is related to the transverse permeability. With an increase of frequency in the range 0.1–10 MHz, the current is distributed near the surface of the conductor, changing both the resistive and inductive components of the total voltage  $V$ . The field dependence of MI is governed by the skin depth  $\delta = \sqrt{2\rho/\omega\mu}$ , where  $\rho$  is the resistivity and  $\mu$  is the permeability of the material. The current distribution is governed by the shape of the conductor, the frequency and the transverse magnetization depending on  $H_{dc}$ .

A very large change of the impedance occurs with an external dc magnetic field  $H_{dc}$ . The change expressed in terms of the giant magneto-impedance ratio (GMIR) is as follows:

$$\text{GMIR (\%)} = 1 - \frac{Z(H_{dc})}{Z(H_{max})} \times 100$$

\* Corresponding author: e-mail: manjura\_hoque@yahoo.com, Phone: +880 2 8626603, Fax: +880 2 8617946

# Structural and magnetic characterization of $\text{Co}_{67}\text{Fe}_4\text{Ni}_2\text{Si}_{15}\text{B}_{12}$

S. Manjura Hoque<sup>a,\*</sup>, F.A. Khan<sup>b</sup>, M.A. Hakim<sup>a</sup>

<sup>a</sup>Magnetic Materials Division, Atomic Energy Centre, P.O. Box-164, Dhaka 1000, Bangladesh

<sup>b</sup>Department of Physics, Bangladesh University of Engineering and Technology, Bangladesh

Received 31 May 2006; received in revised form 2 August 2006; accepted 16 August 2006

## Abstract

Soft magnetic properties of Co-based amorphous alloy of the composition  $\text{Co}_{67}\text{Fe}_4\text{Ni}_2\text{Si}_{15}\text{B}_{12}$  have been investigated by isothermal heat treatment up to the conventional crystallization temperature. In the as-cast condition the Curie temperature of the sample is 272 °C and saturation magnetization is 74 emu/g. Magnetic properties undergo variation depending on the heat treatment temperature. For the heat treatment temperatures of around 420 and 490 °C, superior soft magnetic properties are obtained. For both the temperatures initial permeability,  $\mu'$  reaches value up to ten times the value of permeability in the as-received samples. Annealing effect on giant magneto-impedance has been observed for the current-driving frequencies of 4.5 and 6 MHz. Field dependence of magneto-impedance shows hysteresis at low field, which is related to the changes in the magnetization process of the sample.

© 2006 Elsevier B.V. All rights reserved.

PACS: 75.52.Kj; 75.60.Nt

Keywords: Co-based amorphous alloys; Soft magnetic materials; Giant magneto-impedance; Initial permeability; Hysteresis loop

## 1. Introduction

In recent studies it has been found that heat treatment below the crystallization temperature in the Co-based amorphous alloy of different composition gave rise to the formation of nanocrystalline phase with grain size of about 2 nm, which has been revealed by TEM [1,2]. According to Ref. [3], the formation of the nanocrystalline phase in the Fe-based alloy containing Cu, annealed above the crystallization temperature, gives rise to the reduction of effective anisotropy because the random oriented anisotropies are averaged out by exchange interaction. Similar effect is believed to exist in the Co-based alloy in the early stage of crystallization [4–6].

In this work the aim is to analyze the possible formation of nanocrystalline phases and the relative softening of the magnetic properties in the amorphous alloy by appropriate thermal treatment. Since enhanced magneto-impedance is a characteristic property of Co-rich amorphous alloy we have also investigated the annealing effect on magneto-

impedance at a current-driving frequency of 4.5 and 6 MHz.

## 2. Experimental

The alloy with composition of  $\text{Co}_{67}\text{Fe}_4\text{Ni}_2\text{Si}_{15}\text{B}_{12}$  has been prepared by using Fe(99.98%), Cu(99.9%), Ni(99.9%), Si(99.9%) and B(99.5%) of Johnson Mathey and Co(99.8%) of Chempur Feinchemikalien. The alloy in the form of ribbon with a width of 5 mm and a thickness of 25  $\mu\text{m}$  was prepared by the rapid quenching method. The samples were annealed at 13 different temperatures up to 530 °C for 30 min for studying the annealing effect on permeability. The permeability has been measured on toroidal shaped samples using HP 4192A impedance analyzer with an applied AC field of  $10^{-3}$  Oe. The GMI effect is measured by using the GMI measuring setup with the applied magnetic field ranging from –300 to +300 Oe and operating frequencies of 4.5 and 6 MHz.  $B$ - $H$  loop measurements have been performed with Walker AMH 20  $B$ - $H$  loop tracer. Temperature and field dependence of magnetization has been performed by 880 DMS vibrating

\*Corresponding author. Tel.: +88028626603; fax: +88028617946.

E-mail address: [manjura\\_hoque@yahoo.com](mailto:manjura_hoque@yahoo.com) (S. Manjura Hoque)

## Enhanced initial permeability and magneto-impedance ratio of $\text{Co}_{67}\text{Fe}_4\text{Mo}_2\text{Si}_{15}\text{B}_{12}$

S. Manjura Hoque<sup>a,\*</sup>, F.A. Khan<sup>b</sup>, M.A. Hakim

<sup>a</sup> Magnetic Materials Division, Atomic Energy Centre, P. O. Box 164, Dhaka 1000, Dhaka 1000, Bangladesh

<sup>b</sup> Department of Physics, Bangladesh University of Engineering and Technology, Dhaka 1000 Bangladesh

Received 18 March 2006; accepted 1 July 2006

Available online 21 July 2006

### Abstract

Co-based amorphous alloy exhibits superior soft magnetic properties after appropriate annealing treatment below the crystallization temperature by devitrification of the amorphous phase. The initiation of crystallization temperature has been found as 518 °C from differential thermal analysis for the heating rate of 10 °C/min. Ultra-soft magnetic properties manifested by enhanced initial permeability,  $\mu'$  of the order of  $5.1 \times 10^4$  and reduction of relative loss factor,  $\tan \delta/\mu'$  of the order of  $9 \times 10^{-6}$ , has been achieved for the annealing temperature of 500 °C for 30 min. This has been achieved because at this stage local anisotropy is averaged out by exchange coupling between nanograins embedded in the residual amorphous matrix. Since enhanced magneto-impedance is a typical characteristic of Co-based amorphous alloy, field dependence of magneto-impedance has been measured for as-cast and annealed samples at current driving frequency of 4.5 MHz. Field dependence of magneto-impedance shows hysteresis at low field, which is related to the changes in the magnetization process of the sample

© 2006 Elsevier B.V. All rights reserved

PACS: 75.52 KJ, 75.60 Nt

Keywords: Co-based amorphous alloys; Soft magnetic materials; Giant magneto-impedance; Initial permeability; Relative loss factor

### 1. Introduction

Thermal treatments of amorphous materials below their crystallization temperature relaxes the amorphous structure giving rise to ultra-soft magnetic properties. Changes in the pre-existing anisotropy direction have been observed in some cases due to the rearrangement of the atom pairs during heat treatment even in the absence of external magnetic field and applied stresses [1]. In the recent studies, it was found that heat treatment below the crystallization temperature in the Co-based amorphous alloy gave rise to the formation of nanocrystalline phase with grain size of about 2 nm, revealed by TEM [1] leading to very high value of initial permeability. According to Horzler [2,3], the formation of the nanocrystalline phase in the Fe-based alloy containing Cu, annealed above the crystallization temperature, gives rise to a reduction of the effective anisotropy because the random oriented anisotropies are averaged out by

exchange interaction. A similar effect is believed to exist in the Co-based alloy in the early stage of crystallization [4–7].

In this work the aim is to analyze the possible formation of nanocrystalline phases and the relative softening of the magnetic properties in the amorphous alloy by appropriate thermal treatment. Since enhanced magneto-impedance is a characteristic property of Co-rich amorphous alloy we have also investigated the annealing effect on magneto-impedance in amorphous relaxed state at current driving frequency of 4.5 MHz.

### 2. Experimental

The alloy with composition  $\text{Co}_{67}\text{Fe}_4\text{Mo}_2\text{Si}_{15}\text{B}_{12}$  in the form of ribbon with a width of 5 mm and a thickness of 25  $\mu\text{m}$  was prepared by the rapid quenching method. Characterization of samples in the as-cast and annealed condition has been performed by differential thermal analysis and X-ray diffraction. The samples were annealed at thirteen different temperatures up to 530 °C for 30 min of holding time for studying the annealing

\* Corresponding author. Tel.: +880 2 8626603; fax: +880 2 8617946.

E-mail address: [manjura\\_hoque@yahoo.com](mailto:manjura_hoque@yahoo.com) (S. Manjura Hoque)

## Exchange-spring behavior of nanocrystalline (NdPr)<sub>4</sub>Fe<sub>71</sub>Co<sub>5</sub>Cu<sub>0.5</sub>Nb<sub>1</sub>B<sub>18.5</sub>

S. Manjura Hoque<sup>1</sup>, F. A. Khan<sup>2</sup>, and M. A. Hakim<sup>1</sup>

<sup>1</sup> Materials Science Division, Atomic Energy Center, Dhaka 1000, Bangladesh

<sup>2</sup> Department of Physics, Bangladesh University of Engineering and Technology, Dhaka 1000, Bangladesh

Received 4 December 2006, revised 13 February 2007, accepted 15 March 2007

Published online 23 May 2007

PACS 75.50.Bb, 75.50.Tt, 75.60.Ej, 75.60.Jk

An amorphous alloy of composition (NdPr)<sub>4</sub>Fe<sub>71</sub>Co<sub>5</sub>Cu<sub>0.5</sub>Nb<sub>1</sub>B<sub>18.5</sub> prepared by a melt spinning technique in an argon atmosphere has been studied to observe exchange-spring behavior in the nanocrystalline state. Hysteresis loop measurements at room temperature revealed that the highest value of the coercivity,  $H_c$ , of 4.08 kOe has been obtained for the sample annealed at 913 K for 10 min. At this annealing temperature  $(BH)_{max}$  and  $M_r/M_s$  have been found to be 11.06 MGOe and 0.716, respectively. Steep recoil curves of the samples annealed at 873 and 973 K show typical characteristics of the exchange-spring mechanism having smaller loop area. The temperature dependences of  $H_c$ ,  $M_r/M_s$  and  $(BH)_{max}$  in the range of 5 to 380 K generally decrease with the increase of temperature. From the temperature dependence of the hysteresis loop parameters, it has been found that at 5 K the values of  $H_c$  and  $(BH)_{max}$  are 6.89 kOe and 13.72 MGOe respectively for the sample annealed at 873 K for 10 min and 6.69 kOe and 13.74 MGOe respectively for the sample annealed at 923 K for 10 min. A change in the shape of the hysteresis loops was observed at temperatures below 100 K, related to the spin reorientation in the hard magnetic phase.

© 2007 WILEY-VCH Verlag GmbH & Co. KGaA, Weinheim

### 1 Introduction

Nanocomposite magnets consisting of a uniform mixture of exchange-coupled soft and hard magnetic phases are characterized by their unique combination of high saturation magnetization provided by the soft phase and high coercive field provided by the hard phase [1–6]. Besides high reduced remanence such systems possess a high energy product  $(BH)_{max}$  and a reversible demagnetization curve, which has been called exchange-spring behavior. High reduced remanence characteristic to these materials arises from exchange coupling of magnetic moments across the interface between two phases. This causes the magnetic moments of both the phases to remain in the same direction. It has been demonstrated earlier by Kneller and Hawig [1] that the enhancement of the remanence and coercivity by this mechanism is mainly governed by the crystallite sizes of both phases, in particular the soft phase, which can be controlled by dopants and/or additives and also by controlling heat treatment.

Studies [2–4] of macroscopic reversible and irreversible magnetic behavior in nanocrystalline exchange-coupled two-phase permanent magnetic materials demonstrate relatively steep recoil curves, which possess recoil permeabilities five times greater than those in conventional sintered magnets [1]. By using the demagnetization remanence (DCD) technique it has been demonstrated that when a negative field (lower than the critical field for magnetization reversal of the hard phase) is applied to a previously saturated sample, a near-reversible rotation of the soft-phase magnetization is obtained when the field is decreased back to zero, giving rise to the high recoil permeability.

\* Corresponding author; e-mail: manjura\_hoque@yahoo.com, Phone: +880-2-8626603, Fax: +880-2-8617946

## Effect of Tb substitution on the magnetic properties of exchange-biased $\text{Nd}_2\text{Fe}_{14}\text{B}/\text{Fe}_3\text{B}$

S. Manjura Hoque · M. A. Hakim · F. A. Khan ·  
N. H. Dan

Received: 22 February 2007 / Accepted: 25 May 2007 / Published online: 27 July 2007  
© Springer Science+Business Media, LLC 2007

**Abstract** Tb-substituted  $(\text{Nd,Tb})_2\text{Fe}_{14}\text{B}/\text{Fe}_3\text{B}$  nanocomposite ribbons have been synthesized by melt spinning of  $\text{Nd}_3\text{Tb}_1\text{Fe}_{76}\text{Cu}_{0.5}\text{Nb}_1\text{B}_{18.5}$  alloys. Tb substitution has significantly enhanced the value of coercivity and Curie temperature. Highest value of coercivity has been obtained as 4.76 kOe for the sample annealed at 953 K for 10 min. Curie temperature of Tb substituted sample,  $\text{Nd}_3\text{Tb}_1\text{Fe}_{76}\text{Cu}_{0.5}\text{Nb}_1\text{B}_{18.5}$  is 549 K while Curie temperature of the sample without Tb,  $\text{Nd}_4\text{Fe}_{76}\text{Cu}_{0.5}\text{Nb}_1\text{B}_{18.5}$  is 535 K. Recoil hysteresis loops measured along the major demagnetization curve are steep having small recoil loop area. Temperature dependence of coercivity, remanent ratio and maximum energy product have been measured for the sample annealed at 893 K and 923 K for 10 min. At 5 K, coercivity and maximum energy product of the sample annealed at 893 K for 10 min are 5.2 kOe and 11.5 MGOe respectively and the sample annealed at 923 K for 10 min are 6 kOe and 13.1 MGOe respectively.

### Introduction

Nd-deficient  $\text{Nd}_2\text{Fe}_{14}\text{B}/\text{Fe}_3\text{B}$  based nanocomposite alloys are characterized by their exchange-spring behavior

resulting in remanent ratio  $> 0.5$ , which is highly desirable for permanent magnet development. Magnetic properties of exchange spring magnets are governed by the soft and hard magnetic phases that develop under appropriate annealing condition. High reduced remanence characteristic to these materials arises from exchange coupling of magnetic moments across the interface between two phases. Besides high reduced remanence such systems possess high energy product  $(BH)_{\text{max}}$  and a reversible demagnetization curve, which has been called as exchange-spring behavior. This causes the magnetic moments of both the phases to remain in the same direction. It has been demonstrated earlier by Kneller and Hawig [1] that the enhancement of remanence and coercivity by this mechanism is mainly governed by the crystallite sizes of both the phases in particular the soft phase, which can be controlled by dopants and/or additives and also by controlling heat treatment. Compared to single phase  $\text{Nd}_2\text{Fe}_{14}\text{B}$ , nanocomposite  $\text{Nd}_2\text{Fe}_{14}\text{B}/\text{Fe}_3\text{B}$  based alloys are economic and corrosion resistant. Various dopants and substituents have been used to enhance the value of coercivity. A partial substitution of Nd by heavy rare earth elements like Tb increases the anisotropy field,  $H_A$  which enhances the coercive field, but decreases strongly the remanence due to its antiferromagnetic coupling between rare earth and the transition metal [2]. Tb addition has previously been used to increase the coercivity of  $\text{Pr}_2\text{Fe}_{14}\text{B}$  due to higher anisotropy field of  $\text{Tb}_2\text{Fe}_{14}\text{B}$  [3].

Studies [4–6] of macroscopic reversible and irreversible magnetic behavior in nano-crystalline exchange coupled two-phase permanent magnetic materials demonstrate relatively steep recoil curves, which possess recoil permeabilities five times greater than those in conventional sintered magnets [1]. By using the demagnetization remanence (DCD) technique it has been demonstrated that when a negative field (lower than the critical field for magnetization

S. M. Hoque (✉) · M. A. Hakim  
Materials Science Division, Atomic Energy Center, Dhaka 1000,  
Bangladesh  
e-mail: manjura\_hoque@yahoo.com

F. A. Khan  
Department of Physics, Bangladesh University of Engineering  
and Technology, Dhaka 1000, Bangladesh

N. H. Dan  
Institute of Materials Science, Vietnamese Academy of Science  
and Technology, Hanoi, Vietnam

# Recoil hysteresis and temperature dependence of coercivity of $\text{Nd}_4\text{Fe}_{73.5}\text{Co}_3\text{Hf}_{0.5}\text{Ga}_{0.5}\text{B}_{18.5}$

S. Manjura Hoque<sup>1</sup>, M. A. Hakim<sup>1</sup>, F. A. Khan<sup>2</sup>, and N. H. Nghi<sup>3</sup>

<sup>1</sup> Materials Science Division, Atomic Energy Center, Dhaka, Bangladesh

<sup>2</sup> Department of Physics, Bangladesh University of Engineering and Technology, Dhaka, Bangladesh

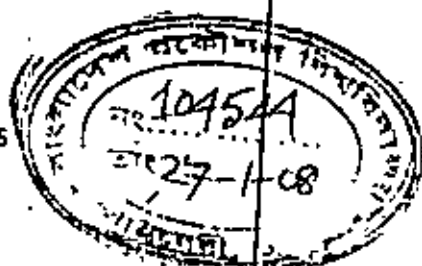
<sup>3</sup> Institute of Engineering Physics, Hanoi University of Technology, Hanoi, Vietnam

Received 14 February 2007, revised 19 July 2007, accepted 2 October 2007

Published online 13 December 2007

PACS 75.50.Bb, 75.50.Tt, 75.60.Ej, 75.60.Jt

\*Corresponding author: e-mail manjura\_hoque@yahoo.com, Phone: +880-2-8626603, Fax: +880-2-8617946



Recoil hysteresis and temperature dependence of coercivity have been measured for the sample of composition  $\text{Nd}_4\text{Fe}_{73.5}\text{Co}_3\text{Hf}_{0.5}\text{Ga}_{0.5}\text{B}_{18.5}$  prepared by rapid quenching method with a wheel speed of 25 m/s and after subsequent annealing in an evacuated quartz tube under a pressure of  $10^{-5}$  mbar at different temperatures and times. In the optimum and over annealed condition, recoil hysteresis loops have been measured by the application of progressively increasing negative field and successive withdrawal to the remanence and found to have steep recoil loop and small recoil area, which is characteristic to exchange-biased system. Temperature dependence of coercivity in the range of 5 K to 350 K has been measured for the sample of composition  $\text{Nd}_4\text{Fe}_{73.5}\text{Co}_3\text{Hf}_{0.5}\text{Ga}_{0.5}\text{B}_{18.5}$ . Variation in the shape of the hysteresis loop has been observed in this temperature range. In the low temperature region i.e. below 150 K, hysteresis loops are constricted due to spin reorientation of  $\text{Nd}_2\text{Fe}_{14}\text{B}$  at 135 K while above this temperature the hysteresis loops are characterized by convex  $M(H)$  curve similar to single-phase permanent magnet.

© 2007 WILEY-VCH Verlag GmbH & Co. KGaA, Weinheim

**1 Introduction** Neodymium deficient Nd–Fe–B based alloys have drawn considerable attention because of their high isotropic remanence, coercivity and energy product in addition to low cost and chemical stability [1–6] compared to single phase  $\text{Nd}_2\text{Fe}_{14}\text{B}$ . Significant efforts are still being provided to enhance remanent ratio, coercivity and energy product by controlling microstructure using thermal treatment and various substituents and/or dopants. Fidler and Schrefl [7] presented an overview of various methods, which are followed to enhance hysteresis loop parameters. There are substituent elements, which replace rare earth or transition metal to change the intrinsic properties, such as saturation magnetization, Curie temperature and magnetocrystalline anisotropy. Elements like Pt, Dy, Tb or Co, Ni, Cr fall into the category of substituents elements. Dopants, which show less solubility within the hard magnetic phase, are segregated in the grain boundary and inhibit grain growth. Fidler and Schrefl [7] performed systematic transmission electron microscopy studies on sin-

tered, melt spun, mechanically alloyed and hot worked magnets and found that two different types of dopants can be distinguished independently of the processing routes which influence the microstructure in a different way. Type 1 dopants, which include Al, Cu, Zn, Ga, Ge and Sn forming binary or ternary solid solution and improves corrosion resistance and type 2 dopants include Ti, Zr, V, Mo, Nb, W forming binary or ternary boride phases in the grain boundary and improve microstructure and corrosion resistance.

In our present work, we have performed thorough investigation on the magnetic properties of  $\text{Nd}_4\text{Fe}_{73.5}\text{Co}_3\text{Hf}_{0.5}\text{Ga}_{0.5}\text{B}_{18.5}$  using the substituent element Co to enhance intrinsic properties such as saturation magnetization and Curie temperature and two dopants, Ga from type 1 and Hf from type 2 to improve microstructure, which leads to the improvement of hysteresis loop parameters and corrosion resistance forming a composition  $\text{Nd}_4\text{Fe}_{73.5}\text{Co}_3\text{Hf}_{0.5}\text{Ga}_{0.5}\text{B}_{18.5}$ . Annealing temperature and an-